

DANIEL MACIAS-VALADEZ

**IMPROVEMENT OF VERTICAL PRECISION IN GPS
POSITIONING WITH A GPS-OVER-FIBER
CONFIGURATION AND REAL-TIME RELATIVE
HARDWARE DELAY MONITORING**

Thèse présentée
à la Faculté des études supérieures de l'Université Laval
dans le cadre du programme de doctorat en Sciences Géomatiques
pour l'obtention du grade de Philosophiae Doctor (PhD)

DÉPARTEMENT DES SCIENCES GÉOMATIQUES
FACULTÉ DE FORESTERIE, DE GÉOGRAPHIE ET DE GÉOMATIQUE
UNIVERSITÉ LAVAL
QUÉBEC

2011

© Daniel Macias-Valadez, 2011

Résumé

Une des principales limitations du positionnement GPS est que la composante verticale est généralement 2 à 3 fois moins précise que la composante horizontale. Pour des applications de haute précision, il est possible d'atteindre, par méthode GPS en mode relatif, des précisions de l'ordre de quelques millimètres en composante horizontale mais non pas en composante verticale. Cependant, plusieurs applications, telles que l'auscultation de structures d'ingénierie, exigent une précision similaire tant en horizontal qu'en vertical. Par simulations, il a été démontré par (Santerre & Beutler, 1993), qu'il est possible d'améliorer la précision du positionnement vertical en utilisant un récepteur à antennes multiples et un calibrage précis du délai de propagation relatif dans les câbles et circuits électroniques séparant les antennes du récepteur. Cependant, aucune implémentation n'avait été faite à ce jour pour prouver le concept. L'objectif principal de ce travail de recherche a donc été de concevoir et d'implémenter un tel système et de démontrer qu'il permet une nette amélioration dans la précision du positionnement vertical. Pour ce faire, le défi principal a été de développer un système permettant simultanément le transport des signaux GPS sur fibres optiques et le calibrage précis du délai de propagation relatif entre ces mêmes fibres en temps réel. Une fois le premier prototype complété et testé, des expériences réalisées sur une poutrelle de calibrage utilisée comme ligne de base de référence démontrent qu'avec le prototype et le système de traitement des données proposé, une nette amélioration dans la précision du positionnement vertical a été observée. Tel que prévu par la théorie et les simulations, une amélioration d'un facteur 2 à 3 a été atteint, permettant ainsi d'obtenir la même précision dans la composante verticale que dans la composante horizontale. Ces résultats, qui représentent une percée importante dans le positionnement GPS de haute précision, permettent ainsi d'envisager le déploiement de ce type de systèmes dans des applications réelles où la même précision dans toutes les composantes tridimensionnelles est essentielle mais n'avait pas pu être atteinte auparavant par positionnement relatif GPS.

Abstract

One of the main limitations of GPS positioning is that the vertical component is generally 2 to 3 times less precise than the horizontal components. For high precision applications in relative mode, it is possible to reach horizontal precision of a few millimeters but not so for the vertical component. However, certain applications, such as monitoring deformation of engineering structures, require the same precision both in the vertical and the horizontal components. In (Santerre & Beutler, 1993), it was shown, using simulations, that it is nevertheless possible to improve the GPS vertical positioning precision by using a multi-antenna receiver and a precise calibration of the relative hardware delay (the propagation delay between the antennas and the receiver). However, no actual implementation of the system was done to prove the concept until now. The main objective of this research was thus to design and implement such a system and to prove that this will indeed enable an improvement in the vertical precision. To do so, the main challenge was the simultaneous operation of a GPS-over-fiber system and the precise real-time calibration of the relative hardware delay between the fiber optic cables. Once the first prototype and the observation processing software completed and tested, experiences were conducted with a calibration beam used as a very precise reference baseline and proved that, as expected by the theory and the simulations, the vertical positioning precision is improved. Specifically, a 2 to 3 improvement factor was observed in the vertical component precision so that it reached the same level of precision as the horizontal components. These results, which represent an important breakthrough in GPS positioning precision, will enable to use this type of configuration in several applications where the same precision in all 3D components is essential and had not been achieved before with standard relative GPS positioning techniques.

Acknowledgements

First of all, I would like to deeply thank my research director, Professor Rock Santerre, for his unrestricted support, guidance and encouragement during the years I worked on this project. I would like also to thank my two co-directors, Professor Sophie LaRochelle from the *Centre d'Optique Photonique et Laser* (COPL) at *Université Laval* and Professor René Jr. Landry from the *École de Technologie Supérieure* at Montreal. Both supported me from the very beginning of the project and gave me valuable advice and technical, scientific and logistical support. It is not easy to make a multi-disciplinary project that involves equipment and personnel from many laboratories, spanning two different Universities and cities, but my advisor and co-advisors always helped in making it possible. I would like to deeply thank Professor Gerhard Beutler, Dr. Michel Poulin and Professor Marc Cocard. It was truly an honor for me having them in my thesis committee. They all gave me very valuable advice to improve the quality of this thesis.

A lot of people helped me in the experimental stages of my research. From the Department of Geomatics Sciences, I would like to thank Stéphanie Bourgon for her help and advice on GPS data processing techniques, and Guy Montreuil and Jean-Claude Brière for their logistic support in installing the GPS antenna equipment. My appreciation also goes to Professor Marc Cocard and PhD student Omid Kamali, with whom I had many informal conversations regarding the project and both gave me valuable advice. From the LACIME laboratory of the *École de Technologie Supérieure* at Montreal, all my appreciation goes to Bruno Sauriol, Jean-Christophe Guay and Marc-Antoine Fortin who did a great job at developing the experimental FPGA-based GPS receiver used in this research and were always very helpful in giving me technical support for its use. From the *Centre d'Optique, Photonique et Laser* (COPL), I want to thank Benoît Filion, David Castonguay, Julien Dutel, Philippe Chrétien and Patrick LaRochelle for their valuable help in the stage of designing and building the prototype of the GPS-over-fiber system.

This research would not have been possible without the financial support coming from a grant given by the Natural Sciences and Engineering Research Council of Canada (NSERC) to my advisor Professor Rock Santerre and a grant given by the NSERC to my co-advisor Professor Sophie LaRoche. Also, the financial help from the *Fonds de Soutien au Doctorat* of the Faculty of Forestry, Geography and Geomatics was also greatly appreciated.

Finally I would like to express a few words of gratitude and thoughts to my best friends, my parents, my sons and specially my wife Lizbeth, who always encouraged and supported me during these years as a PhD student. These words I would like to express them in Spanish, one of my two mother tongues:

A mis amigos “amenos”, Daniel, Miguel, Guillermo, David y Humberto, gracias por su amistad y porque en parte gracias a ustedes, me animé a seguir estudiando. Llama la atención de que entre nosotros haya 3 doctores, 1 maestro y 2 doctores “en proceso”. Creo que valoramos mucho el conocimiento, el pensamiento crítico y el método científico y gracias a nuestra amistad hemos reforzado estos valores. Claro que por encima de todo, está la amistad incondicional en sí y los inolvidables momentos pasados juntos.

A mis padres, agradezco el apoyo y el cariño constante e incondicional. Ustedes me transmitieron el gusto al estudio y a las ciencias y sobre todo, me transmitieron valores humanos y representan para mí un ejemplo a seguir.

Liz, muchas gracias por apoyarme en esta aventura del doctorado. Sé que implicó sacrificios por parte de la familia pero siempre salimos adelante gracias a ti. Tu amor y aliento fueron fuente de inspiración para seguir siempre adelante.

*En honor a mis ancestros Macias-Valadez:
mi bisabuelo Samuel, mi abuelo Daniel y en
especial mi padre Guido, profesionistas
exitosos que supieron transmitir de
generación en generación el amor al estudio
y al conocimiento sin perder nunca los
valores humanos*

Table of contents

Résumé.....	i
Abstract.....	ii
Acknowledgements.....	iii
Table of contents.....	vi
List of tables.....	viii
List of figures.....	ix
List of abbreviations and acronyms.....	xi
List of symbols.....	xiii
1 Introduction.....	1
1.1 Motivation.....	1
1.2 Objectives.....	4
1.3 Methodology.....	5
1.4 Contributions of the research.....	6
1.5 Structure of the thesis.....	7
2 GPS signals: propagation, perturbations, measurements and positioning.....	9
2.1 Time measuring and ranging.....	9
2.2 GPS signal characteristics.....	14
2.3 Atmospheric propagation.....	18
2.3.1 Ionosphere propagation.....	19
2.3.2 Troposphere propagation.....	22
2.4 Transmission line propagation.....	26
2.4.1 Thermal effects on coaxial cable and optical fiber propagation.....	27
2.4.2 Optical fiber propagation and dispersive effects.....	31
2.5 Antenna phase center variation and multipath effects.....	36
2.5.1 Antenna phase center variation.....	36
2.5.2 Multipath effects.....	38
2.6 GPS receiver and its main measurements.....	40
2.7 GPS observations and their equations.....	48
3 System design for the proposed architecture.....	60
3.1 Theoretical background and previous works.....	60
3.1.1 Vertical component precision improvement.....	60
3.1.2 Hardware delay calibration and temperature influence.....	63
3.1.3 GPS-over-fiber systems.....	65
3.1.4 Multi-antenna receiver.....	68
3.1.5 Existing GPS-over-fiber solutions.....	71
3.1.6 Measurement techniques for relative propagation delay.....	72
3.2 Integrated GPS-over-fiber and real-time delay measurement solution.....	75
4 Performance criteria for the proposed GPS-over-fiber architecture.....	85
4.1 Carrier-to-noise performance criterion.....	86
4.1.1 Carrier power level.....	87
4.1.2 Noise power level.....	89
4.1.3 Distortion and phase noise.....	92

4.1.4	Harmonics and cross-interference	97
4.1.5	Summary	100
4.2	Positioning criterion.....	101
4.2.1	Impact of the absolute ionospheric bias on position.....	104
4.2.2	Effects of the relative tropospheric bias on positioning	105
4.2.3	Effects on positioning of the relative hardware bias.....	106
4.2.4	Effect of satellites orbit errors	107
4.2.5	Summary	108
4.3	Relative hardware delay measurement	110
4.4	GPS positioning processing strategy and software.....	120
5	Experimental results	124
5.1	Basic performance tests during the design period	125
5.1.1	Noise measurement tests.....	125
5.1.2	Simulated GPS signal correlation tests.....	132
5.1.3	Real GPS signal correlation tests.....	134
5.1.4	Relative delay monitoring tests.....	137
5.2	Zero baseline tests.....	139
5.2.1	Analysis of interchannel biases and noise with a zero baseline configuration 139	
5.2.2	Positioning analysis using a zero baseline configuration	143
5.2.3	Impact of temperature variations on the RF circuits using a zero baseline configuration.....	150
5.3	Short baseline tests.....	154
5.3.1	Short baseline choice	154
5.3.2	Beam orientation procedure.....	155
5.3.3	Experimental setup and sessions.....	157
5.3.4	Experimental results	158
5.3.5	Multipath analysis.....	167
6	Conclusions and further works	171
6.1	Summary of results and analysis	171
6.2	Suggestions for further works.....	174
	Bibliography	178
	Appendix A Detailed schematics and components' list for the proposed architecture	185
	Appendix B C/N0 comparison between the standard GPS-over-cable case and the proposed GPS-over-fiber case.....	189
	Appendix C Comparison of positioning results without and with tropospheric parameter estimation.....	191

List of tables

Table 2.1 Main characteristics of PRN codes used in GPS	17
Table 2.2 Summary of GPS signals characteristics	18
Table 2.3 Thermal Coefficient of Delay for some type of cables	30
Table 3.1 Improvement factor of the vertical component between the standard and the proposed configurations.....	62
Table 3.2 Main performance criteria for a radio-over-fiber system	67
Table 3.3 Main characteristics of some commercial GPS-over-fiber solutions	72
Table 4.1 Summary of the types of noise in a radio-over-fiber system.....	100
Table 4.2 Example of normalized confidence ellipsoid calculated with a variance-covariance matrix, for mid-latitude site and a 15° elevation mask angle	103
Table 4.3 Ionospheric effect (constant TEC value) for mid-latitude site and a 15° elevation mask angle	104
Table 4.4 Effect of relative zenith tropospheric errors on coordinates for mid-latitude site and a 15° elevation mask angle.....	106
Table 4.5 Effect of relative receiver hardware errors (ΔH) on coordinates for mid-latitude site and a 15° elevation mask angle for the proposed approach	107
Table 4.6 Type of biases affecting GPS positioning	109
Table 4.7 Approximate thermal specifications for some selected components of the RF front-end.....	116
Table 5.1 List of controlled variables for noise measurement tests.....	129
Table 5.2 Average difference (AD) between C/No with and without optical circuit.....	135
Table 5.3 Main characteristics of the calibration beam	155
Table 5.4 Sessions for small baseline experiments.....	158
Table 5.5 Summary of small baseline positioning results	167
Table 6.1 Vertical positioning results for zero baseline	173
Table 6.2 Summary of positioning results for small baseline.....	174
Table A.1 Components' list.....	188

List of figures

Figure 2.1 Comparison of the timekeeping ability of many clocks as a function of the time after synchronization and syntonization	10
Figure 2.2 Example of PRN sequence and its normalized autocorrelation	16
Figure 2.3 Generation of a DSSS signal by mixing an RF carrier with data stream and a spreading code	18
Figure 2.4 Modulation of an optical carrier by a RF signal.....	33
Figure 2.5 Attenuation of a RF-over-fiber signal at 1560 nm due to dispersive effects in a monomode SMF-28 fiber.....	34
Figure 2.6 Block diagram of a typical GPS receiver	41
Figure 2.7 Block diagram of a demodulation channel of a GPS receiver	42
Figure 2.8 Phase noise on PLL	47
Figure 3.1 Comparison between standard baseline configuration and proposed baseline configuration.....	61
Figure 3.2 Proposed architecture for the GPS-over-fiber with real-time relative hardware delay calibration.....	79
Figure 3.3 Spectrum of the signals in the proposed architecture.....	80
Figure 4.1 Basic radio-over-fiber transmission system with both direct modulation of the laser and external optical modulation of a semiconductor optical amplifier	86
Figure 4.2 Typical laser optical spectrum.....	95
Figure 4.3 Phase-shift technique to compare the differential propagation delay between two paths and used in the RDM device	110
Figure 4.4 Proposed architecture with the different hardware delays shown.....	113
Figure 4.5 Zero baseline configuration for hardware delay calibration	117
Figure 4.6 Data flow for the processing software.....	123
Figure 5.1 Model for GPS-over-fiber system	126
Figure 5.2 Experimental setup for noise figure measurements	127
Figure 5.3 Noise figure of the GPS-over-fiber system (IF=24MHz) for various values of the optical power at the SOA input.....	130
Figure 5.4 Measured IMD3 for the system.....	131
Figure 5.5 Experimental setup for simulated GPS signal measurements.....	133
Figure 5.6 Comparison of the C/No for the cases without and with optical circuit	134
Figure 5.7 Comparison of C/No with and without optical circuit for satellites 1, 7 and 11	136
Figure 5.8 Phase comparator's: a) transfer function and b) deviation from linear fit	138
Figure 5.9 Single differences of observations after removing ambiguities for a zero baseline and GPS-over-cable configuration. The satellite tracked by each pair of channels may change during the 15 hour interval.	141
Figure 5.10 Residual noise of single difference observations for a zero baseline and GPS-over-cable configuration	142
Figure 5.11 Experimental setup for zero baseline configuration.....	144

Figure 5.12 Single difference of phase observations (minus integer ambiguity part), output of phase comparator and temperature for session 1	145
Figure 5.13 Single difference of phase observations (minus integer ambiguity part), output of phase comparator and temperature for session 2	146
Figure 5.14 Positioning solution for zero baseline using the standard approach and the proposed solution for session 1	148
Figure 5.15 Positioning solution for zero baseline using the standard approach and the proposed approach for session 2	149
Figure 5.16 Different signal path delays on the zero baseline configuration for temperature variation tests	151
Figure 5.17 (a) Single difference of phase observations (minus integer ambiguity part), (b) output of phase comparator and (c) temperature for session 3	152
Figure 5.18 Standard and proposed approach positioning solution for zero baseline for session 3	153
Figure 5.19 Calibration beam with two antennas mounted	155
Figure 5.20 Reference coordinates of the baseline	156
Figure 5.21 Experimental setup for short baseline configuration.....	157
Figure 5.22 Positioning results for session 148A	160
Figure 5.23 Positioning solution for session 149A.....	161
Figure 5.24 Positioning solution for session 148R	162
Figure 5.25 Positioning solution for session 150A.....	163
Figure 5.26 Comparison of positioning results without and with relative tropospheric zenith delay estimation for session 149A	166
Figure 5.27 Comparison of vertical positioning between day 148 (session 148A) and day 149 (session 149A) for the standard approach.....	168
Figure 5.28 Comparison of vertical positioning between day 148 and day 149 for the proposed approach	168
Figure 5.29 Positioning results for session 149A with the use of sidereal multipath filtering using data from session 148A.....	170
Figure A.1 Detailed schematics for the remote station.....	186
Figure A.2 Detailed schematics for the local station	187
Figure C.1 Comparison without and with tropospheric parameter estimation for session 148A.....	193
Figure C.2 Comparison without and with tropospheric parameter estimation for session 148R.....	193
Figure C.3 Comparison without and with tropospheric parameter estimation for session 150A.....	193

List of abbreviations and acronyms

ACC	: Accumulated Code Phase
ACP	: Accumulated Carrier Phase
ADR	: Accumulated Doppler Range
ASE	: Amplified Spontaneous Emission
A/D	: Analog to Digital
BER	: Bit Error Rate
BPSK	: Binary Phase Shift Keying
CNR	: Carrier-to-Noise Ratio (dB)
C/N ₀	: Carrier-to-Noise Density Ratio (dB/Hz)
DC	: Direct Current
DD	: Direct Detection
DFB	: Distributed FeedBack
DM	: Directly Modulated
DOP	: Dilution Of Position
DSSS	: Direct Sequence Spread Spectrum
EDOP	: East Dilution Of Position
FPGA	: Field-Programmable Gate Array
GIVE	: Grid Ionospheric Vertical Error
GNSS	: Global Navigation Satellite Systems
IF	: Intermediate Frequency
IGS	: International GNSS Service
IMD3	: Third order InterModulation Distortion
LED	: Light-Emitting Diode
LNA	: Low Noise Amplifier
LO	: Local Oscillator
NCO	: Numerically Controlled Oscillator
NDOP	: North Dilution Of Position
PD	: Photo-Detector
PLL	: Phase-Locked Loop
ppm	: parts per million
p-i-n	: p-type semiconductor, intrinsic semiconductor, n-type semiconductor
PMD	: Polarization Mode Dispersion
PPS	: Pulse Per Second
PRN	: Pseudo-Random Noise
PSK	: Phase Shift Keying
RDM	: Relative Delay Monitoring device
RF	: Radio Frequency
RHD	: Relative Hardware Delay
RIN	: Relative Intensity Noise (of a light source)
rms	: Root Mean Square
RTZD	: Relative Tropospheric Zenith Delay
SOA	: Semiconductor Optical Amplifier

TAI	: <i>Temps Atomique International</i> (International Atomic Time)
TCD	: Thermal Coefficient of Delay
TEC	: Total Electron Content (in ionosphere)
UTC	: Coordinated Universal Time
VDOP	: Vertical Dilution Of Position
VHF	: Very High Frequency
VODL	: Variable Optical Delay Line
WAAS	: Wide Area Augmentation System

List of symbols

Latin

A_{eff}	: Effective area of the optical fiber
B, BW	: Bandwidth
c	: Speed of light in vacuum
C_{high}	: Upper threshold for correlation peak (maximum value)
C_{low}	: Lower threshold for correlation (minimal value, ideally = 0)
d_{pc}	: Range error due to antenna phase center variation
$dT^{\text{s}}(t), dT_{\text{r}}(t)$: Satellites and receiver's relative clock errors
$d\dot{T} = d\dot{T}^{\text{s}} + d\dot{T}_{\text{r}}$: Transmitter and receiver clock drift
$d\dot{T}$: Transmitter and receiver clock drift
D	: Dispersion parameter of an optical fiber
e	: Water vapor pressure
f	: Frequency of the signal
F_{t}	: Noise figure
H	: Hardware delay (propagation delay of the signal between the antenna and the receiver or emitter)
$H^{\text{s}}, H_{\text{r}}$: Hardware delay on the satellite and the receiver
i_{d}	: Current driving a laser
i_{pd}	: Current at the photodetector
I_{th}	: Laser threshold current
I_{pd}	: Average photocurrent at the photodiode
I_{dark}	: Photodiode dark current
I_{DC}	: DC driving current of a laser
I_{g}	: Ionospheric error due to the group delay on the signal
I_{p}	: Ionospheric error due to the phase delay on the signal
$I_{\text{e}}, I_{\text{p}}, I_{\text{l}}$: In-phase Early, Prompt and Late Correlators
K	: Observation weight matrix
k_{B}	: Boltzmann constant
L	: Length
m	: Modulation index
m_{p}	: Error due to multipath effect
n	: Refractive index
n_{eff}	: Effective refractive index of an optical fiber
n_{g}	: Effective group refractive index
N	: Refractivity
$N(t_0)$: Integer initial phase ambiguity
N_0	: Electron density (number of electrons per volume)
$n_{2,l}$: Non-linear parameter related to the third order electric susceptibility $\chi^{(3)}$ of the optical fiber material

N	: Normal matrix
p	: Atmospheric pressure
P_r^n	: Pseudorange from receiver (r) to satellite (n)
P_d	: Pressure of the dry atmosphere (mbar)
P_L	: Optical power of a laser
P_{opt}	: Optical power
P_0	: Photon number (number of photons per volume)
q	: Charge of the electron
Q_e, Q_p, Q_l	: In-quadrature Early, Prompt and Late Correlators
R_L	: Load resistance
R_{pd}, R_0	: Responsivity of a photodetector
$s^s(t)$: Signal generated by the GPS satellite
$s_r(t)$: Signal generated by the GPS receiver
$s^s\left(t - \frac{\rho}{c}\right)$: Signal generated by the GPS satellite after propagation of a distance ρ
$s_r(t - \tau)$: Locally generated signal at the receiver with a time shift τ
S	: Path taken by the electromagnetic signal between the satellite and the receiver
t	: GPS time (“true” time)
t_0	: Initial time
T^s, T_r	: Time using the satellites and receiver’s clocks as reference
T	: Temperature (K)
V	: Vector of observations residuals
W	: Misclosure vector (observed – calculated)
X^s, Y^s, Z^s	: 3D geocentric coordinates of the satellite
X_r, Y_r, Z_r	: 3D geocentric coordinates of the receiver
X	: Vector of unknowns

Greek

β	: Spontaneous emission factor in the laser
γ	: Ratio of spontaneous emission to photon lifetime in the laser
Γ	: Tropospheric delay
Γ_z	: Zenith tropospheric delay
$\Gamma_{dry}, \Gamma_{wet}$: Dry and wet tropospheric delay
Δ	: Differentiation operator between a simultaneous observation from one site and the observation from another site to a common satellite
Δf	: Doppler shift (Hz)
ΔH	: Relative hardware delay between receivers
ϵ	: Gain compression parameter of the laser
ϵ_0	: Vacuum permittivity
ϵ_r	: Relative permittivity of a medium
ϵ_p	: Remaining noise and unmodeled biases for a code observation

ε_ϕ	: Remaining noise and unmodeled biases for a phase observation
Φ	: Phase observation
$\phi_c(t), \phi_{LO}(t)$: Carrier and LO phase noise
ϕ_0^s	: Initial phase of satellite oscillator at time t_0
$\phi_{0,r}$: Initial phase of receiver oscillator at time t_0
λ	: Wavelength of an electromagnetic wave
μ_0	: Vacuum permeability
μ_r	: Relative permeability of a medium
v	: Speed of light in a medium
$v_{s,r}$: Relative topocentric radial velocity between the satellite (s) and the receiver (r)
ρ	: Geometric distance between the satellite and the receiver
$\hat{\sigma}^2$: A posteriori variance factor
τ	: Time shift, as controlled by the receiver, of the locally generated signal
τ_I	: Integration time of correlator at the receiver
ω_c, ω_{LO}	: Carrier and LO frequencies
∇	: Differentiation operator between a simultaneous observation to a given satellite and an observation to another satellite

1 Introduction

1.1 Motivation

In standard GPS positioning applications, it is a well-known fact that it is not possible to get the same precision for the vertical component as for the horizontal components. Indeed, experiments and simulations consistently show that the vertical component is 2 to 3 times less precise than the horizontal components. This result holds for low-cost, stand-alone GPS receivers and for high precision geodetic-grade receivers whether in absolute or relative positioning modes. Both the homogeneity of the satellite sky distribution and the strong correlation between the vertical component and some of the main systematic biases (receiver clock error and tropospheric bias) in the observations explain this fact. Indeed, since GPS satellite sky distribution can never be homogenous on the vertical component, as there are no visible satellites under the horizon, errors on the pseudorange and phase observations propagate more adversely on the vertical component than on the horizontal components (Santerre, 1991). This is why biases such as tropospheric delays and receiver clock errors mostly affect the vertical component precision. A simplified way to understand this is to take as an example the effect of a systematic error on the pseudorange from a satellite that is located on the East. If the same systematic error is present on the signal coming from a satellite on the West, this error may partially cancel out on the East-West component. However, an error on the pseudorange from a satellite above the horizon cannot be canceled out by a satellite under the horizon. The effect of the systematic error on the vertical component is thus greater.

For small baselines (up to a few kilometers), in which orbital errors, relative ionospheric biases can be mostly eliminated, the relative tropospheric biases and the receivers' relative biases such as hardware delays in cables and electronics circuits and specially the receiver

clock error, remain the main limiting factor in the vertical component precision. Hardware delays and receiver clock errors are often taken together as a single parameter, called clock parameter, as they are closely related and usually cannot be separated. This clock parameter must be estimated in a least-square adjustment along with the 3D coordinates, either explicitly for single difference between receivers processing, or implicitly for double differences processing, between receivers and between satellites. However, the estimated clock parameter and the optionally estimated tropospheric parameter remain altogether highly correlated with the vertical baseline component and thus limit the vertical precision (Santerre, 1991). Typical correlation factor between the clock parameter and the vertical component is around 0.97.

In applications where vertical precision similar to horizontal precision is needed, GPS positioning solutions alone are not sufficient. They must be complemented with standard geodetic leveling procedures, which are expensive and time consuming and do not enable an automatic, continuous, real-time monitoring. However, there is a growing interest in being able to continuously monitor movements and deformations in man-made structures that have to withstand strong external forces such as bridges, dams, skyscrapers or also in terrains that are subject to movements such as volcanoes, landslides, ground subsidence, etc. GPS solutions already exist but, as mentioned previously, cannot reach the same level of precision in the vertical component as in the horizontal components.

In order to overcome this limitation and, considering what has been exposed in the previous paragraphs, it is clear that one should either provide a better vertical homogeneity of the satellites sky distribution or deal with the relative receivers' biases and the high correlation between the vertical component and the clock parameter by eliminating, reducing and/or accurately quantifying them. The first option is impossible since GPS satellites under the horizon cannot be tracked. However, there are some devices, called pseudolites, whose function is to emulate and transmit GPS satellites' signals and which can be placed under the horizon of the receiver's antenna (Barnes, et al., 2005). The problem with this type of approach is that it is limited to only a few situations where pseudolites can effectively be placed under the receiver's antenna. GPS receivers on aircraft can easily pickup GPS

signals coming from underneath but for civil engineering structures, it is more difficult or even impossible. Additionally, in some countries RF spectrum licenses are required to use pseudolites, short distances between the pseudolites and the receiving antennas may cause saturation problems in the receivers and multipath effects are often present. Due to these inconveniences with the use of pseudolites, we focused on the second option, that is, to deal with the remaining receivers' relative clock error.

How do we deal with this remaining receivers' bias? The first impulse would be to simply do what is traditionally done to remove receivers' clock errors and hardware delays: double difference processing. However, with double differences, even if mathematically we eliminate receivers' biases, the net effect is null when compared with a single difference solution with clock parameter estimation. In fact, the double difference solution is equivalent with a single difference solution with receivers' biases (relative clock error and hardware delay) estimation. As demonstrated and reported by (Lindlohr & Wells, 1985), there exists a fundamental differencing theorem stated as follows: "Linear biases can be accounted for either by reducing the number of observations so that the biases cancel, or by adding an equal number of unknowns to model the biases. Both approaches give identical results."

Thus, a solution with both single difference processing and relative receivers' bias elimination and/or accurate quantification is needed. Relative receivers' biases can further be broken down in two main components: the relative receiver clock errors (ΔClk), that is, the difference between the clock errors of each receiver and the relative hardware delay (ΔH), which represents the difference between the propagation delay of the GPS signal from one of the antennas to the receiver (including propagation on cable and electronic circuits) and the same propagation delay from a second antenna to another receiver. The relative receiver clock error may be eliminated if a common reference clock is used by all receivers or if a single receiver with increased channel capacity so as to accept more than one antenna is used. The first solution is less practical if the receivers are far apart since the clock reference would need to be transmitted to each receiver but can be practical if the receivers are located in the same room (Schreiner, 1990). This second solution was

proposed by (Santerre & Beutler, 1993), in which all the antennas are connected to a single GPS receiver. Along with a careful calibration of the relative delay between the antenna cables (ΔH), receiver clock errors (ΔdT_r) can be eliminated by single differentiation between antennas. Through simulations, it was shown that this configuration would lead to a 2 to 3 times improvement in the precision of the vertical component determination (Santerre & Beutler, 1993). With this improvement, one could ideally reach a few millimeter vertical precision for baselines of up to a few kilometers if ΔH is calibrated at the millimeter level. This breakthrough implies that applications where 3D millimetric positioning precision is needed, such as deformation monitoring of civil engineering structures, could use GPS technology with all its benefits: autonomy, continuous operation and lower cost on the long term. However, to develop a GPS architecture based on this principle, two main issues must be resolved to successfully implement this multi-antenna-to-one-receiver system. First, the distance between the antennas and the single receiver can reach several kilometers. Second, height precision improvement can only be reached if the relative propagation delay between the antennas and the receiver (ΔH), is monitored at the millimeter-level (Santerre & Beutler, 1993). By using “GPS-over-fiber” solutions, we can address the first issue but existing commercial solutions do not include real-time monitoring of these relative propagation delays. Additionally, phase stability is very important for high precision applications that must use GPS carrier phase measurements, so additional noise added by the optical components must be minimized and controlled. The second issue, the real-time monitoring of ΔH has not been addressed before in a GPS high precision positioning application.

1.2 Objectives

Presently, as exposed previously, GPS positioning solutions suffer from an inferior precision in the vertical component compared to the horizontal components and this has limited their deployment in some high precision applications, such as monitoring of man-

made structures. Even if it has been demonstrated, theoretically and through simulations, that this limitation can be overcome (Santerre & Beutler, 1993), no implementation was done before. Considering that the technology for optical transport of RF (radio frequency) signals has become more accessible and available, we have advanced the hypothesis that it is now possible to implement a multi-antenna GPS system with real-time relative hardware delay monitoring in order to achieve a two to three time improvement in vertical positioning precision in relative mode. This improvement in vertical precision, so that it becomes comparable to the horizontal precision, is thus the main objective of this work.

1.3 Methodology

This research is largely based on the experimental validation of the main hypothesis that the vertical precision of relative GPS positioning can be improved with a multi-antenna configuration along with a real-time precise calibration of the relative hardware delay of the GPS signals from the antennas to the receiver. We can divide the research work in two phases: 1) the system design and 2) the experimental validation of the main hypothesis. In the system design phase, additionally to the analysis of similar systems and what the main needs and requirements are for our prototype, we defined the desired performance criteria that the individual parts of the system and the system as a whole should meet. Experimental work using simulated and real GPS signals was done to validate these performance criteria by adjusting the main independent variables of the system.

To sum up, the first phase of the project is a design/optimization/integration process, with the following main steps:

- 1) Design of the real-time relative delay monitoring system and GPS-over-fiber system.

- 2) Optimization for minimal degradation of the GPS signal by the optical circuit and the relative propagation delay monitoring system. Experimental tests of GPS signal and relative delay signal quality using defined performance criteria.
- 3) Integration of the measured relative delay on the optical fiber to the GPS processing software.
- 4) Integration with a multi-antenna GPS software defined receiver.

For the experimental validation of the main hypothesis, reference baselines whose 3D components are already known at sub-millimetric level were used so that the GPS positioning solution could be validated using these external references as “true” references.

Since the main hypothesis implies an improvement with respect to the standard, currently used, GPS processing method, a comparative analysis will be performed by using the standard processing method and the new, proposed processing method. Limitations in the relative hardware delay monitoring capabilities of the system and the presence of additional biases such as multipath effects are factors that must be taken into consideration to analyze the results obtained and their limitations.

1.4 Contributions of the research

We believe that improving the vertical precision of GPS relative positioning for high precision application is a significant breakthrough that could open the GPS positioning to new applications where great precision is needed such as the deformation monitoring of civil engineering structures. This would enable to reach ultimate GPS precision in all 3D components. This improvement is what can be considered the main contribution of this research. For the developed “Fiber optic architecture for high precision GPS”, a patent is pending following an international application on March 2010 (Macias-Valadez, Santerre, & LaRochelle, 2010). Other contributions and novelties are the following:

- Innovative GPS-over-fiber design that allows two signals (GPS and oscillator) to travel simultaneously over fiber without interference.
- Cost optimized design so that the proposed GPS-over-fiber system can be a cost-effective solution compared to current GPS solutions using several receivers.
- The design of the real-time Relative hardware Delay Monitoring device (RDM) that can operate simultaneously with the GPS signal transport over fiber.
- The adaptation of a single difference GPS processing software that enables the use of additional external data (coming from the RDM device).
- New design for the RF front-end that uses only one oscillator (instead of two as the original RF front-end had) to interface with the software defined GPS receiver.

1.5 Structure of the thesis

The structure of this thesis is as follows.

Chapter 2 contains theoretical background and overview of the GPS system, emphasizing on how the main observations are obtained, how they are affected by external biases, particularly when propagating over cable and optical fiber and how the main observations are processed for obtaining a positioning solution.

Chapter 3 describes the previous studies related to this research and how the basic design of the prototype for the proposed GPS-over-fiber architecture was realized.

Chapter 4 presents the main performance criteria we used to test the prototype in order to reach the main objective of this research.

Chapter 5 presents the results of the experiments that were done for meeting the performance criteria exposed in Chapter 4 and for proof-of-concept of the prototype.

Chapter 6 summarizes findings, draws the conclusions and discusses about current limitations and future improvements and topics for further investigation.

Appendix A presents the detailed schematics of the proposed GPS-over-fiber architecture as a complement to Chapter 3.

Appendix B shows, as a complement to Chapter 5, additional experimental results with graphics showing the comparison of the carrier-to-noise ratio for the standard GPS-over-cable system and for the proposed GPS-over-fiber system.

Appendix C shows, as a complement to Chapter 5, additional experimental results comparing the positioning results without and with a tropospheric parameter estimation.

2 GPS signals: propagation, perturbations, measurements and positioning

This chapter gives an overview of how the GPS signals are generated and received, what the main perturbation factors are and how they are used to obtain a positioning solution. The theoretical background given in this overview will help us understand what are the main issues we have to deal with in high precision GPS positioning.

2.1 Time measuring and ranging

GPS positioning is based on ranging between a receiver and several satellites using a particular set of signals generated by the satellites. More specifically, the receiver measures the time it takes for a signal emitted at the satellite to reach the receiver. This signal propagation time is then multiplied by the speed of light in vacuum to obtain the satellite-to-receiver distance. The fundamental variable used in GPS ranging is thus time. Both the satellites and the receiver need clocks to measure time and more specifically in the case of the receiver, the traveling time of an electromagnetic signal. Broadly speaking, a clock is a device in which three steps must be accomplished:

- 1) Choose a regular periodic physical phenomenon.
- 2) Choose an arbitrary reference (Time “zero”) and time frame.
- 3) Count and keep track of the number of periods/cycles of the phenomenon.

The selection of the physical phenomenon has a direct impact on the accuracy and stability of the clock. The more regular the physical phenomenon, the greater the stability of the period/frequency of the phenomenon is. On the other hand, the accuracy is related to how close the period/frequency of the phenomenon is to the period/frequency of a “true” time

reference. Generally, the “true” time reference is arbitrarily chosen but must be more precise and stable than the periodic phenomenon we are measuring. The stability and the accuracy of a clock are not completely independent. Historically, the first physical phenomena used to keep track of time were the Earth’s rotation period, the orbital period of the Earth, the Moon, the other planets, the satellites or the apparent movement of the stars. The movement of these celestial bodies is quite regular and may be considered stable for most applications but not accurate enough to measure small amounts of time (seconds or less). Nowadays, high frequency oscillations such as those provided by a quartz oscillator are used so that better accuracy can be achieved but depending on the quality, the stability may vary considerably. In Figure 2.1, adapted from (Allan et al., 1997), the clock timekeeping ability, which is equivalent to the accuracy, of different kind of clocks is presented as a function of the time since an initial synchronization (time adjustment with respect to the reference time) and an initial syntonization (frequency adjustment with respect to a reference frequency), which is a way of assessing the stability.

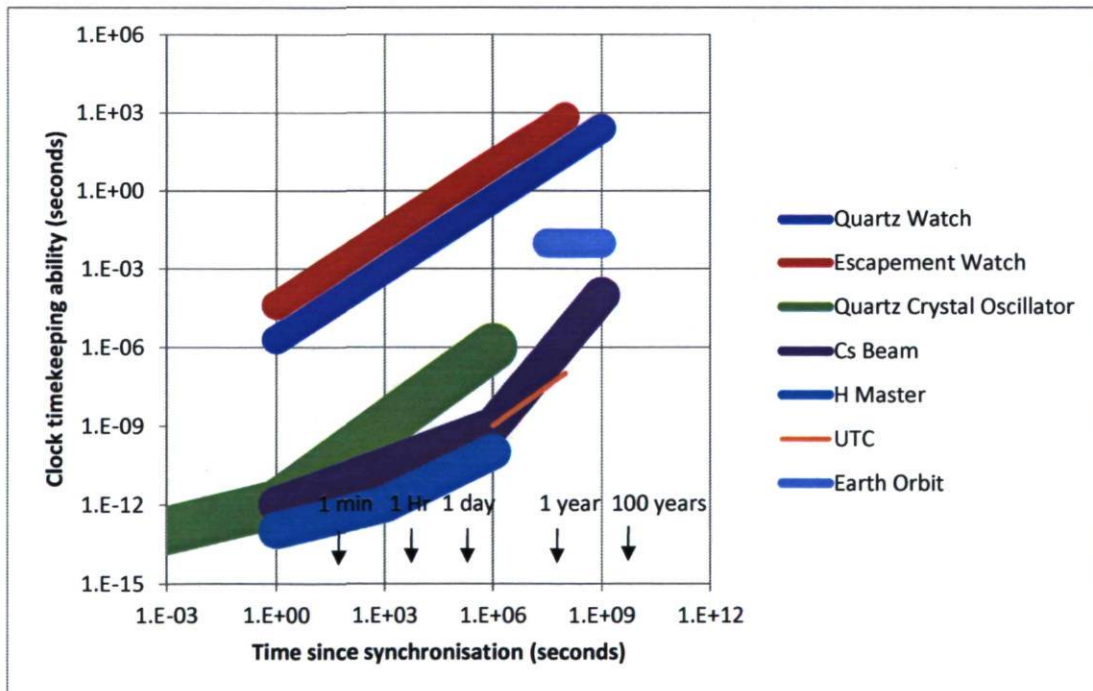


Figure 2.1 Comparison of the timekeeping ability of many clocks as a function of the time after synchronization and syntonization (adapted from (Allan et al., 1997))

In the case of GPS positioning, propagation time of the signals being measured is between 0.07 and 0.09 s approximately, depending on the elevation angle of the satellite (the distance from the surface of the Earth to a GPS satellite is between 20000 and 26000 km). The measurement of this propagation time must be done at nanosecond accuracy in order to get sub-meter accuracy on the range. This accuracy can be achieved with inexpensive quartz crystal oscillators but their stability is not sufficient for GPS applications. This is why atomic clocks are used on GPS satellites and tracking stations. Most GPS receivers use nevertheless a quartz clock, for practical and economic reasons. Indeed, GPS receivers can use inexpensive quartz oscillators because of their ability to synchronize with the satellites' more accurate and stable atomic clocks. That means they can overcome the receiver's clock inferior stability by adjusting continuously to match the satellites' clocks, which are all synchronized to a reference time frame called "GPS time". Before getting into details regarding this matching of the receiver clock to the satellites', let us go back to time measurement. In steps 2 and 3 previously mentioned, the zero time reference and the counting of the cycles must be done with respect to a reference time frame. This reference time frame must be of equal or better accuracy and stability than the clock's and, especially in the case of GPS, all clocks must use the same reference. Nowadays, what is used as a unified reference time is the TAI (*Temps Atomique International*) as defined at the *Bureau International des Poids et Mesures* in France and is the result of the combination of the time kept by various observatories around the world using very precise atomic clocks. From TAI, UTC (Coordinated Universal Time) and GPS time are derived. The latter is a reference time used by the U.S. Naval Observatory and adjusted to differ no more than 1 μ s from TAI (U.S. Naval Observatory, 2010). Additionally, it has a constant time shift of a few leap seconds (15 seconds on January 2009) with respect to TAI. GPS time is the time reference of the whole GPS system and will be referred from now on as the "true" time with the symbol t .

Let us first assume that all satellites and the receiver's clocks are perfectly synchronized with GPS time. If a given satellite generates and transmits a specific signal $s^s(t)$, this signal will be received by the receiver after a certain amount of the time, the propagation time,

which is proportional to the distance between the satellite and the receiver. If we neglect the atmospheric propagation effects, the received signal is: $s^s(t - \frac{\rho}{c})$ where ρ is the distance and c is the speed of light in vacuum. The receiver can generate a replica of this same signal $s_r(t)$ such that $s^s(t) = s_r(t)$. In order to compare the received signal and the locally generated signal and find the distance ρ , the signals $s^s(t)$ and $s_r(t)$ have the following properties:

$$s^s(t) = s_r(t) \quad 2.1$$

$$\int_{t_0}^{t_0 + \tau_1} \left| s^s\left(t - \frac{\rho}{c}\right) \cdot s_r(t - \tau) \right| dt \geq C_{high} \text{ for } \tau = \frac{\rho}{c} \quad 2.2$$

$$\int_{t_0}^{t_0 + \tau_1} \left| s^s\left(t - \frac{\rho}{c}\right) \cdot s_r(t - \tau) \right| dt \leq C_{low} \text{ for } \tau \neq \frac{\rho}{c} \quad 2.3$$

for $0 < \tau < t_{max}$

where,

$s^s\left(t - \frac{\rho}{c}\right)$: Received signal after propagation of a distance ρ

$s_r(t - \tau)$: Locally generated signal at the receiver with a time shift τ

t_0 : Initial time of signal processing

τ_1 : Integration time

C_{high} : Upper threshold for correlation (maximum value), depends on design and implementation

C_{low} : Lower threshold for correlation (minimal value, ideally = 0)

τ : Time shift (this can be controlled by the receiver)

These properties mean that a high correlation value must exist between the received signal, $s^s(t - \frac{\rho}{c})$ and the time shifted locally generated signal $s_r(t + \tau)$ only if $\tau = \frac{\rho}{c}$. These properties are chosen because they enable a practical implementation. By multiplying (mixing) the received and the locally generated signal, integrating (accumulating) the resulting signal and comparing it with threshold values, the receiver can adjust τ until it matches $\frac{\rho}{c}$ and thus obtain the distance between the receiver and the satellite.

In the previous paragraph, it was assumed that satellites and receivers were perfectly synchronized with GPS time. More realistically, satellites and receivers' clocks drift with respect to GPS time and a clock error exists between their clock and GPS time:

$$T^s = t + dT^s(t) \quad 2.4$$

$$T_r = t + dT_r(t) \quad 2.5$$

where,

T^s, T_r : Time using the satellites and receiver's clocks as reference

dT^s, dT_r : Satellites and receiver's clock errors

In this case, the time shift τ determined by the receiver contains not only the true range $\frac{\rho}{c}$ but also the satellite and receiver's clock errors:

$$t + dT^s - \frac{\rho}{c} = t + dT_r - \tau$$

$$\tau = \frac{\rho}{c} - dT^s + dT_r \quad 2.6$$

The satellite clock error for each satellite is accurately estimated by the control segment of the GPS and broadcasted by the satellites to the receivers so they can take it into account. The receiver's clock error cannot be neglected, especially for quartz oscillators, since even a drift of a few microseconds can translate into an error in the estimated range of several

hundred meters. By using observations from different satellites, the receiver's clock error may be estimated as an additional parameter or it may be eliminated through differentiation. Details will be given in the following chapters.

Finally, we must take into account that in the previous paragraphs, additional propagation biases and noise that affect the signal were neglected. Equation 2.6 must then be corrected to take into consideration all these additional biases.

$$\tau = \frac{\rho}{c} - dT^s + dT_r + z(t) \quad 2.7$$

where $z(t)$ represents all the additional propagation biases and errors including noise that affect the signal. Traditionally, the time shift τ is multiplied by c to obtain the pseudorange, so called because it contains the true range information but contaminated by errors and biases. The GPS signal sent by the satellite $s^s(t)$ is a combination of three signals: a radio-frequency carrier modulated by a pseudorandom sequence, itself modulated by a binary navigation message. At the receiver, after demodulation, phase or delay information from the carrier and the pseudorandom sequence can be extracted and thus there are two main observations available that can be used to obtain the pseudorange, each with its own of precision. However, the term "pseudorange" is traditionally reserved to pseudorange extracted using the pseudorandom sequence. A more detailed description of the GPS signal is given in Section 2.2. The explanation of how the observations are obtained from the receiver is given in Section 2.6. Information about the main biases affecting the GPS signal is given in Sections 2.3, 2.4 and 2.5.

2.2 GPS signal characteristics

We have described in a simplified way how the receiver measures the pseudorange by comparing a locally generated replica of the received signal with the received signal itself.

Here we will explain what kinds of signals are used for this purpose and how they are modulated to be efficiently sent through space. Only the fundamentals will be presented here. For a more detailed explanation, the reader is referred to (Kaplan & Hegarty, 2006).

The main purpose of the GPS signal is to be used to measure the range between the satellite and the receiver. However, for practical reasons, it also contains useful data regarding the satellites (such as the satellite's clock error) and must be carried by an RF carrier so that it propagates efficiently in free space. As a receiver obtains signals from many satellites, interference of signals must be avoided.

Since the pseudorange is estimated when the received signal and the locally generated one perfectly match in the time domain, we need signals that offer strong correlation only when they match but very low correlation when they do not, so that the receiver can unambiguously determine the pseudorange. Additionally, signal from one satellite must have a low correlation to one from another satellite in order to avoid interference since all satellites share the same spectrum. Pseudo-Random Noise (PRN) codes offer this kind of behavior. Since they have a noise-like behavior, the auto-correlation is very low for any non-zero time shift. PRN codes are sequences of n binary numbers (ones and zeros) that approximates a random sequence. There is however a periodicity in the signal because the sequence of n binary numbers repeats itself continuously. An example of a PRN sequence and its autocorrelation is shown in Figure 2.2. Two main parameters of the PRN sequence are the chip period and the sequence length. The chip period is the temporal length of one binary digit.

Precision is proportional to the chip length, so smaller chip length yields better precision; however it also increases the bandwidth and the susceptibility to noise and multipath. On the other hand, the sequence length has an impact on the sensitivity of the receiver. With a longer sequence, the ratio between the autocorrelation peak and the typical autocorrelation is higher and the receiver can detect weaker signals by incrementing the integration time. However, high rate GPS observations (in kinematic applications) may limit the integration

time available and thus the sequence length. Also, the presence of data modulating the PRN sequence may also limit the integration time.

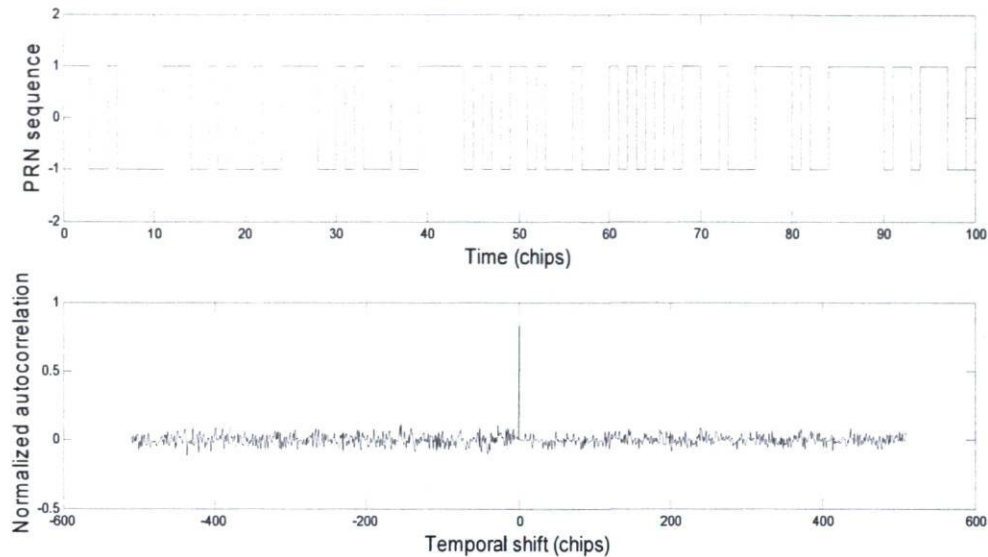


Figure 2.2 Example of PRN sequence and its normalized autocorrelation

For GPS, two kinds of code sequences have been available since the beginning of operation of the GPS system: the C/A code and the P(Y) code. The first one is intended for civilian use and the second for U.S. military use. New codes have been incorporated in the last years and some are planned for future use. Examples of these new codes are the ones used on the modernized L2C and L5 signals. A list of these codes is presented in Table 2.1.

As can be inferred from Table 2.1, P(Y) code theoretically offers a 10 times higher resolution than C/A code since the chipping rate is 10 times faster. However, bandwidth use is also 10 times larger.

Table 2.1 Main characteristics of PRN codes used in GPS (from (Kaplan & Hegarty 2006))

	C/A code	P(Y) code	L2C		L5
			CM (with data)	CL (dataless)	I/Q
Sequence length (chips)	1023	6.1871×10^{12}	10230	767250	10230
Sequence length (time)	1 ms	1 week	20 ms	1500 ms	1 ms
Chip period (ns)	977.5	97.8	1955 (each)		97.75
Chipping rate (Mchips/sec)	1.023	10.23	0.5515 (each) / 1.023 (total)		10.23
Range of one chip (m)	293	29.3	586		29.3

GPS signals contain not only the PRN codes but also a binary navigation data signal. This data signal has a much slower bit rate than the chip rate. Currently the data rate is 50 bits/sec. Modulation of data is done by mixing with the C/A or P(Y) code, also called spreading codes because, due to their higher rate (1.023 Mchips/sec for C/A), they increase (spread) the spectrum of the signal. This could be considered as an inconvenience but it is compensated by the fact that many signals can share a common spectrum. The use of PRN codes to modulate data is referred to as Direct Sequence Spread Spectrum (DSSS). Finally, the resulting signal must be modulated on top of a RF carrier to propagate into space. Currently, L1 (1575.42 MHz) and L2 (1227.6 MHz) bands are used but L5 band (1176.45 MHz) is beginning to be used. For C/A and P(Y) codes on L1 and L2, BPSK (Binary Phase Shift Keying) is the RF modulation method used. Since both codes share the same spectrum, one of them is sent with the RF carrier in-phase (I) and the other with the RF carrier in quadrature (Q), that is, shifted 90°. In BPSK type of modulation, the phase of the RF carrier is changed 180° each time a bit (or chip) changes. An illustration of this type of modulation is shown in Figure 2.3. For modernized GPS signals, more complex modulation schemes such as QPSK (Quadrature Phase Shift Keying) or BOC (Binary Offset Carrier) are used. A summary of GPS signals characteristics is shown in Table 2.2.

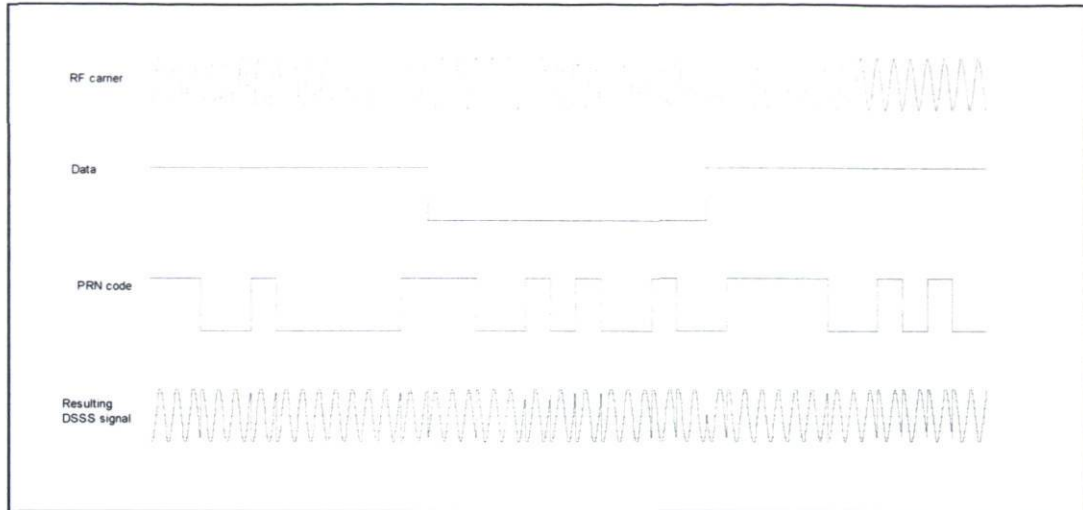


Figure 2.3 Generation of a DSSS signal by mixing an RF carrier with data stream and a spreading code

Table 2.2 Summary of GPS signals characteristics (from (Kaplan & Hegarty 2006))

RF carrier	L1 (1575.42 MHz)			L2 (1227.6 MHz)		L5 (1176.45 MHz)	
PRN code	C/A	P(Y)	L1C	L2C	P(Y)	L5	
Status (as of 2010)	Fully operational		Future	Partially operational	Fully operational	Partially operational	
Phase	Q	I		Q	I	I	Q
Sub-codes				CM	CL		
Modulation type	BPSK	BPSK	BOC(1,1)	BPSK	BPSK	QPSK	
Data rate (bits/s)	50	50	50	25		50	50
PRN sequence length	1023	6.1871×10^{12}	10230	10230	767250	6.1871×10^{12}	10239
Chipping rate (Mchips/s)	1.023	10.23	1.023	0.5515	0.5515	10.23	10.23
Bandwidth (MHz)	2.046	20.46	4.092	2.046		20.46	20.46

2.3 Atmospheric propagation

Between the satellite and the receiver, the GPS signal has interactions with microscopic and subatomic particles in its path that result in dispersion, refraction and/or delays. Within the atmosphere, stronger effects of these interactions occur in the ionosphere, because of the presence of charged particles and in the troposphere, where concentration of molecules is

high. Between the satellite and the upper limits of the ionosphere, space can be considered as a vacuum and perturbation of the signal is minimal.

2.3.1 Ionosphere propagation

The ionosphere, which is the uppermost part of the atmosphere and begins approximately 80 km above the ground, is a medium in which electrons and electrically charged atoms exist due to ionization by the solar radiation. This plasma is a dispersive medium for the radio frequencies and these radio signals suffer from frequency dependent refraction. This refraction causes that the path between the satellite and the receiver is not a straight line and the measured range is different than the true range. The measured range is thus contaminated by an additional error, the ionospheric error. This error is normally 5-15 m in the zenith direction but can reach 100 m in worst case scenarios: during strong solar activity, at midday, near the Equator and for low elevation angles (Klobuchar, 1987). It obviously cannot be neglected. Four strategies can be used to deal with this error:

- Take advantage of the frequency selectivity nature of this error and model this bias using multiple frequency receivers.
- Use existing ionospheric models and/or external measurements to model the ionospheric error in relative positioning.
- Use ionospheric error cancelation by using multiple receivers and simultaneous observations.
- Estimate an additional ionospheric parameter in the least-squares estimation process.

The first strategy gives a direct, real-time measurement of the ionospheric error but multiple frequency receivers are needed and the noise of the linear combination of L1 and

L2 observations is amplified by a factor of 3 compared with the L1-only observation. Multiple frequency receivers are more expensive and not always available. For the second strategy, there exists several ionospheric models but most of them use the Total Electron Content (TEC) of the ionosphere, which causes the ionospheric refraction on the signal. TEC is a measure of the electron content along a defined path, such as the one between a satellite and a receiver. Typical VTEC (Vertical TEC) values range from 0.5×10^{17} to 5×10^{17} electrons/m². From the TEC, it is possible to calculate the ionospheric error (I) with the following equation:

$$I_g = \frac{40.3TEC}{f^2} \quad I_p = -\frac{40.3TEC}{f^2} \quad 2.8$$

where:

f : Frequency of the signal (Hz)

I_g : Ionospheric error due to the group delay on the signal (meters)

I_p : Ionospheric error due to the phase delay on the signal (meters)

We can see that the ionospheric effects have a different sign for the pseudorange observations and for the phase observations. In the first case, the range as measured by the pseudorange is longer (positive group delay) than the pseudorange without ionospheric effects whereas for the second case, the range as measured by the carrier phase is shorter (negative phase delay). The TEC is a function of many variables such as solar activity, magnetic activity, season, time of day, user location and viewing direction. Predictive models attempt to calculate TEC using a mathematical model using coefficients and the user's location. In the GPS message itself, these coefficients are transmitted such that a stand-alone receiver may estimate the ionospheric error in real-time. Since TEC is dependent on a specific path, the VTEC (Vertical TEC) is generally used, which is the TEC along the vertical direction (90° elevation angle). The TEC for a specific elevation angle may then be derived from the VTEC. The model transmitted in the GPS message, based on

(Klobuchar, 1987), has a performance of 50% rms reduction of the ionospheric error. This reduction, which is acceptable for low-precision stand-alone applications, is not enough for high precision applications. More precise corrections of the ionospheric error are also available in real-time through external means such as in WAAS (Wide Area Augmentation System), among others. Post-processing models, which use a combination of measurements of TEC by several means, are generally much more precise. For example, the International GNSS Service (IGS) offers data products such as the Rapid ionospheric TEC grid and the Final ionospheric TEC grid, with latencies of 24 hours and 11 days respectively (International GNSS Service, 2010). The third strategy is based on the principle that if two or more receivers are used and are not too far apart, their ionospheric errors will be similar and may be largely eliminated through differentiation between receivers. Most high precision positioning applications use the differential approach but depending on the separation of the receivers, an ionospheric model may also be used. The second and third strategies are thus not mutually exclusive. A final note regarding the first approach, which would seem the better one, is that using linear combination of observations at different frequencies to remove the ionospheric bias is not always the best approach. Authors of (Astronomical Institute - University of Bern, 2004) recommend, for baselines shorter than 10 km, a L1 only solution in combination with a GNSS-derived ionosphere model. The reason behind this recommendation is that experiments have shown that for baselines smaller than 10 km, “GNSS-derived ionosphere models are very efficient in removing or greatly reducing the ionosphere-induced scale bias under homogeneous and moderate ionospheric conditions” (Astronomical Institute - University of Bern, 2004, p. 254).

Even using one of the strategies to deal with the ionospheric error, the ionosphere may have unpredictable short-term behavior and rapid fluctuations that can affect correct reception of the signals, particularly during high solar or magnetic activity. Cycles slips and loss of lock in the receiver are some of the potential effects of these increased activities.

2.3.2 Troposphere propagation

The troposphere is the lowest portion of the Earth's atmosphere. Although electrically neutral when compared with the ionosphere, the troposphere has the greatest concentration of matter, with approximately 75% of the atmosphere's mass. It has a depth of 8 to 20 km, depending on the location on Earth and the season. The nature of the main components of the troposphere (nitrogen, oxygen, argon, carbon dioxide, water vapor) and their physical characteristics (temperature, density, pressure) cause a reduction in the speed of electromagnetic waves with respect to their speed in vacuum. This reduction in speed is quantified by the refractive index of the medium (n) and the refractivity (N):

$$n = \frac{c}{v} \quad N = 10^6 (n - 1) \quad 2.9$$

where,

c : Speed of light in vacuum

v : Speed of the electromagnetic wave in the medium

The speed of the electromagnetic wave in the medium depends on the relative permittivity (ϵ_r) and permeability (μ_r) of the medium:

$$v = \frac{c}{\sqrt{\epsilon_r \mu_r}} = \frac{1}{\sqrt{\epsilon_0 \epsilon_r \mu_0 \mu_r}} = \frac{c}{n} \quad 2.10$$

The general form of the empirical relationship between the refractivity and the temperature and pressure of the gases of the atmosphere is the following (Essen & Froome, 1951):

$$N = K_1 \frac{p_d}{T} + K_2 \frac{e}{T} + K_3 \frac{e}{T^2} \quad 2.11$$

where,

p_d : Pressure of the dry atmosphere (mbar)

e : Water vapor pressure (mbar)

T : Temperature (K)

K_1, K_2, K_3 : Empirical parameters

ϵ_0, μ_0 : Permittivity and permeability in the vacuum

The values of K_1, K_2, K_3 can be found in several sources such as (Thayer, 1974).

As can be seen in Equation 2.11, water vapor is treated separately because water vapor, as a dipolar molecule, induces an additional dipolar polarization on the electromagnetic field. As the GPS signal crosses the troposphere, a cumulative effect of the speed reduction and deviation of the signal builds up. The resulting tropospheric delay is:

$$\Gamma = 10^{-6} \int_S N(s) ds \quad 2.12$$

where,

Γ : Tropospheric delay (m)

S : Path taken by the electromagnetic signal between the satellite and the receiver

Regarding the variable S , it should be noted that the difference with true geometric range (S_{geo}) due to bending of the electromagnetic signal through troposphere is negligible for high elevation angles. For practical GPS applications, where an elevation mask of 10 to 15° is frequently used, the difference between S and S_{geo} may be neglected. Bock & Doerflinger (2001) estimated that the difference is below 1 cm for an elevation angle of 15°. The resulting error on the tropospheric error is less than 0.1%.

Practical application of Equation 2.12 is difficult because it implies the knowledge of the true spatial distribution of the atmospheric temperature, pressure and water vapor pressure (and thus the refractivity), taken as scalar fields, along the path. Usually, as a first approximation, it is considered that the distribution of the atmosphere is vertically layered so that the refractivity is only dependent on the altitude. Vertical profiles of temperature and pressure are usually available through models and/or external measurements. With this data and a given model a zenith tropospheric delay may be calculated. Then, using a cosine function, the tropospheric delay for any angle is calculated. One of the first practical models for calculating the zenith tropospheric delays is the one proposed by (Saastamoinen, 1972) :

$$\Gamma_z = 0.002277 \left(p + \left(\frac{1255}{T} + 0.05 \right) e \right) \quad 2.13$$

where,

p, T, e : Pressure (mbar), temperature (K) and water vapor pressure (mbar) at the receiver

The tropospheric delay at any zenith angle z is then:

$$\Gamma = \Gamma_z \frac{1}{\cos(z)} \quad 2.14$$

However, the cosine function is based on the assumption of a perfectly layered flat Earth. To overcome this simplistic approach, mapping functions, replacing the simple cosine function, are used:

$$\Gamma = \Gamma_z m(z)$$

Many authors have proposed different empirical mapping functions, each with its strengths and weaknesses. A comprehensive list is presented in (Mendes & Langley, 1994). Almost all of them recommend separating the tropospheric delay into its “dry” and “wet” components since water vapor has a different and more unpredictable behavior compared to the other gases of the atmosphere:

$$\Gamma = \Gamma_{\text{dry}} + \Gamma_{\text{wet}} = \Gamma_{\text{zd}} m_d(z) + \Gamma_{\text{zw}} m_w(z) \quad 2.15$$

The wet component, although smaller, is more variable and unpredictable. For example, in studies conducted on several stations over the world and presented in (Mendes & Langley, 1994), the mean dry zenith delay ranged from 2.3 m, at stations near sea level to 1.9 m for a station at 1600 m above sea level. Standard deviation was small in all cases, around 1 to 2 cm. The dry zenith delay is highly dependent on the atmospheric pressure and thus on the station altitude, with little variability due to day-to-day pressure and temperature changes. On the other hand, the mean wet zenith delay ranged from 0.03 m at a dry, arctic location to 0.27 m at a wet tropical location, with standard deviations ranging from 2 to 8 cm. Also, the wet zenith delay is much more variable. In the same paper, a comparison is made to assess the performance of different mapping functions.

Compared with the ionospheric effect, the strategies to deal with the tropospheric error are similar but in this case, the use of multi-frequencies receiver has no effect since the tropospheric effect is not frequency dependent for radio frequency waves. We are thus left with three strategies:

- Use atmospheric models and external measurements to model the tropospheric error.
- Use tropospheric error cancelation by using multiple receivers and simultaneous observations.
- Estimate an additional tropospheric parameter in the least-squares estimation process.

Of these strategies, the preferred and most commonly used for high precision applications is the estimation of the tropospheric bias. Indeed, when using models and external measurements, these must be very accurate to not have an impact on high precision applications. For example, as presented on (Astronomical Institute - University of Bern, 2004), a 1% error on the relative humidity measurement, which is less than what is

typically achieved for humidity measurement devices, for a hot and humid environment translates into a 4 mm error on the zenith tropospheric delay, which in turn translates into a 1 cm height bias. The authors conclude then that “This is why experience tells that estimation of troposphere parameters is a necessity if high accuracy is required and if only ground meteorological data are available”. However, in some cases, for short baselines with large height difference when there is no atmospheric layer inversion, it is still possible to use a differential tropospheric model such as the differential model of Essen and Froome, which has already been tested for deformation monitoring applications (Akrou, 1998) and was first described by (Rothacher et al., 1986).

On the other hand, tropospheric error cancelation is difficult to achieve since, as refractivity is strongly dependent on the station’s altitude, only for short baselines with almost no height difference between stations, is tropospheric error cancellation possible. We conclude that, depending on the weather, baseline length and height difference between stations, one of the three strategies has to be chosen. Since in some cases, the choice might not be straightforward, data processing can be done using each of the three strategies and a comparison can be made between them.

2.4 Transmission line propagation

Ranging between the satellite and the receiver is based on the free space propagation of an electromagnetic signal. Geometrically, a straight line propagation is necessary and assumed once we take into account the small deviations induced by the ionosphere and troposphere. Strictly speaking though, ranging is done between the phase center of the satellite’s antenna and the phase center of the receiver’s antenna. The phase center of an antenna is the physical place where the conversion from radio waves to electrical current is done. However, signal generation at the satellite and signal processing at the receiver are done at electronic circuits that may be a few centimeters to several meters away from the phase

center of the antenna. Between them, there are connectors such as coaxial cables and conditioning electronic circuits such as amplifiers and filters. Range as estimated by the receivers thus includes the time it takes for the signal to travel through all these interconnect circuits and components. Since the straight line geometry between satellite and receiver is only valid between the antennas' phase centers, the additional propagation time through the transmission lines and electronic circuits must then be considered as additional error to the range. Traditionally, this additional delay, which we will refer to as hardware delay (H), is integrated in the receiver and satellite's clock errors and, as such, is not given much importance. When the receiver's clock error is estimated, it already includes the hardware delay. However, in our project, the configuration and type of receiver used enable us to eliminate the relative receiver's clock but relative hardware delay remains. The relative hardware delay has a direct impact on the positioning precision and must be carefully quantified, in real-time. Additionally, over-fiber propagation between the antenna and the receiver is also considered so the impact of this different type of signal propagation must be evaluated.

2.4.1 Thermal effects on coaxial cable and optical fiber propagation

When dealing with the wireless propagation of the GPS signal between the satellite and the receiver, we focused on the external variables that have a direct impact on the propagation and make it depart from the ideal, free-space case. This departure from the ideal case was quantified as additional error. For the ionospheric case, the main affecting variable is the Total Electron Content (TEC) and for the tropospheric case, the main affecting variables are the scalar fields of temperature, pressure and water vapor. In the case of the hardware delay, we need to also find the variables that affect the propagation of the signal.

The transmission between the antenna and the receiver is usually carried out with coaxial cable as it is best suited for RF signals. In special cases, such as in our project, optical fiber may be used. We will then focus on these two types of transmission lines. In both cases,

propagation of the electromagnetic signal is a guided type of propagation. The electromagnetic wave is thus physically confined in a waveguide. However, in a similar way as wireless propagation, the delay depends basically on the physical properties of the medium. The delay in a waveguide is given by:

$$H_{line} = \frac{L}{v} = \frac{L}{c} n_g \quad 2.16$$

where,

H_{line} : Hardware delay on the line (sec)

L : Length of the line (m)

n_g : Effective group refractive index of the propagation mode

v : Speed of light in the cable

c : Speed of light in the vacuum

Equation 2.16 is simple to use but, for high precision applications, the propagation delay must be accurately determined so a further analysis is needed to take into consideration how and by how much the propagation delay may change as a function of time. Let us analyze the two variables of Equation 2.16:

- The length of the waveguide (L) changes as a result of temperature and pressure changes and external mechanical stress applied. The amount of elongation or contraction also depends on the material used.
- The refractive index of a material may change as a result of temperature, pressure, mechanical stress and the type of dielectric used. In certain cases, the refractive index may also be proportional to the signal's frequency (dispersive medium) or the electromagnetic field intensity (nonlinear medium). As some waveguide may have more than one type of material, for example the core and cladding of an optical

fiber, we use the effective refractive index, which depends on the refractive index of each type of material and the shape and construction of the waveguide. Additionally, for modulated carriers, one must take into account the group propagation speed, which explains the use of the effective group refractive index (n_g). Finally, a waveguide may have several propagation modes and propagation in each mode may have a different speed so the refractive index must be specified for each propagation mode.

In both cases, the most important parameters are the temperature and the type of material. Indeed, except for the case of a waveguide where air is used as the dielectric, pressure can be considered constant for solid dielectrics. Mechanical stress may be carefully controlled or avoided and dispersion and non-linearity are issues that will be presented later for the case of optical fiber, since in our project, the longest runs are on optical fiber.

The variation of the propagation delay as a function of temperature (T) is:

$$\begin{aligned} \frac{dH_{line}}{dT} &= \frac{1}{c} \frac{d}{dT} [L(T)n_g(T)] \\ &= \frac{1}{c} \left[\frac{dL(T)}{dT} n_g(T) + L(T) \frac{dn_g(T)}{dT} \right] \end{aligned} \tag{2.17}$$

Equation 2.17 shows that the variation of the delay with respect to the temperature depends not only on the physical elongation or contraction of the waveguide $\frac{dL(T)}{dT}$ but also on the change of the refractive index $\frac{dn_g(T)}{dT}$. The combined effect is a change in the electrical length of the waveguide, where the electrical length is defined as the number of wavelengths of the signal propagating in the medium. The electrical length, a concept that applies also to optical fibers, takes the refractive index of the medium in consideration so that if, for example, the propagation speed in the waveguide is 0.80 times that of the speed of light in vacuum, the electrical length will be $1/0.80 = 1.25$ times the physical length. For

practical applications, the Thermal Coefficient of Delay (TCD) is used to characterize the thermal variability of the electrical length:

$$TCD = 10^6 \frac{\Delta H_{line}}{H_{line} \Delta T} \quad (ppm/^{\circ}C) \quad 2.18$$

The value of TCD may be experimentally measured or given as a specification by the manufacturer for each type of coaxial cable or optical fiber. Table 2.3 presents some TCD values as experimentally measured in (Lutes & Diener, 1989).

Table 2.3 Thermal Coefficient of Delay for some type of cables as measured in (Lutes & Diener 1989)

Type of cable	TCD at 18°C (ppm/°C)	TCD at 23°C (ppm/°C)	TCD at 28°C (ppm/°C)	TCD at 33°C (ppm/°C)
RG-223 coaxial	-40	-60	-90	-115
SF-214 coaxial	-152 *	-167*	-173*	-176*
	-160**	-175**	-175**	-159**
Single mode optical fiber	7	7	7	7
Low TCD single mode optical fiber	<1	<1	<1	<1
*: Increasing temperature		**: Decreasing temperature		

As can be seen through these measurements, coaxial cables' TCD is not constant and depends on temperature. Moreover, values of TCD for coaxial cables change depending on whether the temperature is increased or decreased and are higher than those for optical fiber. From this, we can conclude that if we wish to control propagation delay in the cables at a few picoseconds level (millimeter level), thermal effects must be taken into account. Indeed, even for a few meters of coaxial cable run and a few degrees of temperature change, the electrical length of the cable can change by a few millimeters. For example, for 10 m of RG-223 coaxial cable at 23°C, an increase of 5°C in temperature translates into 3 mm of electrical length increase. Optical fiber is more thermally stable but for long runs of a few kilometers, small thermal variations may cause several millimeter length changes. For example, 1 km of standard monomode optical fiber has a 7 mm optical length change for 1°C of temperature change (Lutes & Diener, 1989).

2.4.2 Optical fiber propagation and dispersive effects

In the case of optical fiber, since it is a dispersive medium, variations of the refractive index as a function of the frequency must be taken into account. Dispersion in an optical fiber means that each of its constitutive frequencies undergoes a different time delay. The resulting group delay of a given signal is different from the phase delay of each of the frequencies. The propagation in an optical fiber is characterized by an effective refractive index n_{eff} for each guided mode that is comprised between the core refractive index (n_1) and the cladding refractive index (n_2):

$$n_2 < n_{eff} < n_1 \quad 2.19$$

The effective refractive index characterizes the propagation in the fiber. The determination of n_{eff} depends on many fiber parameters such as the core and cladding diameters, their refractive index profiles and the wave guiding characteristics of the fiber. Its calculation is derived from electromagnetic theory using Maxwell equations applied to the particular waveguide structure of the fiber. Details of this may be found in (Keiser, 2000). The effective refractive index n_{eff} , as stated before, is frequency (or wavelength) dependent and the group refractive index, different from the effective refractive index, must be calculated for a signal propagating on the fiber. The group index is calculated as follows:

$$n_g = n_{eff}(\lambda_0) - \lambda_0 \frac{dn_{eff}}{d\lambda} \Big|_{\lambda=\lambda_0} \quad 2.20$$

where,

λ_0 : Central wavelength

This group refractive index must now be used to estimate the delay as expressed in Equation 2.16:

$$H_{fiber} = \frac{L}{v} = \frac{L}{c} n_g \quad 2.21$$

Dispersion effects are accounted for by higher order derivatives of the refractive index. In practical applications only the second and third order derivatives are considered. Most of them will even use the second order only. For the second order, the dispersion parameter D is generally used:

$$D = -\frac{\lambda}{c} \frac{d^2 n_{eff}}{d\lambda^2} \left(\frac{ps}{nm.km} \right) \quad 2.22$$

This parameter is different for each type of optical fiber and given as a specification, with respect to wavelength, by the manufacturer. Given the dispersive characteristics of the fiber, dispersion effects can be calculated for a particular signal traveling on the fiber. In our case, if a RF oscillator and/or GPS signal is transmitted on fiber, the magnitude of the dispersion effects will be proportional to the spectrum width of the signal and to the frequency of the RF carrier if standard Double Sideband (DS) modulation of the optical carrier is used. For the former effect, the larger the signal spectrum of the signal, the faster its frequencies components will spread. However, the spectrum of the GPS signal is relatively narrow, when compared to the bandwidth offered by the optical fiber. Considering a 20 MHz spectrum for the GPS signal and a standard monomode fiber with $D=17 \frac{ps}{nm.km}$ and an optical carrier at 1560 nanometers (nm), the dispersion effect for this signal is:

$$\begin{aligned} d = D\Delta\lambda &= D \frac{\lambda^2}{c} \Delta f = 17 \frac{1560^2}{3 \times 10^8 \times 10^9} 20 \times 10^6 \\ &\approx 0.003 ps/km \end{aligned} \quad 2.23$$

Compared to the spectral width (20 MHz = 1/50 ns), the dispersive effect is thus negligible even for several hundreds of kilometers.

For the second effect, even if a RF signal with negligible spectrum width is transmitted on fiber, dispersive effects appear because of the presence of a sideband on each side of the optical carrier if standard double sideband modulation is used, as illustrated in Figure 2.4.

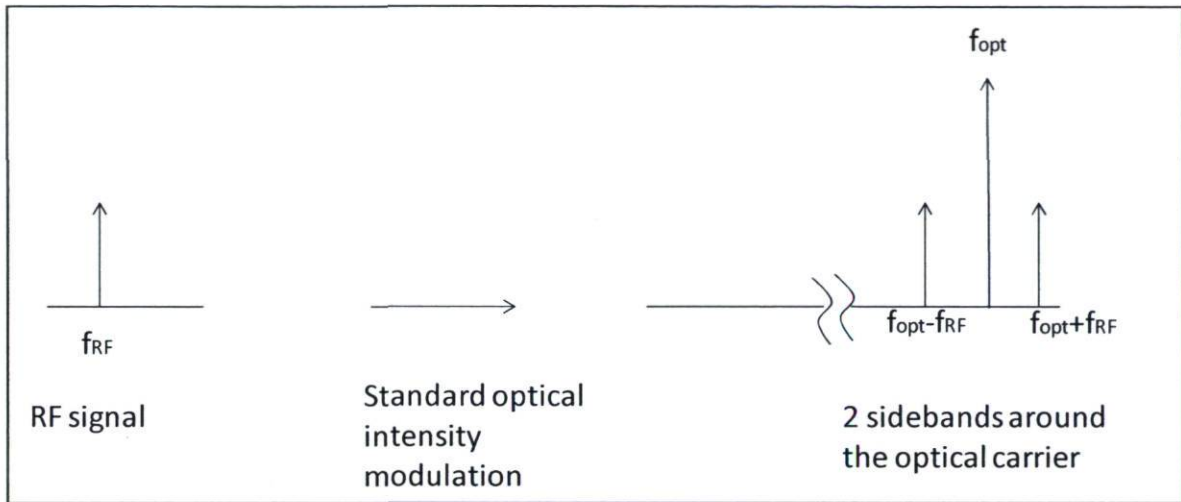


Figure 2.4 Modulation of an optical carrier by a RF signal

When the signal is converted back to electrical form, the two sidebands combine through the quadratic effect of the photodetector. The quadratic effect arises because the current at the photodetector is proportional to the square of the optical field:

$$i_{pd}(t) \propto R_{pd} \langle E^2(t) \rangle \quad 2.24$$

If the dispersive effects are neglected and non-coherent photodetection takes place, then the optical phase information may be neglected and the photodetector current may be taken as simply proportional to the optical field intensity:

$$i_{pd}(t) \propto R_{pd} P_{opt}(t) \quad 2.25$$

However, with dispersive effects taken into account, the two sidebands can be out of phase and the optical phase information cannot be neglected anymore. The net effect is an

attenuation of the signal proportional to the dispersive factor of the fiber. Hilt (2000) calculates the additional attenuation factor (A_D) on a RF signal after photodetection due to the dispersion of the fiber as:

$$A_D = \cos \left(cD\pi L \left(\frac{f_{RF}}{f_{opt}} \right)^2 \right) \quad 2.26$$

So that the photocurrent is now proportional to:

$$i_{pd}(t) \propto R_{pd}P_{opt}(t)A_D \quad 2.27$$

Figure 2.5 shows the values of A_D (dB) for a standard SMF-28 fiber ($D=17 \frac{\text{ps}}{\text{nm.km}}$) at 1560 nm for RF frequencies of 1.5 GHz and 3.0 GHz. As can be seen, the dispersive effect is negligible even for long runs of fiber. We can thus conclude that using standard monomode fiber, GPS RF signals can be transported over several kilometers without dispersive effects being a significant issue.

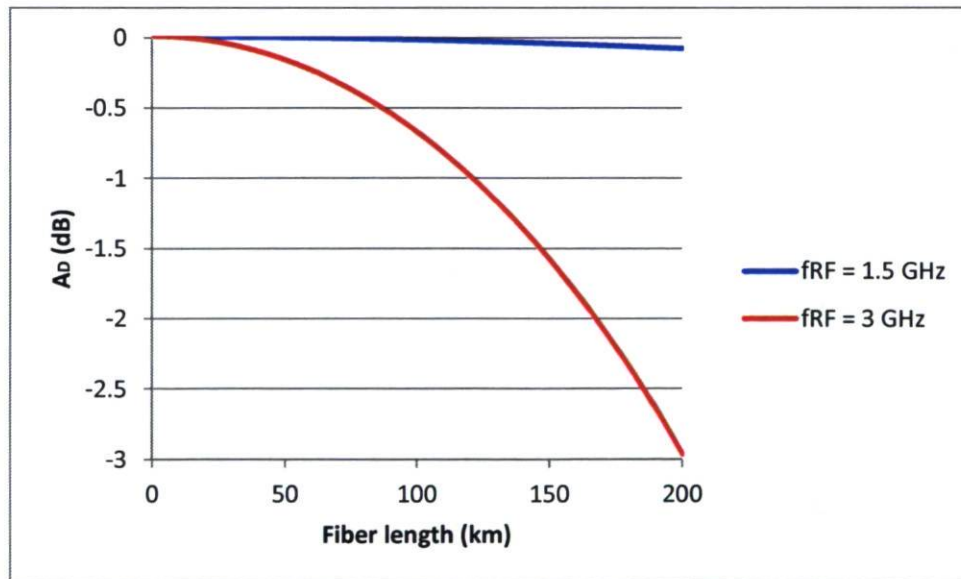


Figure 2.5 Attenuation of a RF-over-fiber signal at 1560 nm due to dispersive effects in a monomode SMF-28 fiber

We have been considering the dispersive effect as a function of frequency (called chromatic dispersion) under the assumption of a monomode propagation. If multimode fiber is used, then an additional dispersive effect must be taken into account: modal dispersion. This effect arises due to the different propagation speed for each mode that travels in the fiber. Multimode fiber systems are generally cheaper since LED (Light-Emitting Diode) sources and not only laser sources can be efficiently coupled to them. However, modal dispersion limits the maximum bandwidth that can be transmitted on a multimode fiber. Even if bandwidths of a few GHz per km have been achieved on multimode fibers, monomode fibers are still preferable for signals in the GHz range to avoid modal dispersion.

Another type of dispersion effect that is present in optical fibers is the polarization mode dispersion. This effect arises due to the birefringence of the fiber, which affects the polarization states propagating inside the fiber. More specifically, birefringence is the property of a material which is non-isotropic and as a result, the refractive index depends on the polarization direction. Ideally, standard optical fiber should have little birefringence. However, deviations from perfect circularity of the fiber during the fabrication and external stress increase the birefringence of the fiber. When the refractive index depends on the polarization state of the light, the polarization orientation will rotate with distance and the resulting propagation times between the polarization mode results in dispersion. (Keiser, 2000, Ch.3). This type of dispersion, polarization mode dispersion (PMD) varies randomly and as such, can only be statistically predicted to account for its effect. PMD effects increase with fiber length and manufacturers of optical fiber generally give a PMD parameter, D_{PMD} which is the mean value of the differential group delay (between the two polarization modes). For standard SMF-28 monomode fiber, the value is around $0.2\text{ps}/\sqrt{\text{km}}$. This value can change due to external mechanical and environment factors. PMD is an effect that has to be taken into account for long, high-throughput links. In our case, since we are planning on links of less than 2 km and relatively low bandwidth (20 MHz for GPS signal), PMD effects are less than 1 ps and can be neglected.

2.5 Antenna phase center variation and multipath effects

For high precision applications, two biases that must be considered are multipath interference and antenna phase center variation because both effects can introduce errors of up to a few centimeters. Both of them are related to the antenna and how it picks up the received electromagnetic signal. For multipath, the problem arises when the antenna not only picks up the main direct signal but also reflected versions of it. Sometimes, it only picks up the reflected signals. These reflected signals arrive with a certain amount of delay so that they are out of phase with respect to the main signal and cause a time-varying power level. For antenna phase center variation, the problem arises because the physical place where the electromagnetic signal is converted to an electrical signal by the receiver antenna varies with respect to the signal incoming elevation angle and azimuth.

2.5.1 Antenna phase center variation

The phase center of a receiver antenna is the location within the antenna where the actual conversion from the radio wave to electrical current is performed. This phase center does not generally correspond to the actual geometric center of the antenna. Additionally, the phase center is not a fixed point but changes according to the incoming direction of the electromagnetic wave (Bourassa, 1994). One must then know the phase center for each azimuth and elevation angle in order to correct for the bias between the geometric center and the phase center. Three methods are generally used to determine the phase center of antennas:

- Absolute antenna phase center measurement in an anechoic chamber using artificial signals.
- Absolute antenna phase center measurements using real GPS signals.

- Relative antenna phase center measurements using real GPS signals.

In the first method, the antenna is placed in an anechoic chamber and the absolute phase center is obtained by measuring the change of the received phase of a simulated GPS signal when the antenna is rotated and tilted. In the second method, the antenna is placed on a robotic arm which rotates and tilts with great precision the antenna as it receives the GPS signals. By taking advantage of the fact that satellite constellations repeat every 23 hr 56 min, it is possible to form differences in time to remove multipath effects (additional details about this will be given in Sections 2.5.2 and 5.3.5). Also, by forming differences between the reference (zero) position and the rotated/tilted position the following day, it is possible to measure the phase center variation. Finally, in the third method, the phase center of an antenna is obtained with respect to the phase center of a reference antenna. Usually an accurately known small baseline is used so that the GPS observations give us an estimation of the relative phase center variation as a function of the azimuth and elevation of the satellites. Each method has its strengths and weaknesses. The third method is the easiest and least expensive method but has the main disadvantage that it depends on a specific reference antenna. The main disadvantage of the first and second method is their high cost because specialized equipment is needed. However, for the determination of long baselines, absolute calibration is preferable.

In the absence of calibration procedures for obtaining the phase center variations, one has generally only access to the average phase center specification given by the manufacturer. This is the average phase center location averaged over all azimuth and elevation angles. However, the difference between the actual phase center for a specific azimuth and elevation angle and the average phase center may reach several millimeters (Tranquilla & Colpitts, 1989) (Görres et al., 2006). The phase center variation is different for each model and type of antenna and for each frequency used. Then, if we use different antenna models for a baseline, there is a differential bias that can reach several millimeters or even centimeters due to antenna phase center variation. Even if we use the same antenna model for each site, the antennas must have the same orientation as the actual phase center position is not symmetrical with respect to the average phase center. Experiments such as

the one conducted by (Bourassa, 1994) have shown that with identical and similarly orientated antennas, the relative average phase center between antennas can be kept within a few millimeters for horizontal and vertical components. For example, for experiments conducted for a specific session of 5 hours using a high precision 1 m calibration beam and two identical and similarly orientated antennas, it was found that the average relative phase center was 0.3 mm for the north component, 0.1 mm for the east component and 1.1 mm for the vertical component (Bourassa, 1994). By using the same type of identically orientated antennas, it is thus possible to keep the relative phase center variations between antennas at millimeter level.

2.5.2 Multipath effects

The multipath effect arises when the antenna picks up, in addition to the main signal, reflected versions of this same signal. As these reflected signals are delayed with respect to the main signal, they have a different phase and can therefore interfere and affect the main signal if their power is sufficiently strong. Multipath effects are therefore greater in the presence of high reflectivity surfaces such as metallic structures because in that case, the reflected signal can have almost the same power as the incident one. It has been shown that the error on the GPS observation due to multipath effects can reach up to 5 m for the pseudorange and up to $\frac{1}{4}$ wavelength (about 5 cm for L1) for the phase observation (Georgiadou & Kleusberg, 1988), (Arbour, 1994). On the other hand, because GPS satellites are constantly moving, the satellite-reflector-receiver geometry constantly changes and so does the interference combination of the main and the reflected signals. Because of this movement, multipath effects are periodic and depending on the reflector's distance, orientation and reflective properties, the period of the multipath goes from a few minutes to a few hours (Arbour, 1994). Thorough analysis of multipath effects is difficult because of the geometry change and also because of the difficulty to take into consideration simultaneously all the possible reflective surfaces and the cases where multiple reflections

occur. On the other hand, traditional differentiation techniques that are used to reduce or eliminate other biases do not work with multipath as its effects are specific to each site. Because multipath effects cannot be eliminated with differential techniques, it is often recommended to choose sites which are free of reflective obstacles. As this is not always possible and multipath effects may still persist, four different approaches have generally been used to deal with multipath effects:

- Use an antenna with stronger multipath rejecting properties by using choke rings or other specialized antenna designs. Most manufacturers such as Trimble, NovAtel, Ashtech, offer choke ring antennas.
- Use multipath “resistant” receivers employing special correlation techniques, such as the narrow correlator spacing (van Dierendonck, et al., 1992), now implemented in most receivers or, more recently, the use of a window correlator (Bétaille et al., 2006), among many other techniques.
- Use post-processing techniques to partially filter out multipath effects, by analyzing the CNR, the observations, the residuals, the coordinates or other post-processing products. Due to the movement of the satellites, multipath effects are cyclic, so one possibility is to perform a spectral analysis to detect and filter out these effects (see for example (Souza & Monico, 2004)). Also, one can take advantage of the repeatability of the satellites position each sidereal day (see for example, (Zhong et al., 2009)), in static applications where the antennas do not move.

The first approach is a pure “hardware” approach. Its main advantage is that the rejection of multipath effects is immediate and that it can be used in real-time processing. However, multipath-rejecting antennas are generally more expensive than standard antennas, they may not be available and their multipath-rejecting properties are generally limited to reflected signals coming from below the antenna ground plane.

The second approach is a hardware or software approach, depending on the type of receiver. If the receiver is software-defined (and/or FPGA-defined) GPS receiver, it is possible to change the correlation technique by reprogramming the software and/or FPGA.

The third approach is a “software” approach. It requires changes in the software that performs the processing of the observations.

2.6 GPS receiver and its main measurements

This section gives a brief overview of the operation of a typical GPS receiver in order to identify how the main observations for GPS positioning are generated and what their limitations in accuracy are.

The received GPS signal is a combination of a low bit-rate navigation data signal (50 bits/sec) on top of a spreading PRN code at 1.023 or 10.23 Mc/sec modulating a RF carrier (1.575 / 1.227 / 1.176 GHz). The main purpose of the receiver is to extract the navigation data to obtain useful information about the satellites and to compare the received PRN code with the locally generated one, to calculate the pseudorange between the receiver and the satellite. As the carrier phase must also be tracked, this information can be used to have a more precise, but ambiguous, estimation of the pseudorange. More information concerning this issue will be provided later.

Figure 2.6 shows a generic GPS receiver block diagram. The RF front-end amplifies and downconverts the RF signal to an IF (Intermediate Frequency) so that it can be more easily converted to digital form by the A/D converter. Most modern receivers use parallel processing so that multiple channels, each with its own correlator, are used simultaneously. The correlator is the part of the receiver that demodulates the received signal and allows it to extract the data and pseudorange information. A more detailed block diagram of one of the channel correlators is shown in Figure 2.7.

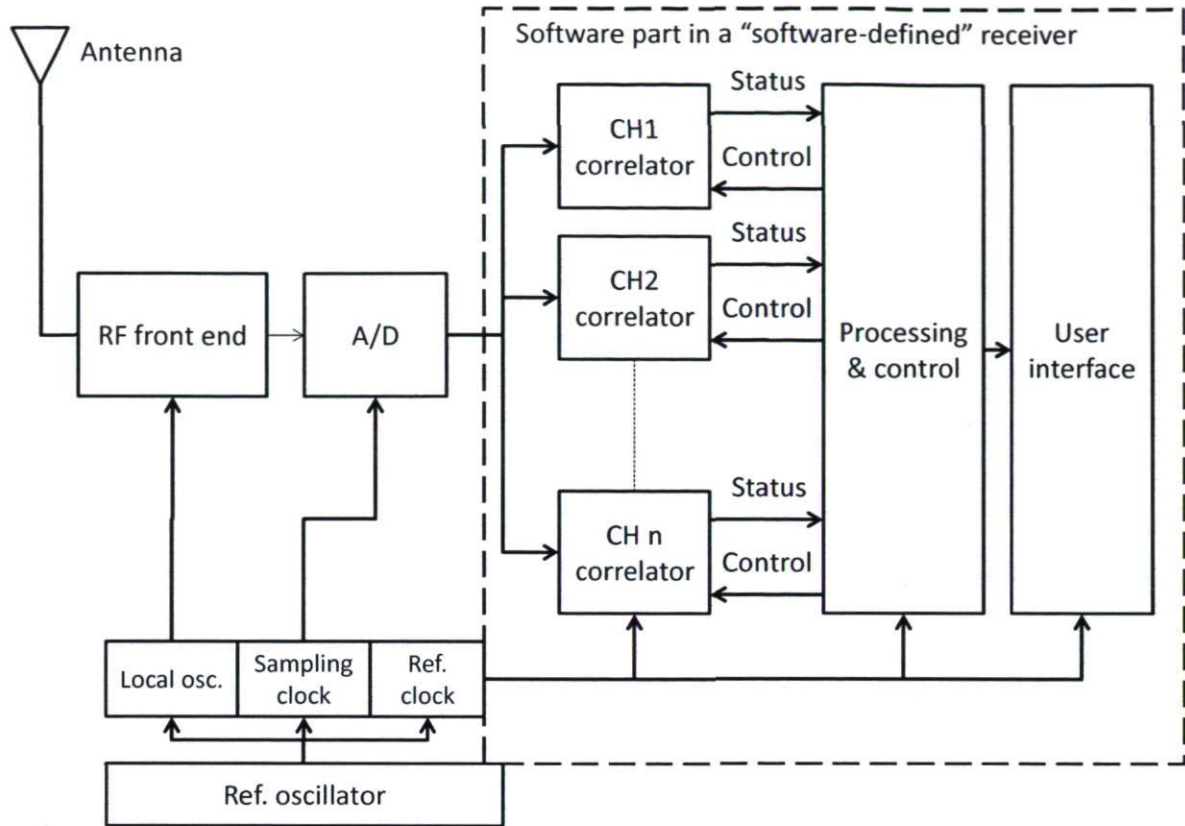


Figure 2.6 Block diagram of a typical GPS receiver

In a typical demodulation (correlator) channel, the received IF digital signal is both mixed with a replica of the IF carrier signal (carrier wipeoff) and a locally generated PRN code (code wipeoff). The resulting signal is integrated for a certain amount of time to search for the peak correlation. A correlation peak will only appear if the locally generated IF carrier and PRN code matches the received signal, so there is a feedback loop where the systems continuously shift the carrier and code phases until a correlation peak is found. The longer the integration time, the higher the probability of obtaining a correlation peak is. However, because a 50 bps data signal is present in the case of the L1 C/A and P(Y) signals, the correlation integration time cannot be longer than $1/50 = 20$ ms, because the possible change of sign of a data bit may destroy the correlation peak. The correlation peak must then be found within a data bit and thus careful control must be done to align the data bit transition boundaries and the Integration & Dump (I&D) process. In Figure 2.7, we can see

that the demodulation process is more complex and uses an I/Q IF carrier generator, where both the in-phase (I) and quadrature-phase (Q) signals are mixed with the received signal. This is necessary if we wish to unambiguously retrieve the carrier phase information of the signal. Also, the code generator creates an early, prompt and late versions of the PRN code that are $-1/2$, 0 and $+1/2$ chip delayed respectively. The use of these three versions helps in the correlation peak searching process.

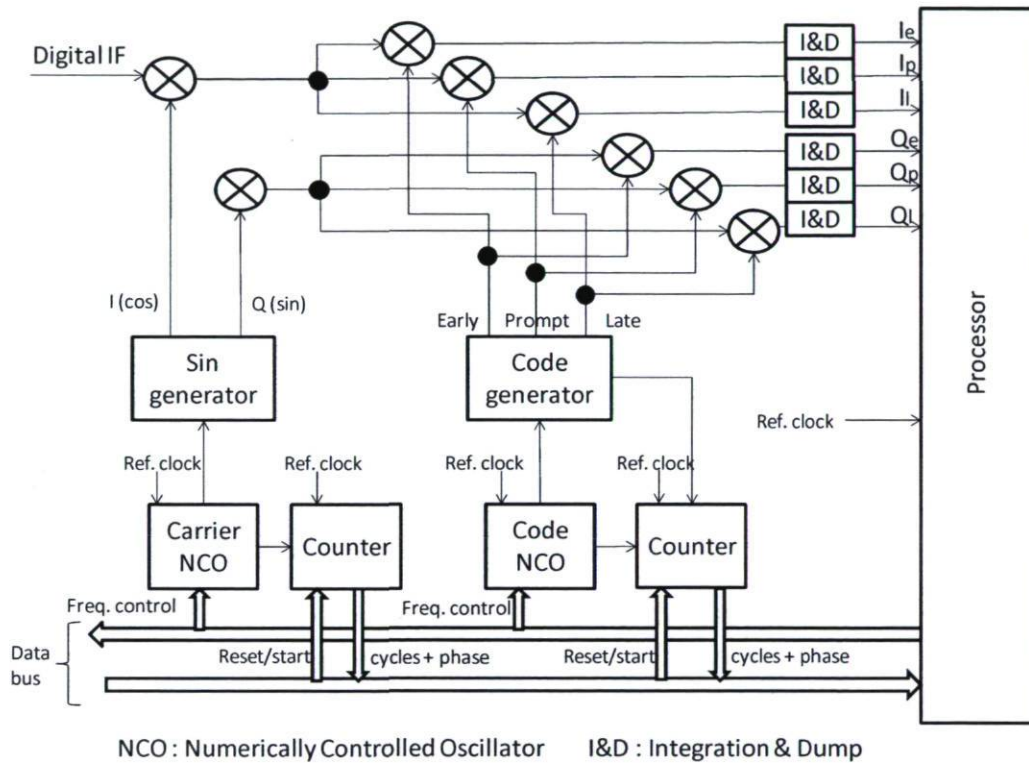


Figure 2.7 Block diagram of a demodulation channel of a GPS receiver

As the GPS satellites are continuously moving at speeds of up to 4 km/sec with respect to the Earth, a Doppler frequency shift is present on the received signal. This Doppler shift may reach a few kHz. This is why the carrier NCO's frequency must be continuously shifted. Thus, the search for phase and code locks may be viewed as a two dimensional process, since two variables, Doppler shift and code time shift must be continuously changed to acquire and maintain lock. Once the receiver's carrier and code generators are

in lock with the received signal, the following information is available and will be useful for positioning:

- The Doppler frequency, available through the control signal sent to the carrier's NCO by the processor.
- The accumulated carrier phase information (ACP), available through the counter attached to the carrier's NCO.
- The accumulated code phase information (ACC), available through the counter attached to the code's generator and NCO.
- The navigation data, which can be extracted from the sign of the correlation peak, Ie, Ip, Il, Qe, Qp & Ql.

The ACP consists of the integer number of carrier cycles plus the fractional (carrier phase) part. The ACC consists of the integer number of complete PRN sequences (PRN cycles) plus the fractional (code phase) part. For example, for C/A code, a PRN cycle is 1023 chips long and the code phase lies between 0 and 1022 chips. Because ACP and ACC are driven and reset by the receiver's clock, knowing the number of cycles and fractional part since a given reference time defined by the receiver's clock allows a pseudorange to be estimated. In the case of the ACC, the pseudorange will be calculated as a function of the number of chips counted. By multiplying by the time length or distance length per chip, the pseudorange may be obtained in seconds or meters. For example, using the C/A code, if there is a code phase of 515.03 chips as measured with the local clock, the measured pseudorange will be $515 \text{ chips} \times 293 \text{ meters/chip} = 150903.8 \text{ meters}$. The true distance between a receiver on Earth and a satellite ranges, however, between 20000 km and 26000 km approximately whereas the pseudorange as measured with the C/A code phase can only have values between 0 and 300 km (1023 chips). There is thus an initial code phase ambiguity. Since we only need a coarse (within 300 km) approximate value for the pseudorange, the satellite coordinates in the navigation message and approximate coordinates of the receiver can be used to provide this coarse approximate value and the

C/A code phase is used to obtain a more precise pseudorange value, directly on the receiver. How precise is the pseudorange obtained using the C/A code? Most receivers are designed so that they can measure the code phase within 0.01 chip, or approximately 3 meters. This resolution is controlled by the number of bits of the code counter. However, noise and feedback filtering ultimately limit the precision so that adding more bits to the counter does not help after a certain point. According to (Kaplan & Hegarty, 2006, p.197), a 0.01 chip 1-sigma precision may be reached using a ½ chip correlator spacing, a 0.2 Hz bandwidth feedback filtering, an integration time of 20 ms and a carrier-to-noise density ratio (C/N_0) of at least 25 dBHz.

ACP information is rarely used as such because it depends on the IF frequency. Generally, the IF frequency is extracted so that only the number of cycles of the Doppler frequency shift is counted. The measurement obtained is called the Accumulated Doppler Range (ADR). This measurement does not depend on the IF frequency and is directly linked to the original RF frequency. Indeed, the Doppler shift is proportional to the velocity of the source with respect to the receiver and the nominal frequency of the signal:

$$\Delta f = \left(-\frac{v_r^s}{c} + d\dot{T} \right) f_0 = -\frac{v_r^s}{\lambda_0} + d\dot{T} f_0 \quad 2.28$$

where,

Δf : Doppler frequency shift (Hz)

v_r^s : Velocity of the source with respect to the receiver (m/s)

f_0 : Nominal frequency of RF signal (Hz)

λ_0 : Nominal wavelength of RF signal (m)

$d\dot{T} = d\dot{T}^s + d\dot{T}_r$: Transmitter and receiver clock drift

The ADR, measured in RF cycles, can be used to calculate a more precise pseudorange value. Indeed, since L1, L2 or L5 have wavelength (λ_0) of around 0.2 m, the pseudorange

using ADR can be calculated within 0.2 m. Considering, once again, that typical receivers can estimate the ADR with a 0.01 cycle resolution, the expected resolution of the ADR observation is 2 mm. However, ADR also contains an initial phase ambiguity. We need a first absolute value for the pseudorange with a precision better than $\lambda_0/4$. In the next section, more details will be provided concerning the ADR observation and the initial phase ambiguity.

The feedback mechanism in the demodulation process is very important. The system continuously monitors the values of the Integration & Dump circuits, I_e , I_p , I_l , Q_e , Q_p & Q_l and adjusts the frequency of the phase and code NCOs (Numerically Controlled Oscillators) and the time shift of the code generator to maintain the phase and code locked to the received signal. The circuit that monitors the values of I_e , I_p , I_l , Q_e , Q_p & Q_l and controls the NCOs accordingly is called the discriminator. Often, a mathematical combination of these values is used and thresholds are defined to take a corresponding action. Generally, a different discriminator is used for the code NCOs and for the carrier NCOs because the dynamics and expected precision are different. One example is the Costas discriminator, in which the decision is based on the discrimination algorithm $\text{atan2}(Q_p, I_p)$ (the arctangent function). Several types of discriminators exist and can be dynamically changed depending on the application and acquisition phase. Often, a priori information, such as the satellite expected location, is also used to help the peak search process. For example, during a cold-start, when no a priori information is available, the search for the correct code and phase may take longer and as such, a coarser search process and a quicker type of discriminator may be used. Once a small correlation peak is obtained or if a priori information about the visible satellites is available, a finer search process and a more accurate but slower discriminator is used. If the receiver is used in a dynamic environment, the search strategy may be different or additional external information, such as the one provided by an inertial measurement unit may be used.

Previously, it was stated that the precision of the pseudorange, as measured with the ACC or the ADR, is limited by the receiver's noise and feedback mechanism. Indeed, when the receiver continuously adjusts the Doppler frequency and code time shift to keep the signal

in lock, the response time of the discriminator limits the speed at which the adjustments can be performed. Additionally, filtering can be added to intentionally increase the response time and filter out high frequency noise. The feedback mechanism in the correlator is similar to the one in PLLs (Phase Lock Loops), where there is a discriminator (phase comparator) and a filter. The correlator tries to keep the received and the locally generated signal in phase. The main issue is then to determine the phase error of the phase tracking mechanism because this, in turn, will give us the expected pseudorange precision. The phase tracking performance is limited by the phase noise of the local oscillator and the added noise to the received signal. Filtering is then used to limit this phase noise at the price of filtering out some of the phase dynamics of the received signal. There is thus a trade-off to be made. The tracking phase error of a PLL due to thermal noise exclusively is (Kaplan & Hegarty, 2006, p. 185):

$$\sigma_t = \sqrt{\frac{B_n}{C/N_0} \left(1 + \frac{1}{2\tau_I C/N_0}\right)} \text{ (cycles)} \quad 2.29$$

where,

B_n : Carrier loop bandwidth, which depends on loop filter (Hz)

C/N_0 : Carrier to Noise as a ratio in a 1 Hz bandwidth (Hz)

τ_I : Integration time (s)

On the other hand, the influence of the oscillator phase noise on the tracking phase error for a third order PLL is (Kaplan & Hegarty, 2006):

$$\sigma_p = \frac{1}{2.25} \frac{\sigma_A f_L}{B_n} \text{ (cycles)} \quad 2.30$$

where

σ_A : Allan deviation of the oscillator (dimensionless)

f_L : Carrier frequency (Hz)

It is important to retain of these two equations that there is a trade-off regarding the carrier loop bandwidth. A large bandwidth (a high-cutoff frequency low-pass filter) is preferable so that the system can follow the dynamics of the received signals but a small bandwidth is preferable in order to filter out the phase noise of the receiver's oscillator. In practice, a bandwidth of a few Hz is used as an adequate trade-off (Kaplan & Hegarty, 2006). Figure 2.8 shows the graphical representation of Equations 2.29 and 2.30, for typical values. The carrier-to-noise of 40 dB.Hz was chosen as it is the typical minimal value for a received signal from an unobstructed, medium-to-high satellite elevation angle. As can be seen, a bandwidth between 5 and 15 Hz is a good trade-off between thermal noise and the oscillator's phase noise. Also, we can see that the phase error can, as stated before, reach around 0.01 cycle. For the FPGA-based software GNSS receiver (Sauriol & Landry, 2007) used in this research, the bandwidth chosen was 10 Hz. Details for this receiver will be given in Section 3.2.

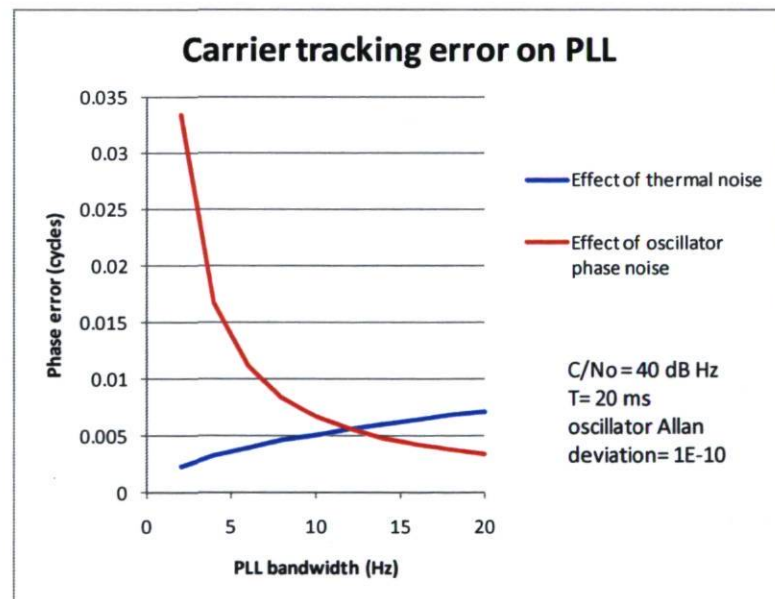


Figure 2.8 Phase noise on PLL (based on Equations 2.29 and 2.30)

2.7 GPS observations and their equations

In the previous section, we briefly explained how the GPS receiver processes the received signal in order to retrieve the observations that are necessary to positioning applications. In this section, we are going to show how these observations are used to derive the observation equation that is necessary for positioning applications.

As already stated, there are three main messages and observations generated by the receiver:

- The navigation message (M)
- The code pseudorange (P)
- The accumulated Doppler range (ADR), also called carrier phase observation

We can also include the Doppler frequency (D) observation, which is closely related to the ADR. The navigation message is mainly used in real-time applications as it contains readily available information about the satellites' positions and status (ephemeris and almanacs) and also useful information such as an ionospheric model, the satellites' clock corrections. For low-precision (a few meters) positioning applications, the pseudorange (P) and the navigation message (M) can be used to obtain a user's position. However, for high precision applications, Doppler information (D) and specially the ADR, must be used since, as presented before, ADR measurements can reach millimetric precision. We will present first the case of pseudorange measurements and how positioning can be achieved. If we take Equation 2.7, and multiply by the speed of light in vacuum c , we obtain the pseudorange in meters:

$$P(t) = c\tau = \rho + c(dT_r(t) - dT^s(t)) + z(t) \quad 2.31$$

This is the basic observation equation for code pseudorange. If we expand the additional errors $z(t)$, we get :

$$P = c\tau = \rho + c(dT_r - dT^s) + I + \Gamma + H^s + H_r + m_p + d_{pc} + \varepsilon_p \quad 2.32$$

where,

ρ : True range between the satellite and the receiver (m)

dT^s, dT_r : Satellite and receiver's clock errors (sec)

I : Ionospheric bias (m)

Γ : Tropospheric bias (m)

H^s, H_r : Satellite and receiver hardware delay (m)

m_p : Error due to multipath effect (m)

d_{pc} : Error due to antenna phase center variation

ε_p : Remaining noise and unmodeled biases

Except for special cases, the hardware delay cannot be separated from the clock errors so that often they are treated as a single variable:

$$dT^{s'} = dT^s + \frac{H^s}{v} \quad dT_r' = dT_r + \frac{H_r}{v} \quad (s) \quad 2.33$$

where,

v : Propagation speed in the hardware components (m/s)

Note that the propagation speed in the hardware components is different depending on the nature of each component. For a RG-58 coaxial cable, the propagation speed is approximately 66% of the speed of light in vacuum (c) (Suhner Holding AG, 1999) and for a SMF-28 optical fiber, it is approximately 68% of c (Corning Inc., 2002)

The observation equation is available for each channel that tracks a specific satellite so that for each observation epoch, we have a set of observation equations. The position of the receiver is contained in the range ρ :

$$\rho = \sqrt{(X^s - X_r + \theta Y_R)^2 + (Y^s - Y_r - \theta X_R)^2 + (Z^s - Z_r)^2} \quad 2.34$$

where,

X^s, Y^s, Z^s : 3D geocentric coordinates of the satellite

X_r, Y_r, Z_r : 3D geocentric coordinates of the receiver

$\theta Y_R, \theta X_R$: Additional correction factors to take into account the rotation of the Earth between the transmission and the reception times (Sagnac effect)

By combining the observation equations of n satellites, we have a system of n equations and four unknowns: X_r, Y_r, Z_r, T_r . For the proposed approach, we have only three unknowns, X_r, Y_r, Z_r , since the clock parameter is eliminated. The additional parameters, such as $X^s, Y^s, Z^s, T^s, I, \Gamma$ are calculated using information of the navigation message, or by using external measurements and used as known variables. This is the traditional strategy for positioning applications, but depending on the application, some of the additional parameters may be taken as additional unknowns or if the receiver coordinates are already known, they may be included as known parameters. Since Equation 2.34 is not linear, a linear approximation using a priori known values for X_r, Y_r, Z_r is generally used to more easily solve the system of equations (Misra & Enge, 2001):

$$\begin{aligned} \rho &= \rho_0 + \frac{d\rho}{dX} \Delta X_r + \frac{d\rho}{dY} \Delta Y_r + \frac{d\rho}{dZ} \Delta Z_r \\ &= \rho_0 + \frac{(X^s - X_0)}{\rho_0} \Delta X_r + \frac{(Y^s - Y_0)}{\rho_0} \Delta Y_r + \frac{(Z^s - Z_0)}{\rho_0} \Delta Z_r \end{aligned} \quad 2.35$$

where,

ρ_0 : Range between the satellite and the known a priori receiver position

X_0, Y_0, Z_0 : A priori receiver position, must be sufficiently close to the real position so that the linear approximation is valid

$\Delta X_r, \Delta Y_r, \Delta Z_r$: Corrective values to be added to the a priori position (X_0, Y_0, Z_0) to find the receiver position (X_r, Y_r, Z_r)

By combining Equations 2.32 and 2.35, we obtain the linear observation equation:

$$P = \rho_0 + \frac{(X^s - X_0)}{\rho_0} \Delta X_r + \frac{(Y^s - Y_0)}{\rho_0} \Delta Y_r + \frac{(Z^s - Z_0)}{\rho_0} \Delta Z_r + c(dT_0 + dT_r' - dT^{s'}) + I + \Gamma + d_{pc} + m_p + \varepsilon_p$$

where

dT_0 : A priori receiver clock parameter (generally taken as zero)

dT_r' : Clock parameter corrective value to be estimated

If we consider that there is an observation equation for each channel and that the number of equations is generally larger than the number of unknowns, we can put the system in the following matrix form (Misra & Enge, 2001):

$$P - \rho_0 - Z = \frac{d\rho}{dX} \Delta X + V \quad 2.36$$

where

$$P = \begin{bmatrix} P_r^1 \\ \dots \\ P_r^n \end{bmatrix} \quad \rho_0 = \begin{bmatrix} \rho_0^1 \\ \dots \\ \rho_0^n \end{bmatrix} \quad Z = \begin{bmatrix} I_r^1 + \Gamma_r^1 + \dots \\ \dots \\ I_r^n + \Gamma_r^n + \dots \end{bmatrix} \quad \text{: Vectors of observations and calculated parameters}$$

$$\Delta X = \begin{bmatrix} \Delta X_r \\ \Delta Y_r \\ \Delta Z_r \\ c\Delta T_r' \end{bmatrix} \quad \text{: Vector of unknowns}$$

V : Vector of observation residuals

P_r^n : Pseudorange from receiver (r) to satellite (n)

Equation 2.36 is generally written in the following form:

$$W = AX + V \quad 2.37$$

where,

$$A = \frac{d\rho}{dX} = \begin{bmatrix} -\frac{X^1-X_0}{\rho^1} & -\frac{Y^1-Y_0}{\rho^1} & -\frac{Z^1-Z_0}{\rho^1} & -c \\ \dots & \dots & \dots & \dots \\ -\frac{X^n-X_0}{\rho^n} & -\frac{Y^n-Y_0}{\rho^n} & -\frac{Z^n-Z_0}{\rho^n} & -c \end{bmatrix} \text{ (Standard approach)} \quad 2.38$$

X^n, Y^n, Z^n : Coordinates of satellite n

X_0, Y_0, Z_0 : A priori coordinates of the receiver

ρ^n : A priori range between satellite n and receiver

If only the three unknown coordinates of the receiver are estimated (no relative clock error, as possible with the proposed approach), we have for A :

$$A = \frac{d\rho}{dX} = \begin{bmatrix} -\frac{X^1-X_0}{\rho^1} & -\frac{Y^1-Y_0}{\rho^1} & -\frac{Z^1-Z_0}{\rho^1} \\ \dots & \dots & \dots \\ -\frac{X^n-X_0}{\rho^n} & -\frac{Y^n-Y_0}{\rho^n} & -\frac{Z^n-Z_0}{\rho^n} \end{bmatrix} \text{ (Proposed approach)} \quad 2.39$$

Using a least squares approach, the system may be solved using the following steps:

1) Calculation of the normal matrix : $N = A^T K A$ with K : Observation weight matrix

2) $U = A^T K W$

- 3) Estimation of the vector of unknowns: $\hat{\mathbf{X}} = \mathbf{N}^{-1}\mathbf{U}$
- 4) Estimation of the residuals vector: $\mathbf{V} = \mathbf{AX} - \mathbf{W}$
- 5) Estimation of the a posteriori variance factor: $\hat{\sigma}^2 = \frac{\mathbf{V}^T\mathbf{P}\mathbf{V}}{n-u}$
- 6) Estimation of the variance-covariance matrix of the estimated unknowns:
 $\Sigma_{\mathbf{X}} = \hat{\sigma}^2\mathbf{N}^{-1}$

Additionally, the number of satellites and their sky distribution (geometric configuration) can be quantified by the DOP (Dilution Of Precision) factors. These factors give us an estimate of how the precision in the (random) range (pseudorange or ambiguity fixed phase) measurement propagates to each of the unknown parameters, 3D coordinates and the receiver's clock error (for the standard approach). One can also estimate the DOP (Dilution Of Precision) factors by calculating the matrix \mathbf{Q} (Misra & Enge, 2001):

$$\mathbf{Q} = (\mathbf{A}^T\mathbf{A})^{-1} = \begin{bmatrix} q_x^2 & q_{x,y} & q_{x,z} & q_{x,T} \\ q_{y,x} & q_y^2 & q_{y,z} & q_{y,T} \\ q_{z,x} & q_{z,y} & q_z^2 & q_{z,T} \\ q_{T,x} & q_{T,y} & q_{T,z} & q_T^2 \end{bmatrix} \text{ (Standard approach)} \quad 2.40$$

For the proposed approach, the $\mathbf{A}^T\mathbf{A}$ has 3×3 dimensions (3 unknowns instead of 4), so the cofactors matrix \mathbf{Q} is as follows:

$$\mathbf{Q} = (\mathbf{A}^T\mathbf{A})^{-1} = \begin{bmatrix} q_x^2 & q_{x,y} & q_{x,z} \\ q_{y,x} & q_y^2 & q_{y,z} \\ q_{z,x} & q_{z,y} & q_z^2 \end{bmatrix} \text{ (Proposed approach)} \quad 2.41$$

It is important to point out that the elements of the \mathbf{Q} matrix for the proposed approach are not the same as the first elements of the \mathbf{Q} matrix for the standard approach since for the proposed approach only a 3×3 matrix at each epoch has to be inverted. The DOP factors are:

Geometric Dilution Of Precision : $GDOP = \sqrt{q_x^2 + q_y^2 + q_z^2 + q_T^2}$ (standard approach)

Position Dilution Of Precision : $PDOP = \sqrt{q_x^2 + q_y^2 + q_z^2}$

The matrix Q can be transformed to a local topocentric coordinate system (North, East, Up)

$$Q_{NEU} = \begin{bmatrix} q_N^2 & q_{N,E} & q_{N,U} & q_{N,T} \\ q_{E,N} & q_E^2 & q_{E,U} & q_{E,T} \\ q_{U,N} & q_{U,E} & q_U^2 & q_{U,T} \\ q_{T,N} & q_{T,E} & q_{T,U} & q_T^2 \end{bmatrix} \quad \text{(Standard approach)} \quad 2.42$$

$$Q_{NEU} = \begin{bmatrix} q_N^2 & q_{N,E} & q_{N,U} \\ q_{E,N} & q_E^2 & q_{E,U} \\ q_{U,N} & q_{U,E} & q_U^2 \end{bmatrix} \quad \text{(Proposed approach)} \quad 2.43$$

North Dilution Of Precision : $NDOP = \sqrt{q_N^2}$

East Dilution Of Precision : $EDOP = \sqrt{q_E^2}$

Vertical Dilution Of Precision : $VDOP = \sqrt{q_U^2}$

The meaning of these factors is that, for example, if $VDOP=3$, a random error of 1 m in the pseudorange will translate into an error of 3 m in the vertical position, a deterioration by a factor 3. For the standard approach, $VDOP$ values are usually up to 2 to 3 larger than the $NDOP$ and $EDOP$ factors, so horizontal coordinates are usually 2 to 3 times more precise than vertical coordinates (Santerre, 1991). For the proposed approach $VDOP$ values are similar to $NDOP$ and $EDOP$ values.

A way to understand why $VDOP$ values are lower for the proposed approach compared to the standard approach is using a geometrical interpretation of the DOP factors (Santerre &

Geiger, 1998). In general terms, for the proposed approach, the VDOP factors are related to the volume of the polyhedron formed by the unit vectors between the receiver and the satellites. For the standard approach, the VDOP factors are instead related to the volume of the polyhedron formed by the differences of these unit vectors between themselves. Since for the first case the volume is usually larger, we can expect the VDOP values to be lower (the VDOP factors being inversely proportional to the volume of the polyhedron described above). Further details and figures showing this geometrical interpretation are given in (Santerre & Geiger, 1998).

For ADR measurements, also commonly called carrier phase measurements, they can be related to the pseudorange in the following way, for an ideal case (no biases):

$$ADR = \int_{t_0}^t \Delta f dt = - \int_{t_0}^t \frac{v_r^s}{\lambda_0} dt = \frac{1}{\lambda_0} [\rho(t) - \rho(t_0)] \quad 2.44$$

where,

Δf : Doppler shift interpolated between times t_0 and t

v_r^s : Relative topocentric radial velocity between the satellite (s) and the receiver (r)

λ_0 : GPS nominal signal wavelength

In the real case, biases affect the ADR measurement in a similar way to the pseudorange measurements, so that Equation 2.44 is modified:

$$ADR = \frac{1}{\lambda_0} [\rho(t) - I + \Gamma + cdT_r' - cdT^{s'} + m_\phi + d_{pc} + \varepsilon_\phi - \rho(t_0)] \text{ (cycles)} \quad 2.45$$

In this case, the ionospheric effect (I) is negative because as the ionosphere is a dispersive medium, the phase velocity is greater than the speed of light in vacuum (c) whereas the group velocity is inferior c as was the case for the code measurements. There is an additional unknown, the range $\rho(t_0)$ at reference time t_0 . This value is nevertheless constant as long as the receiver maintains phase lock and we will call it the initial range.

The initial range is unknown but it can be considered to be an integer number of cycles plus the initial oscillators' phase. More explicitly, the range at the initial reference time t_0 may be considered as the satellite's oscillator phase at transmit time $(t_0 - \rho(t_0)/c)$ plus an integer number of cycles plus the receiver the receiver oscillator phase at time t_0 :

$$\rho(t_0) = \lambda_0 [N(t_0) + \phi_0^s(t_0 - \rho(t_0)/c) + \phi_{0,r}(t_0)] \quad 2.46$$

where,

ϕ_0^s : Initial phase of satellite oscillator at time t_0 (fraction of a cycle)

$\phi_{0,r}$: Initial phase of receiver oscillator at time t_0 (fraction of a cycle)

$N(t_0)$: Integer initial phase ambiguity (integer number of cycles)

However, ϕ_0^s and $\phi_{0,r}$ are usually included in the clock parameter:

$$dT^{s''} = dT^{s'} + \frac{\lambda_0}{c} \phi_0^s \quad dT_r'' = dT_r' + \frac{\lambda_0}{c} \phi_{0,r} \text{ (seconds)} \quad 2.47$$

Then, the ADR measurement contains an integer initial phase ambiguity:

$$ADR = \frac{1}{\lambda_0} [\rho(t) - \lambda_0 N(t_0) - l + \Gamma - c dT^{s''} + c dT_r'' + m_p + d_{pc} + \varepsilon_\phi] \quad 2.48$$

where,

$N(t_0) = N$: Initial phase ambiguity which is an integer value when measured in cycles

The set of ADR observation equations may be solved in a similar way as for the code pseudorange observations, that is, with a least squares approach. However, there are additional unknown parameters: the initial phase ambiguity N for each observed satellite. But, since these values do not change as long as the receiver keeps track of the satellite, the number of initial phase ambiguity parameters remains constant and observations may be accumulated for many epochs. ADR observations are far more precise than code

pseudoranges and, as such, the calculated additional biases such as tropospheric and ionospheric errors and the satellites' coordinates must also be precisely calculated. This is why, to fully take advantage of the precision offered by ADR observations, biases must be either precisely determined or eliminated. This can be achieved in two ways:

- 1) Use external, high precision estimates of the satellites' coordinates and the remaining biases such as satellites' clock errors and ionospheric and tropospheric biases.
- 2) Use linear combinations of observations between receivers and/or satellites to reduce or eliminate biases.

The first approach is used in PPP (Precise Point Positioning) (Kouba & Héroux, 2001). The second approach is the most commonly used in high precision applications and consists of using more than one receiver and make differences between observations. Generally, one receiver is defined as a base station and is located on a site whose coordinates are precisely known. The other receiver is located on the site whose coordinates are to be determined. With observations from two sites, the single difference between receivers' observations can be done. In this kind of combination, the observations to a common satellite from both sites are subtracted.

$$\Delta\Phi = \frac{1}{\lambda_0} [\Delta\rho - \lambda_0\Delta N - \Delta I + \Delta\Gamma + c\Delta dT_r'' + \Delta m_p + \Delta d_{pc} + \varepsilon_{\Delta\phi}] \text{ (cycles)} \quad 2.49$$

where,

Δ : Differentiation operator between a simultaneous observation from one site and the observation from another site to a common satellite

The main advantage of single differencing of observations (between stations) is that the satellites' clock error and satellites' hardware delays are eliminated. Moreover, remaining biases such as ionospheric and tropospheric errors are considerably reduced, especially for

short baselines. However, relative receivers' clock error $\Delta dT_r''$ remain and can be high enough ($1 \mu s \approx 300 \text{ m}$) and correlated to the phase initial ambiguities ΔN , so that simultaneous estimation of $\Delta dT_r''$ and ΔN may be difficult or even impossible. A different approach has to be used so that a search pattern for different candidate values for ΔN is established and statistical tests are done to find the correct value for ΔN and then, coordinates and $\Delta dT_r''$ are estimated (See (Hatch, 1990) and Section 4.4 for further details). In double differences processing, a second differentiation is performed between different satellites observations:

$$\nabla \Delta \Phi = \frac{1}{\lambda_0} [\nabla \Delta \rho - \lambda_0 \nabla \Delta N - \nabla \Delta I + \nabla \Delta \Gamma + \nabla \Delta m_p + \nabla \Delta d_{pc} + \varepsilon_{\nabla \Delta \phi}] \quad 2.50$$

where,

∇ : Differentiation operator between a simultaneous observation to a given satellite and an observation to another satellite

The main advantage of double differencing is the elimination of the receivers' clock errors and receiver hardware delays. Ionospheric and tropospheric errors are further reduced. The process of fixing ∇N or $\nabla \Delta N$ to an integer value helps to further improve the precision of the positioning. However, if remaining biases increase such as, for example, the ionospheric bias for a long baseline or the multipath, ambiguity fixing may become difficult or impossible. Statistical tests are usually done to try to correctly fix $\nabla \Delta N$ to their integer values. Ambiguity fixing is a non-trivial problem and as such, many algorithms, statistical tests and approaches have been proposed, depending on the type of application. More details on the ambiguity fixing problematic may be found in (Teunissen, 1996). For our project, in which single difference processing is used, the ambiguity resolution algorithm used is explained in Section 4.4.

Double difference processing is the most common type of processing used in commercial precision positioning software. However, one has to keep in mind that double differencing

has some disadvantages such as the reduction of the number of observations and the increase in noise in the observations.

Finally, if multi-frequency receivers are used, a linear combination of the observations for the different frequencies may be used. The main advantage of this type of combination is the elimination of the ionospheric bias by taking advantage of the dispersive nature of this phenomenon (see Section 2.3.1). Using linear combinations of multi-frequency observations may also help in the cycle slip detection and the ambiguity fixing processes.

3 System design for the proposed architecture

In this chapter, we will present how the proposed architecture was designed and the various steps and performance considerations that had to be made. First, previous related works are reviewed. Particularly, an overview will be given of the theoretical works that are the basis of the prototype and on the existing GPS-over-fiber, relative delay propagation measurement techniques and multi-antenna configurations. Finally, we will present the prototype and explain its operation principles.

3.1 Theoretical background and previous works

3.1.1 Vertical component precision improvement

The starting point of this research project is based on the results of the simulations presented by (Santerre & Beutler, 1993), where a multi-antenna-to-one-receiver configuration is proposed. With this type of configuration (see Figure 3.1b), the receivers' clock error may be eliminated in single difference processing. Equation 2.49 for standard single difference processing is thus modified in the following way:

$$\Delta\Phi = \frac{1}{\lambda_0} [\Delta\rho - \lambda_0\Delta N - \Delta I + \Delta\Gamma + \Delta H_r + \Delta m_p + \Delta d_{pc} + \varepsilon_{\Delta\phi}] \text{ (cycles)} \quad 3.1$$

The main difference here is that the receiver clock error (ΔdT_r) and the initial phase of receiver oscillator (ϕ_{0_r}) are eliminated but the receiver hardware delay (ΔH_r) remains. To confirm that, with the proposed configuration, an improvement in the vertical component precision is to be expected when compared with the standard method (Figure 3.1a), a simulation technique based on the one presented in (Santerre, 1991) was used in (Santerre & Beutler, 1993). With this simulation, it became possible to compare the confidence ellipsoids of the station coordinates between the two methods and to quantify the error propagation on the coordinates of systematic errors such as the hardware delay and the tropospheric bias. The impact of the satellite sky distribution and the elevation mask angle

were taken into consideration as well. With the results of this simulation, (Santerre & Beutler, 1993) showed that with the proposed configuration, a significant increase in the precision of the vertical component is obtained as compared to the standard method. The precision of the vertical component is then of the same magnitude as that of the horizontal components.

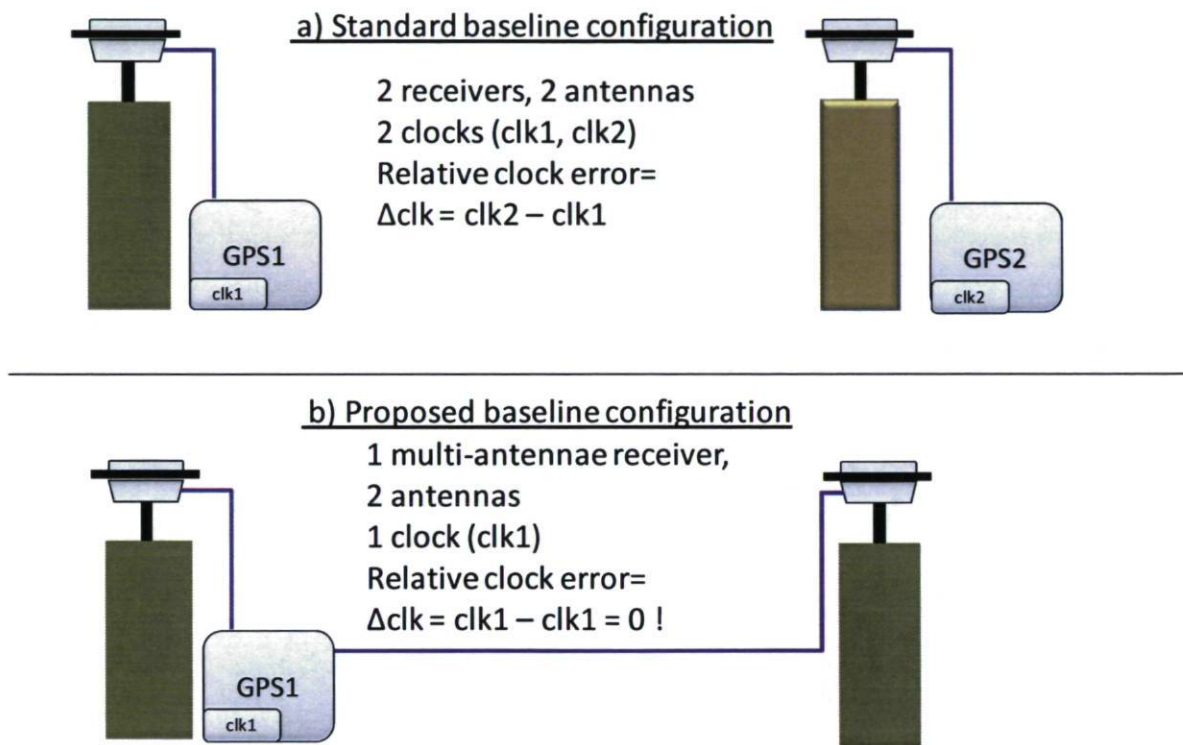


Figure 3.1 Comparison between standard baseline configuration and proposed baseline configuration

The comparison is shown in Table 3.1.

Table 3.1 Improvement factor of the vertical component between the standard and the proposed configurations as simulated by (Santerre & Beutler, 1993)

Latitude	Elevation Mask	Improvement factor	
		Without tropospheric parameter estimation	With tropospheric parameter estimation
0° (Equator)	10°	2.7	2
	20°	3.6	2
45° (Mid-latitude)	10°	2.5	2
	20°	3.3	2
90° (Poles)	10°	3.1	2
	20°	5.1	2

Note that these results hold as long as the remaining biases are carefully controlled. In the paper, the effect of a systematic bias such as the one caused by the hardware delay, is studied. Its impact is very important on the precision of the vertical component. Indeed, (Santerre & Beutler, 1993) showed that each millimeter of error on the relative receiver hardware delay (ΔH_r) translates into -0.8 to -2.0 mm of error on the vertical component. Thus, if our objective is to achieve millimetric precision in the vertical component, it is necessary to calibrate ΔH_r at the millimeter level (corresponding to a few picoseconds). This calibration may be realized with a zero baseline configuration, that is, a configuration in which the signal coming from one antenna is split and fed to the 2 cables/optical fibers linked to the receiver. With a zero baseline, the difference between the phase observations contains only the hardware delay and the remaining noise error:

$$\Delta\Phi = \frac{1}{\lambda_0} [\Delta H_r + \varepsilon_{\Delta\Phi}] \quad 3.2$$

However, calibration with a zero baseline configuration is static, that is, it can be done once before the final setup implementation but will not be valid if the expected variations of ΔH_r are larger than the precision of the measurement during the calibration process. For instance, if ΔH_r is calibrated within the millimeter (which is necessary) then the variation of ΔH_r once the final setup is implemented must not be larger than 1 mm. However, as stated

in Section 2.4.1, expected optical fiber and coaxial cable length variations due to normal temperature changes are often larger than 1 mm. This is why a real-time monitoring of ΔH_r for a successful implementation of the configuration becomes mandatory.

3.1.2 Hardware delay calibration and temperature influence

The hardware delay calibration problem is also encountered in time and frequency transfer applications using GPS. This is why we find it useful to analyze works by researchers in this domain. As already explained in the previous chapter, once the receiver is locked, it is synchronized to GPS time. The GPS receiver thus becomes a very useful and precise time reference for applications such as telecommunications systems. In such applications, the main goal is to estimate the receiver's clock error as precisely as possible. However, as mentioned previously, the receiver's clock error parameter obtained is a combination of the receiver's clock error ΔdT_r , the hardware delay, ΔH_r and the initial phase of receiver oscillator (ϕ_{0r}) combined in a single parameter, ΔdT_r ". Time transfer applications need to separate these components as the hardware delay may change due to temperature variations affecting the cables. In works by (Bruyninx et al., 2000) and (Rieck et al., 2003), experiments were performed on zero baselines and short baselines in order to study the influence of temperature on time and frequency transfers using GPS. In (Bruyninx et al., 2000), an experiment with a zero baseline allowed it to isolate the effects of the hardware delays (cables and electronic circuits). Time transfer was done with code and phase observations and the non-controlled room temperature was monitored. What turned out is that the correlation between the temperature variations and the single difference phase observations was important. The coefficient between both variables is approximately 30 ps/°C (around 10 mm/°C). On the other hand, for code observations, noise was about 100 times greater but correlation with temperature was less important. This experiment confirms the necessity of a precise control of the temperature of the antennas, cables and

electronic circuits for accurate time transfer. Frequency stability reached after 1 day was 6×10^{-16} for phase observations and 2×10^{-15} for code observations.

In (Rieck et al., 2003), the authors confirm the significant impact of temperature on time transfer applications with phase observations. They propose three approaches:

- 1) A zero baseline configuration, similar to (Bruyninx et al., 2000).
- 2) The use of a vector voltmeter and a signal generator.
- 3) The use of a 1 Pulse Per Second (PPS) signal and an event counter.

The purpose of these experiments is to calibrate the delays in the components (antennas, cables, electronic circuits) that are susceptible to vary with temperature. As the first approach is the same as the one presented by (Bruyninx et al., 2000) and the third approach was not validated through experimentation, we will focus on the second one. For this method, the vector voltmeter can measure not only the amplitude but also the phase difference between two signals. Thus, it is possible to measure the propagation delay of a signal through a component by comparing the phase of the signal at the input with the one at the output. The test signal comes from a waveform generator with a stable oscillator reference. This method generally gives better results than the zero baseline configuration. However, the propagation path of the test signal is not exactly the same as that of the GPS signal because it does not include the antenna and the receiver itself. Nevertheless, most of the propagation delay comes from the coaxial cable (or optical fiber) separating the receiver and the antenna. The propagation delay through some of the electronic circuits such as the LNAs (Low Noise Amplifier) can also be measured with this technique. The main results of the experiments conducted by (Rieck et al., 2003) are that there exists an approximately linear relationship between the temperature and the delay on the antennas' LNAs, cables and electronic components. For the LNA's, the results are $-0.1 \text{ ps}/^\circ\text{C}$ ($-0.03 \text{ mm}/^\circ\text{C}$) above 20°C and $0.17 \text{ ps}/^\circ\text{C}$ below 15°C . What can also be concluded is that a zero baseline is practical for hardware delay measurement because no extra equipment is needed: the GPS receiver itself does the measurements. However, the main drawback is that the

measurements cannot be performed once the normal baseline configuration is reestablished. The method with the reference signal and vector voltmeter is simple but must be adapted to work along with the GPS signal in real-time. Because the thermal influence is so important, it is clear that a real-time hardware delay calibration is preferable. It might be possible to thermally isolate the cables and electronic components but for long-runs of cable, this might be expensive, not practical or even impossible.

3.1.3 GPS-over-fiber systems

If the antenna and the receiver are separated by more than a few hundred meters, the use of coaxial cable is not possible without using amplification. For RF signals at microwave frequencies (above 0.3 GHz), the attenuation of coaxial cable is very large. For example, at 1.0 GHz, attenuation is 0.61dB/m for a RG-58 coaxial braided cable (Suhner Holding AG, 1999). However, the use of amplification along the line may be cumbersome and has also its limits as additional noise is added at each amplification step. The use of optical fiber therefore is a natural choice for the transmission of RF signals over long distances. The attenuation of the signal inside optical fiber is very low compared to the attenuation inside coaxial cable (about 0.0002 dB/m or 0.2 dB/km at 1550 nm for standard monomode fiber (Corning Inc., 2002)). Another advantage of optical fiber over coaxial cable is its immunity to external electric RF interferences. Additionally, if optical fiber is used instead of coaxial cable, the thermal expansion coefficient is much smaller, as seen in Section 2.4.

The conversion of the electric RF signal to the optical domain, its transport over optical fiber and its conversion back to electrical domain introduce noise and performance degradation that has to be quantified. It should be convenient then to analyze the performance criteria of fiber-optic based systems for RF signal transportation, also called radio-over-fiber systems. In (Ackerman & Cox, 2001), an overview of the main performance criteria for radio-over-fiber systems is given. As the optical fiber transports an analog (RF) signal instead of a digital one as in most of the fiber-optic applications, the

performance criteria are different. Whereas in digital signals over fiber, the main performance criterion is the BER (Bit Error Rate), in radio-over-fiber systems it is the Carrier-to-Noise Ratio (CNR). However, other performance criteria are used and will be presented shortly. Firstly, it is convenient to present the four main parts of a radio-over-fiber system: the optical source, the light modulator, the optical fiber and the photodetector. The system may also include optical and electrical amplifiers and passive optical and electrical components for filtering, connecting, splitting or impedance matching purposes. For the optical source, a laser or LED may be used. However, due to the broader spectrum of LED sources, these are generally not used for radio-over-fiber application. For the optical fiber, monomode fiber is preferred, as explained in Section 2.4.2. For the photodetector, the most common component used is the p-i-n photodiode, which is made of an intrinsic semiconductor (i) sandwiched between a p-type semiconductor (p) and n-type semiconductor (n) and which is optimized either for 1.3 μm or 1.5 μm wavelength operation. The conversion of the RF signal to the optical domain may be done either by directly modulating the supply current of the optical source (direct modulation) or by modulating the light with a separate device (external modulation). Direct modulation is simpler and cheaper since no additional components are needed. However, because laser wavelength changes as the supply current varies; direct modulation induces a chirping effect (variation of the frequency of the optical signal) which limits the modulation speed. This is why external modulators are preferred for high speed signals.

In Table 3.2, we present the main performance criteria for a radio-over-fiber system and for each of the main components that determine them.

Table 3.2 Main performance criteria for a radio-over-fiber system

Criteria	Critical components
Attenuation, power losses	Efficiency of the optical source (electrical-to-optical power efficiency)
	Efficiency of the modulator (electrical-to-optical power efficiency)
	Attenuation, absorption and scattering losses of the optical fiber
	Efficiency (optical-to-electrical power efficiency) of the photodetector
Bandwidth	Time response of the optical source due to the photon and electron lifetimes in the laser cavity
	Time response of the external modulator
	Time response of the photodetector due to transit and diffusion time of the photocarriers and RC (Resistance-Capacitor) time constant
Noise figure	Intensity noise due to spontaneous emission and current & temperature variations of the laser
	Intensity noise due primarily to quantum and thermal noise in the photodetector
Frequency selective delay (group delay distortion)	Chromatic dispersion of the optical fiber
Frequency selective noise (phase noise)	Converted laser low frequency noise to RF phase noise through non-linearities of laser & photodetector
Additional frequencies generation (harmonics, multi-wave mixing, spectrum broadening)	Non-linearities of the laser and the photodetector
	Non-linear optical effects of the optical fiber

These criteria and the physical processes briefly described in Table 3.2 will be explained in more detail in Chapter 4. We must, however, state that items in Table 3.2 may not be independent and may have an impact on the others. For example, there is a tradeoff between bandwidth and efficiency of the photodetector: the larger the bandwidth, the smaller the efficiency. Another example is the tradeoff between bandwidth and linearity: a larger bandwidth generally requires more optical power, which, in turn, increases the non-linear effects of the optical components. Each of the criteria can guide us in the proper choice of components and design of the radio-over-fiber system. For the first one, a power budget can be elaborated knowing the characteristics of each component of the system. Amplifiers can then be inserted to compensate the losses if needed. The second criterion, the bandwidth, allows us to choose the right components for the required bandwidth of the system. The noise figure is an important criterion since it cannot be compensated, as was

the case for the power losses. We can only try to minimize the noise figure by careful choice of components and operation points optimization and see the impact on the system performance based on a selected performance threshold. The three last performance criteria, frequency selective attenuation, phase noise and additional frequencies generation have more impact on long fiber runs and high bandwidth systems. However, tests and/or calculations must be performed to confirm that these effects can be neglected in our particular configuration (see Sections 4.1.3 and 4.1.4).

3.1.4 Multi-antenna receiver

With a multi-antenna, single receiver configuration, it is possible to eliminate the relative receiver clock error in single differences, but not the remaining relative hardware delay. This type of configuration has already been used in similar applications and is very common in GPS attitude measurements applications.

In (He et al., 2005), the authors used a multi-antenna and one receiver configuration to monitor a dam in China. In this case, they wanted to minimize costs and use a standard receiver instead of a multi-antenna receiver, which must have more channels and is thus more expensive. In order to use a standard (one antenna) receiver, they built a commutation system that sequentially connects it to up to 8 antennas. Two options were considered to establish the interconnection sequence:

- The receiver is connected to one antenna for 1 observation epoch and then switches to the next antenna for 1 epoch and so on. The main disadvantage of this option is that the observations flux is interrupted for each antenna causing cycle slips that cannot be easily corrected with conventional methods. However, for static or quasi-static (slow movements) applications, it is still possible to solve for the ambiguities by using the coordinates of the previous epoch.

- The receiver is connected to each antenna for a period of time long enough to solve for the initial double differences phase ambiguities.

The second option was the one the authors chose (He et al., 2005). The connection between the commutation system and the antennas is made with coaxial cable and is limited to 30 m due to the strong attenuation. However, with the use of low-noise amplifiers, they were able to extend this distance to 1 km. Alternatively, optical fiber might but was not used in this experiment. A wireless link transports the GPS data to a control center. By using 10 minute switching gates for each antenna and 15 second epochs, it was possible to reach 3 mm precision in horizontal components and 7 mm precision in the vertical component. This paper is interesting because it confirms that millimetric precision may be reached with GPS in dam monitoring applications but also that the vertical precision is two times less due to double difference processing. In this case, the problems associated with the calibration of the delay in the cables vanishes but it has a repercussion on the vertical precision. The motivation of using a single receiver is driven by cost issues and not by the wish to remove the relative clock error in single differences processing.

Special multi-antenna receivers are commonly used for GPS attitude control applications. The problems related to relative hardware delays are thus also encountered in this type of applications if single difference processing is used. In attitude applications, instead of the 3D coordinates, the three rotation angles of a platform, namely the roll, the pitch and the yaw angles, are determined. Due to the same reasons that cause the vertical component to be less precise than the horizontal components in standard GPS positioning, the roll and pitch angles are 2 to 3 times less precise than the yaw angle. In (Li et al., 2004), there is an interesting approach for GPS attitude control in which both double and single difference observations are used. First, double differences observations are used to obtain a first ambiguities-fixed solution for the pitch, yaw and roll angles. Then, this solution is applied to the single difference observations to obtain the relative hardware delay (ΔH). Finally, the ambiguities in the single difference solution are fixed using the determined value of ΔH to find an ambiguity-fixed single difference solution for the pitch, roll and yaw angles. The main advantage of the method proposed by the authors is that no external measurement is

needed to find the relative hardware delay (ΔH) and that it is a method that allows it to do single difference processing without receiver clock parameter estimation. As expected, the roll and pitch precision are improved with this approach and are, with this approach, similar to the yaw precision. These results hold as long as there is no variation in the relative hardware delay. For longer cable runs, where temperature variations would make the relative hardware delay (ΔH) change significantly, an external, real-time calibration of this delay would be necessary.

Many suppliers offer specialized receivers for attitude control, which can be connected to up to four antennas. Let us mention, for example, the JNS-Gyro 2T from Javad (Javad Navigation Systems, 2010) or the VS101/VS111 GPS compass from Hemisphere GPS (Hemisphere GPS, 2010). However, this type of receivers is much more expensive than standard geodetic-type receivers (around \$30000 for a 4 antenna system). Thus, we also considered the option of using separate, standard receivers using a common oscillator. Most geodetic receivers offer the possibility to use an external oscillator. The receivers must, however, also share the same clock reference and in order to eliminate the relative receiver clock error in single differences. A few receivers offer the possibility to use an external clock reference. An example is the Ashtech Z12-T, no longer available, which had a 1 PPS (Pulse Per Second) input. An example of a currently available receiver which accepts external clock references is, e.g., the Topcon's E160 T OEM's receiver (Topcon Positioning Systems, 2010), which has an "event marker" input which may be used to feed an external clock reference.

Most commercial receivers are "black boxes": one connects the antenna on one side and collects the data on the other. It is difficult to have access to all signals generated inside the receiver. This is why the use of "open", experimental receivers is an attractive option for our purpose because we need to transport the GPS signal over fiber and have an accurate control of the propagation delay on the cables and electronic circuits and of the clock reference. A research team from the *Laboratoire de Communications et d'Intégration de la Micro Électronique* (LACIME) of the *École de Technologie Supérieure* (ÉTS) in Montreal, Canada, has developed an FPGA-based software GNSS receiver (Sauriol & Landry, 2007)

that offers up to 36 channels and 4 antennas and a flexible architecture. This receiver was used in our project. More information is provided in Section 3.2.

3.1.5 Existing GPS-over-fiber solutions

GPS-over-fiber systems are not new. In 1992, (MacDoran et al., 1992) proposed a system where the GPS signal received on an antenna is amplified and downconverted to Intermediate Frequency (IF) and then converted to an optical signal and transported over 4 km of optical fiber. At the other end of the fiber, the signal is converted back to the electrical domain and is successfully processed by the receiver. According to the authors, they estimate that the maximum fiber length could reach 100 km. Nowadays, several companies offer specialized equipment for transmitting GPS signals between the antenna and the receiver using optical fiber and associated converters. Let us mention the FOGSPAL (Fiber optic GPS Antenna Link), offered by GPS Networking Inc (GPS Networking, 2010), the Vialite Metro-GPS form PPM (Pulse Power & Measurement) Ltd. (Vialite-PPM, 2010) and the Fiber optic DUC-1 from Raven Precision – ATC (Raven Precision, 2010). Table 3.3 shows the main characteristics of these systems.

Note that using multimode 660 nm fiber instead of monomode fiber, such as in the case of the DUC-1 of Raven Precision-ATC, decreases cost. However, this is only possible because the GPS signal is downconverted to a lower, IF frequency. This variety of equipment is well suited for standard GPS applications. For the application we need, however, real-time relative delay calibration is not offered by these equipments since it is not needed in standard GPS applications.

Table 3.3 Main characteristics of some commercial GPS-over-fiber solutions

Product model	FOGSPAL	Vialite Metro-GPS	Fiber optic DUC-1
Company	GPS Networking Inc	PPM (Pulse Power & Measurement) Ltd	Raven Precision – ATC
Number of antenna interfaces	1	2	1
Number of optical fiber interfaces	1	2	1
Frequencies	L1/L2	L1/L2	L1
Main parts	1 RF-to-OPT convertor + 1 OPT-to-RF + 1 power supply + 1 antenna	1 RF-to-OPT convertor + 1 OPT-to-RF + 1 power supply + 1 antenna	1 RF-to-OPT convertor + 1 OPT-to-RF + 1 power supply
Type of fiber & connectors	Monomode 1310 nm / FP/PC connector	Monomode 1310 nm / FP/PC connector	Multimode 660 nm / ST connector
Noise figure	15 dB	18 dB	Not available
IF down-conversion	No	Not available	Yes
Price	US\$9000	US\$9000	US\$1450

3.1.6 Measurement techniques for relative propagation delay

Most of the techniques used to measure the delay in a propagation medium rely on the use of a reference signal, the propagation time of which is estimated. In free space, Radar and Lidar are perhaps the most commonly known techniques. GPS itself measures a propagation delay between the satellite and the receiver. In the Radar and Lidar cases, the transmitter and receiver of the reference signal are usually on the same device so that the system relies on the reflection of the signal on a reflective surface to estimate the round-trip propagation time of the signal. On the other hand, in the GPS system, the transmitter and receiver are different devices, allowing only for the estimation of a one-way direct propagation time. In this case, both the receiver and the transmitter must be perfectly synchronized to calculate an accurate propagation time. Apart from being categorized according to transmitter/receiver separation, propagation measurement techniques may be

further divided into categories depending on the type of reference signal used. The three most common techniques are the pulse method, the phase-shift and the frequency-shift methods (Larson & Paulter Jr., 2007). In the first method, a pulse-like signal is sent by the transmitter and the receiver uses a time interval counter triggered by the transmitted, the received and/or a locally generated pulse to estimate the propagation time. In the second method, a continuous carrier wave is sent and the phase of the received signal is compared to a locally generated carrier that is synchronized with the transmitted carrier or to the transmitted carrier itself. Finally, the third method is a refinement of the second in which the frequencies of the transmitted and the received signal are compared. The frequency of the received signal may have changed due to the Doppler effect, in which case the velocity of the target may be estimated or due to the frequency modulation of the transmitted signal, in which case the difference in frequencies between the received and transmitted signals gives us the propagation time if the frequency modulation pattern is known. This is simply a basic description of the three methods; many refinements have been proposed depending on the particular application. In the case of the GPS system, the ranging technique uses a combination of the three methods: the PRN code observations may be considered as a variation of the pulse method, where the PRN code represents a sequence of pulses; the Doppler observations may be considered a frequency-shift method and the phase observations represent a phase-shift method.

For the relative propagation delay on two different transmission lines, a single reference signal is generally used. This signal is split and sent on the two lines and the relative delay is measured at the other end by comparing the signals. All three methods exposed previously may be used but, for simplicity, the phase-shift method is usually preferred because simple and inexpensive devices such as RF mixers may be used for phase comparison. Because of the ever increasing oscillator speed and stability requirements in the telecommunications applications, there is a growing need to accurately measure relative propagation delays. On the other hand, optical fiber is taking a predominant place in long, high speed telecommunication links. Over the last decades, increasing precision has been achieved using the phase-shift method and optical fiber. In 1982, (Costa et al., 1982), using

the phase-shift technique with LED's sources, a 32 MHz reference signal and a vector voltmeter as the phase comparator, obtained a precision of a few picoseconds in relative delay measurements. In 1997, (Mechels et al., 1997), using a laser source, a multimode fiber, a 1.9 GHz reference signal and a vector voltmeter, obtained 0.2 ps precision. Other more recent examples of phase-shift relative delay measurements include the experiments by (Dennis & Williams, 2005) and (Larson & Paulter Jr., 2007), where 72 fs (femtoseconds) and 90 fs precision in relative delay measurements, respectively, have been achieved. Of course these are only a few examples of the capabilities of the phase-shift techniques. They have in common that the reference signal is a VHF/Microwave signal modulated onto an optical carrier. It is clear that the higher the frequency, the shorter the wavelength, and the better the precision we can achieve. For higher precision requirements it is possible to use the optical carrier itself as the reference signal and to compare the optical phase in order to estimate the relative delay (optical interferometric approach). In this case, as the wavelength of typical optical carriers is around 1 μm , a precision below 3 fs can theoretically be achieved. However, in this case, a more sophisticated setup is necessary, with laser phase lock mechanisms to ensure high spectral purity. An example of this kind of setups is presented by (Cliche & Shillue, 2006), where two lasers are synchronized with an optical PLL to remove lasers' phase fluctuations. As the two lasers have different wavelengths, a high spectral purity RF carrier is generated, the frequency of which is equal to the frequency difference of the lasers. At the same time, a fiber stretcher compensates automatically the optical fiber length fluctuations using the relative delay measurements.

In summary, we conclude that the phase-shift method is a proven technique that we may use for our project. It has the main advantage that it is simple to implement and precisions better than 1 ps can be achieved with microwave reference signals and a simple phase detector. In Section 4.3, we will present more details about the actual implementation and the performance requirements.

3.2 Integrated GPS-over-fiber and real-time delay measurement solution

After analyzing existing GPS-over-fiber and multi-antenna configurations, the main points that have to be considered for our own design and solution are:

- Real-time, high precision calibration (better than 1 mm) of the relative hardware delay is necessary to achieve millimetric precision in the vertical component with GPS relative positioning.
- The GPS signal by itself cannot be used to calibrate this delay. Zero baselines cannot be used in real-time and double difference solutions are not accurate enough.
- If an additional signal is used for calibration of the relative hardware delay, it must not interfere with the GPS signal and propagate through the same cable/fiber.
- Current commercial GPS-over-fiber solutions and multi-antenna receivers do not offer relative real-time hardware delay calibration.
- Signal degradation after electrical-to-optical and optical-to-electrical conversion must be minimized.

With these considerations, we proceeded to design and build a system prototype which combines the characteristics of a GPS-over-fiber system, a real-time relative delay calibration system based on the phase shift technique using a reference 1.55142 GHz signal, and a multi-antenna receiver. As will be shown later, the 1.55142 GHz frequency was chosen because, on one hand, its wavelength is short enough so that millimetric variations of the relative hardware delay can be measured and on the other hand, its closeness to the GPS L1 frequency allows it to be used as a local oscillator for downconverting to a 24 MHz IF.

Regarding the GPS-over-fiber design, most solutions consist of two parts, one for electrical-to-optical conversion at the antenna side (remote station) and one for the optical-to-electrical conversion at the receiver side (local station) with an optical fiber between them. At the remote station, as the received GPS signal is very weak, some conditioning of the signal must be done. Two kinds of approaches are generally used: 1) amplify the received RF signal enough to modulate an optical source (RF-over-fiber) or 2) amplify and downconvert the signal to an intermediate frequency (IF) prior to modulation of an optical source (IF-over-fiber). Both approaches have their advantages and disadvantages. In the first case, the main advantage is that the remote-station circuitry is simpler as no external oscillator is needed. However, amplifiers, optical modulators and optical sources working at RF frequencies are more expensive and the system is more sensitive to dispersion in the fiber. In the second case, the main disadvantage is the use of an additional external oscillator but, as will be explained shortly, this can be turned into an advantage if this oscillator is used to monitor the relative delay by using the phase-shift technique. However, if each remote-station has its own external oscillator to downconvert the RF signal, this introduces a different oscillator reference for each received signal and thus a relative clock error that will not be eliminated by single differentiation between antennas. As pointed out previously, it is very important that a common oscillator and clock reference are used in the entire system. A proposed solution is to send a common reference oscillator signal generated at the receiver (local station) to all remote stations. This reference oscillator will then be used to downconvert the RF signals to IF. This adds some complexity to the system, which now would be bidirectional, and one could be tempted to rather stick to the RF-over-fiber solution. However, with a refinement of this kind of configuration, the real-time relative propagation monitoring can be realized. The reference oscillator can be used, not only for the IF down-conversion but also as a reference signal to measure the relative propagation time between the paths from the local station to each remote station. The signal is split at the local-station and makes a round-trip to each remote station before their relative phase is compared. Additionally, a common optical source can be located at the local station and sent to each remote station so that only one optical source is used for the entire system, which reduces costs. We have thus combined the GPS-over-fiber architecture

with a real-time calibration of the relative delay on the fibers with the phase-shift technique. The system is illustrated by Figure 3.2, where only the main functional blocks of the system are shown. A detailed version, with all the electronic and optical components involved is presented in Appendix A. The system works as follows:

- A LO (Local Oscillator) 1551.42 MHz signal is generated at the local station, this signal must be synchronized with the GPS receiver's main oscillator.
- The 1551.42 MHz modulates the supply current of a DFB (Distributed FeedBack) laser operating in the 1550 nm band. At 1.5 GHz, direct modulation of the laser is possible and a simpler alternative to external modulation.
- The modulated optical signal is split with a 50/50 optical power splitter. If more remote stations are used, further splitting is required with, e.g., a 1×4 or 1×16 tree coupler module (AFW Technologies, 2010).
- The resulting modulated optical signal (called LO-over-fiber) is sent through standard, monomode optical fiber to the remote stations.
- At each remote station, the optical signal is split once again. One part goes to an external optical modulator, in our case, a SOA (Semiconductor Optical Amplifier). The other part goes to a photodetector.
- The resulting electrical at 1551.42 MHz out of the photodetector is amplified and used as the reference oscillator to downconvert the received L1 GPS signal (1575.42 MHz) to an IF (Intermediate Frequency) of 24 MHz with the RF front-end, which comprises mixing, amplifying and filtering steps.
- The resulting IF signal (GPS-IF) modulates the supply current of the SOA so that the optical signal at the output of the SOA is now twice modulated: first by the 1551.42 MHz at the local station and now by the GPS-IF at the SOA.

- The output optical signal at the SOA is sent back to the local station by means of a second standard monomode optical fiber. The optical signal is now called GPS-IF&LO-over-fiber.
- At the local station, the optical signal is converted back to electrical form with a photodetector.
- The resulting electrical signal, which contains both the GPS-IF and the LO signals is divided into two equal parts with a 50/50 power splitter.
- One part of the electrical signal is low-pass filtered to remove the LO signal and feed the remaining GPS-IF signal to the GPS receiver.
- The other part of the electrical signal goes to a phase comparator where the phase of the LO signals coming from both remote stations is compared.
- The real-time output of the phase comparator is digitized and stored for post-processing in the current prototype version.

To illustrate what happens to the GPS signal and the LO signal in each processing step, Figure 3.3 shows the evolution of the spectrum of the signals as they travel through the system. One of the main concerns is the simultaneous transport of the GPS and LO signals and how they can be separated at the local station. However, as some of the devices introduce non linear effects, some crossover effects may appear between the two signals. This effect is further analyzed in Chapter 4.

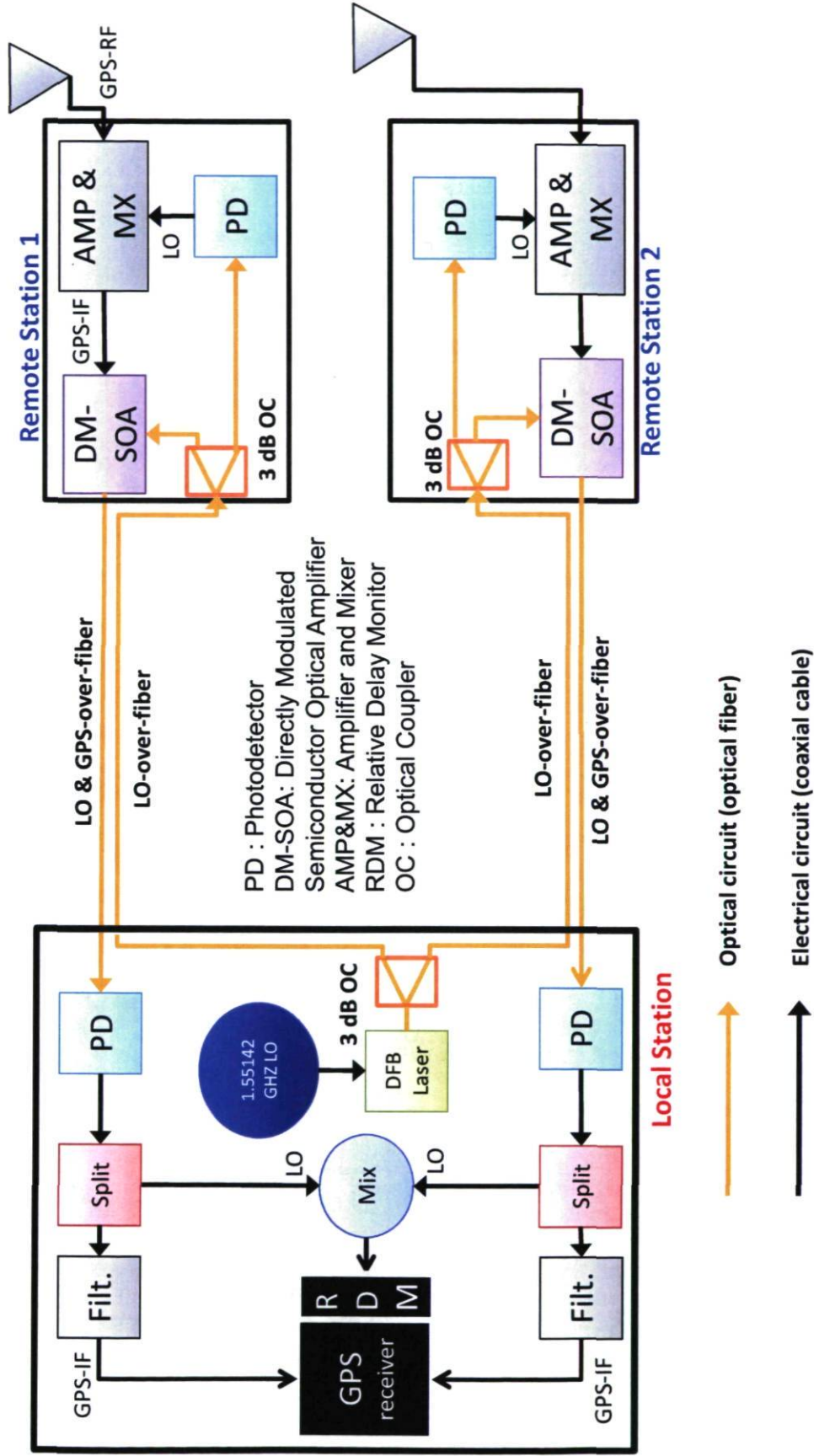


Figure 3.2 Proposed architecture for the GPS-over-fiber with real-time relative hardware delay calibration

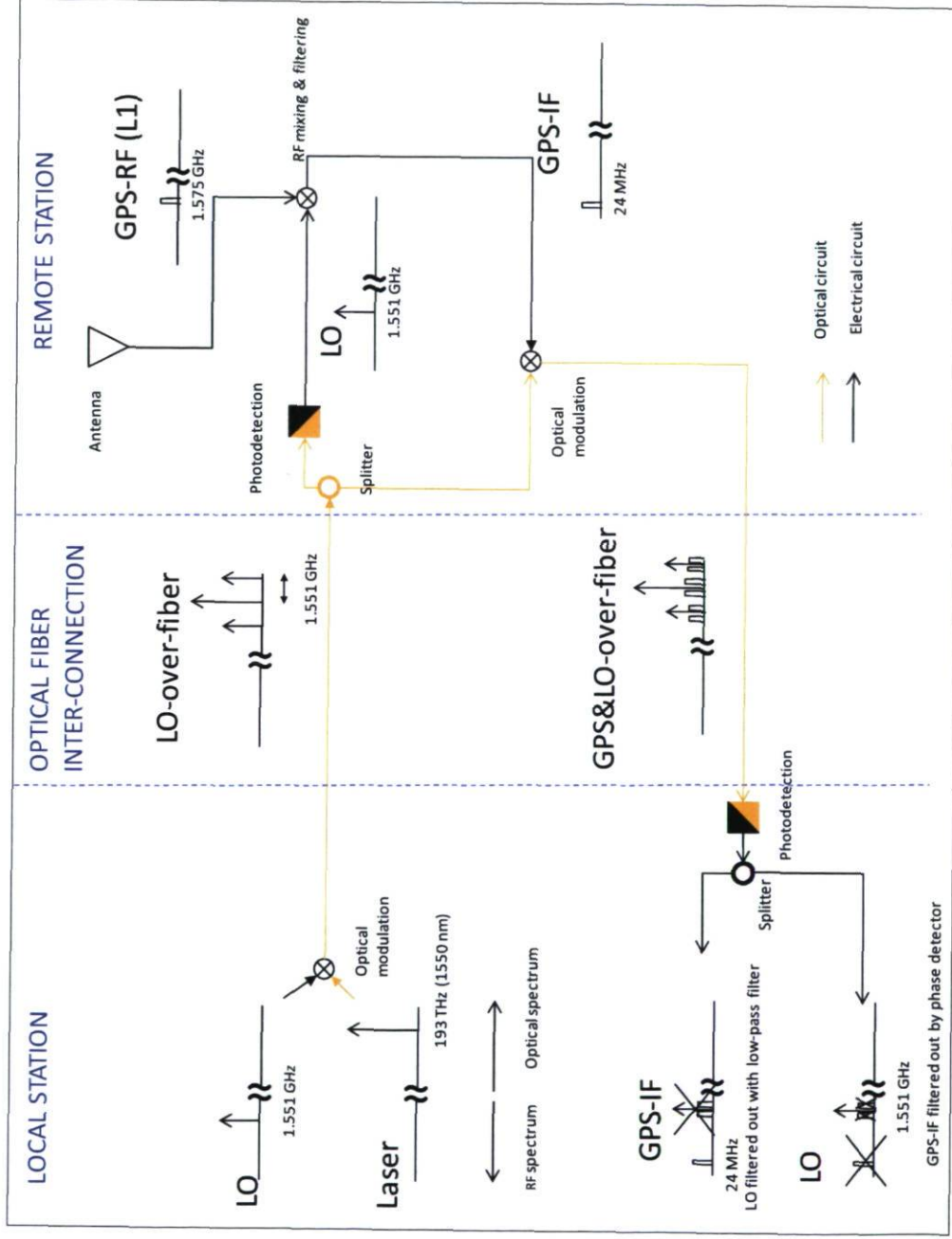


Figure 3.3 Spectrum of the signals in the proposed architecture

The main motivation of the choice of this architecture is, as stated previously, to have a GPS-over-fiber, multi-antenna system with real-time relative delay calibration in order to improve the vertical component precision. However, cost and simplicity were also taken into consideration in order to have a cost-effective alternative to other systems. Most of the components are off-the-shelf electronic and optical devices. In Appendix A, the list and approximate cost of the components is presented. To be a cost-effective alternative to other systems, our goal was to build a system with two remote stations for a material cost of under US\$10000. Currently, the prototype still needs external laboratory equipment, such as laser temperature controllers and signal generators and uses discrete electronic components. The final version is planned to include integrated electronics to reduce costs and size. Here is a brief list of the main parts of the system and the motivation behind the choice of that particular item:

- The optical source is a semiconductor DFB (Distributed FeedBack) laser. As stated in Section 3.1.3, a laser source is preferable to LED's for radio-over-fiber applications. The type of laser, DFB, was chosen because of its common use in 1550 nm telecommunication applications and because of its single-mode operation, as opposed to Fabry-Perot lasers (Keiser, 2000). However, other type of lasers might be used as well.
- The optical fiber is a standard ITU-T G.652 type monomode optical fiber, in this case, a Corning SMF-28 (Corning Inc., 2002).
- The photodetectors are high speed InGaAs p-i-n photodiodes which can operate up to 10 GHz and which have integrated preamplifiers. These photodiodes are commonly used in telecommunications applications and were chosen because of their operating frequency ranges covering the 1.5 GHz band.
- The RF front-end, which is an amplifying and mixing stage for the GPS-RF signal, consists of low-cost, off-the-shelf amplifiers, mixers and filters (See Appendix A).

- The Semiconductor Optical Amplifier (SOA) is used as an external optical modulator. The choice of this device was the least straight-forward of all the components. This is the most expensive device of the remote station. Several options were analyzed before turning to SOA. The most common external modulator is the Electro Optic Modulator (EOM) based on the Mach-Zehnder interferometer, where the light is separated into two paths and in one of them, the phase is modulated by means of the Pockels effect (RP Photonics Consulting, 2010). The two beams then recombine and the phase modulation is translated into an intensity modulation. The main disadvantages of this type of modulators are their sensitivity to light polarization, the relatively large voltages needed to modulate them and the need for an additional amplifier stage for the GPS signal. Another type of modulator that was considered is the electro-acoustic modulator. In this type of modulator, the modulating signal is transformed into an acoustic signal and the resulting oscillating mechanical pressure modifies the refractive index of the optical medium (RP Photonics Consulting, 2010). The main disadvantage of this type of modulators is their limited bandwidth, which is generally less than 200 MHz. Finally, SOA's are not generally used as external optical modulators but, based on the previous experiments using SOA's as optical modulators such as the ones conducted by (Vacondio et al., 2006), we decided that they would be a viable alternative to Mach-Zehnder modulator due to their lower sensitivity to light polarization. SOA's have the disadvantage of greater added noise but, by choosing the right operation points, this noise can be minimized. This aspect will be further explained in Chapters 4 and 5.

- The relative delay monitoring device consists of a phase detector and a data acquisition device. As stated in Section 3.1.6, this is a simple method to measure the phase difference between two propagation paths and to deduce the relative delay. The data acquisition device simply digitizes the data so that it can be processed by the GPS positioning software. If more than two remote stations are used, the phase difference is measured between a chosen reference propagation path and the

remaining propagations paths. If there are using n remote stations then $n-1$ phase detectors are needed.

- The GPS receiver is a multi-antenna geodetic-type receiver, which can process phase observations from two or more antennas. More specifically, we used the FPGA-based software receiver developed at the *École de Technologie Supérieure* in Montreal, Canada (Sauriol & Landry, 2007). The main advantage of this receiver is its great flexibility, where the IF frequency, the type of GNSS satellites, among other characteristics can be easily changed by modifying the software. The main characteristics of this receiver are the following:
 - It is a software-defined GNSS receiver using FPGA-based design to allow both high throughput and flexibility.
 - Up to 36 channels are available in the same FPGA, with the flexibility to assign them to up to 8 antennas.
 - It can be programmed to use GPS, Glonass and Galileo multifrequency (L1/L2/L5) signals.
 - It can be adapted to different IF frequencies depending on the RF front-end.
 - Its performance is comparable to a geodetic-type receiver with both pseudorange and phase observations.

More information about the receiver may be found in (Sauriol & Landry, 2007).

- The RF front-end that comes with the FPGA-based software receiver was redesigned to use one oscillator instead of two. Previously, there was a 2-step signal down-conversion (from 1575.42 MHz to 70 MHz and from 70 MHz to 15 MHz) which used two local oscillators. This setup was replaced, at *Université Laval* and for our project, by a one-step down-conversion (from 1575.42 MHz directly to 24

MHz). The final IF frequency was thus changed from 15 MHz to 24 MHz to avoid spectral overlap.

4 Performance criteria for the proposed GPS-over-fiber architecture

When designing the proposed architecture presented in Figure 3.2, we had in mind the following two objectives regarding the expected performance:

- The GPS signal received by the antennas should be transported to the receiver with minimum performance degradation compared to the standard GPS-over-cable case (with small distance between antenna and receiver) case. The electric-optical circuit along with the optical fiber must then be almost “transparent” to the end-user.
- The measured relative hardware delay should be precise and reliable enough so that when included as a correction to the GPS phase observations in single difference processing, we should obtain a net and significant improvement in the prediction in the vertical component.

What are the performance criteria that we can use to meet and quantify these objectives? For the first objective, the main performance criteria to measure the possible degradation caused by the GPS-over-fiber system were already presented in Table 3.2. These criteria are attenuation, bandwidth, noise figure, distortion (frequency selective attenuation), phase noise and generation of additional frequencies (such as harmonics). Attenuation can be compensated for and bandwidth is not an issue if we choose the right components, namely a laser optical source and an optical modulator capable of operating at frequencies larger than the GPS RF. Our focus will then be directed to the last four criteria which can be described, in a general way, as additional noise. To achieve the first objective, we will quantify and minimize this noise by careful selection of components and their operation points.

To meet the second objective, two main performance criteria will be used. Firstly, the hardware relative delay precision will be estimated by comparing with the actual physical changes in the optical fiber and the electronic and optical components. Secondly, the

estimated position precision of the GPS positioning will be validated by comparison with an external reference and by analyzing the root mean square (rms) value (with the average value removed) of the 3D coordinates.

4.1 Carrier-to-noise performance criterion

The additional noise added to the GPS signal by the GPS-over-fiber system is quantified by the noise figure, which is a measure of the degradation of the Carrier-to-Noise Ratio (CNR) at the output of the system when compared to the CNR at the input. Let us take into account that the basic GPS-over-fiber system as used in our application has the following basic parts: a laser, which is directly modulated by an RF signal $s(t)$, an optical fiber and passive couplers, an optical amplifier and a p-i-n photodetector with an associated electrical amplifier (Figure 4.1).

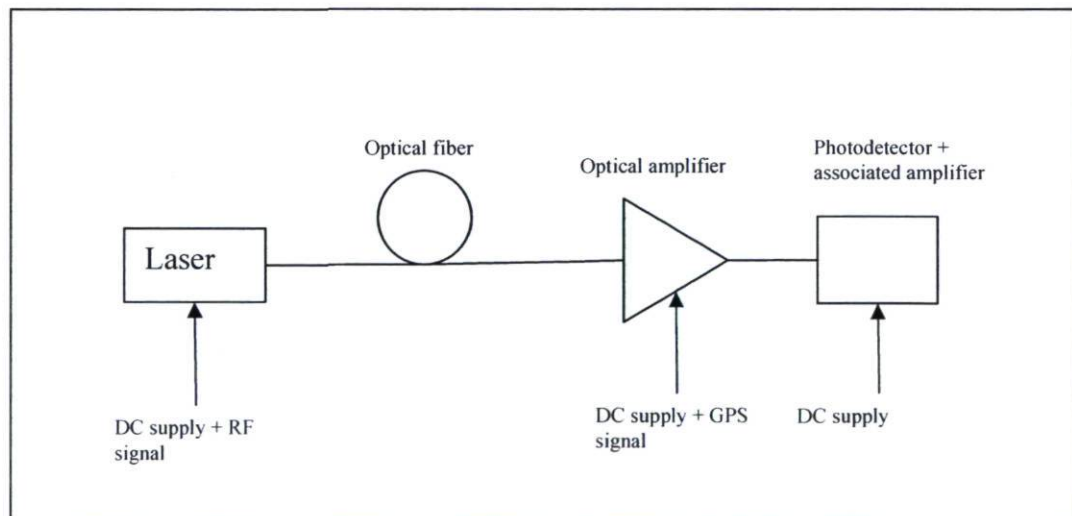


Figure 4.1 Basic radio-over-fiber transmission system with both direct modulation of the laser and external optical modulation of a semiconductor optical amplifier

4.1.1 Carrier power level

Let us first consider the changes in the carrier power level (C) as the RF signal travels through the system. The first component, the laser, is directly modulated by the RF signal $s(t)$ but also needs a bias current so that the total drive current to the laser is the sum of a fixed DC current and the RF signal current. The optical power of the laser is proportional to the drive current if this current is kept within specified limits, above the threshold current (I_{th}) and below the maximal allowed current (I_{max}) which are both specified by the manufacturer. Although the relationship between the optical power and the drive current is not strictly linear even within these limits, we assume, as a first approximation, that:

$$P_L = k(i_d - I_{th}) \quad 4.1$$

where,

P_L : Optical power of the laser (W)

i_d : Current driving the laser (A)

I_{th} : Threshold current of the laser (A)

k : Laser transfer function, assumed as a constant for $I_{th} < i_d < I_{max}$

If the drive current is modulated by a signal current $i_s(t)$, we have:

$$P_L(t) = k (I_{DC} - I_{th} + i_s(t))$$
$$P_L = k (I_{DC} - I_{th}) \left(1 + m \frac{i_s(t)}{i_{peak}} \right) \quad 4.2$$

where,

m : Modulation index $m = \frac{i_{peak}}{I_{DC} - I_{th}}$

i_{peak} : Peak current value of $i_s(t)$ (A)

I_{DC} : DC driving current of the laser (A)

If the optical signal goes through an optical fiber with attenuation α_o and an optical amplifier with amplification factor A_o :

$$P_e(t) = \alpha_o A_o P_{DC} \left(1 + m \frac{i_s(t)}{i_{peak}} \right) \quad 4.3$$

Finally, after photodetection and DC filtering, the power of the RF signal is given by:

$$P_e(t) = R_L \left(A_e \mathcal{R}_0 \alpha_o A_o P_{DC} m \frac{i_{RMS}}{i_{peak}} \right)^2 \quad 4.4$$

where

\mathcal{R}_0 : Responsivity of the photodetector (p-i-n type) (A/W)

R_L : Load resistance (Ω)

A_e : Amplification of the RF amplificatory after photodetection

i_{RMS} : rms (Root Mean Square) value of $i_s(t)$ (A)

P_{DC} : DC optical power ($P_{DC} = k(I_{DC} - I_{th})$) (A)

As can be seen in Equation 4.4, it is possible to compensate the carrier power losses with the proper electrical and optical amplification. However, as will be shown in Section 4.1.2, amplification stages introduce additional noise.

4.1.2 Noise power level

Each stage of the radio-over-fiber system adds a certain amount of noise to the RF signal. The main contributions to the noise figure for each part of the system will be presented.

1) Semiconductor laser

In a semiconductor laser, the added noise is a result of fluctuations in the optical power that arise as a result of current and temperature variations and spontaneous emissions contained in the laser output. This noise is called Relative Intensity Noise (RIN) and is a characteristic of each type and model of laser. More specifically, RIN is defined as the ratio of the mean-square fluctuations of the laser optical power to the mean squared average laser power (\bar{P}_L^2) (Keiser, 2000):

$$RIN = \frac{\langle (\Delta P_L)^2 \rangle}{\bar{P}_L^2} \quad 4.5$$

where,

$\langle \rangle$: Mean averaging operator over time

Experiments can be done to measure the RIN or it may be given as a specification by the manufacturer. However, RIN is not constant as it is proportional to the driving current of the laser. The relationship is the following (Keiser, 2000):

$$RIN \propto \left(\frac{I_{DC}}{I_{th}} - 1 \right)^{-3} \left(\frac{1}{Hz} \right) \quad 4.6$$

Thus, for direct intensity modulation, the only thing that can be done to control the amount of intensity noise once a specific semiconductor laser is chosen, is to change the laser driving current. The larger the laser driving current is, the smaller the amount of intensity noise. For example, for a HP LSC2500 DFB laser as used in the project, the threshold

current is approximately 20 mA and the maximal DC bias current is 150 mA. The decrease in RIN by biasing the laser at 150 mA compared to 30 mA, using Equation 4.6, is:

$$10 \log \left(\frac{\left(\frac{150}{20} - 1\right)^{-3}}{\left(\frac{30}{20} - 1\right)^{-3}} \right) \approx -33 \text{ dB}$$

This value is only an approximation using Equation 4.6, actual values may differ, especially if modulation is present.

2) Photodetector and associated amplifier

For a p-i-n photodiode, the main sources of noise are the quantum noise and the thermal noise. Quantum noise arises due to the statistical nature of the photon to electron conversion as the number of photons hitting a photodetector can be approximated by a Poisson type process. Quantum noise is given by the following relation (Keiser, 2000):

$$\langle i_q^2 \rangle = 2q(I_{pd} + I_{dark})B \quad 4.7$$

where,

q : Charge of the electron (C)

I_{pd} : Average photocurrent at the photodiode (A)

I_{dark} : Photodiode dark current, which is the current that flows in the device when no light is incident on it (A)

B : Bandwidth (Hz)

For the thermal noise, due to the associated amplifier and load resistance, we have (Keiser, 2000):

$$\langle i_t^2 \rangle = \frac{4k_B T}{R_L} B F_t \quad 4.8$$

where,

k_B : Boltzmann constant (W.s/K)

T : Temperature (K)

F_t : Noise figure of the amplifier (dimensionless)

B : Bandwidth (Hz)

R_L : Load resistance (Ω)

Depending on the operating conditions, either quantum or thermal noise dominate. Generally, for small optical power levels, the average photocurrent at the photodiode is also low, the resulting quantum noise is small and thermal noise thus dominates. For larger optical power levels, quantum noise dominates.

3) Optical amplifier

The Semiconductor Optical Amplifier (SOA) has a similar structure as a laser. As such, the noise it adds is also similar to the one the laser adds. Similarly to lasers, the cavity of SOA generates spontaneous emission of photons that generate noise. This spontaneous emission is called Amplified Spontaneous Emission (ASE). After photodetection, ASE adds shot noise and interacts with the signal. As ASE has a broad spectrum that encompasses the signal spectrum, beating of the spectral components of the ASE and the signal takes place. As a result, there are the following noise contributions of the optical amplifier (Agrawal, 2002, Ch. 6):

- Signal-ASE beating noise
- ASE shot noise

- ASE-ASE beating noise

As the optical amplifier, as the name implies, has optical gain, the noise contributions can be quite high. In the case of the SOA, it is often considered the noisiest device of an electro-optical circuit. Thus, most system designs have the focus on optimizing the operation points of the SOA to minimize added noise (see Section 5.1.1).

4.1.3 Distortion and phase noise

- 1) Optical fiber chromatic dispersion

One of the main distortion factors for the RF signal is the optical fiber chromatic dispersion. This effect was analyzed in Section 2.4.2 and it was concluded that for the conditions of our project (1.55142 GHz signal, monomode fiber and fiber length limited to a few kilometers), the dispersion effect of the fiber could be neglected.

- 2) Added phase noise by the photodetector

Concerning phase noise, which can be considered as a frequency dependent noise, it is our main concern here to study the impact of the optical components on the phase stability of the transported RF signal. The photodetection may be considered as a demodulation process in which a signal in the optical frequency is transformed back to the radio-frequency spectrum.

If we take demodulation in general, whether optical or electrical, the simplest technique for demodulation of an amplitude (or intensity) modulated signal is the envelope detection, where the modulating signal $S(t)$, being the low frequency “envelope” of the carrier, is detected and the carrier frequency filtered out. In this case, the carrier phase information is lost and the carrier phase noise has no impact on the received signal. In the particular case of photodetection, the simple direct-detection (DD) photodetectors such as p-i-n

photodiodes may be considered as envelope detectors. The photocurrent is simply proportional to the optical power as long as the dispersive effects of the fiber are neglected. As we are dealing with an intensity modulated optical carrier with DD photodetection, laser (carrier) phase noise can be neglected at the photodetector.

In the RF domain, envelope detection has been largely replaced by heterodyne detection, in which a mixing of the received signal with a local oscillator (LO) is performed. The main advantage is that phase information of the carrier can be retrieved and thus phase and frequency modulation, which offer better noise immunity and flexibility, can be used. However, the demodulated signal may be affected by both the carrier and local oscillator's phase stability. We consider that the resulting signal after demodulation $S_D(t)$ is:

$$S_D(t) = S(t)\cos(\omega_c t + \phi_c(t))\cos(\omega_{LO}t + \phi_{LO}(t)) \quad 4.9$$

where

$S(t)$: Modulating signal

ω_c, ω_{LO} : Carrier and LO angular frequencies

$\phi_c(t), \phi_{LO}(t)$: Carrier and LO phase noise

$S(t)\cos(\omega_c t + \phi_c(t))$: Signal after modulation of the carrier by $S(t)$

If carrier and LO frequencies are the same we have, after filtering the double frequency component:

$$S_D(t) = \frac{1}{2}S(t)\cos(\phi_c(t) - \phi_{LO}(t)) \quad 4.10$$

The signal $S(t)$ is thus affected by the phase noise of the carrier and the LO. This is why it is usually recommended that the carrier and local oscillator have phase stability equal or better than the received signal. The demodulation circuit is more complex than in the case of the envelope detector. In the RF domain, these two issues rarely present a challenge

nowadays because, on one hand, carriers and LO often have similar or better phase stability than the received signal and on the other hand, large-scale integration and high volume production have made heterodyne demodulation circuits affordable. In the optical domain, phase modulation and heterodyne demodulation, more commonly called coherent detection are also taking over intensity modulation and DD in high speed applications. Indeed, optical phase modulation offers several advantages such as an increased immunity to laser RIN and to thermal noise (Kalman et al., 1994). In the optical domain, however, the two issues previously presented are more challenging. On one hand, laser phase noise is generally considerably larger than most baseband and RF signals phase noise so that additional measures must be taken such as using small linewidth, stabilized lasers (Gliese et al., 1991), or phase-correlating the laser used as the carrier and the one used as LO, among other measures. On the other hand, the use of a laser as a LO considerably increases the cost and complexity of the photodetector.

3) Laser low frequency RIN

As stated in Section 4.1.2, noise in a semiconductor is caused mainly by current and temperature fluctuations and spontaneous emission. This noise is quantified by the RIN (Relative Intensity Noise), which was considered as flat, white noise. However, this noise is only flat beyond a certain offset frequency from the main laser frequency. It is not constant but inversely proportional to the third power of the laser driving current (Equation 4.6). For an unmodulated laser, the RIN decreases as the frequency shifts away from the nominal frequency and has a flat shape beyond a certain point (Figure 4.2a). However, if the driving current is modulated, the RIN shape slightly changes and low-frequency RIN appears at the modulating frequency (Figure 4.2b).

This increase in the RIN with the appearance of additional noise close to the RF signal with the same shape as noise around the optical carrier is called low-frequency up-converted laser noise and is primarily due to the non-linearities of the laser (Bibey et al., 1999). After photodetection, this additional up-converted RIN translates into additional phase noise to the RF signal. It is thus important to quantify this additional up-converted noise. Using the

laser rate equations, a “Noise Translator Factor” $T(\omega)$, which is “the N/S (Noise-to-signal) ratio at the modulation frequency divided by the RIN value of the low-frequency noise”, was defined by (Lau & Blauvelt, 1988).

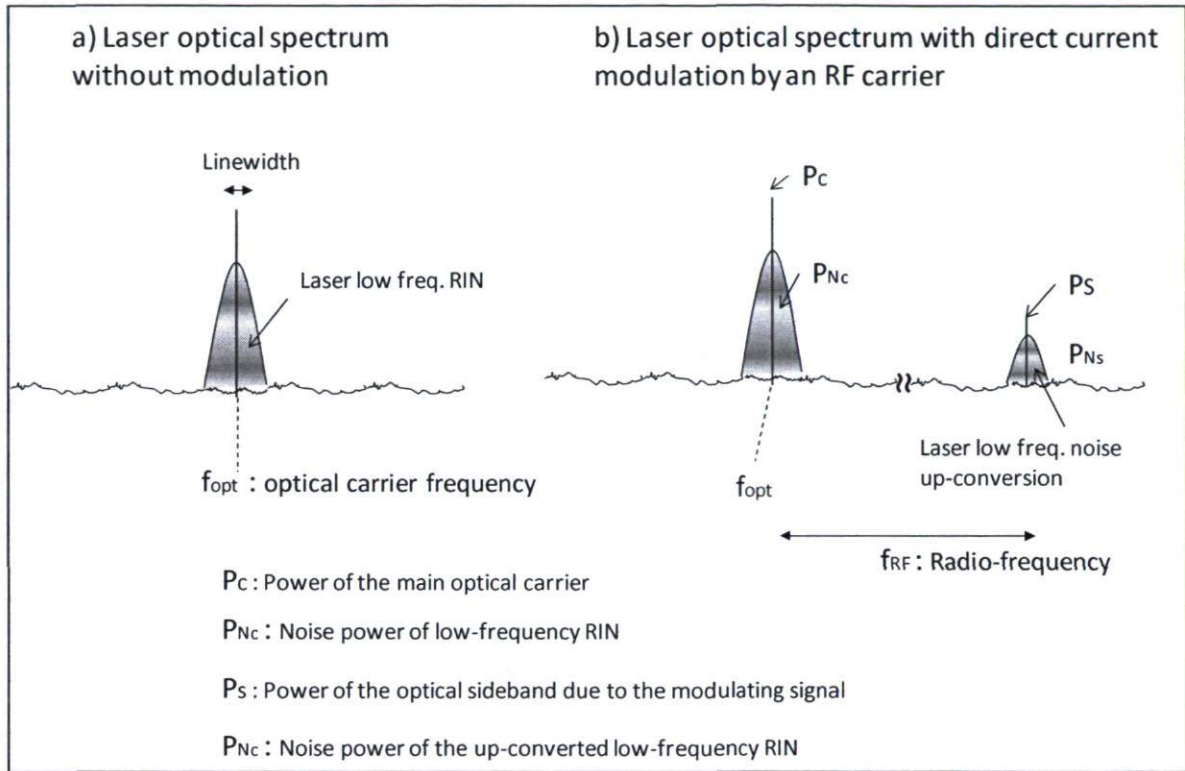


Figure 4.2 Typical laser optical spectrum

Using the power levels defined in Figure 4.2, the expression for $T(\omega)$ is:

$$T(\omega) = \frac{P_{Ns}/P_s}{P_{Nc}} \quad 4.11$$

Thus, using the Noise Translator Factor and the nominal RIN of the laser, one can estimate the additional noise close to the RF frequency due to the low-frequency up-converted laser noise. Assuming small signal approximation, the expression for $T(\omega)$ is, according to (Lau & Blauvelt, 1988):

$$T(\omega) = \frac{[g(\omega) + \gamma\epsilon P_0][P_0 + \beta + h(\omega)]}{\sqrt{2}f(\omega)} \quad 4.12$$

where,

$$g(\omega) = i\omega + \gamma(1 - N_0) + \gamma\epsilon P_0$$

$$h(\omega) = i\omega + 1 + P_0$$

$$f(\omega) = h(\omega)g(\omega) + \gamma N_0(P_0 + \beta)$$

and,

γ : Ratio of spontaneous emission to photon lifetime in the laser

β : Spontaneous emission factor in the laser

ϵ : Gain compression parameter of the laser

P_0 : Photon number density (number of photons per volume)

N_0 : Electron density (number of electrons per volume)

ω : Angular frequency (rad/s)

The expression for $T(\omega)$ is not simple and it depends on laser parameters (γ, β, ϵ) and laser operation points (P_0, N_0). We are interested in having an order of magnitude of this parameter as a function of the frequency. As $T(\omega)$ is also dependent on the optical power at the laser (P_0), (Lau & Blauvelt, 1988) provide some theoretical and experimental values for $T(\omega)$ as a function of the relaxation oscillation frequency (ω_R) resulting in $T(\omega)$ not being dependent on the laser power. Relaxation oscillations of a laser are additional oscillations (usually damped) appearing at some specific frequencies that are also dependent on the laser power level. In the case of DFB lasers operating in the 1.5 μm band, relaxation oscillations are in the GHz range. For this type of lasers, (Kakimoto & Watanabe, 1998) experimentally found that resonance relaxation frequency is about 3.2 GHz/mW^{1/2}. For

modulating frequencies near the relaxation resonance frequency (ω_R), $T(\omega)$ approaches unity so that all low-frequency laser noise is up-converted. For large modulating frequencies, above ω_R , $T(\omega) \rightarrow -3\text{dB}$. For low frequencies, below ω_R , $T(\omega)$ monotonically decreases reaching values of approximately -20 dB for $\omega = \frac{\omega_R}{10}$. These results tell that one should keep the modulating signal frequency well below the relaxation resonance frequency to avoid up-converted low-frequency laser noise. The only way to control this is, apart from the choice of the type of DFB laser, through the optical power of the laser. The larger the optical power, the larger the relaxation resonance frequency is. We therefore have less up-converted low-frequency laser noise. However, this control has its limits and for large modulating frequencies, above a few GHz, one should better consider external laser modulation. In our case, for 1.5 GHz, it is possible to use direct modulation of the laser if optical output power is about 0 dBm or above since in that case, $T(\omega) \approx -10\text{ dB}$ and up-converted low-frequency laser noise can be neglected.

4.1.4 Harmonics and cross-interference

Non-linearities in the transfer function of the optical and electronic devices modify the spectrum of the signal by adding new frequencies.

1) Optical fiber

In the case of the optical fiber, non-linearities arise due to the fact that the refraction index n depends on the optical intensity:

$$n = n_0 + n_{2,I}I \quad 4.13$$

where,

$n_{2,I}$: Non-linear parameter related to the third order electric susceptibility $\chi^{(3)}$ of the optical fiber material (m^2/W)

I : Optical intensity or optical power per unit area (W/m^2)

This dependence of the refractive index on the optical intensity causes an additional nonlinear phase shift of the signal, which in turn, translates into additional frequencies on the signal spectrum. However, the effects of optical fiber non-linearities are only significant for high optical intensities and/or long propagation distances. An important parameter that can help us determine whether non-linear effects in the fiber are significant is the non-linear length (Agrawal, 2001):

$$L_{NL} = \frac{1}{\gamma P_0} \quad 4.14$$

where,

$$\gamma = \frac{n_{2,I}}{\lambda A_{\text{eff}}}$$

A_{eff} : Effective area of the optical fiber (m^2)

λ : Wavelength (m)

P_0 : Maximal optical power (W)

If the fiber length L is considerably shorter than L_{NL} , the nonlinear effects of the fiber may be neglected:

$$L \ll L_{NL} \rightarrow \text{Nonlinear effect can be neglected}$$

In our case, we consider standard monomode fiber at 1550 nm, $n_{2,I} = 3.2 \times 10^{-20} \text{ m}^2/\text{W}$, $A_{\text{eff}} = 80 \text{ } \mu\text{m}^2$ and a maximal optical power of 10 dBm (10 mW), which is more than enough for our purposes and the typical limit of bulk DFB lasers. With these values, we obtain $L_{NL} \approx 390 \text{ km}$.

The nonlinear effects of the optical fiber can thus safely be neglected for our application.

2) Laser and photodetector

The transfer function of the laser and the photodetector are not perfectly linear and, as such, additional frequencies in the form of harmonics appear. For single frequency or small bandwidth signals traveling alone, harmonic generation can be easily suppressed through filtering. However, when two or more signals travel simultaneously, cross-interference or intermodulation between them appear as a result of the non-linear behavior of the devices. Some intermodulation products can be filtered out as in the case of a single signal but some cannot be filtered because they fall in the same spectral domain as the main signals. The most affecting intermodulation products in this latter category are the third-order intermodulation products (IMD3), particularly for signals with neighboring frequencies. The IMD3 are the generated third harmonic signals arising from the mixing of two given tones at different frequencies due to non-linearities. For example, for two tones at frequencies f_1 and f_2 , third order harmonics appear at frequencies such as $3f_1$, $3f_2$ but are usually ignored since they can be easily filtered out. However, two particular IMD3 products, at frequencies $(2f_1-f_2)$ and $(2f_2-f_1)$, may cause interfering problems to the main signals.

As in our case, the optical carrier is both modulated by the 1.55142 GHz oscillator and the GPS-IF signal with double sideband modulation, the resulting spectrum contains several frequencies (see Figure 3.3). Cross-interference is then highly likely to occur. Third order intermodulation products (IMD3) can nevertheless be measured by a standard Two-Tone Third-Order Intermodulation Distortion Measurement, in which two closely spaced tones are sent and the resulting IMD3 tones are measured. As will be shown in Section 5.1.1, this experiment was carried with our setup and it was possible to minimize IMD3 tones to negligible levels by careful selection of operation points of the devices and of the power of the signals.

4.1.5 Summary

Table 4.1 summarizes the carrier power level evolution and the main types of added noise by the opto-electrical system and indicates which parameters can be adjusted to control the power level and the added noise.

Table 4.1 Summary of the types of noise in a radio-over-fiber system

Criterion	Device	Type of noise or effect	Parameter to control
Flat noise	Laser	RIN	Supply current to laser
	Photodetector and associated amplifier	Quantum and thermal noise	Incident optical power
	Optical amplifier	Signal-ASE beating noise, ASE shot noise & ASE-ASE beating noise	Supply current to amplifier, optical input power
Carrier power level	Laser	Laser transfer function	Supply current to laser and modulation index
	Photodetector	Responsivity and electrical amplification	Incident optical power
	Optical fiber	Attenuation	Fiber type and length
	Optical amplifier	Optical amplification	Supply current to amplifier and incident optical power to amplifier
Frequency selective delay (group delay distortion)	Optical fiber	Chromatic dispersion of the optical fiber	Fiber type and length
Frequency selective noise (phase noise)	Laser	Converted laser phase noise to RF phase noise through non-linearities of laser	Supply current to laser
Additional frequencies generation	Laser, photodetector and optical amplifier	Harmonics generation by non-linearities of the laser, the photodetector and optical amplifier	Signals power level, supply current to laser, optical power
	Optical fiber	Non-linear optical effects of the optical fiber	None (negligible in our project)

4.2 Positioning criterion

The positioning criterion is the ultimate performance criterion for our developed system. After all, the main objective is to improve the precision of the GPS vertical positioning. By comparing the estimated position with an external reference, we may validate the overall performance of the system. We need to understand, however, what are the main factors that limit the performance of the system from the positioning perspective.

First, we can summarize the factors that affect the observation (the range between a satellite and a receiver) precision in three categories:

- The received signal's carrier-to-noise ratio
- The receiver sensitivity (discriminator integration time, loop bandwidth, receiver's oscillator stability,...)
- The external and internal biases (satellites orbits, ionospheric and tropospheric delays, receiver clock error, multipath effect, antenna phase center variation,...)

The propagation of the observation errors into the estimated position is a function of:




- The number of simultaneously observed satellites and their geometry in the sky
- The processing technique (estimation of unknowns, observations' accumulation, use of a differential approach,...)

Depending on the received CNR and the receiver's sensitivity, it was shown in Section 2.6 that it is possible to estimate the expected precision in carrier phase observations. If we take the example of Section 2.6, with a received signal CNR above 40 dB-Hz, a discriminator integration time of 20 ms, a loop filter bandwidth of 5 Hz and a quartz oscillator's Allan deviation of 10^{-10} , we expect a phase measurement precision of 0.01 cycle or 2 mm. Thus, by taking care of the received CNR and the added noise by the radio-over-fiber system (as shown in Section 4.1), we are able to estimate the phase observation precisions. The

random errors due to noise will then propagate to the 3D coordinates and the additional parameters estimated (such as the relative clock error) according to the variance-covariance matrix $\Sigma_{\hat{\mathbf{x}}} = \hat{\sigma}^2 \mathbf{N}^{-1}$ (see Section 2.7). However, the variance-covariance matrix is continuously changing depending on the number of visible satellites and their position, the number of unknowns and the processing techniques. (Santerre, 1991) was nevertheless able to predict, with a new simulation technique, the behavior of the variance-covariance matrix as a function of the site latitude, the elevation mask angle and the number and type of unknowns. More details on this simulation method are provided in (Santerre, 1989) and (Santerre, 1991). For a mid-latitude site, a 15° elevation angle mask, and analyzing three typical scenarios for the number and type of unknowns, the resulting confidence ellipsoids are presented in Table 4.2. For the case, not shown in Table 4.2, where the 3D coordinates, a clock parameter and a tropospheric parameter are estimated simultaneously, the confidence ellipsoids are more elongated towards the zenith ($\sigma_z \approx 10$). The best results are obtained when only three unknowns, namely the 3D coordinates, have to be estimated. It is, however, important to study propagation of the systematic biases onto the coordinates. This will be done in the next paragraphs.

All additional internal and external biases will have a direct impact on the positioning precision. For example, if the ionospheric bias is 20 meters and ignored in absolute positioning, then the measured pseudorange will be 20 m off the true range and the resulting estimation position will be off the true value. The propagation of the biases in the pseudorange or phase observations into the estimated position cannot be derived from the variance-covariance matrix as was the case for random errors. Systematic observation errors propagate in the coordinates throughout the normal equation $\hat{\mathbf{X}} = \mathbf{N}^{-1} \mathbf{A}^T \mathbf{K} \mathbf{W}$ (see Section 2.7), replacing the misclosure vector \mathbf{W} by $\Delta \epsilon_p$ (in single differences), which refer to a systematic range (phase) error.

Table 4.2 Example of normalized confidence ellipsoid calculated with a variance-covariance matrix, for mid-latitude site and a 15° elevation mask angle, adapted from (Santerre & Beutler, 1993)

Elevation mask / site latitude	15° / mid-latitude (45°)		
Parameters of adjustment	3D coordinates & clock parameter	3D coordinates only	3D coordinates & tropospheric parameter
<p>Confidence ellipsoid assuming random, white noise on phase observation</p>	<p>σ_z: 3.7 180°, 85°</p>  <p>σ_x: 1.8 0°, 6°</p> <p>σ_y: 1.4 90°, 0°</p>	<p>σ_z: 1.0 180°, 66°</p>  <p>σ_x: 1.9 0°, 24°</p> <p>σ_y: 1.4 90°, 0°</p>	<p>σ_z: 1.8 180°, 86°</p>  <p>σ_x: 1.9 0°, 9°</p> <p>σ_y: 1.4 90°, 0°</p>
<p>Notes</p>	<p>1) σ_x: Uncertainty in North component , σ_y: Uncertainty in East component, σ_z: Uncertainty in Vertical component 2) Normalization with respect to z for the '3D coordinates only' case 3) The two numbers below the uncertainties are the azimuth and the elevation angle of the respective semi-axis.</p>		

An important work on the study of the propagation of some important systematic errors in precise static relative positioning on the coordinates and the impact of satellite sky distribution was performed by (Santerre, 1989), where the satellite sky distribution is assumed as continuous and homogeneous, except for the specific shadow areas which depend on the user's latitude. For a user located at 45°N, there is a shadow area (an area where no satellites are found) roughly between -45° and 45° azimuth angles. This shadow area is latitude dependent and is a consequence of the GPS satellites' orbits inclination angle with respect to the equatorial plane. With this simulation technique, it is possible to estimate how a particular bias ($\Delta\epsilon_p$) will translate into a positioning error (and into errors for the additional unknowns that are estimated). Shadow areas, whose shape and extension

depend on the user's latitude, were taken into account and different cases were analyzed (equatorial site, mid-latitude site, polar site) to study the impact of the different satellites' sky distribution. The systematic biases analyzed by (Santerre, 1989) are: relative tropospheric bias, absolute ionospheric bias and the offset in the horizontal and vertical coordinates of the fixed station. The unknowns were the station coordinates, the relative clock error parameter and the relative tropospheric zenith delay parameter.

4.2.1 Impact of the absolute ionospheric bias on position

If we first analyze the case of the absolute ionospheric bias, which is assumed to be directly proportional to the Total Electron Content (TEC), we see in Table 4.3 that the main effect is the contraction of the baseline length through a scale factor K. These results are the same whether or not the relative clock error parameter and/or the tropospheric zenith delay parameter are estimated.

Table 4.3 Ionospheric effect (constant TEC value) for mid-latitude site and a 15° elevation mask angle, adapted from (Santerre 1991)

TEC	K (scale factor)	Length effect (L = 1 km)	Length effect (L = 2 km)
$1 \times 10^{17} \text{ el/m}^2$	-0.67 ppm	-0.7 mm	-1.3 mm
$5 \times 10^{17} \text{ el/m}^2$	-3.4 ppm	-3.4 mm	-6.7 mm

We can see in these results that for TEC values above $1 \times 10^{17} \text{ el/m}^2$ and a baseline longer than 1 km, the effect on the baseline is larger than 1 mm. Since TEC values above $1 \times 10^{17} \text{ el/m}^2$ can often occur, especially during strong solar activity, we cannot neglect the ionospheric effect. For example, TEC values for year 2000, when a solar maximum was observed, reached up to around $6 \times 10^{17} \text{ el/m}^2$ for a mid-latitude site (US Naval Observatory) and up to around 12×10^{17} for a low latitude site (Arequipa, Peru) (Skone et

al., 2001). It is important to take into account the ionospheric biases if we wish that their effects on the baseline remain below a 1 mm baseline contraction. As stated in Section 2.3.1, the use of dual-frequency receivers can help in removing the ionospheric bias by using a linear combination of L1 and L2 observations. However, this combination is about three times noisier than the L1-only noise and is not recommended for high precision applications and short baselines. It is better to use, for real-time applications, an ionospheric model such as the one sent by the WAAS (Wide Area Augmentation System). The ionospheric model used by the WAAS is a grid model (5 degrees Latitude/Longitude grid) and for each grid point, the vertical ionospheric delay and Grid Ionospheric Vertical Error (GIVE) information is sent to the users. This ionospheric information is calculated by a network of ground-based reference stations and transmitted to geostationary WAAS satellites. The WAAS ionospheric model corrects approximately 90% rms of the ionospheric error (Klobuchar, 2001). Thus, during normal ionospheric conditions (without solar storms), the GIVE is generally under 1 m. Using a dual-frequency receiver, it is possible to correct 99% rms of the ionospheric error (Klobuchar, 2001). For post-processing, it is also possible to use the ionospheric model provided by the International GNSS Service (IGS).

4.2.2 Effects of the relative tropospheric bias on positioning

If we now analyze the tropospheric bias, we can see from Table 4.4 that, regardless of the baseline length, a small error of 1 mm on the relative tropospheric zenith delay produces more than 2 mm of error in the vertical baseline component. For the standard approach, that is, with a relative clock parameter estimation, the vertical component error is higher than for the proposed approach, with no relative clock parameter estimation. However, the effect on the vertical component has opposite signs when comparing one approach to the other. With the proposed approach, there is also an effect on the horizontal coordinates by means of an error on the North component. The shadow area on the North direction for a mid-

latitude site has thus an impact on the propagation of the tropospheric bias onto the horizontal component for the proposed approach. We can conclude from Table 4.4 that even a small error on the relative tropospheric zenith delay has a significant impact on the positioning error for both approaches. It is recommended to estimate a tropospheric parameter instead of using external ground meteorological measurements. The only exception would be when using a differential tropospheric model (see Section 2.3.2) for short baselines with large height differences.

Table 4.4 Effect of relative zenith tropospheric errors on coordinates for mid-latitude site and a 15° elevation mask angle, adapted from (Santerre & Beutler, 1993)

Systematic error on the relative tropospheric zenith delay	Standard approach		Proposed approach	
	Baseline error in the Vertical component	Baseline error in the North component	Baseline error in the Vertical component	Baseline error in the North component
1 mm	3.2 mm	-0.0 mm	-2.0 mm	0.8 mm
5 mm	16.0 mm	-0.1 mm	-10.2 mm	4.1 mm

4.2.3 Effects on positioning of the relative hardware bias

In the proposed approach, the relative hardware delay must be externally measured. Santerre and Beutler (1993) analyze the impact of measurement delay error into the positioning. Table 4.5 summarizes the results. From Table 4.5, we can draw two main conclusions. First, these results confirm the fact that relative hardware delay calibration at precisions better than 1 mm is needed in order to limit the errors in vertical positioning to below 1 mm. Second, with the estimation of a tropospheric parameter, the offset in vertical positioning due to an error in relative hardware delay slightly decreases. However, as shown in Table 4.2, the estimation of a tropospheric parameter increases the vertical component of the confidence ellipsoid. A trade-off must then be made. For example, if high precision relative hardware delay is available (better than 1 mm precision) and for short baselines with large height differences, it is usually better not to estimate a tropospheric

parameter and to use a tropospheric model such as the differential model of Essen and Froome, which has already been used in deformation monitoring applications (Akrou, 1998) and was adapted by (Rothacher et al. 1986) (see Section 2.3.2).

Table 4.5 Effect of relative receiver hardware errors (ΔH) on coordinates for mid-latitude site and a 15° elevation mask angle, adapted from (Santerre & Beutler, 1993) for the proposed approach

Error on relative hardware delay (ΔH)	Proposed approach			
	Without tropospheric parameter estimation		With tropospheric parameter estimation	
	Baseline error in the Vertical component	Baseline error in the North component	Baseline error in the Vertical component	Baseline error in the North component
1 mm (3 ps)	-1.4 mm	0.2 mm	-0.9 mm	0.0 mm
5 mm (17 ps)	-6.8 mm	1.1 mm	-4.3 mm	0.1 mm

4.2.4 Effect of satellites orbit errors

(Beutler et al., 1988) propose the following relation for the propagation of the orbit errors into a baseline error:

$$\Delta x \approx \frac{l}{d} \Delta X \quad 4.15$$

where,

ΔX : Error on the satellite's orbit (m)

Δx : Resulting error on the baseline (m)

l : Baseline length (m)

d : Average distance between the satellite and the receiver (m) ($\approx 20000 - 25000$ km)

Thus, if we have, for example, a 2 km baseline, the error on the baseline is about 0.2 mm if we use broadcast ephemeris ($\Delta X \approx 2.5$ m) or 0.004 mm if we use precise IGS satellites' orbits ($\Delta X \approx 5$ cm). The satellite orbit errors can thus be neglected for short baselines.

4.2.5 Summary

In summary, taking the information from Table 4.3, Table 4.4, Table 4.5 and Section 2.5 into account, we propose the following guidelines to meet the millimetric positioning criterion in relative positioning:

- The relative hardware delay must be known to or below the millimeter level. This is achieved by using the proposed relative delay monitoring system (RDM).
- The Relative Tropospheric Zenith Delay (RTZD) must also be known at the millimeter level by using, for example, the Essen and Froome differential model for short baselines with large height differences. If this cannot be achieved, it is recommended to estimate the RTZD as an additional unknown.
- The TEC must be known with a 10 TECU ($1 \text{ TECU} = 10^{16} \text{ electrons/m}^2$) precision level so that the ionospheric effects are kept below 1 mm of baseline contraction for a 1 km baseline (see Section 4.2.1). This is possible using IGS ionospheric products, which offer a 2 to 8 TECU precision or, in certain cases (low solar activity), using WAAS ionospheric products which can be used in real time.
- Relative antenna phase variation must be carefully controlled. To do so, the same antenna model and orientation must be used (see Section 2.5.1).
- Multipath must be avoided to the extent possible. This can be done, by avoiding reflective surfaces near the antennas and/or using specially designed antennas (e.g.,

with choke rings) that further attenuate reflections. If residual multipath effects still remain, post-processing strategies can be used to further mitigate these effects.

- Remaining noise may be further reduced by temporal accumulation of observations as long as the accumulation period is sufficiently short so that the dynamics information of the baseline is not lost. For example, if we are interested in characterizing the first order oscillating frequency f_1 of a structure, then the observation accumulation period should be shorter than $1/2 f_1$.

These results are also summarized in Table 4.6.

Table 4.6 Type of biases affecting GPS positioning

Type of bias	Elimination of bias through single difference between receivers?
Receiver hardware delay	Integrated with receiver clock error (standard approach), to be calibrated (proposed approach) - see Section 4.2.3
Tropospheric	Partial (depending mainly on stations' altitude difference) - see Section 4.2.2
Ionospheric	Partial (depending on baseline length) - see Section 4.2.1
Antenna phase center variation	Almost complete if same antenna model and same orientation - see Section 2.5.1
Satellite clock error + hardware delay	Complete elimination
Multipath	No - see Section 2.5.2
Satellite orbit	Complete elimination for baselines < 100 km - see Section 4.2.4
Receiver clock error	No elimination if two independent receivers (standard approach), complete removal if same receiver with the proposed approach

4.3 Relative hardware delay measurement

Our technique for the relative hardware delay measurement is based on the phase-shift technique (see Section 3.1.6). In this technique, in its simplest form, the phase of a single reference signal is measured after propagation through two different paths (see Figure 4.3). The difference in path propagation time is reflected in the phase difference of the two signals.

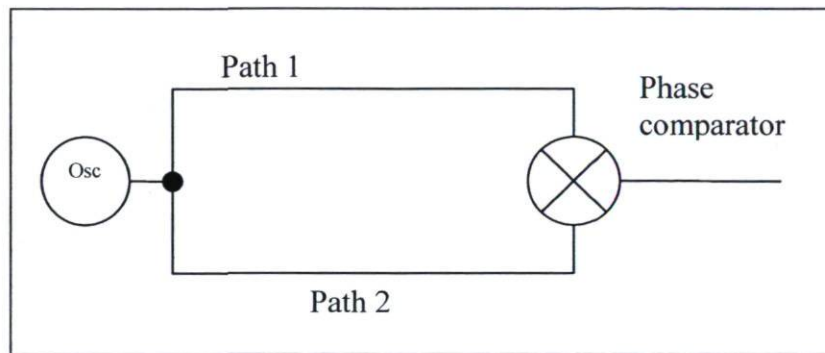


Figure 4.3 Phase-shift technique to compare the differential propagation delay between two paths and used in the RDM device

The relative delay ΔH as a function of the measured phase difference $\Delta\phi$ (in degrees) is then given by:

$$\Delta H = \frac{\Delta\phi}{360^\circ f} \text{ (seconds)} \quad 4.16$$

The rms error $\sigma_{\Delta H}$ of the relative delay depends mainly on the frequency f and the rms error in the phase difference $\sigma_{\Delta\phi}$ introduced by the phase comparator.

$$\sigma_H = \frac{\sigma_{\Delta\phi}}{360^\circ f} \quad 4.17$$

The higher the frequency of the reference signal, the shorter the wavelength and thus a higher precision can be reached. However, a smaller range of relative delay variations can be measured due to the inherent limitations of the phase difference measurement, which is limited between -180° and 180° . For example, using Equation 4.17 for a 1.55142 GHz signal and if the precision of the phase difference measurement is 1° , the resulting relative delay measurement precision is $\sigma_{\Delta H} = 1.85$ ps within a range of ± 333 ps. What are our main requirements in precision and range? In the first chapter and in Section 4.2, it was stated that a millimetric precision was needed for the relative hardware delay in order to fulfill our main objective. A 1 mm precision translates roughly into 3 ps delay in free air (around 4.9 ps inside the optical fiber with $n=1.4682$). On the other hand, if we consider a standard monomode fiber with a thermal coefficient of 7 ppm/ $^\circ\text{C}$ and a worst case scenario of 1 km difference in fiber length and thermal differences between fibers of 10°C , the maximum differential stretch between the fibers is 70 mm. Thus in this case, with a 6 ps precision objective and ± 35 mm differential length variation, a 1.5 GHz signal and a phase comparator with a precision of $\pm 1^\circ$ is suitable.

For the phase comparator, a simple RF mixer can be used. This type of device takes two RF signals and mixes them so that the output is a signal that is the sum and difference of their respective frequencies. The equivalent mathematical operation of this mixing is the multiplication of the signals. If both signals have the same angular frequency (ω), then the output signal contains both a signal which has double frequency (2ω) and that must be filtered out and a near-DC component which contains the information about the phase difference between the signals:

$$\begin{aligned} & \cos(\omega t + \varphi_1) \cos(\omega t + \varphi_2) & 4.18 \\ & = \frac{1}{2} [\cos(2\omega t + \varphi_1 + \varphi_2) + \cos(\varphi_1 - \varphi_2)] \end{aligned}$$

The main disadvantage is that the resulting signal does not contain the phase difference but the sinus (or cosinus) of this quantity. Since the sinus function is not linear, the precision of the phase difference degrades as the phase difference approaches $\pm 90^\circ$. Some

manufacturers offer specialized phase detector circuits, which contain at their core a mixer but also additional components so that a greater range of signal power levels may be used. Also, they have two main output voltages: one is directly proportional to the phase difference thanks to a greater linearity range and the other is proportional to the power difference. An example of this type of phase detector circuits is the Analog Devices AD8302, which was used for our project and offers $\pm 1^\circ$ precision within a range of $\pm 128^\circ$.

From a practical standpoint, the performance of the phase detector may be measured by modifying the optical length of one of the fibers and by measuring the resulting voltage variation at the phase detector. To modify the electrical length we can either mechanically stretch the fiber, which is not recommended because the stretching may modify the physical characteristics of the fiber, or use a variable optical delay line, in which the length may be adjusted at sub-millimeter level. The linearity and resolution of the phase detector are the most important characteristics for accurate delay measurements. Thus, the main performance criterion used is the mean deviation from the best fit line between the independent variables (the fiber length) and the dependent variables (the measured voltage).

Once the correct performance of the phase detector is confirmed (as performed experimentally and presented in Section 5.1.4), we still need to establish the relationship between the measured relative delay by the phase detector using the 1.55142 GHz reference signal and the relative hardware delay of the GPS signal. Ideally, these should be the same. In practice, however, the 1.55142 GHz signal and the GPS signal do not always follow the same paths. To better understand this, let us decompose the hardware delays as shown in Figure 4.4.

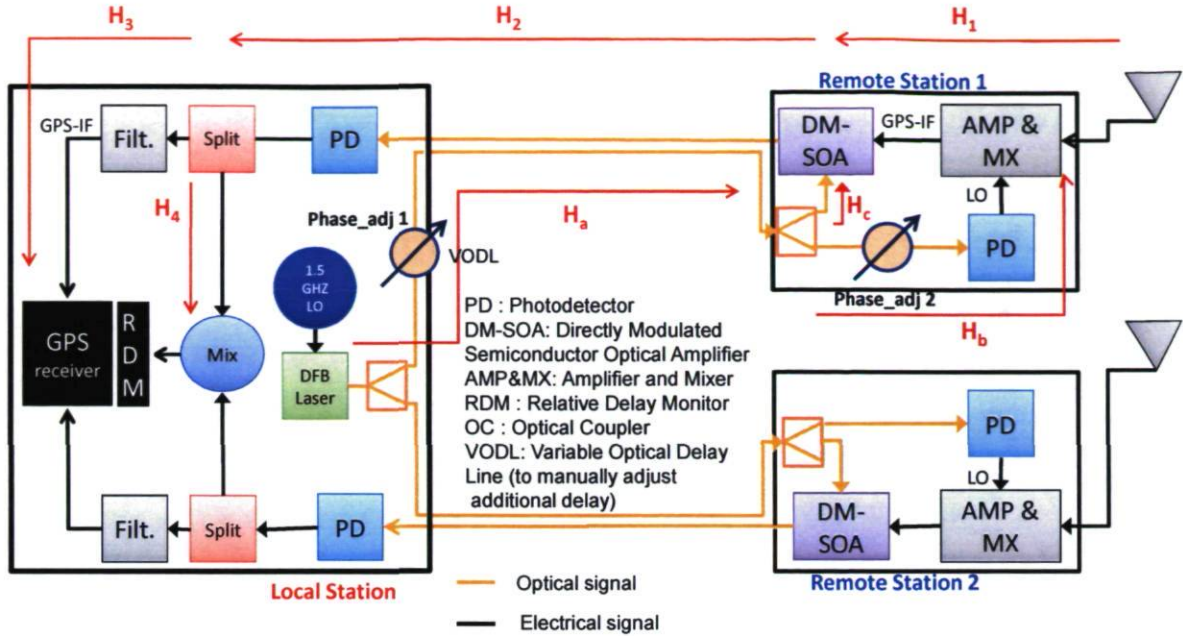


Figure 4.4 Proposed architecture with the different hardware delays shown

Note that even though hardware delays are often expressed in meters, those delays do not correspond to actual physical lengths but rather to the electrical (or optical) lengths. The hardware delay for the GPS signal is:

$$\begin{aligned}
 H_G &= H_1 + H_2 + H_3 + \text{phase}(H_a + H_b) \\
 &= H_1 + H_2 + H_3 + (z_a + z_b)
 \end{aligned}
 \tag{4.19}$$

where,

$$z_a = H_a - N_a \text{ (phase or fractional part of } H_a)$$

$$z_b = H_b - N_b \text{ (phase or fractional part of } H_b)$$

On the other hand, the hardware delay for the 1.55142 GHz signal is:

$$H_{RDM} = H_a + H_c + H_2 + H_4 \tag{4.20}$$

Let us analyze the hardware delay for the GPS signal. The first part (H_1) includes the path of the signal from the antenna to the RF front-end, usually through a coaxial cable, the path through the whole RF front-end (amplifiers, filters and mixers) and the path from the RF front-end to the optical modulator (DM-SOA). The second part (H_2) includes the optical propagation path in one of the optical fiber up to the photodetector at the local station and the electrical propagation path from the photodetector to the splitter (including amplification stages in between). The last part, (H_3) includes the path from the splitter to the GPS receiver, including filtering and amplification stages in between. However, as seen in Equation 4.19, the GPS hardware delay also includes z_a+z_b . This is due to the fact that in the RF front-end the GPS signal is downconverted to IF by mixing the signal with the oscillator coming from the local station. When a signal is mixed with an oscillator, the phase of the oscillator subtracts to that of the main signal. In this case, the phase of the oscillator depends on the hardware delay from the oscillator at the local station to the RF-front end mixer (H_a+H_b).

If we compare H_G with H_{RDM} , we can see that they are not the same. Since we are working in differential mode, it is better to compare ΔH_G with ΔH_{RDM} :

$$\begin{aligned}\Delta H_G - \Delta H_{RDM} &= \Delta(H_1 + H_3 - H_4 + H_b - H_c - N_a - N_b) \\ &= \Delta C\end{aligned}\quad 4.21$$

H_2 and H_a , which correspond to the delays on the optical fiber, are common to H_G and H_{RDM} and therefore, do not appear in the difference. This is important because H_2 and H_a are the terms that are expected to show the highest variation. For the remaining terms, if we consider that the variation of ΔC with respect to time is almost zero, or, at least, inferior to 1 mm, we may consider that variations in ΔH_{RDM} will follow variations in ΔH_G .

$$\Delta H_{RDM} = \Delta H_G + \Delta C \quad 4.22$$

Note that ΔC contains the term ΔN_a . If the variations on the differential fiber length are inferior to one cycle (19 cm), which is valid when both fibers have similar thermal variations and lengths, we may consider ΔN_a as constant. However, since it is an integer

number of cycles, it is possible to monitor its change with the RDM device when a cycle overflow is present, that is, when the measured phase goes from 180° to -180° or vice versa. Indeed, the RDM device gives only phase values between -180° to 180° so that, strictly speaking, the observation available at the RDM device is $\Delta z_{RDM} = \text{phase}(\Delta H_{RDM})$.

$$\Delta H_G = \Delta z_{RDM} + \Delta N_{RDM} + \Delta C = \Delta z_{RDM} + \Delta C' \quad 4.23$$

where,

ΔN_{RDM} : Initial phase ambiguity at the RDM device, which can be integrated with ΔC

Since we are interested in the external measurement of ΔH_G but only Δz_{RDM} is available, it is thus important that:

- 1) The variation of ΔC with respect to time is small (below 1 mm).
- 2) An initial value for $\Delta C'$ is known with a precision better than 1 mm.
- 3) Cycle overflows in the RDM device are monitored.

If the initial value for $\Delta C'$ is not known, there will be an offset in the resulting vertical positioning. If we are only interested in the temporal variation of the vertical component with respect to an initial value, as is often the case in deformation monitoring, it is possible to ignore requirement 2). However, requirement 1) is unavoidable as temporal variations of ΔC will have a direct impact on the temporal evolution of the vertical positioning.

For the first objective, it is therefore important that all cables in the RF front-end and from the antenna to the RF front-end are kept as short as possible to minimize thermal length variations. Ideally, we should be able to quantify the expected delay variations for all components and cables by using the manufacturers' information. Unfortunately, this information is not always available or reliable. In Table 4.7, we present some data that we gathered for some of the components. This information should not be taken as final as in most cases, there were no specifications provided by the manufacturer and a pessimistic scenario was taken based on the internal components. We have also to keep in mind that,

for our project, we are interested in relative delays (between 2 paths) and not in absolute delays.

Table 4.7 Approximate thermal specifications for some selected components of the RF front-end

Component	Model	Maximum Delay	Approximative thermal variation
Mixer	Mini-circuits ZX-05-C24-S	< 150 ps (rise time=0.35/BW)	Negligible (≈ 1 pF junction capacitance for Schottky diode ring)
BP filter	Mini-circuits SIF-214	≈ 8 ns	0.1% / °C (8 ps / °C)
LP filter	Mini-circuits SLP-30	≈ 10 ns	0.1 % / °C (10 ps / °C)
IF Amplifier	Mini-circuits ZFL-500	≈ 0.7 ns	0.5% / °C (3.5 ps / °C)
RF Amplifier	Mini-circuits ZX60-2522M-S+	≈ 0.1 ns	0.5% / °C (0.5 ps / °C)
Photoreceiver	Bookham PP-10G	< 50 ps	Negligible

Given the difficulty to accurately model the thermal variations of the components of the RF front-end based on the specifications, we preferred to take an experimental approach by applying extreme thermal variations and measuring the effect on both the relative hardware delay measurement and the GPS measurements. This approach will be presented in Section 5.2.3.

For the second requirement, that is, to define an initial value for $\Delta C'$, we use two approaches: the zero baseline approach and the known baseline approach. In the first case, the setup needs to be modified so that only one antenna is used, as shown in Figure 4.5. Following the antenna, a splitter is used to divide the signal in two, which then are fed into each of the remote stations. All biases, except the relative hardware delay, cancel out in this configuration.

For the zero baseline, the phase observation equation reads as:

$$\Delta\Phi^i = \Delta H_G + \varepsilon_{\Delta\phi} = \Delta N_H(\delta t) + \Delta z_H + \varepsilon_{\Delta\phi} \text{ (cycles)} \quad 4.24$$

where,

$\Delta N_H(\delta t) = N_{Ha}(t_a) - N_{Hb}(t_b)$: Integer phase ambiguity due to the fact that, even for a common satellite, the channel a (upper branch from local station to remote station 1) and channel b (lower branch from local station to remote station 2) do not necessarily lock at the same time (t_a, t_b). This term can be neglected.

Δz_H : Fractional part of the relative hardware delay (between 0 and 1 cycle)

i : Satellite number

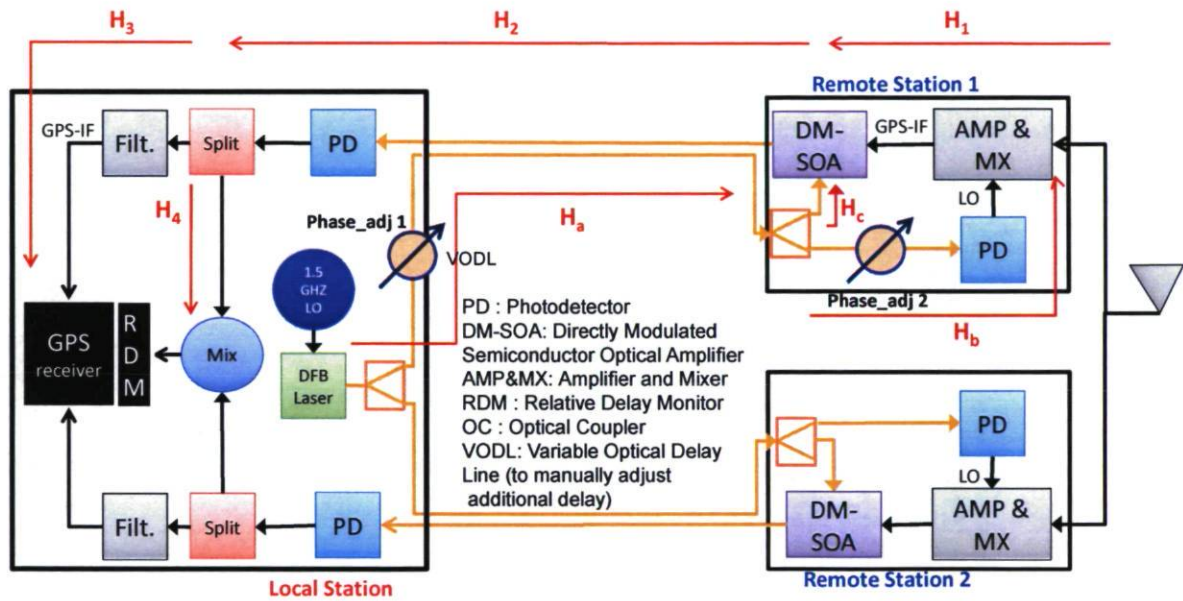


Figure 4.5 Zero baseline configuration for hardware delay calibration

A zero baseline gives thus an estimation of the relative hardware delay within 0 and 1 cycle plus residual noise. However, before going on, it is convenient to divide Δz_H into two parts: a part which is common to all channels in a receiver and a part which is channel-specific. The first part is generally much larger than the second one because it includes the path from the antenna to the receiver, whereas the second part includes the path of the signal within the receiver for each channel. We then have:

$$z_H = \bar{z}_H + z_{ch_j} \quad 4.25$$

Or, in relative mode:

$$\Delta z_H = \Delta \bar{z}_H + \Delta_{jk} z_{ch} \quad 4.26$$

where,

\bar{z}_H : Fractional part of the hardware delay common to all channels of the receiver for one remote station

Δ : Differential operator between the upper branch (remote station 1) and the lower branch (remote station 2)

Δ_{jk} : Differential operator between channel j of upper branch and channel k of lower branch

z_{ch} : Propagation delay inside a channel of the receiver

$\Delta_{jk} z_{ch}$: Inter-channel propagation delay (bias) between channel j and channel k

In a fictitious case, if we have four satellites (numbered 1 to 4) and the channel number corresponds to the satellite number, observations equations take the following form:

$$\left. \begin{aligned} Z\{\Delta\Phi^1\} &= \Delta\bar{z}_H + \Delta_{11}z_{ch} + \varepsilon_{\Delta\phi1} \\ Z\{\Delta\Phi^2\} &= \Delta\bar{z}_H + \Delta_{22}z_{ch} + \varepsilon_{\Delta\phi2} \\ Z\{\Delta\Phi^3\} &= \Delta\bar{z}_H + \Delta_{33}z_{ch} + \varepsilon_{\Delta\phi3} \\ Z\{\Delta\Phi^4\} &= \Delta\bar{z}_H + \Delta_{44}z_{ch} + \varepsilon_{\Delta\phi4} \end{aligned} \right\} \quad 4.27$$

where,

Z : Fractional part operator

The number of equations is not sufficient to separate the common relative hardware delay $\Delta\bar{z}_H$ from the interchannel bias, that is, the difference between the propagation delay

in one channel and in that of another channel of the GPS receiver. Additionally the residual noise term $\varepsilon_{\Delta\phi}$ is still present. We may, however, assume:

$$\Delta\bar{z}_H \gg \Delta_{jk}z_{ch} \quad \text{and} \quad \mathbb{E}\{\varepsilon_{\Delta\phi i}\} = 0$$

where \mathbb{E} represents the expectation or mean value operator.

These approximations are valid because on one hand, as stated before, the interchannel biases occur within the receiver, generally within an integrated circuit and are much smaller than the common hardware bias and on the other hand, the residual noise may be considered as white. We can then estimate the common relative hardware delay as:

$$\Delta\bar{z}_H \approx \mathbb{E}\{Z\{\Delta\Phi^i\}\} = \frac{\sum_{i=1}^n Z\{\Delta\Phi^i\}}{n} \quad 4.28$$

where n is the number of observed satellites

Finally, by subtracting $\Delta\bar{z}_H$ from the observed values $Z\{\Delta\Phi^i\}$, it is possible to control the interchannel bias so that it is similar for all channels. This interchannel bias is assumed to be very small and negligible in most modern receivers (see experimental results in Section 5.2.1). Then, we can obtain the initial value:

$$\Delta C = \Delta H_G - \Delta N_H - \Delta z_{RDM} = \Delta\bar{z}_H - \Delta z_{RDM} \quad 4.29$$

where Δz_{RDM} is the actual phase difference measured by the phase comparator.

Because it is only possible with the zero baseline technique to calibrate the relative hardware delay between the splitter after the antenna and the receiver, it is important to keep in mind that the path between the antennas and the splitter is not calibrated. It is also important to use identical length coaxial cables between the antennas and the splitter and identical antennas.

Another method to calibrate the relative hardware delay is the short known baseline method which is similar to the zero baseline technique except that a very precise knowledge of the

baseline is needed. In this case, if the baseline is very short, (and antennas are of identical type and identically orientated) almost all biases disappear and the remaining bias is the relative hardware bias:

$$\Delta\Phi^i = \Delta\rho + \Delta H + \Delta\varepsilon_\phi = \Delta\rho + \Delta N_H(\delta t) + \Delta z_H + \Delta\varepsilon_\phi \text{ (cycles)} \quad 4.30$$

By including in $\Delta\rho$ the precisely known coordinates of the baseline, the technique is equivalent to the zero baseline method. If we want ΔH to be calibrated at a millimetric level, then $\Delta\rho$ needs also to be known at millimetric level. The advantage of this method is that the calibrated relative delay is the one from the antenna to the receiver. The main disadvantage is that the same cable/fiber configuration and length must be used and that additional biases may contaminate the calibrated relative delay. These biases may translate into an initial offset in the vertical positioning. However, for deformation monitoring applications, we are more interested in the relative temporal variations of the vertical positioning even if there is an initial offset so that the initial calibration is less important.

4.4 GPS positioning processing strategy and software

For this research project, a customized GPS processing software partially based on DETECSAT software of the Department of Geomatic Sciences of *Université Laval* (Lamoureux, 1998) was developed. The need arose from the fact that current commercial GPS processing tools usually operate with double difference observation processing, whereas our processing strategy is based on single difference observations. Also, the software has to accept external data coming from the relative delay monitoring (RDM) device and to combine all measurement types in the processing. As one of the intended applications is the deformation monitoring of structures, a positioning solution is preferably needed for each epoch. Alternatively, the observations from a few epochs may be cumulated if the expected movements of the structure are slow. For example, if observations are taken at 30 second intervals (epochs), it could be possible to accumulate

the observations for ten epochs in order to have a positioning solution every five minutes. However, information about rapid movements occurring within a five minute interval would be lost. A decision is to be made depending on the expected dynamics of the structure and observations could be taken at shorter intervals (1 sec or less). In the designed software, we provide the flexibility to choose the accumulation period in such a way that the software may work in a kinematic-like mode (one independent solution per epoch) or with observations accumulation (providing one solution per a given number of epochs).

The ambiguity fixing technique is loosely based on the Least-Squares Ambiguity Search Technique (LSAST) (Hatch, 1990), used in kinematic applications but has been adapted for structure monitoring applications (Lamoureux, 1998). In this kind of applications, small movements, below one L1 wavelength (19 cm), are expected and the baselines are relatively short so that ionospheric effects are generally not an issue for ambiguity fixing. A priori coordinates are used to determine initial ambiguities values:

$$\Delta N_0^i = \Delta \Phi^i - \Delta \rho_0^i - \Delta \Gamma^i - \Delta Z_H \quad 4.31$$

where ΔZ_H is the measured relative hardware delay as measured by the RDM device.

These a priori initial ambiguities are then fixed to their nearest integer values. Several sets of candidate integer values for each ambiguity are used. Depending on the accuracy of the a priori coordinates, the search space for integer ambiguity values may be expanded or narrowed. For example, if a priori coordinates are available with an accuracy better than 10cm, if the baseline is short and if multipath effects are small, it is usually sufficient to restrict the space search to the nearest integer within one cycle:

$$\Delta N^i(\text{fixed}) = \left\{ \begin{array}{c} \text{round}(\Delta N_0^i) - 1 \\ \text{round}(\Delta N_0^i) \\ \text{round}(\Delta N_0^i) + 1 \end{array} \right\} (\text{cycles}) \quad 4.32$$

where,

round : Function that rounds the value to its nearest integer

Once we have different fixed ambiguities sets, a new positioning solution is calculated with each set of ambiguities. The positioning solution, the single difference phase residuals and the a posteriori variance factor are compared and statistically tested for each set. Normally, only one set passes all tests and is thus kept as the “winner” set of fixed ambiguities and used for the final positioning solution. A simple cycle slip detector is implemented by comparing the ambiguity with the one of the previous epoch. The data flow diagram of the GPS single difference observation processing is shown on Figure 4.6. One of the main differences when comparing with other GPS processing software is the inclusion of the RDM delay measurement as an additional observation. The software can, however, also operate in the standard mode, that is, without using the RDM delay measurement and instead estimate a relative clock parameter (or relative hardware delay) per epoch. Optionally, the software can also estimate a tropospheric parameter.

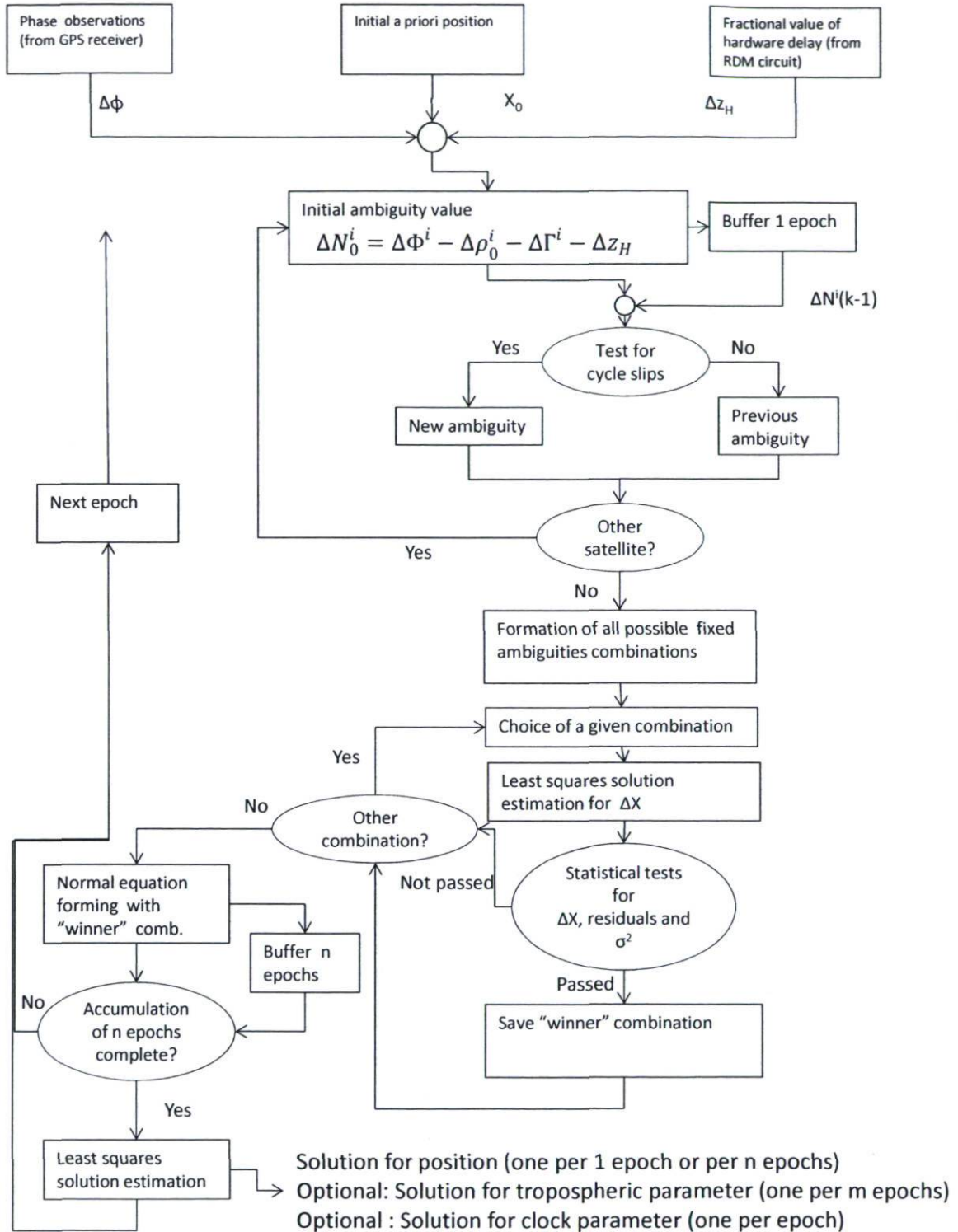


Figure 4.6 Data flow for the processing software

5 Experimental results

During the design and implementation of the prototype, several tests and experiments were performed to validate the following aspects of the project:

- The GPS-over-fiber system performance using the carrier-to-noise criterion.
- The relative delay calibration system by comparing with actual physical changes on the fiber.
- The phase measurements quality and GPS-over-fiber performance using a zero baseline configuration.
- The complete prototype positioning performance with a short baseline of precisely known coordinate differences.

These aspects correspond roughly to the chronological evolution of the implementation of the project. First, several options were considered for the GPS-over-fiber system and their performance measured by using the carrier-to-noise criterion and simulated signals. Then, the relative delay calibration system was implemented and tested, first independently and then combined with the GPS-over-fiber system. By combining the GPS-over-fiber and the relative delay measurement system, we then had a first prototype of the architecture with only one remote station and a local station. The system was thus tested with real GPS signals using a zero baseline. Finally, a final prototype with two remote stations was implemented and a small reference baseline was used. Details for each step and results will be presented in the following section.

5.1 Basic performance tests during the design period

5.1.1 Noise measurement tests

Keeping in mind the performance criteria for radio-over-fiber systems in Figure 5.1 and the analysis of each criterion in Section 4.1, we conclude that we have to focus on the following aspects: the added noise, the carrier power level and the cross-talk interference between the signals. Other aspects, such as the chromatic dispersion of the fiber and the optical fiber nonlinearities can be neglected. Each component of the system adds a certain amount of noise depending on parameters such as the bias and modulation current. As the change of one parameter may affect the performance of more than one component simultaneously, we chose to analyze the system as a whole. The inputs for this model are the GPS-IF at 24 MHz (real or simulated) and the 1.55142 GHz oscillator signals, the power levels of which are to be controlled. The output signal is sent to a measurement device. The main independent control parameters, as seen in Section 4.1, are the laser DC bias current, the SOA DC bias current and the modulating signal power level. The optical power level at the input of the SOA and at the input of the photodetector are also important parameters having an impact on the added noise but are dependent on the operation points of the laser and the SOA. However, in order to have control over the optical power without changing the currents, an additional optical attenuator was used. The system approach is shown in Figure 5.1. Only one of the internal parameters, the optical power level, is measured and controlled through the optical attenuator. The results of these experiments were also presented by (Macias-Valadez et al., 2009a) and (Macias-Valadez et al., 2009b).

The setup used for the experiment is shown in Figure 5.2. By comparing with Figure 5.1, we can identify the input signals, the control variables and the output signal. Since there are many control variables, we chose to set all of them except one to a fixed value and then change the remaining variable. This is done with all variables. Here are the range values for each variable:

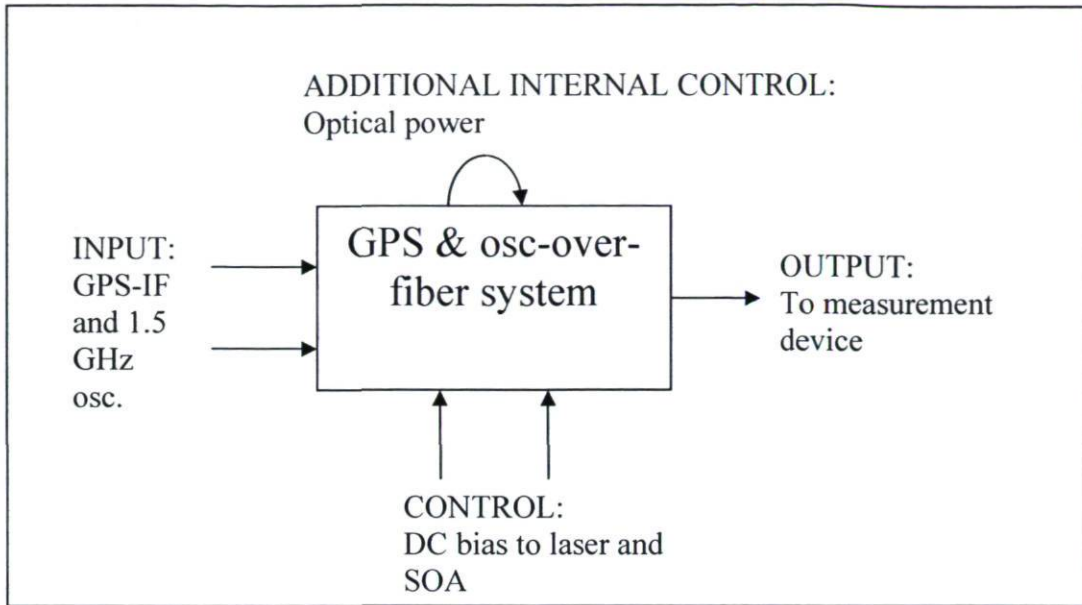


Figure 5.1 Model for GPS-over-fiber system

- Laser DC current (I_{DC}): from 20 to 150 mA. These values correspond to the threshold and maximal values allowed for the HP LSC2500 DFB laser. As explained in Section 4.1.2, the laser's RIN is lower for large values of I_{DC} . We therefore chose to fix I_{DC} to a large value and then control the optical power with the variable optical attenuator. However, since the laser's driving current also includes a modulating signal, we must then choose a driving current such that $I_{DC} + i_{peak} < 150$ mA where i_{peak} is the peak current of the modulating signal. If we take into account that the 1.55142 GHz signal used has a maximum power of 17 dBm, this corresponds roughly to $i_{peak} \approx 30$ mA so that $I_{DC} < 120$ mA.
- SOA DC current (I_{SOA}): from 150 to 500 mA. The first value corresponds to the approximate minimum current for the SOA to have amplification and the latter corresponds to the SOA's maximal allowed current. The model used is CIP's SOA-L-OEC-1550. In a similar way as the laser, the SOA supply current also includes a modulating signal, the GPS-IF signal, which is why we must make sure that $I_{SOA} + i_{GPS-IF_peak} < 500$ mA.

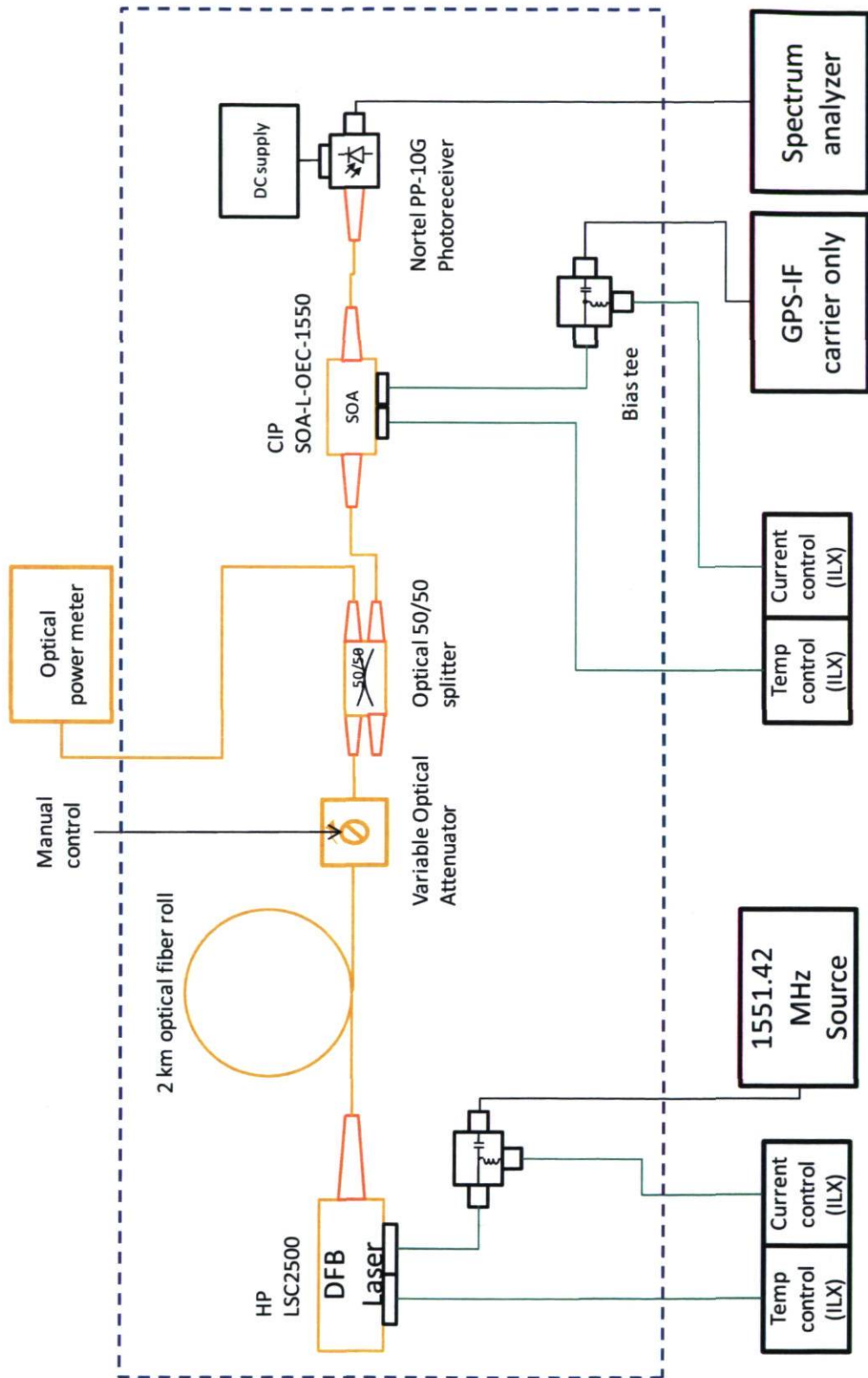


Figure 5.2 Experimental setup for noise figure measurements

- Optical power at the input of the SOA (P_{in-SOA}): the maximum optical power input for CIP's SOA-L-OEC-1550 is 13 dBm. However, with the selected laser and the optical power losses at the 50/50 splitter and in the optical fiber, the achieved maximum optical input power at the SOA was -1 dBm.

The power levels of the two input signals can also be controlled:

- 1.55142 GHz oscillator (P_{osc}) : The maximal power level for the signal generator used is 17 dBm.
- GPS-IF signal: This signal was simulated, first by a carrier at 24 MHz and then by a simple IF-modulated PRN signal generated by a signal generator. The power level is kept in the -30 dBm range, since this corresponds to the expected power level at the output of the RF front-end.

We first made measurements on the noise figure for a carrier at the GPS-IF frequency (24 MHz). Measurements were made with an Agilent HP E4440A spectrum analyzer; the power of the carrier/signal was measured directly by the analyzer. The noise level was measured by using the option of "channel power level" measurement of the spectrum analyzer and by choosing a measuring gate, i.e. the bandwidth used for the noise measurement, of 2 MHz a few kHz offset from the carrier. The resolution bandwidth used was 100 kHz. The GPS-IF carrier was generated using an Agilent 33120A arbitrary function generator used without any modulation. The 1.55142 GHz oscillator was generated with an Agilent E4438C vector signal generator. Of the five variables that can be controlled, we fixed the laser DC current at 120 mA and the IF carrier at -30 dBm. A summary of the all the variables and of their range is presented in Table 5.1. The results are shown in Figure 5.3

Table 5.1 List of controlled variables for noise measurement tests

Variable	Value
Laser DC current (I_{DC})	120 mA
SOA DC current (I_{SOA})	150 to 500 mA
Optical power at SOA (P_{in-SOA})	-15 to -1 dBm
1.55142 GHz oscillator power level (P_{osc})	17 dBm
GPS-IF power level (P_{GPS-IF})	-30 dBm

These results show that the noise figure is lower for high values of P_{in-SOA} and for I_{SOA} around 200 mA. On the other hand, the effect of the 1.55142 GHz signal on the IF carrier is negligible for high P_{in-SOA} values whereas for lower P_{in-SOA} values, the noise figure may deteriorate by up to 20 dB due to cross-interference between the signals. The most important result here is that the SOA must be operated near optical saturation in order to minimize noise figure and cross-interference between the GPS and the 1.55142 GHz signals.

To analyze non-linear effects, we also measured the Third Order Intermodulation Distortion (IMD3) by using two IF tones close to each other (2 MHz separation, which corresponds to the C/A signal main lobe width). We now fixed the SOA optical input to its maximum value (-1 dBm), as it was shown that this is optimal to minimize noise figure. The results are shown in Figure 5.4

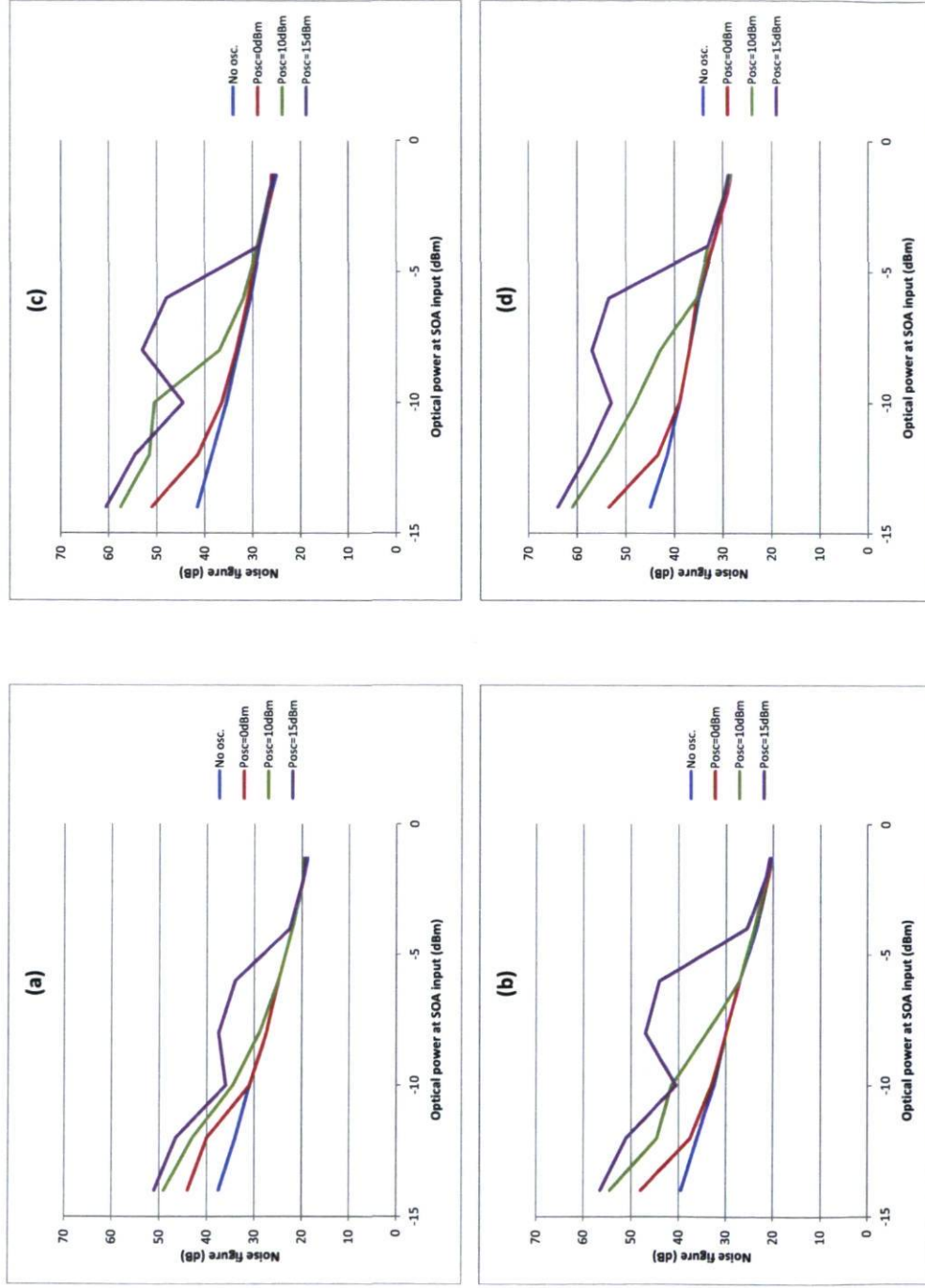


Figure 5.3 Noise figure of the GPS-over-fiber system (IF=24MHz) for various values of the optical power at the SOA input and a) ISOA=200 mA b) ISOA=300 mA c) ISOA=400 mA d) ISOA=500 mA

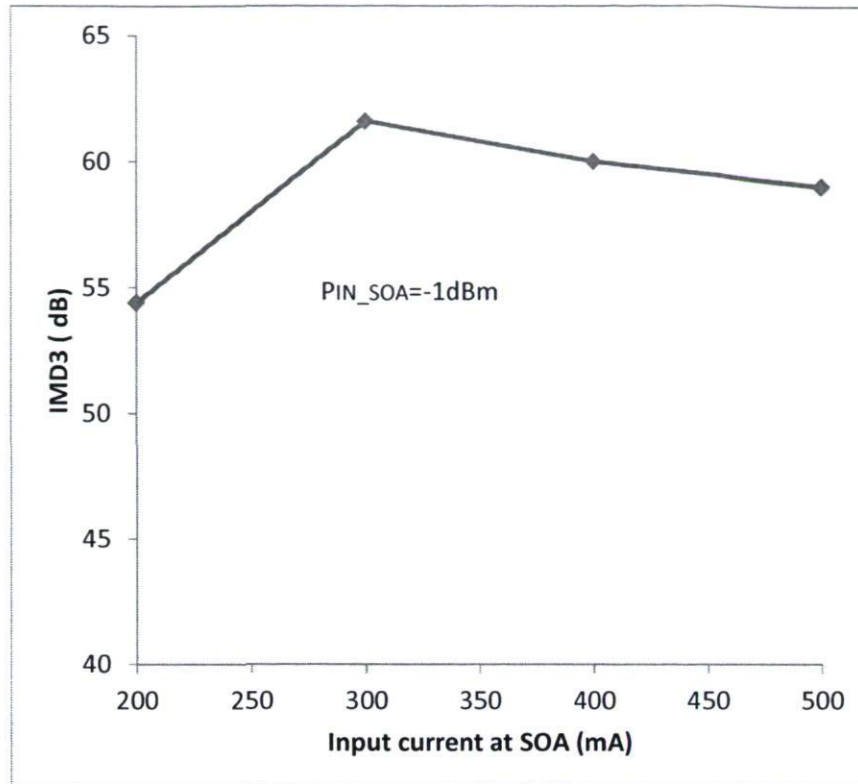


Figure 5.4 Measured IMD3 for the system

From IMD3 measurements results, we can see that values of IMD3 are always above 50 dB. Additional noise due to non-linearities may thus be neglected, considering the small bandwidth occupied by a GPS signal and its strong immunity to noise. From noise figure and IMD3 measurements, we then decided that the following operation points would be used for the system:

- Laser DC current I_{DC} : 120 mA.
- SOA DC current I_{DC} : 300 mA. This maximizes IMD3 and is close to optimum for noise figure.
- SOA optical input power P_{in-SOA} : -1 dBm or over. This minimizes noise figure.
- 1.55142 GHz signal $P_{1.5G}$: 15 dBm. Lower values may be used but larger values are preferable because the RF front-end mixer needs power levels greater than 3 dBm.

5.1.2 Simulated GPS signal correlation tests

With the optimal operation points established, we may still consider that the noise figure of the system is still quite high (20 dB). However, this noise figure was calculated using a carrier instead of a real GPS signal. The spread spectrum and phase modulation characteristics of the GPS signal help to make it more insensitive to noise. The next step in the experimental tests was to use a simulated GPS signal and a basic receiver to see the effects of the system on the carrier-to-noise-density (C/N_0) ratios after correlation in the receiver. The experimental setup is shown in Figure 5.5. A simulated GPS-IF signal is generated by a signal generator, in this case with an Agilent E33120A arbitrary waveform generator. This signal is not a full GPS signal but contains instead one single PRN sequence, with no data on it, and is modulated onto a PSK IF carrier. This signal was generated in Matlab and transferred into the Agilent E33120A as an arbitrary waveform. The demodulation of the signal after optical/electrical propagation is performed with a Matlab routine after having a segment of the signal digitized and stored on a computer. Captured data was processed in 1 ms frames, which corresponds to the length of the C/A pseudorandom code. The receiver, i.e. the Matlab routine, finely adjusts the code and phase of a locally generated signal until a correlation peak is detected, just as it is done in a real GPS receiver. The correlation peak strength is then compared to the average, noise level to compute the carrier-to-noise-density of the correlated signal (C/N_0) adjusted to a 1 Hz bandwidth. To estimate the deterioration introduced by the optical circuit, a comparison is made for the same emulated GPS signal with and without (electrical back-to-back) the optical circuit. Two cases were analyzed depending on the type of simulated signal: a noise-free PRN code and a PRN code buried 20 dB below the white noise, which is artificially generated by the waveform generator, which is a more realistic case. Results are shown in Figure 5.6. It is interesting to note that the C/N_0 degradation is just 1 dB for the ideal, noise-free case and 2 dB for the case where the GPS signal is buried 20 dB below the noise.

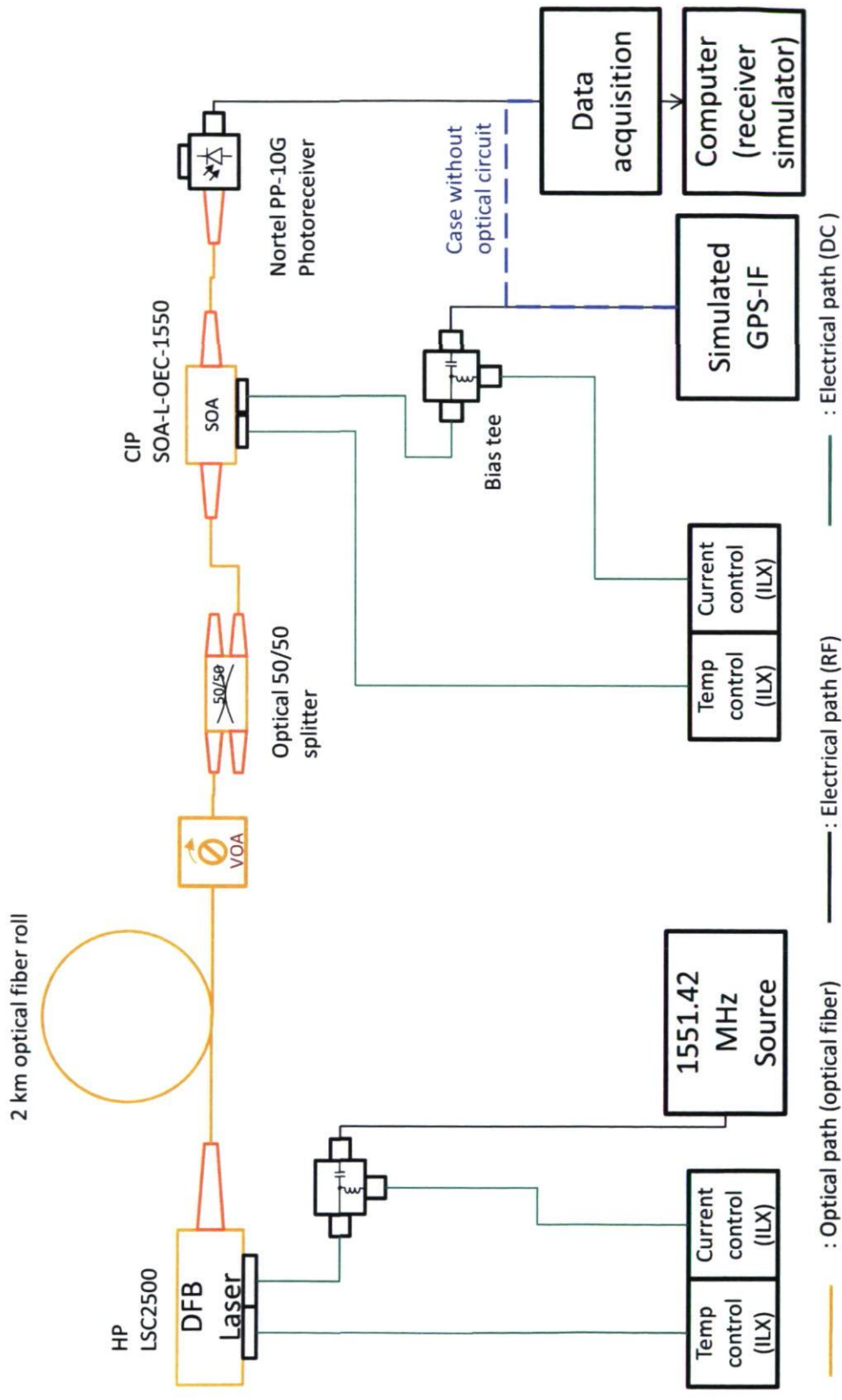


Figure 5.5 Experimental setup for simulated GPS signal measurements

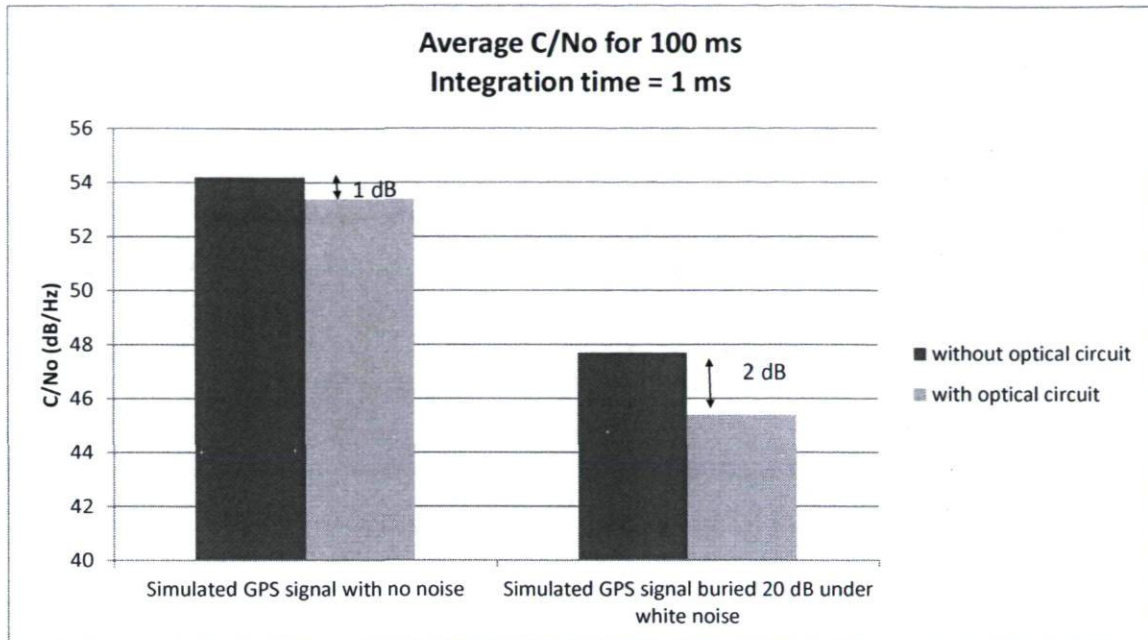


Figure 5.6 Comparison of the C/N_0 for the cases without and with optical circuit

5.1.3 Real GPS signal correlation tests

We now repeat the previous experiment with real GPS signals and the FPGA-based GPS receiver developed by the *École de Technologie Supérieure*. The experimental setup is similar to the one shown in Figure 5.5, except that, on one hand, the simulated GPS-IF is replaced by the signal coming from the GPS antenna and the RF front-end and on the other hand, the computer used as the receiver simulator is replaced by the GPS receiver. It is important to keep in mind that all the operation points were kept to their optimum values as obtained in the first experiment. In this case, we also compared the C/N_0 for the standard case (with no optical circuit) with the case using the proposed setup. As we are using here real GPS signals, the C/N_0 depends on the number of satellites and these will continuously vary depending on their elevation angle. For comparison, we took advantage of the fact that the satellite configuration repeats itself after a 23 hr 56 min period. Then, for day 1, we took the C/N_0 measurements without the optical circuit and for day 2 (23 hr 56 min) later,

we took the C/N_0 measurements using the proposed architecture (with the optical circuit). The results are shown for a few satellites in Figure 5.7. The results for all the satellites are shown in Appendix B. Visually, it is clear that C/N_0 are very close together in both cases. Thus, C/N_0 deterioration due to the optical circuit is minimal. We wanted, however, to confirm this impression by calculating the average difference between the C/N_0 in both cases. The results are presented in Table 5.2. We found that the C/N_0 deterioration is below 2 dB in all cases and around 1 dB in most cases.

Table 5.2 Average difference (AD) between C/N_0 with and without optical circuit

Average Difference (AD) between C/N_0 without optical fiber and C/N_0 with optical fiber								
Satellite	1	2	3	4	5	6	7	8
AD (dB)	-0.3	N/A	0.1	N/A	-1.8	-0.3	-0.5	-0.6
Satellite	9	10	11	12	13	14	15	16
AD (dB)	-1.6	-0.5	-1.7	-0.8	-0.7	-0.9	-2.3	0.9
Satellite	17	18	19	20	21	22	23	24
AD (dB)	N/A	-2.1	-0.9	-1.2	-1.3	-1.7	0.1	-1.6
Satellite	26	27	28	29	30	31	32	
AD (dB)	-1.1	-1.5	0.1	-0.3	-0.4	0.3	-0.6	

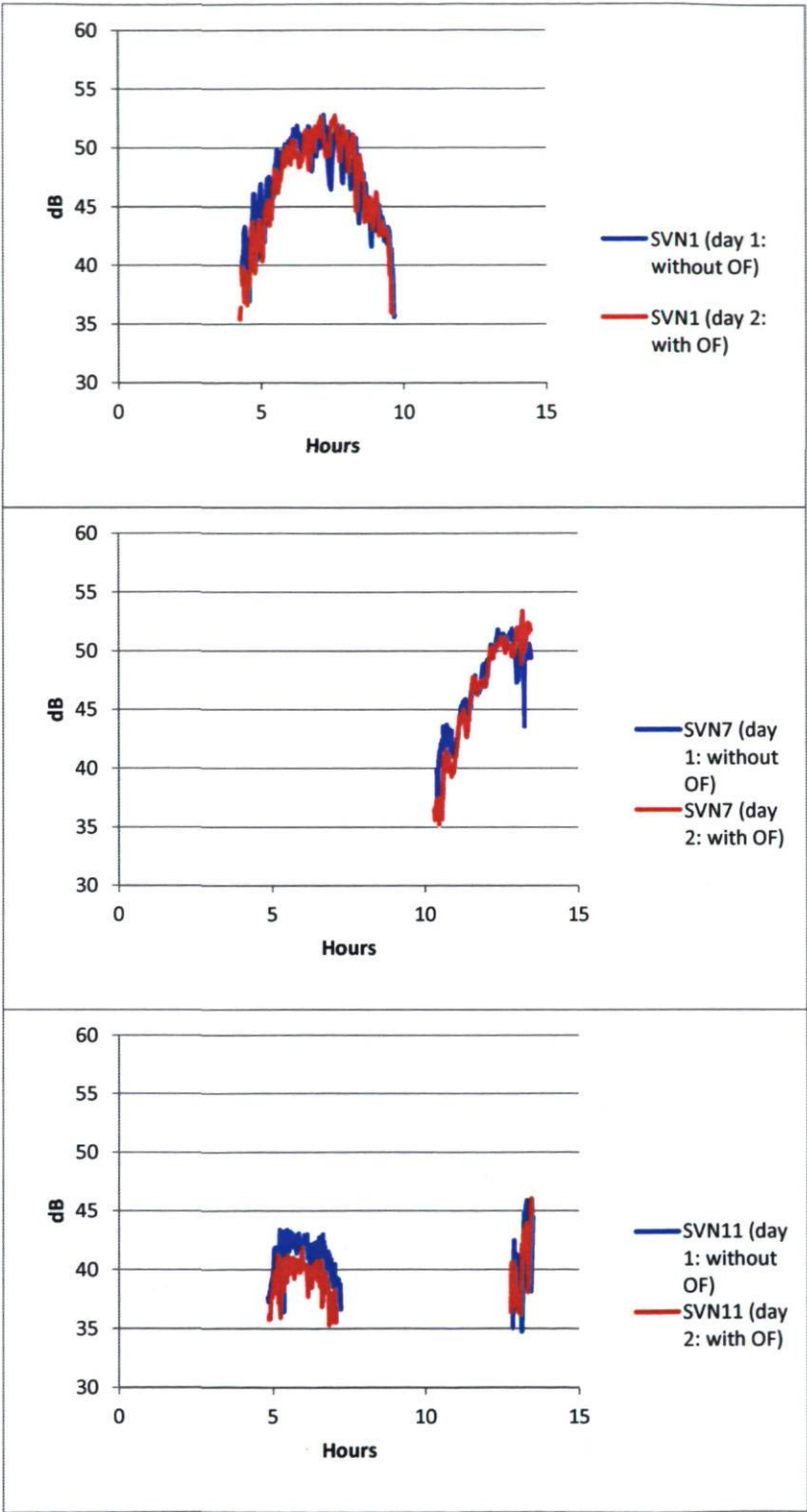


Figure 5.7 Comparison of C/N0 with and without optical circuit for satellites 1, 7 and 11

5.1.4 Relative delay monitoring tests

The phase comparator performance was tested by using the complete setup and by adding a variable optical delay line (VODL) in one of the optical fibers. The phase comparator compares the phase of the 1.55142 GHz after transport in the optical fibers. By adjusting the VODL in 0.5 mm increments, we were able to see the resulting voltage at the end of the phase comparator. In this case, we were interested in the linearity of the comparator and its optimum operation range. Note that, inside the VODL, the optical signal changes from guided over-fiber propagation to free space propagation and a reflective surface can be moved to change the length of the free space gap. As the optical signal makes a round-trip inside the gap, a change of 1 mm in the gap length corresponds to 6.66 ps of delay, instead of 3.33 ps as would be expected for one-way, free space propagation. The results are shown in Figure 5.8.

The linearity range where the error is less than 1 mm (4°) goes approximately from 40° to 145° , corresponding to a range of approximately 105° . The equivalent length range is 30 mm inside the VODL (60 mm taking into account the round-trip of the optical signal) or approximately 40 mm inside standard SMF-28 optical fiber ($n=1.4682$). This means that the phase comparator will give millimetric precision as long as the relative delay is kept within ± 20 mm and the initial phase difference is around 90° . The latter condition is easily met by using the VODL to adjust the relative delay until the phase difference is 90° . The ± 20 mm constraint may be tight in some cases. For example, for two 1-km long standard optical fiber runs, the relative temperature difference between them should not be higher than $\pm 3^\circ\text{C}$ since that would translate into a differential delay of $7 \frac{\text{mm}}{\text{km}\cdot^\circ\text{C}} \times \pm 3^\circ\text{C} \times 1 \text{ km} = \pm 21 \text{ mm}$. The phase comparator was used for all tests and gave good results. However, alternatives are considered for future use (see Section 6.2).

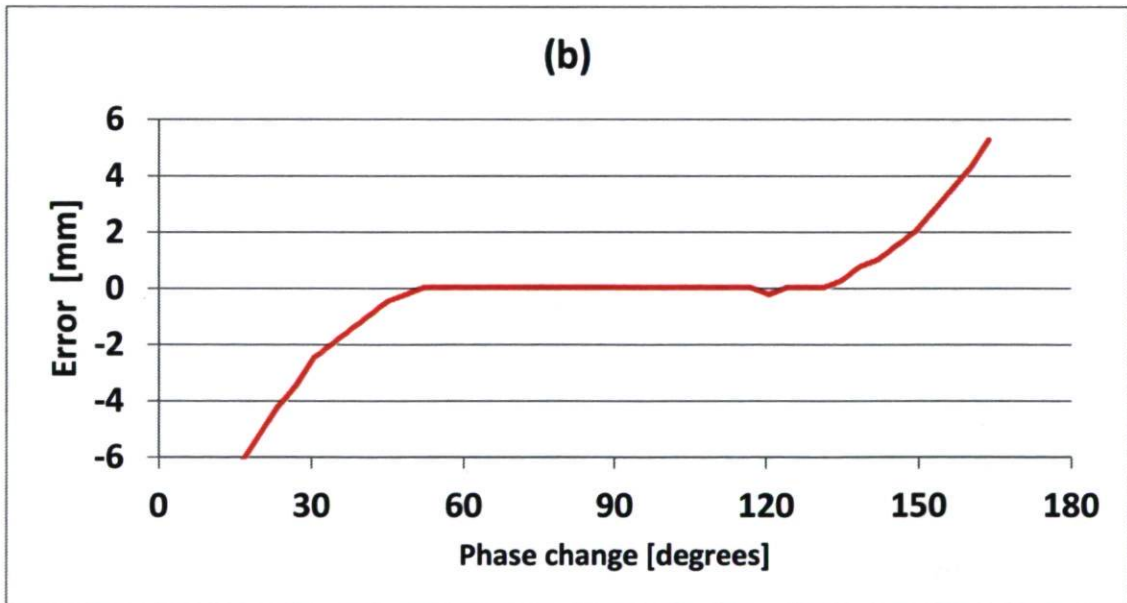
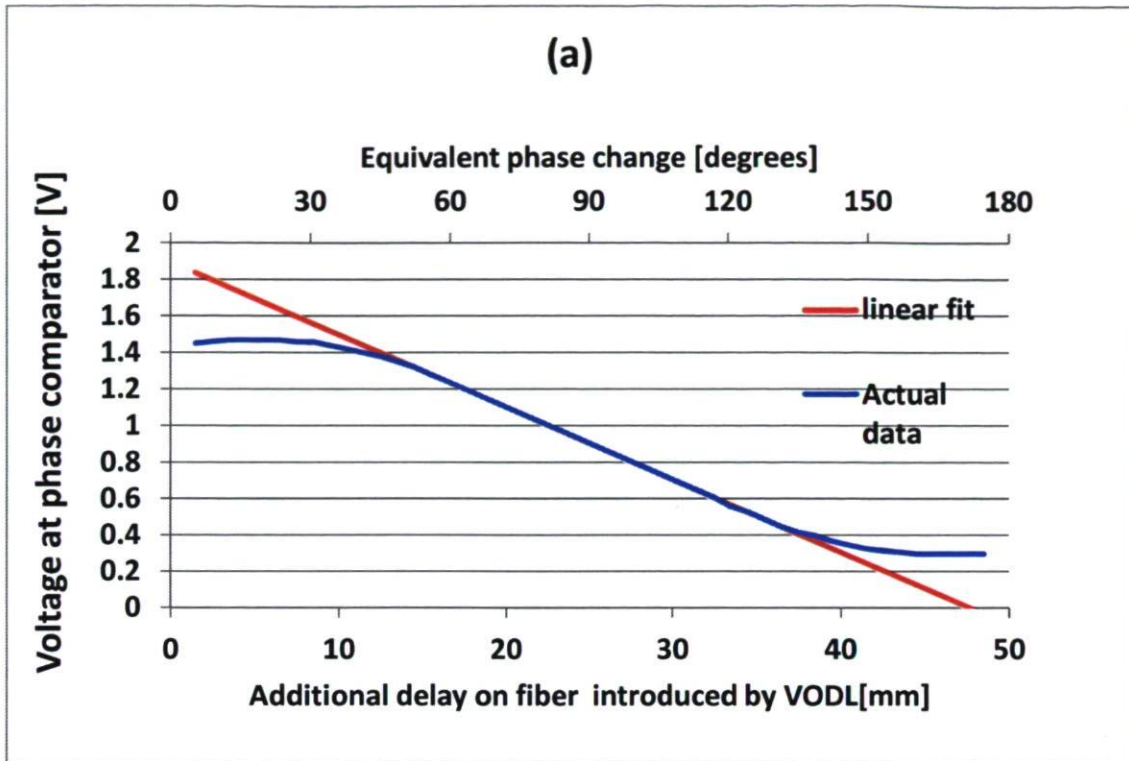


Figure 5.8 Phase comparator's: a) transfer function and b) deviation from linear fit

5.2 Zero baseline tests

Once the prototype completed and the preliminary tests shown on the previous sections performed, the first test to prove the concept was done on a zero baseline. In this type of configuration, the signal coming from one antenna is split to both remote stations. The main advantage of a zero baseline configuration is that all errors, except the relative hardware error (including inter-channel bias and the hardware error on the optical components), are eliminated. If a positioning solution is performed with a zero baseline, the differential reference position is (0,0,0) and any departure from this position is an indication of the remaining biases and the residual noise of the receiver. Also, by analyzing the DOP factors and the precision of each component, we get a first indication of the success of our proposed configuration if the vertical precision is improved.

5.2.1 Analysis of interchannel biases and noise with a zero baseline configuration

First we will analyze only the single differences of the observations. Equation 4.24 tells that the hardware delay may be estimated from the single difference of observations:

$$\Delta\Phi^i = \Delta H + \varepsilon_{\Delta\phi} = \Delta N_H(\delta t) + \Delta z_H + \varepsilon_{\Delta\phi}$$

Figure 5.9 shows the result of taking the single difference observations $\Delta\Phi^i$ and removing the ambiguity $\Delta N_H(\delta t)$, to find $\Delta z_H + \varepsilon_{\Delta\phi}$. In this experiment, a standard GPS-over-cable configuration was used since we wanted to focus on the receiver inter-channel bias and residual noise. The receiver has 24 channels, of which channels 1 to 12 are used for remote station 1 and channels 13 to 24 are used for remote station 2. The receiver has a master-slave configuration so that channel 13 is locked to the same satellite as channel 1, channel 14 is locked to the same satellite as channel 2, and so on. Not all channels track satellites

simultaneously because there are generally less than 12 satellites at all times. This is why blanks appear in the graphics of Figure 5.9. About 15 hours of observations were taken at 30 seconds intervals, which is generally sufficient for static applications. For all single differences, $\Delta z_H + \epsilon_{\Delta\phi}$ have values at around 10.5 mm for the first 6 hours and around 11 mm for the remaining 10 hours, with rms values of 0.2 mm and 0.4 mm respectively. The variation is probably due to temperature changes of the cables and electronic circuits, thus affecting the hardware delay. These values have no particular meaning; any value within an L1 cycle (19 cm) might occur, depending on external parameters such as the cables and optical fibers' length and temperature. However, the fact that they have all similar values and similar behavior indicates the fact that the relative hardware delay is common to all channels. This common relative hardware delay is calculated by taking the average value for all the epochs for the first 6 hours (10.5 mm) and for all the epochs for the remaining epochs (11 mm). By removing this average value to the single differences observation, we obtain the residual noise, which contains also the interchannel bias. Figure 5.10 shows this noise. We conclude that for this receiver, the interchannel bias is negligible and that the remaining noise is kept under 1 mm. The rms values for the noise is around 0.2 mm.

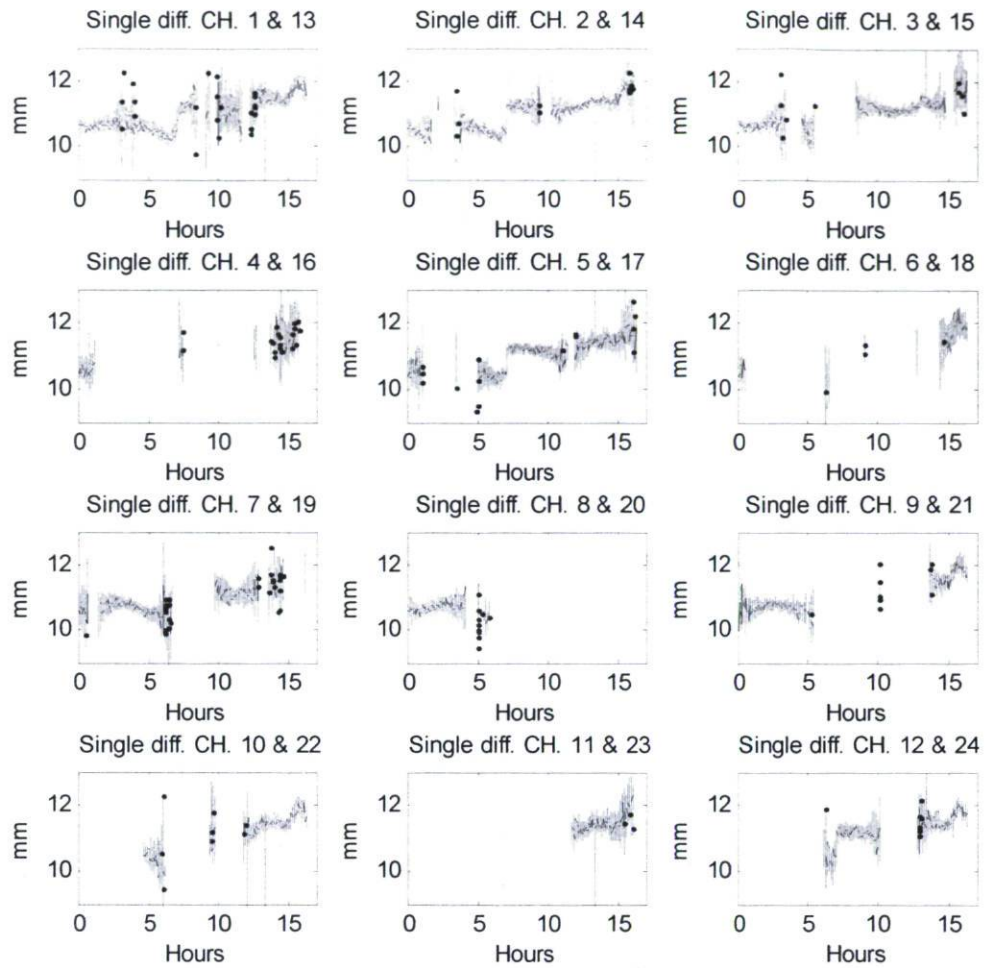


Figure 5.9 Single differences of observations after removing ambiguities for a zero baseline and GPS-over-cable configuration. The satellite tracked by each pair of channels may change during the 15 hour interval.

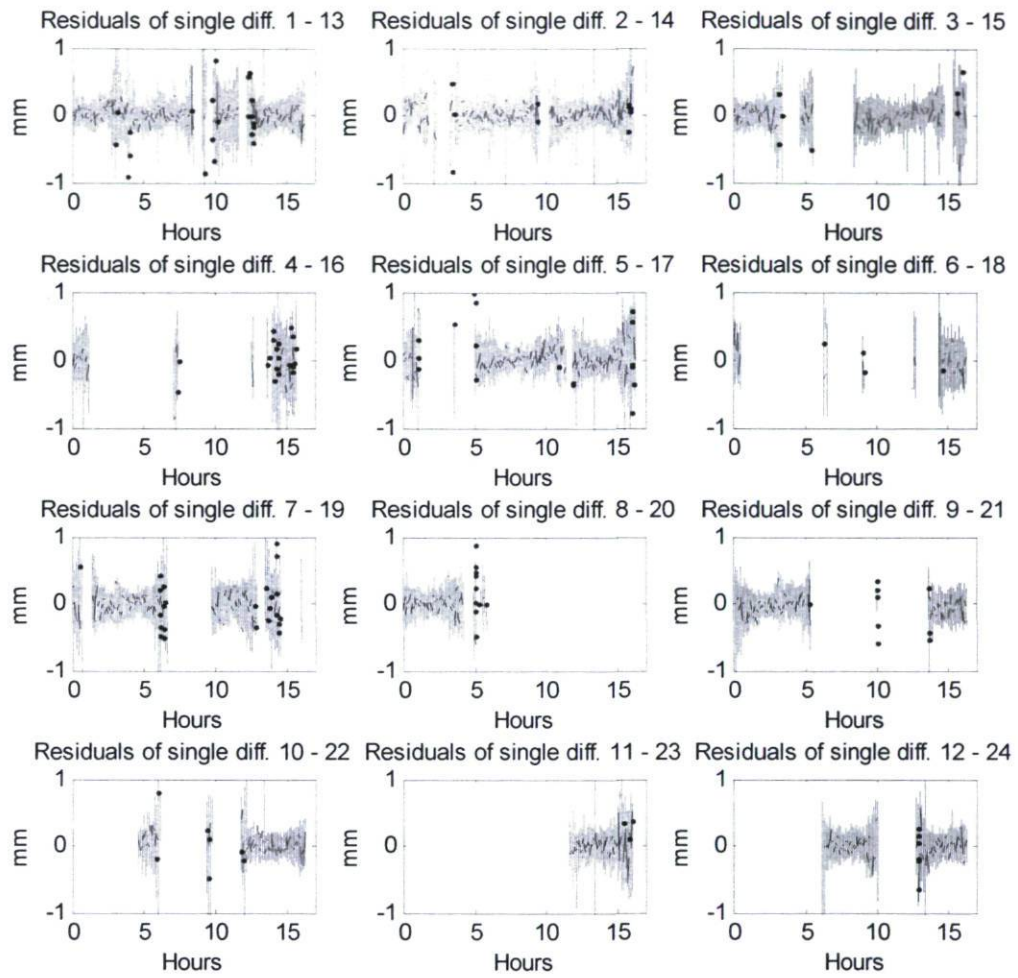


Figure 5.10 Residual noise of single difference observations for a zero baseline and GPS-over-cable configuration

5.2.2 Positioning analysis using a zero baseline configuration

Using a zero baseline with two remote stations in the setup shown in Figure 5.11, we analyzed the positioning solutions using two approaches:

- The standard approach: in this case, the observations from both remote stations are post-processed in single difference mode with the estimation of the relative clock parameter at each epoch (or more exactly the relative hardware delay because the clock is common), which is equivalent to double differences. This is called the standard approach since it is the usual technique in relative GPS positioning applications. In this case, the information from the relative delay monitoring (RDM) device is not used.
- The proposed approach: in this case, we use single difference mode post-processing but we additionally include the relative hardware delay measurements by the RDM device, taken at the same sampling rate as the GPS observations (up to 240 Hz sampling rate is nevertheless available), instead of estimating it as an additional parameter. By comparing the results with the standard approach, we are able to determine whether an improvement in vertical precision is achieved or not.

Two 12 hour sessions, called session 1 and session 2, with observations taken at 30 second intervals, were analyzed. In both cases, only small temperature variations were observed since the fiber optic rolls are inside a controlled temperature laboratory. Temperature fluctuations, measured with a thermometer located on top of the optical fiber rolls, were below 4°C. These small temperature changes were sufficient to observe changes of a few hundredths of cycle (a few millimeters) in the hardware relative delay. The elevation mask angle used was 15° and the antenna used was an Ashtech 700228 geodetic, active antenna.

Figure 5.12 and Figure 5.13 show the variation of three parameters: 1) the single difference of phase observations ($\Delta\Phi^i$) excluding the integer (ambiguity) part ($\Delta N_H(\delta t)$), which, for a zero baseline, gives an estimation of the relative hardware delay (Δz_H), 2) the output at the

phase comparator, which is also related to the relative hardware delay by the following relation $\Delta z_{RDM} = \Delta z_H - \Delta C$ (see Section 4.3 and Equation 4.24) and 3) the room temperature. The three figures show, as expected, that the parameters are correlated. Except for a constant bias (ΔC), the first two graphics should, ideally, be the same. However, if the relative (between remote stations) RF delay between the antenna and the optical modulator, which is not monitored, begins to change, it will be reflected only on the first graphic and not on the second one. This will be reflected in the final solution. This problem will be further analyzed in Section 5.2.3.

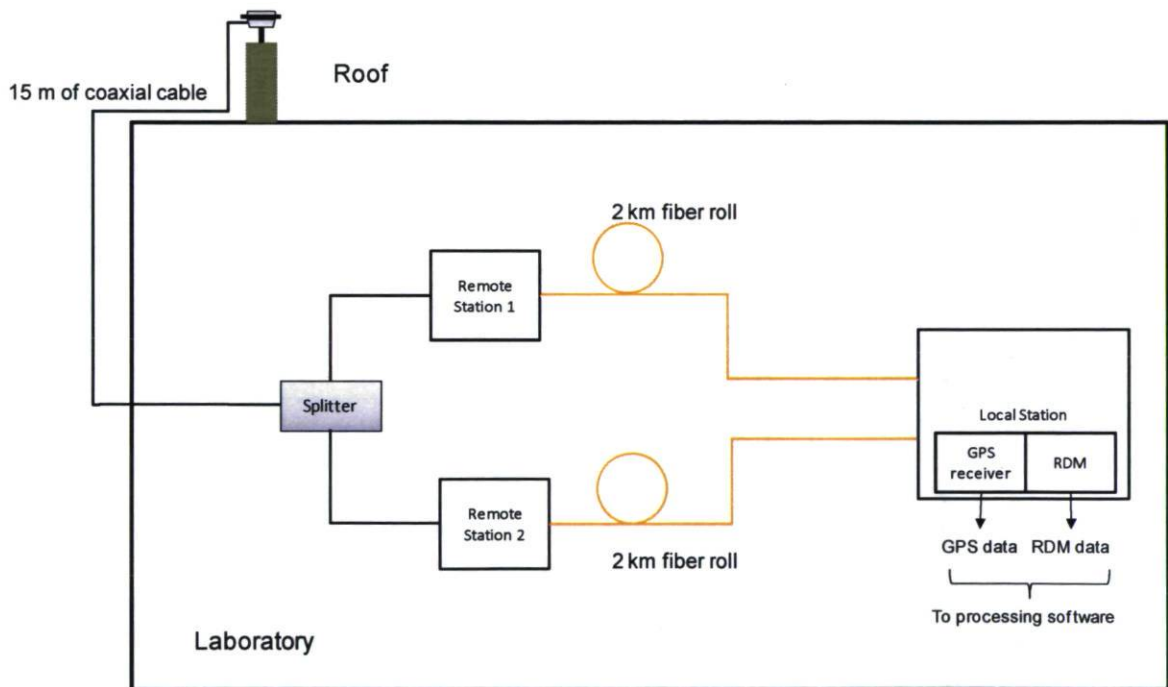


Figure 5.11 Experimental setup for zero baseline configuration

By subtracting the value for the first observation from the first parameter ($\Delta\Phi^i$) to the value for the first observation of the second parameter (Δz_{RDM}), we obtain an initial value for parameter ΔC (see Section 4.3), which will be used for the data processing to find the baselines coordinates (see Figure 4.6).

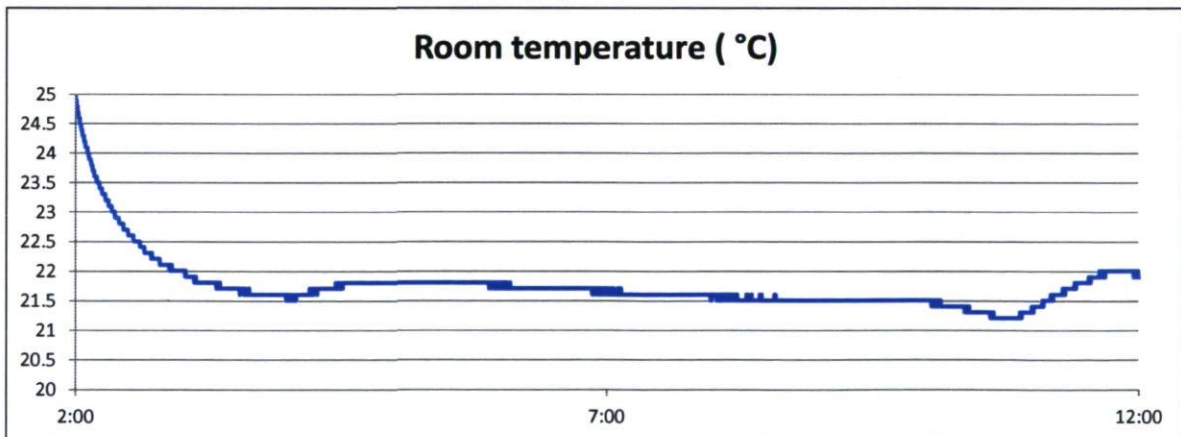
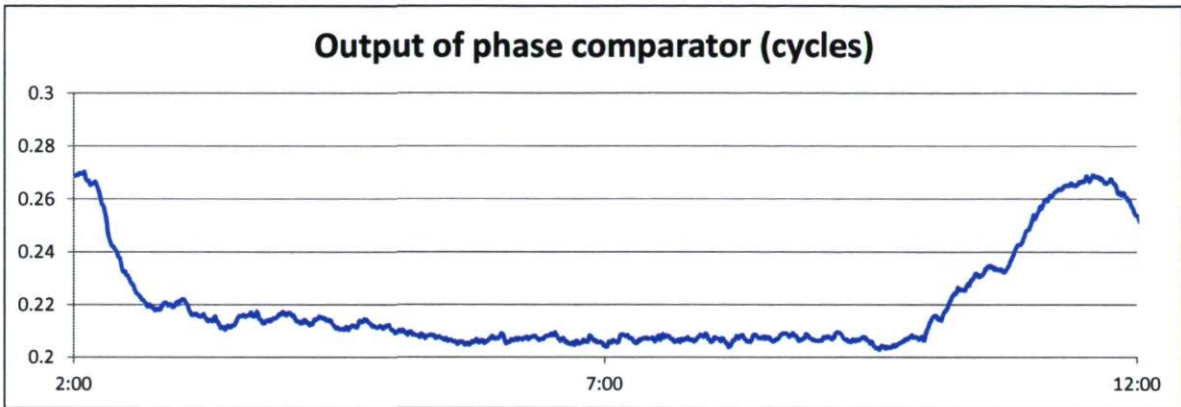
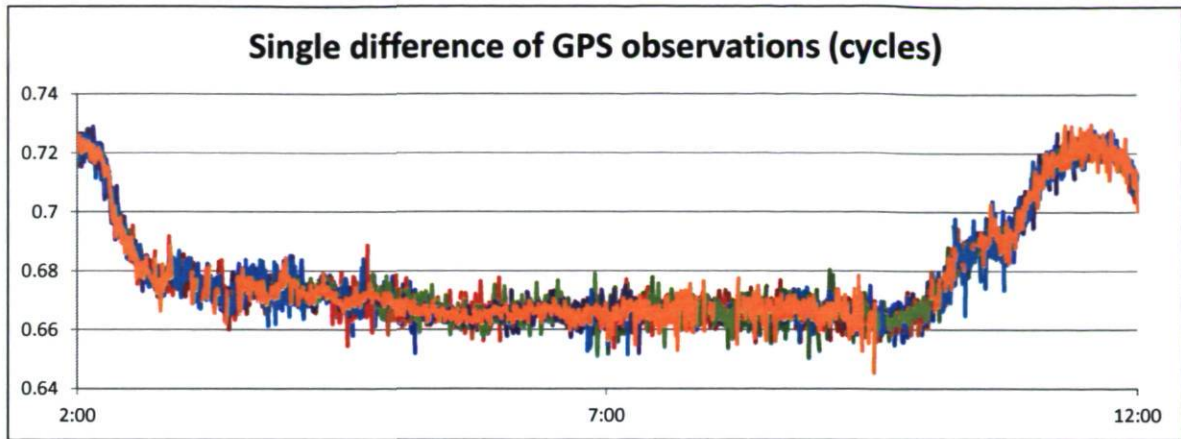


Figure 5.12 Single difference of phase observations (minus integer ambiguity part), output of phase comparator and temperature for session 1

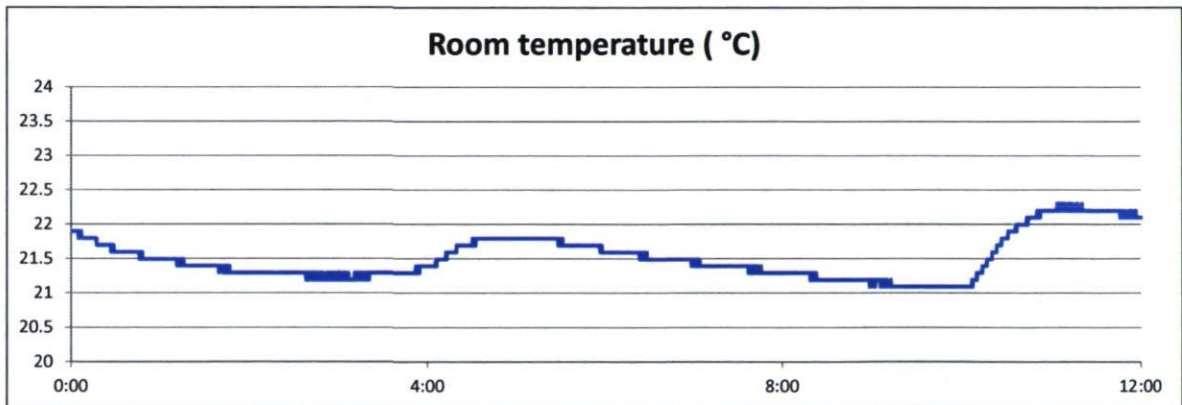
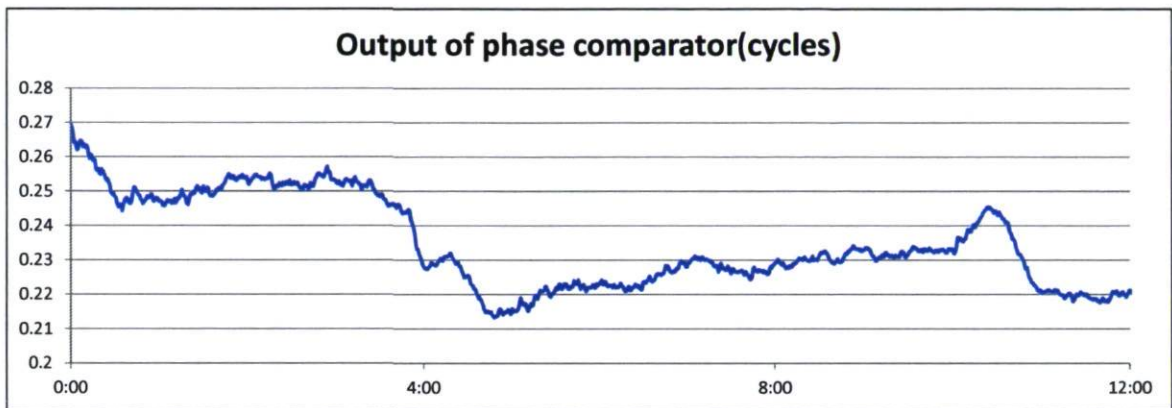
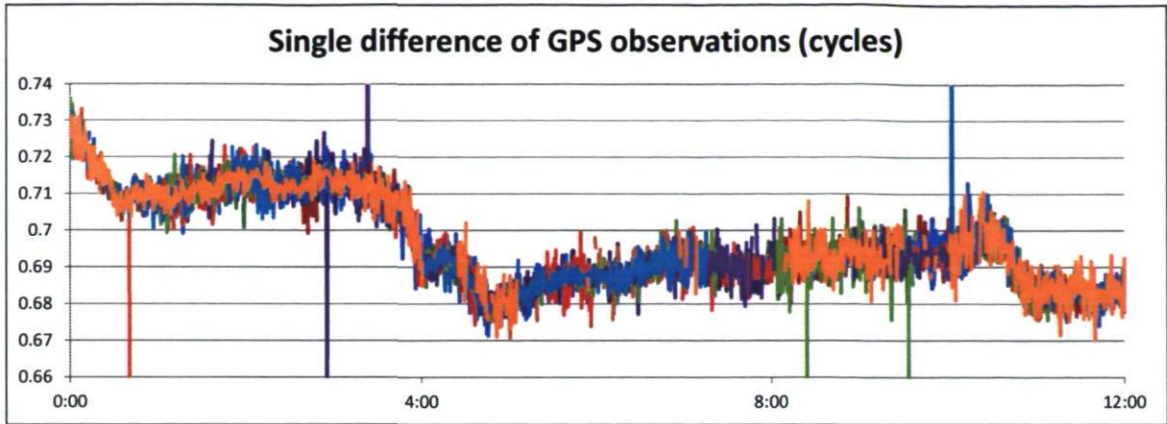


Figure 5.13 Single difference of phase observations (minus integer ambiguity part), output of phase comparator and temperature for session 2

The reference coordinates for a zero baseline are (0,0,0). The results for the positioning solution, using our software, for session 1 are shown in Figure 5.14 whereas those for session 2 are shown in Figure 5.15. Both sessions have a length of 12 hours and the observations are taken at 30-second intervals.

The improvement in the vertical component with the proposed approach is remarkable and substantial compared with the standard approach. As theoretically expected, the VDOP is two to three times smaller, which in turn, translates into an improvement in the rms value of the vertical coordinates by a factor of two to three. The rms values are calculated with respect to the average value. For session 1, the rms value for the vertical coordinates is 0.6 mm for the standard approach and improves to 0.3 mm for the proposed approach, i.e. a factor 2 improvement was achieved. For session 2, the rms values for the vertical coordinates are 0.7 mm for the standard approach and 0.3 mm for the proposed approach, representing more than factor 2 improvement. In both sessions, the rms value for the vertical coordinate then becomes similar to that of the horizontal coordinates. These results are in good agreement to what was predicted in simulations by (Santerre & Beutler, 1993). A careful analysis of the figures for the vertical component in the proposed approach reveals a small offset from the zero average value of about 1 mm in the zero baseline configuration. This anomaly, which is barely significant in this case, will be further analyzed in Section 5.3.

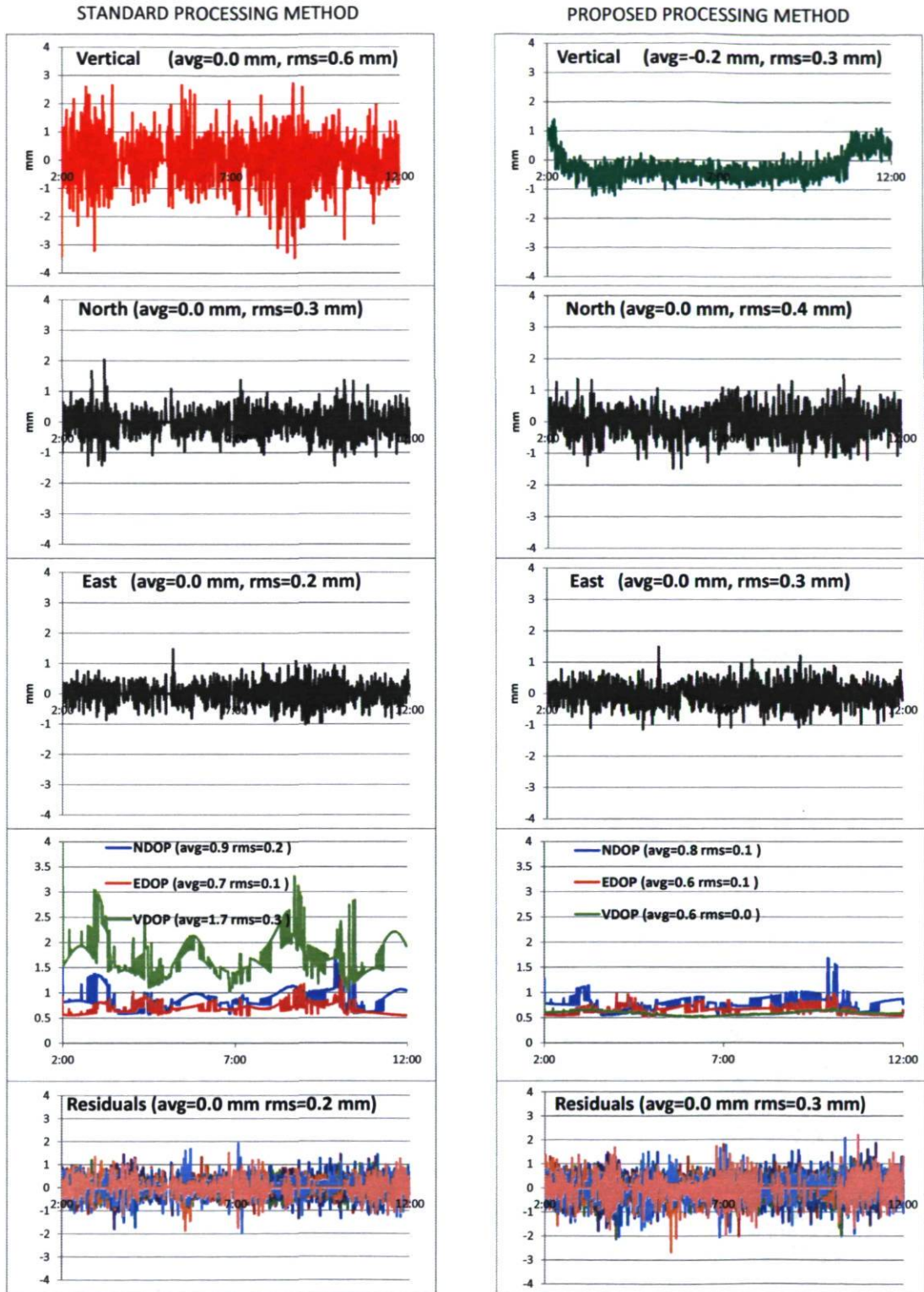


Figure 5.14 Positioning solution for zero baseline using the standard approach and the proposed solution for session 1 (12 hour session, 30 second epochs, 15° elevation mask)

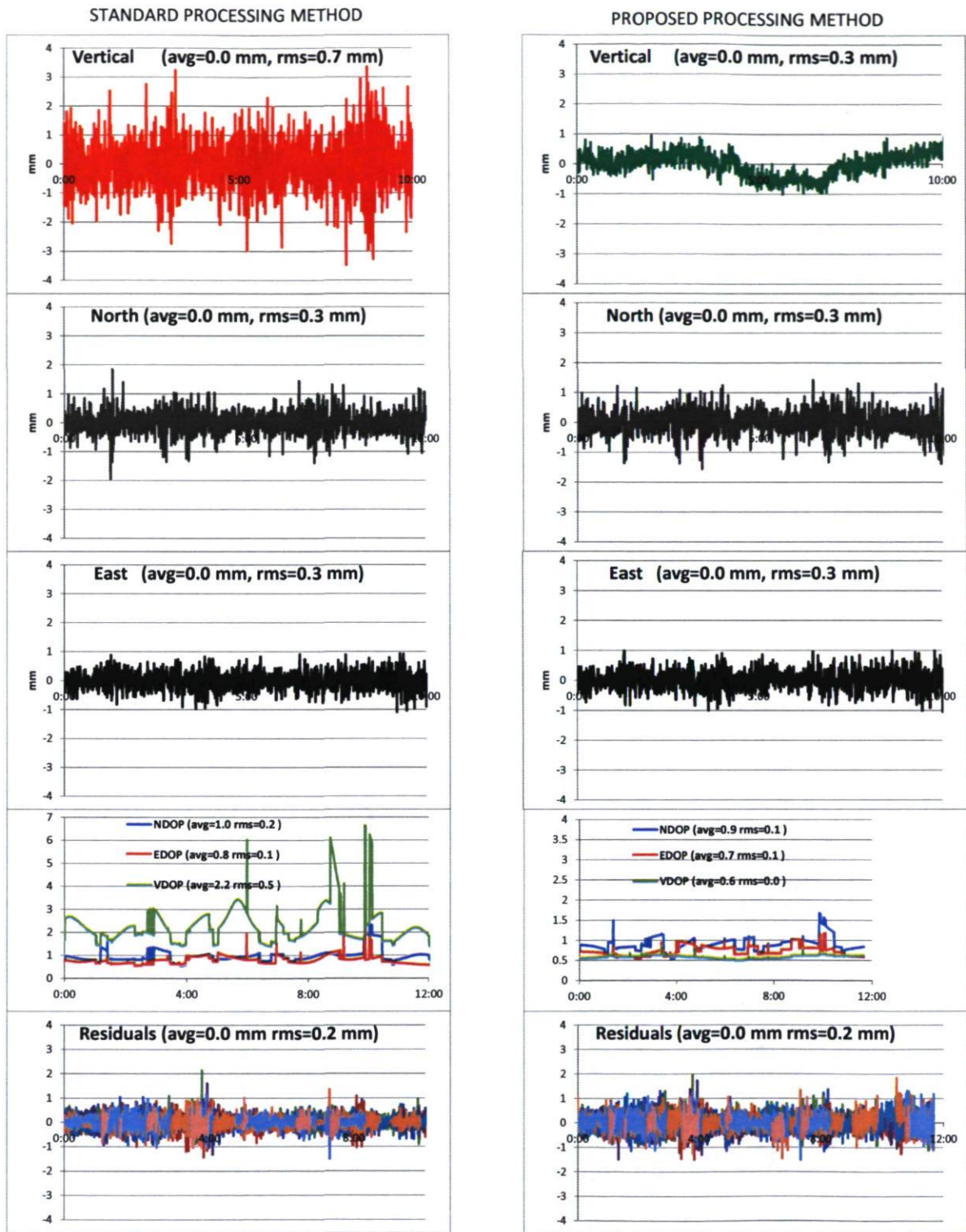


Figure 5.15 Positioning solution for zero baseline using the standard approach and the proposed approach for session 2 (12 hour session, 30 second epochs, 15° elevation mask)

5.2.3 Impact of temperature variations on the RF circuits using a zero baseline configuration

As stated in Section 4.3, one of the main limitations of the proposed GPS-over-fiber architecture with real-time relative delay monitoring has to be seen in the fact that this monitoring does not cover the signal path between the antenna and the optical modulator (H_1). In Figure 5.16, this means that the relative delays ΔH_1 (in the local station) and ΔH_3 , ΔH_b (in the remote stations) are not monitored by the Relative Delay Monitoring (RDM) device. As the temperature is stable within the local station and the coaxial cables are short, ΔH_3 may be neglected. However, for the remote stations, the temperature difference can be more important. This is why we conducted additional tests to see whether severe temperature changes in one of the remote stations have an impact on the positioning solution. More specifically, these severe temperature changes affect unmonitored paths H_1 and H_b in one of the remote stations (see Figure 5.16). The setup used is the same as the one presented in the previous section. We took measurements during a third session, which we will call session 3 (20-minutes session with observations at 30-second intervals), and in this case, the RF components of one of the remote stations were heated up from 25°C to 60°C for a short amount of time (a few minutes). In Figure 5.16, the area that was heated is shown in a red circle. This heating has a direct impact on ΔH_1 and ΔH_b . Figure 5.17 and Figure 5.18 show the results.

First, we note that, as expected, the output at the phase comparator of the RDM device is stable (Figure 5.17, center) even if the RF circuit is considerably heated (Figure 5.17, bottom). This is normal since the RDM does not track the changes along ΔH_2 and ΔH_b paths. However, the relative phase observations, which contain the relative hardware delay of the GPS signal do experience a change as a result of the temperature change (Figure 5.17, top). In the standard approach, the change in the relative hardware delay is absorbed by the estimated clock/hardware parameter and thus the vertical component is not affected (see Figure 5.18, left). In the proposed approach, however, there is an additional 1 mm deviation of the vertical component (see Figure 5.18, right). We conclude nevertheless that

heating of the RF components has a negligible effect on the positioning. Indeed, 40°C of temperature difference between remote stations 1 and 2 only caused 1 mm of additional shift in the vertical component. This temperature gradient is quite extreme. In real situations, we do not expect such temperature gradients and thus, no temperature stabilization in remote stations would be needed.

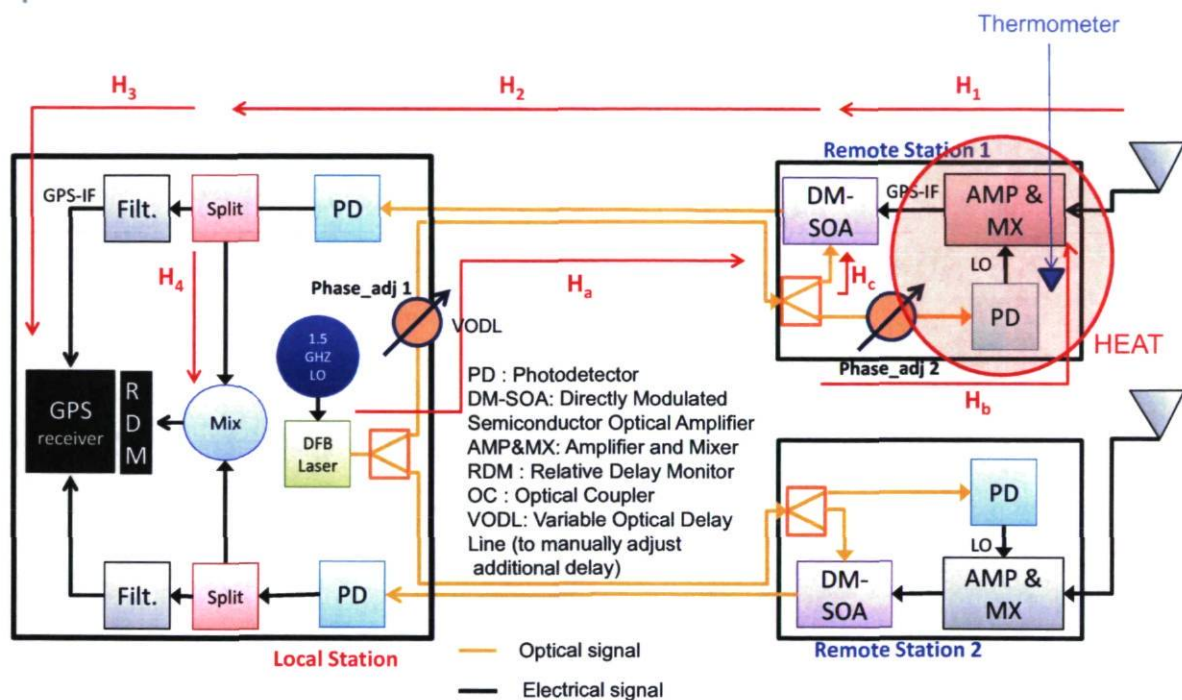


Figure 5.16 Different signal path delays on the zero baseline configuration for temperature variation tests

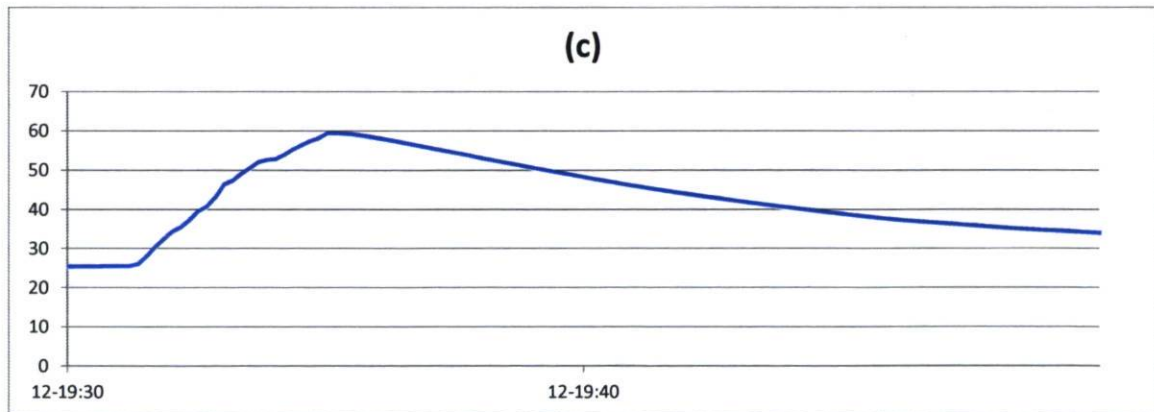
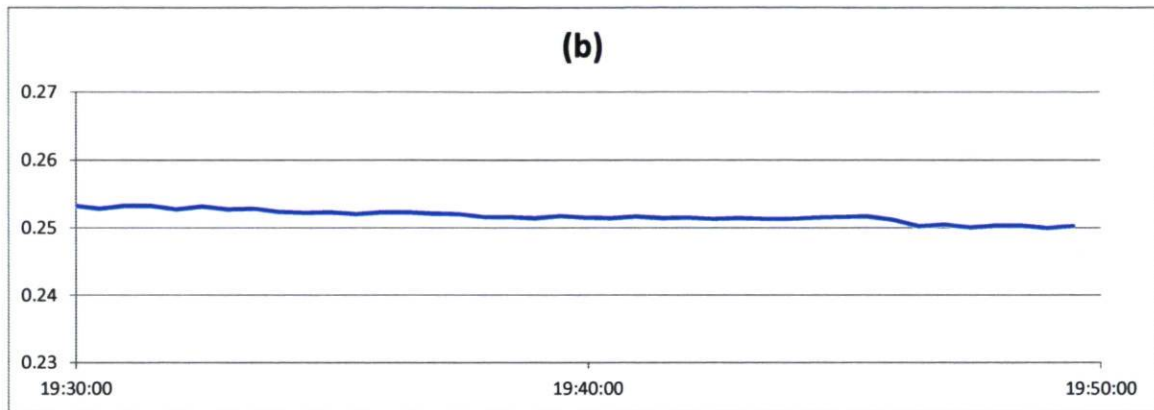
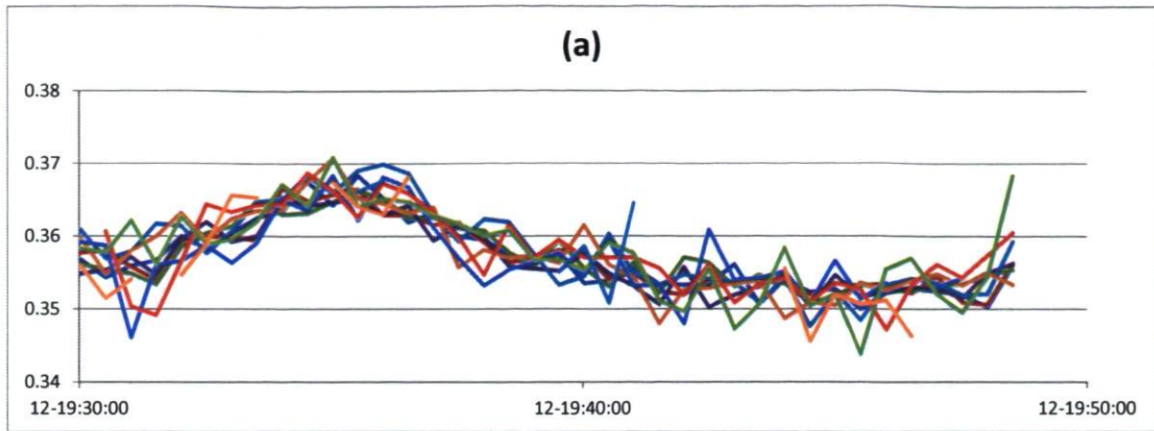


Figure 5.17 (a) Single difference of phase observations (minus integer ambiguity part), (b) output of phase comparator and (c) temperature for session 3

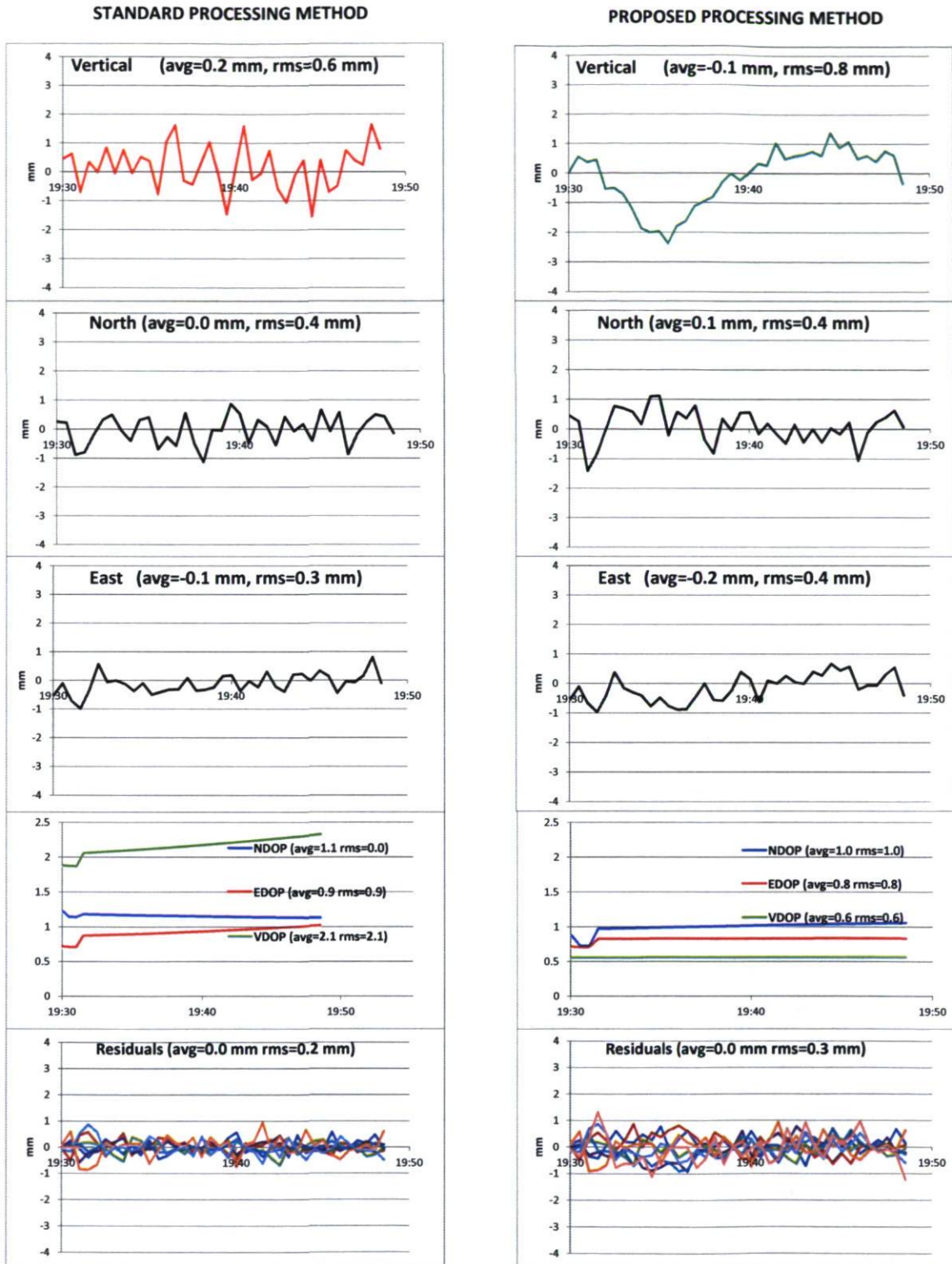


Figure 5.18 Standard and proposed approach positioning solution for zero baseline for session 3 (20 minute session, 30 second epochs, 15° elevation mask)

5.3 Short baseline tests

Even though the zero baseline tests were conclusive, the final proof of concept must be achieved on a standard baseline. The intended applications for this system include the deployment of remote stations several hundreds of meters or even a few km apart along a civil engineering infrastructures such as dams or bridges. We could not perform a realistic experiment of this kind because, the 3D components of the structure must already be known to the millimeter-level in order to compare the GPS solution with a “true”, external reference. Also, the prototype developed is not yet weather-proof. The proof of concept must therefore be deployed on a precisely known short baseline. Additionally, if we use a very short baseline, additional biases such as tropospheric, ionospheric and orbit errors cancel out almost entirely. In these tests, the interval between observations is 30 seconds, the elevation mask angle 15° and the antennas used are DSNP model NAP002 geodetic antennas.

5.3.1 Short baseline choice

Under the constraints mentioned, we decided to perform the tests on a small beam the 3D components of which are accurately known at sub-millimeter level. This calibration beam is shown in Figure 5.19. This beam, fabricated at the Laboratory of Metrology of *Université Laval*, is made of aluminum, weighs approximately 22 kg and is 1.1 meter long. It has two antenna bases, one at each end, the distance between the mounting screws being about 1 m. In the middle, a permanently fixed theodolite is orientated to 90° with respect to the longitudinal axis of the beam. Several adjusting knobs allow it to precisely adjust the orientation of the beam with respect to the three axis. Leveling of the beam is done with the help of two bubble tubular levels. After several calibration procedures (Bourassa, 1994), the main characteristics of the beam were established and are summarized in Table 5.3.

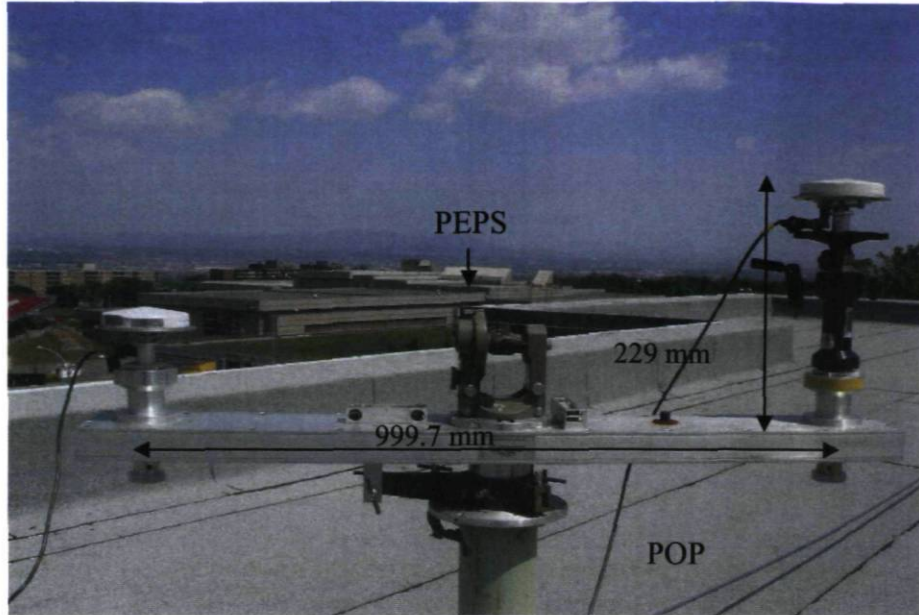


Figure 5.19 Calibration beam with two antennas mounted

Table 5.3 Main characteristics of the calibration beam

	Value	Uncertainty
Length	999.7 mm	± 0.1 mm
Leveling	0.0 mm	± 0.1 mm
Centering	0.0 mm	± 0.5 mm

5.3.2 Beam orientation procedure

The calibration beam was installed on the roof of the POP (*Pavillon d'Optique Photonique*) of *Université Laval* and the beam was orientated towards a known geodetic point on the roof of the PEPS building also located at *Université Laval* campus. The coordinates of the POP site were determined by post-processing a 24-hour session of GPS phase observations using the PEPS' permanent station as the base station. The distance between the center of the beam and the known geodetic point is 384.8 meters. The leveling and orientation of the

beam were not perfect because no anchor base is available on the roof of the POP building and the beam was thus installed in non-optimal anchoring conditions. This resulted in small unstabilities in the leveling of the beam of around one division on the tubular bubble level. This translates into a rotation of the beam of about 30" or an equivalent vertical movement at the extremities of the beam of about 0.1 mm. This movement can nevertheless be neglected. Also, the resulting orientation error with the theodolite due to the above mentioned unstabilities was estimated to be around 0.02°. This orientation error translates into a maximum error in the beam horizontal components of around 0.3 mm. The 3D components and orientation of the beam are presented in Figure 5.20.

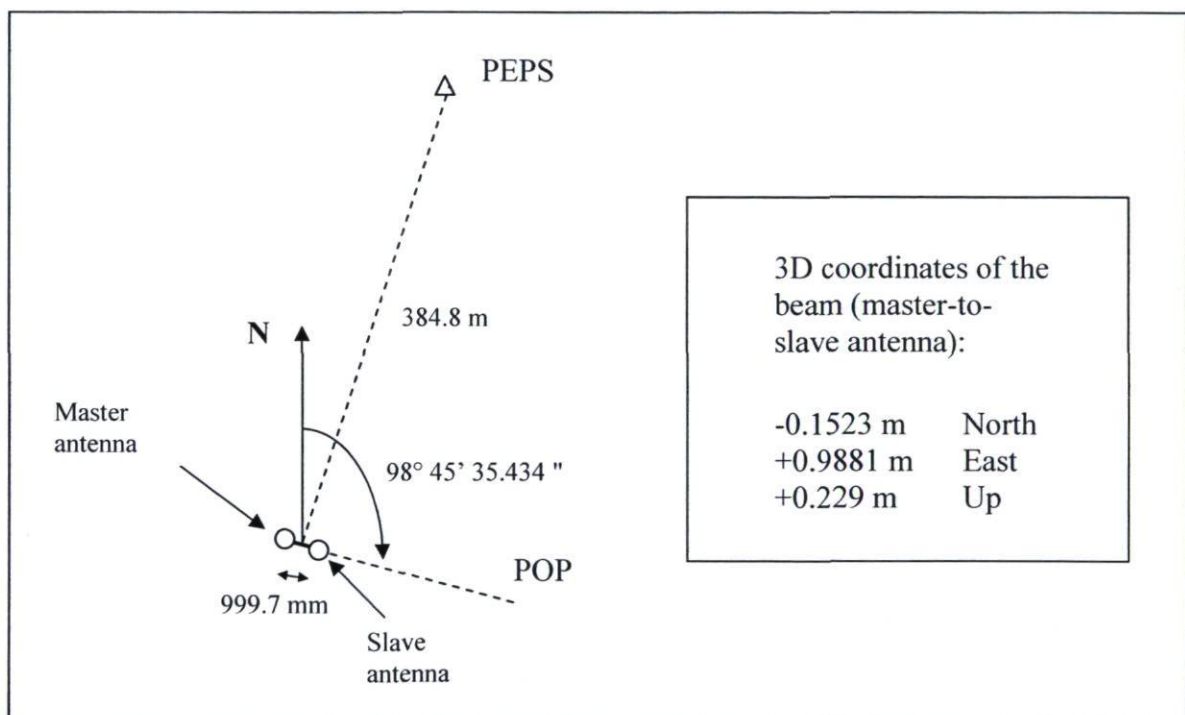


Figure 5.20 Reference coordinates of the baseline

Figure 5.20 also presents the reference coordinates of the beam and of the slave antenna with respect to the master antenna which are the result of the accurate orientation of the beam. The vertical height difference of 0.229 m between the antennas is due to the presence of an elevating column (see Figure 5.19), which will be used to create vertical movement of

the slave antenna. The height of the elevating column was measured with ± 0.1 mm at the Laboratory of Metrology.

5.3.3 Experimental setup and sessions

The data processing and the experimental setup were similar to the ones used in the zero baseline experiments. Data was processed at 3 and 30 second intervals in two modes: the standard approach (without using data from the Relative Delay Monitoring (RDM) device and estimating the relative delay as an additional parameter at each epoch) and the proposed approach (using the RDM data in the solution without the additional parameter). The experimental setup is shown in Figure 5.21. Two 15 meter coaxial cables interconnect the antennas to the remote stations. This interconnection distance should ideally be much shorter to avoid remaining biases as will be explained in Section 5.3.5. However, the current prototype does not allow the remote stations to be located outdoors.

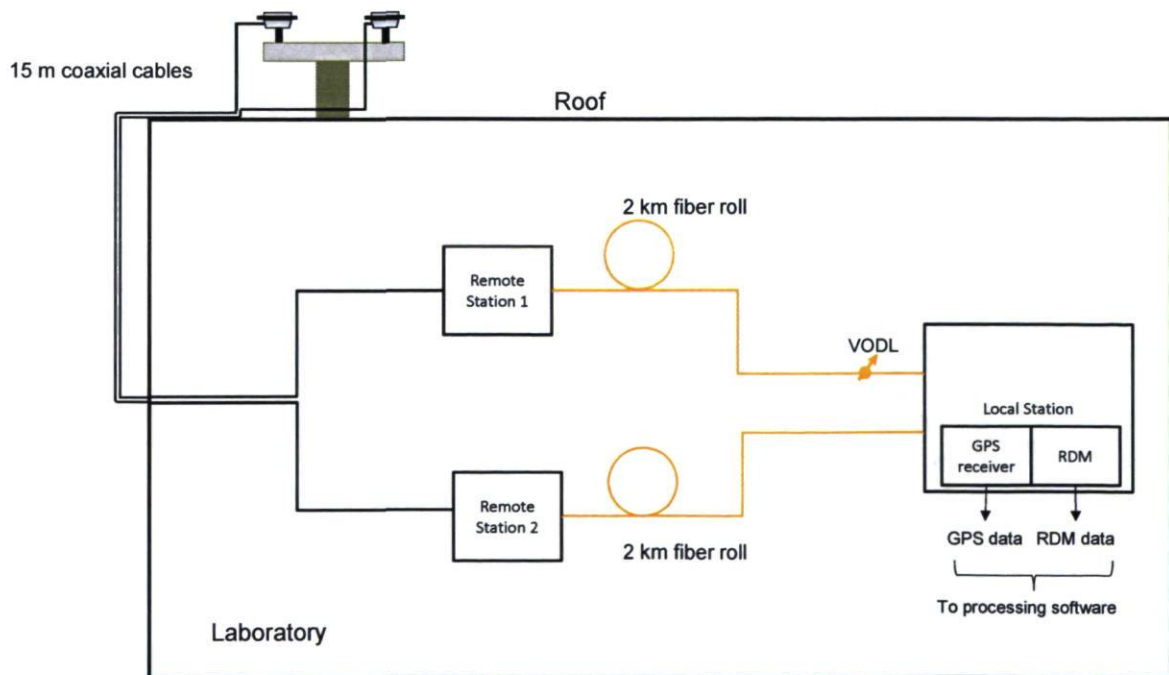


Figure 5.21 Experimental setup for short baseline configuration

The experimental sessions are summarized in Table 5.4. Some experiments were done while adding a controlled vertical movement of the slave antenna in order to see if the GPS positioning solution can “follow” accurately these movements. The experiments with vertical movement were performed using 3 second intervals while those without movement static case were performed using 30 second intervals. Table 5.4 also includes the manual adjustments made to the variable optical delay line (VODL) so that the initial relative delay is in the linear part of the transfer function of the phase comparator (phase difference = 90°). This previous calibration ensures that relative delay measurements stay within the linear and more precise part of the transfer function of the phase comparator.

Table 5.4 Sessions for small baseline experiments

Session no.	Interval (UTC time)	Conditions
Previous to 148A	A few minutes before 148A	VODL adjustment so that phase difference=90° - no data collection
148A	05/28/2010 (day 148) 00:00 – 10:00	No vertical movements on slave antenna (stays at 0.229 m with respect to the other)
Previous to 148R	A few minutes before 148R	VODL adjustment so that phase difference=90° - no data collection
148R	05/28/2010 (day 148) 16:00 – 00:00	Vertical movement on slave antenna from 0.229 m to 0.289 m and back
Previous to 149A	A few minutes before 149T	VODL adjustment so that phase difference=90° - no data collection
149A	05/29/2010 (day 149) 19:00 – 00:00	No vertical movements on slave antenna (stays at 0.229 m with respect to the other)
Previous to 150A	A few minutes before 150A	VODL adjustment so that phase difference=90° - no data collection
150A	05/30/2010 (day 150) 00:00 – 16:00	Vertical movement on antenna from 0.289 m to 0.229 m

5.3.4 Experimental results

We first present the results for the sessions in which no movements occurred at either antenna, i.e., sessions 148A and 149A. A positioning solution is calculated for each epoch (30 seconds). Figure 5.22 and Figure 5.23 show the results. We can see that by using the proposed method, there is a significant improvement in the rms value (with respect to the

average) of the vertical coordinate when compared to the standard method. In both sessions, the rms value improves by almost a factor of 3: from 11.1 to 4.1 mm in the first session and from 9.2 to 3.2 mm in the second session. The rms value of the vertical component is then of the same size as the rms value of the horizontal components. This is the expected result.

The improvement in the vertical positioning by using the proposed approach is also evident when looking at the DOP factors. Indeed, in all cases, the VDOP decreased from an average around 2 to less than 1. With the proposed approach, the VDOP has similar or even slightly better value as the EDOP and NDOP values. With the standard approach the VDOP is always larger than the EDOP and NDOP by a factor of 2 to 3. This improvement is in agreement with the expected confidence ellipsoids that were calculated by (Santerre & Beutler, 1993) (see Table 4.2). As DOP factors are dependent on the number of satellites and their geometry in the sky, we expect that when additional satellites will be available from other GNSS systems such as Galileo, all DOP factors will further improve.

If we compare the average value of the coordinates, we do not see any improvement. One might therefore argue that for long periods and static baselines, there is not much improvement in using the proposed method because the position converges to the same values. However, in applications where small movements are expected, which is the case for the intended applications, having lower error in the vertical position is advantageous since we use the instantaneous, epoch-specific position. This is why we did some slow vertical displacements during sessions 148R and 150A (indicated by the red line) on the slave antenna to see how well the GPS positioning solution can track these movements. These cases are presented in Figure 5.24 and Figure 5.25. We can clearly see in those cases that with the proposed solution, the small vertical movements are more accurately tracked.

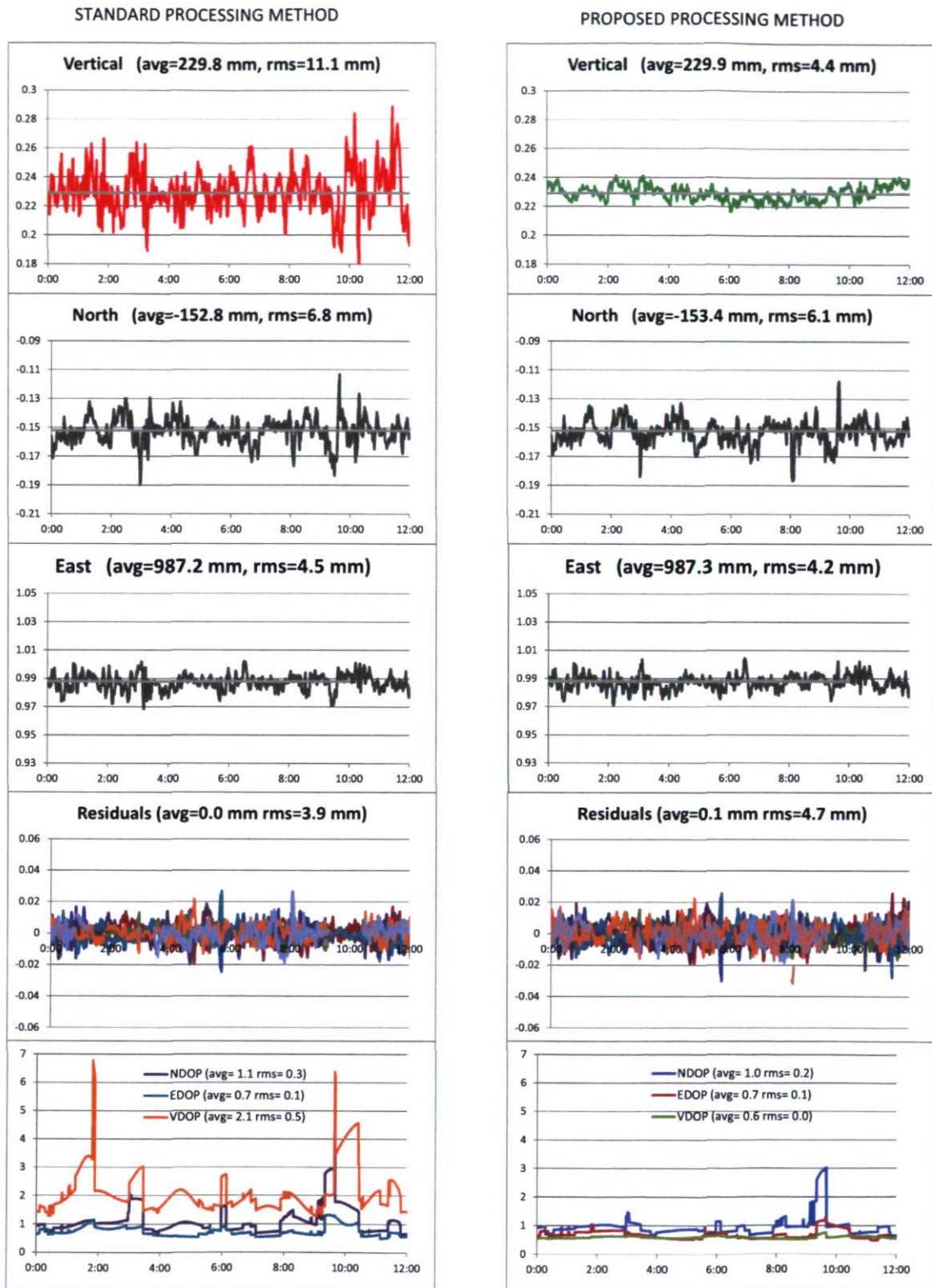


Figure 5.22 Positioning results for session 148A (12 hour session, 30 second data rate, 15° elevation mask)

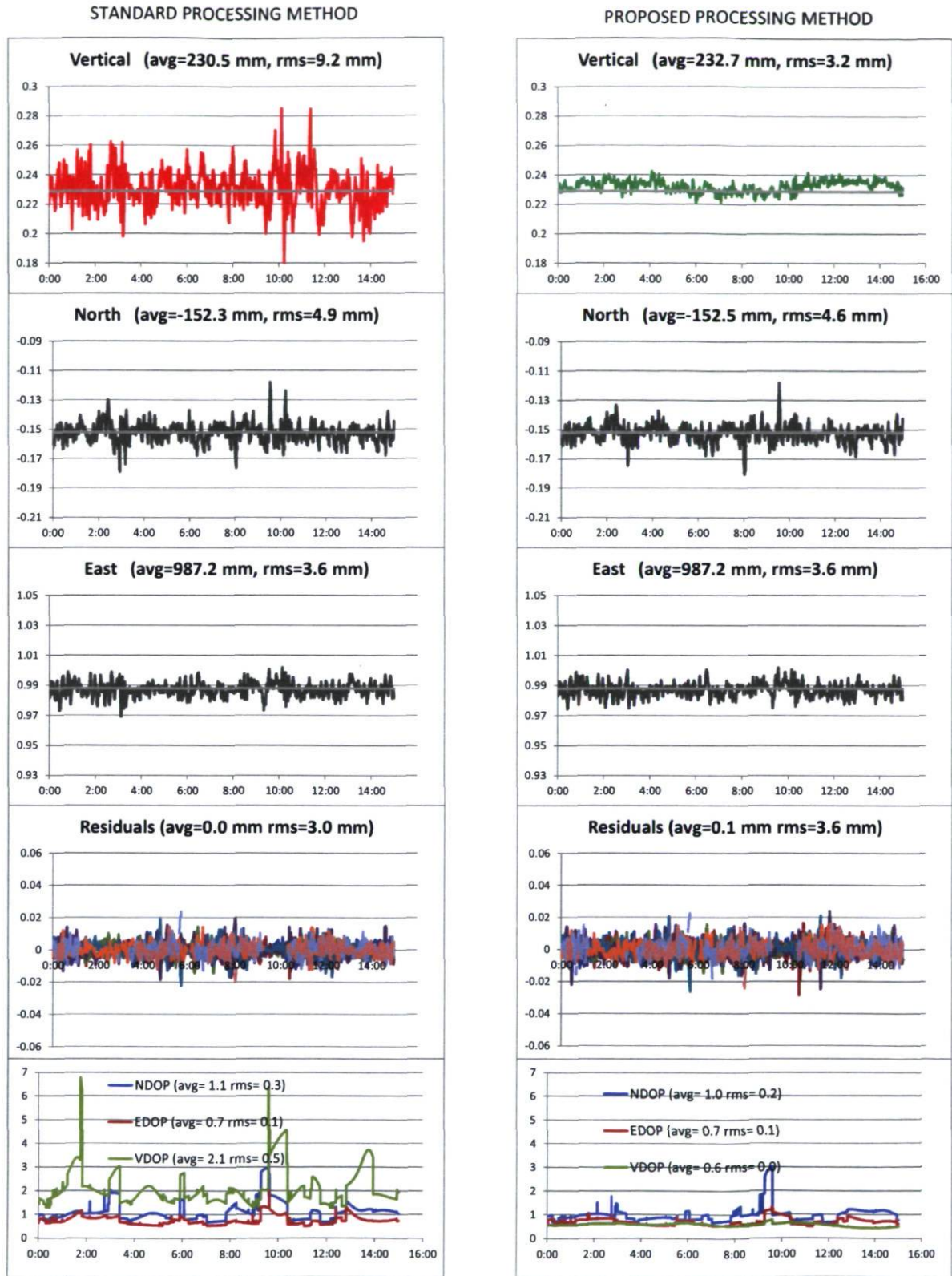


Figure 5.23 Positioning solution for session 149A (15 hour session, 30 second data rate, 15° elevation mask)

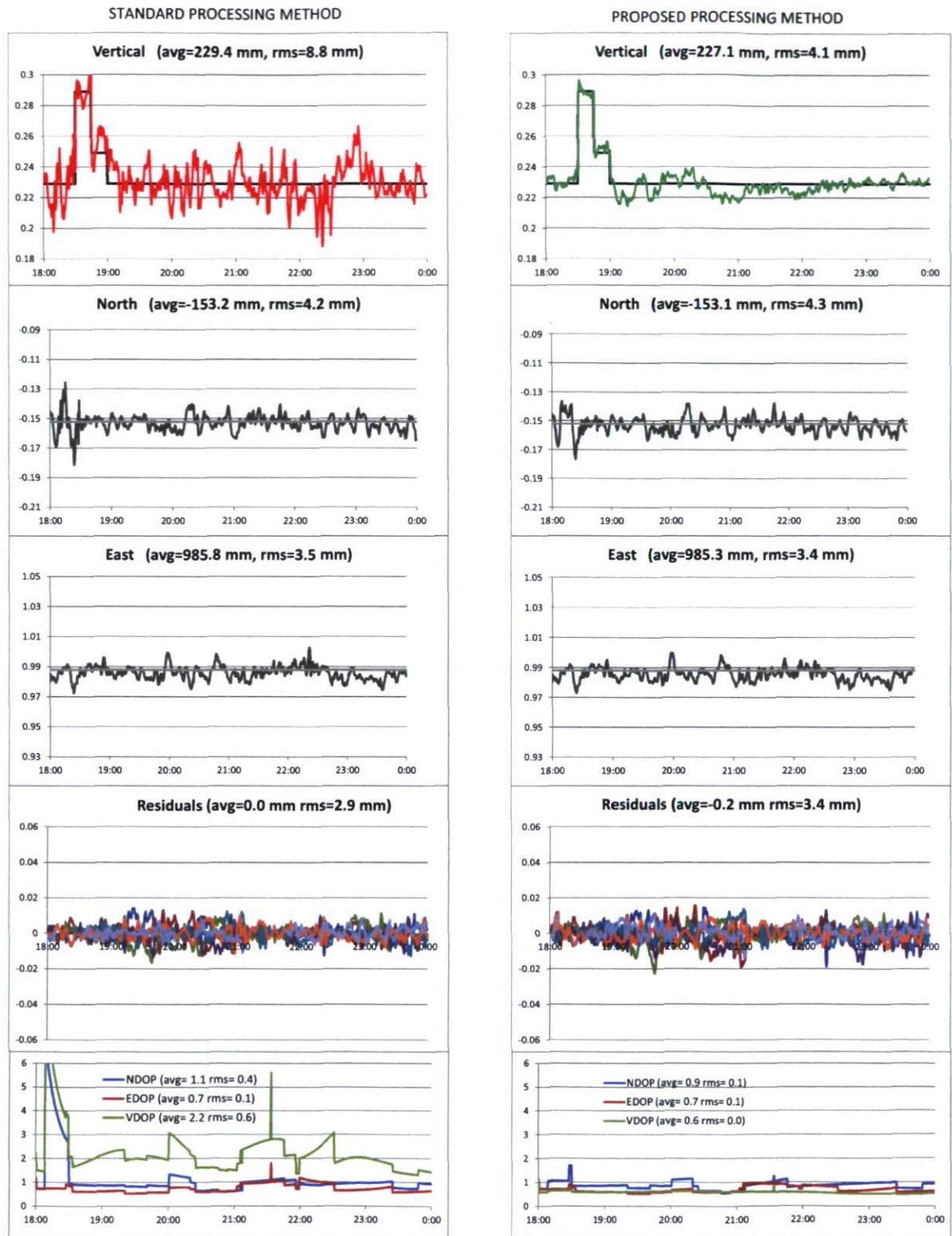


Figure 5.24 Positioning solution for session 148R (6 hour session, 3 second data rate, 15° elevation mask)

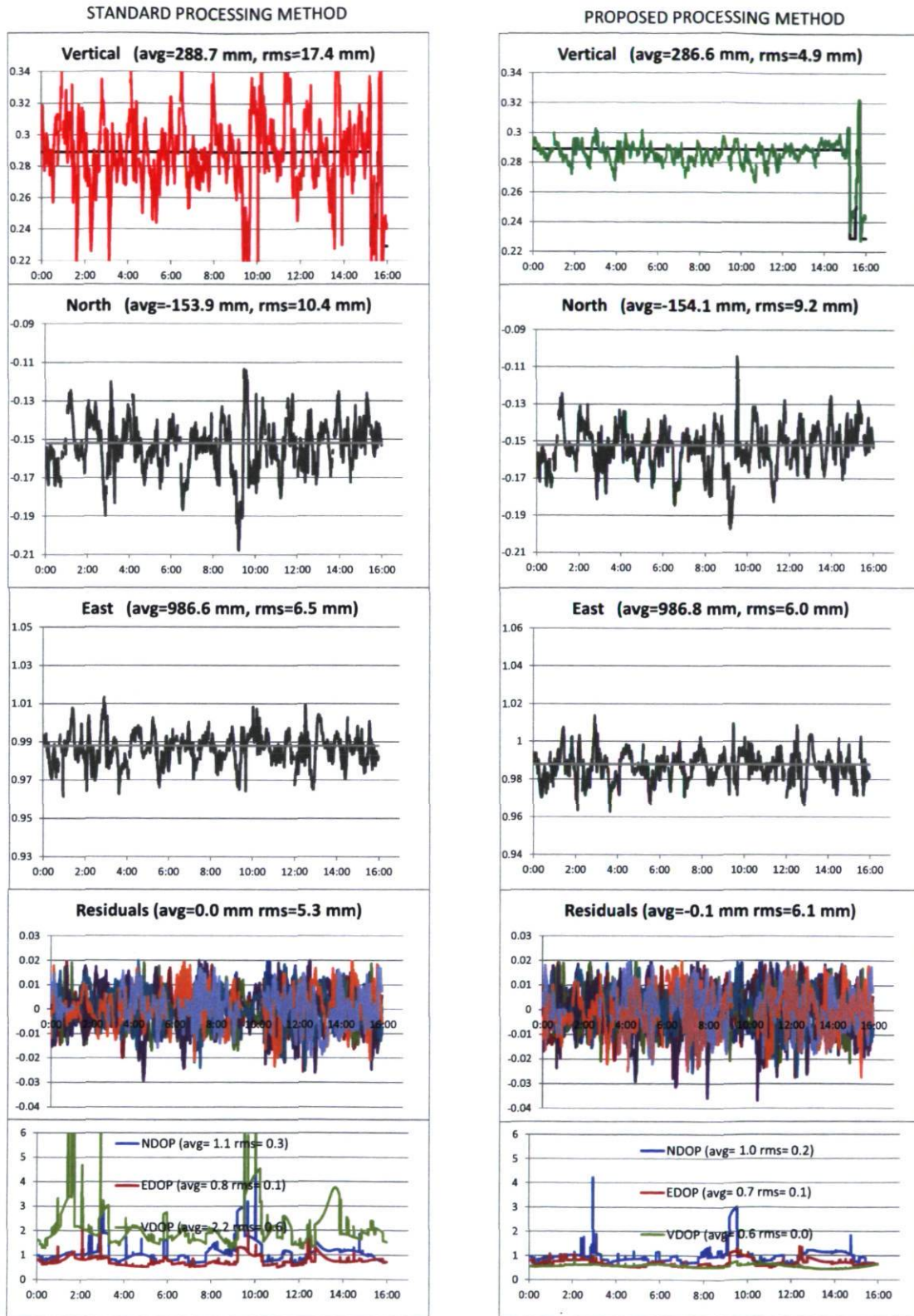


Figure 5.25 Positioning solution for session 150A (15 hour session, 3 second data rate, 15° elevation mask)

If we analyze the residuals, we can see that their rms value slightly increases for the proposed approach when compared to the standard approach. For example, for session 149A, the rms value increases from 3.0 mm for the standard approach to 3.6 mm for the proposed approach. This is because in the standard approach, an additional unknown, the relative receiver clock parameter, is estimated and partially “absorbs” some of the noise. For the proposed approach, only the three coordinates are estimated. However, the rms of the residuals still remains at approximately the same value as the rms of the error on the coordinates.

If we carefully analyze the average values of the vertical positioning we can see that there is a small drift or bias in the vertical coordinate for the proposed solution (see Figure 5.26). In the proposed solution, any small deviation or error in the relative hardware delay measurement directly affects the vertical positioning. As stated by (Santerre & Beutler, 1993), a 1 mm error in the relative delay measurement translates into -1.4 mm bias in the vertical position (see Table 4.5). If a bias is present in the vertical position then two possibilities arise:

- The RDM device is not measuring the hardware delay with enough precision (better than 1 mm).
- An unmonitored relative bias, such as the relative path in the cables between the antennas at the remote stations which is not monitored by the RDM, is varying by more than 1 mm, which then translates into -1.4 mm bias as previously mentioned.

The first possibility would only arise if the relative hardware delay changes by a value greater than 100° (1/3 cycle) or about 40 mm (see Section 5.1.4). This is not the case in the experiments we performed, where small temperature changes caused only relative delay changes of less than 0.1 cycle. We thus have to check the second possibility. The main suspects are the relatively long coaxial cables between the antennas and the remote stations, each about 15-meter-long. These cables should ideally be as short as possible. Unfortunately, we were not able to shorten these cables because the remote stations were not weather-proof. We initially thought that since these cables are close together, any

temperature change would be common to both and the relative effect would be negligible. However, a RG-58 coaxial cable has a thermal coefficient of around 175 ppm/°C, therefore 15 meters of cable experience a length change of 2.6 mm/°C. Then, if we have a temperature gradient of only 1°C between the cables, the relative hardware delay increases or decreases by 2.6 mm, which then translates into an additional bias in the vertical coordinate of more than 3 mm. This temperature gradient could easily appear if one of the cables is more affected by the Sun than the other. By using shorter cables (less than 1 meter), the problem should be resolved, or at least the effect kept under 1 mm.

The previous results were calculated without estimating a tropospheric parameter. However, we also analyzed the case where a tropospheric parameter is estimated. By estimating a tropospheric parameter, the effects of an error on the relative hardware delay on the vertical component are reduced. (Santerre & Beutler, 1993) showed that, by including a relative tropospheric bias as an additional unknown, the effect of a 1 mm bias in the relative hardware delay translates in a -0.9 mm bias in the vertical component (for mid-latitude sites and an elevation mask of 15°) instead of the -1.4 mm, mentioned previously for the case when no tropospheric parameters are estimated (see Table 4.5). In other words, the vertical component is less sensitive to variations in the relative hardware delay. We processed the data for session 149A including the relative tropospheric zenith delay (RTZD) as an additional unknown parameter and compared the results with the previous ones where no RTZD was estimated. A tropospheric parameter was estimated every hour. Generally, a 1 to 2 hour interval is recommended (Astronomical Institute - University of Bern, 2004, ch. 11). Figure 5.26 shows the results. It is clearly seen that, by estimating a RTZD, the bias in the vertical component is reduced. We can see that the average value changes from 232.7 mm to 230.5 mm, which is closer to the reference value of 229 mm. The estimation of the RTZD greatly reduces the remaining biases in the estimation of the relative hardware delay (RHD). The estimation of a tropospheric parameter was also done for the other three sessions. The results are presented in Appendix C. In all cases, the average value of the vertical components improves and approaches the reference value. Even if the estimation of the RTZD helped in reducing the bias in the vertical component,

one has to keep in mind that one should focus on avoiding this bias by minimizing the coaxial cable length between the antennas. Once this issue is solved, the decision of whether to estimate a RTZD parameter or not should be taken considering other factors such as height difference between stations (see Sections 2.3.2 and 4.2.3).

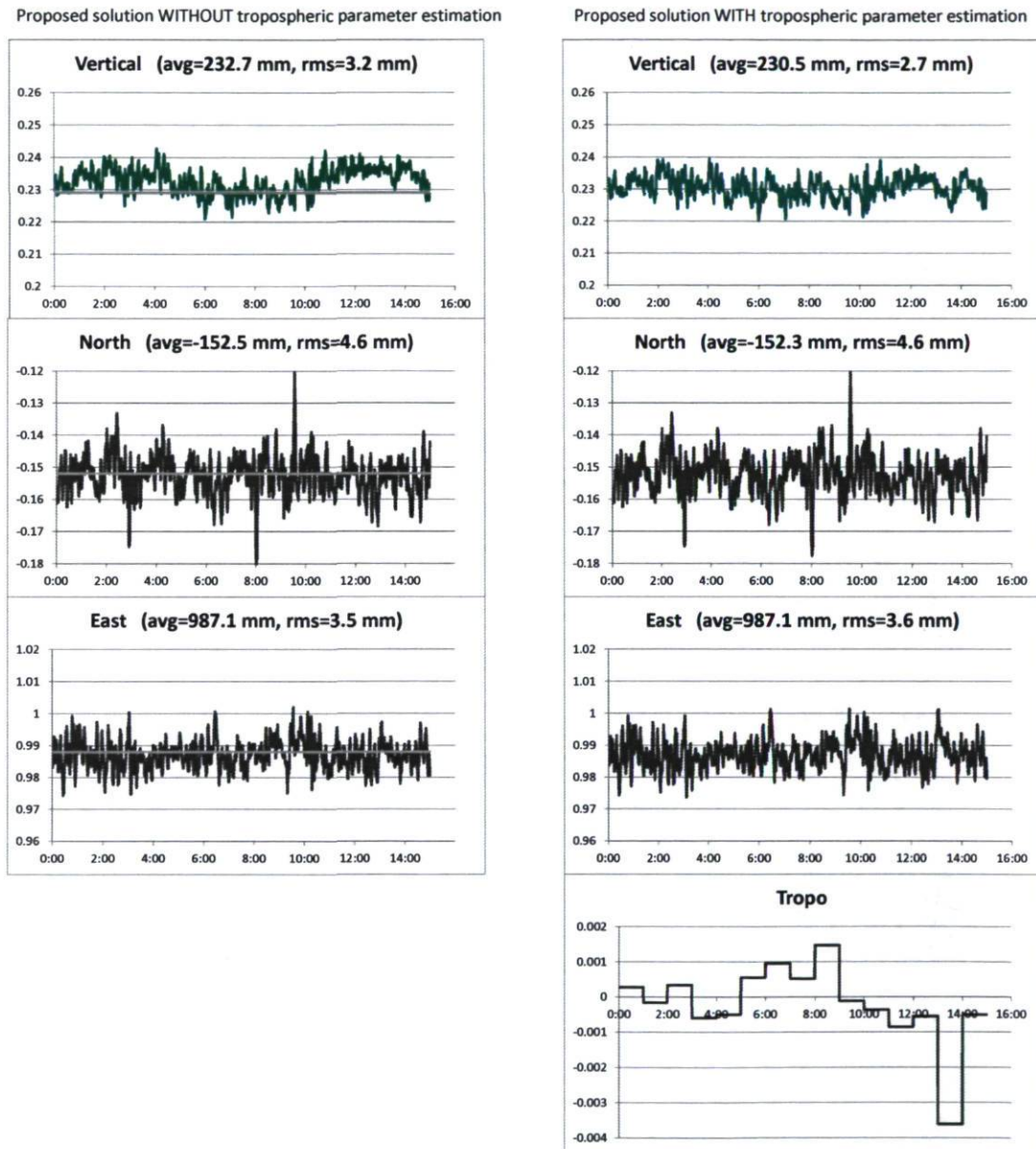


Figure 5.26 Comparison of positioning results without and with relative tropospheric zenith delay estimation for session 149A (15 hour session, 30 second data rate, 15° elevation mask)

The results are summed in Table 5.5.

Table 5.5 Summary of small baseline positioning results

		STANDARD SOLUTION	PROPOSED SOLUTION (without tropospheric parameter estimation)	PROPOSED SOLUTION (with tropospheric parameter estimation)
Session	Baseline 3D component	Average/rms value (Average with respect to "true" value)	Average/rms value (Average with respect to "true" value)	Average/rms value (Average with respect to "true" value)
148A	Vertical	229.8 / 11.1 mm (0.8 mm)	229.9 / 4.4 mm (0.9 mm)	229.4 / 3.6 mm (0.4 mm)
	North	-152.8 / 6.8 mm (-0.8 mm)	-153.4 / 6.1 mm (-1.4 mm)	-152.9 / 6.3 mm (-0.9 mm)
	East	987.2 / 4.5 mm (-0.8 mm)	987.3 / 4.2 mm (-0.7 mm)	987.1 / 4.1 mm (-0.9 mm)
149A	Vertical	230.5 / 9.2 mm (1.5 mm)	232.7 / 3.2 mm (3.7 mm)	230.5 / 2.7 mm (1.5 mm)
	North	-152.3/ 4.9 mm (-0.3 mm)	-152.5 / 4.6 mm (-0.5 mm)	-152.3 / 4.6 mm (-0.3 mm)
	East	987.2 / 3.6 mm (-0.8 mm)	987.1 / 3.5 mm (-0.9 mm)	987.1 / 3.6 mm (-0.9 mm)
148R	Vertical	229.4 / 8.8 mm (0.4 mm)	227.1 / 4.1 mm (-1.9 mm)	228.5 / 3.7 mm (-0.5 mm)
	North	-153.2/ 4.2 mm (-1.2 mm)	-153.1 / 4.3 mm (-1.1 mm)	-153.3 / 4.3 mm (-1.3 mm)
	East	985.8 / 3.5 mm (-2.2 mm)	985.3 / 3.4 mm (-2.7 mm)	985.3 / 3.4 mm (-2.7 mm)
150A	Vertical	288.7 / 17.4 mm (-0.3 mm)	286.6 / 4.9 mm (-2.4 mm)	287.6 / 5.0 mm (-1.4 mm)
	North	-153.9/ 10.4 mm (-1.9 mm)	-154.1 / 9.2 mm (-2.1 mm)	-153.6 / 9.1 mm (-1.6 mm)
	East	986.6 / 6.5 mm (-1.4 mm)	986.8 / 6.0 mm (-1.2 mm)	986.8 / 6.1 mm (-1.2 mm)
Reference 3D components of the baseline : -152 mm North, 988 mm East, 229 mm Vertical (289 mm Vertical for session 150A)				

5.3.5 Multipath analysis

We have seen that a significant improvement in the vertical positioning precision could be achieved with the proposed approach with respect to the standard approach. This is important since it was the main purpose of this research. However, with further analysis of all the time series presented in Section 5.3.4, we can see that the expected rms of the estimated values for the positioning is large considering the short baseline and that there is

a significant periodicity of the coordinates difference (error). This effect is documented by Figure 5.27 and Figure 5.28.

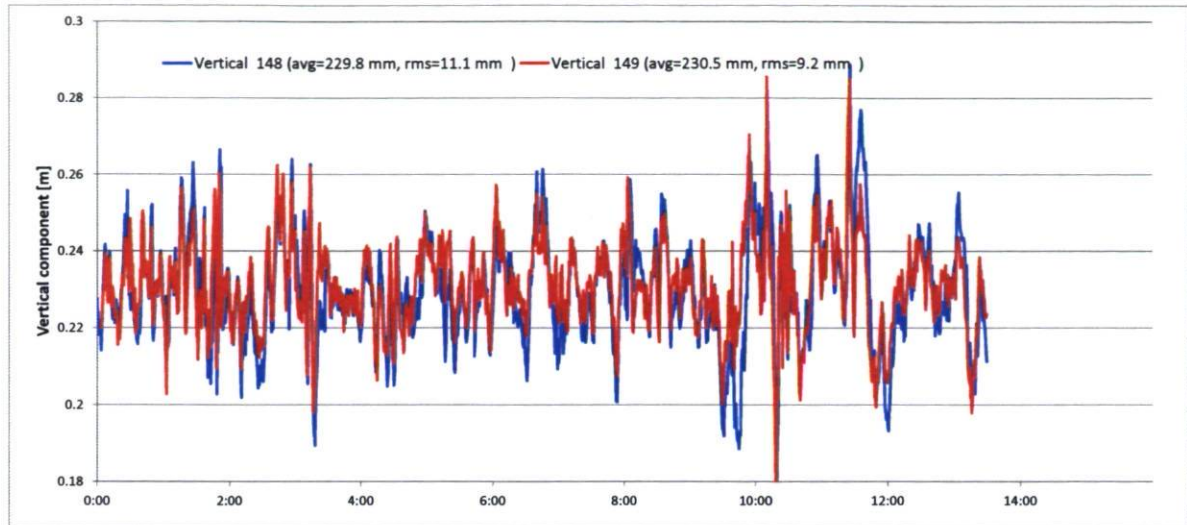


Figure 5.27 Comparison of vertical positioning between day 148 (session 148A) and day 149 (session 149A) for the standard approach

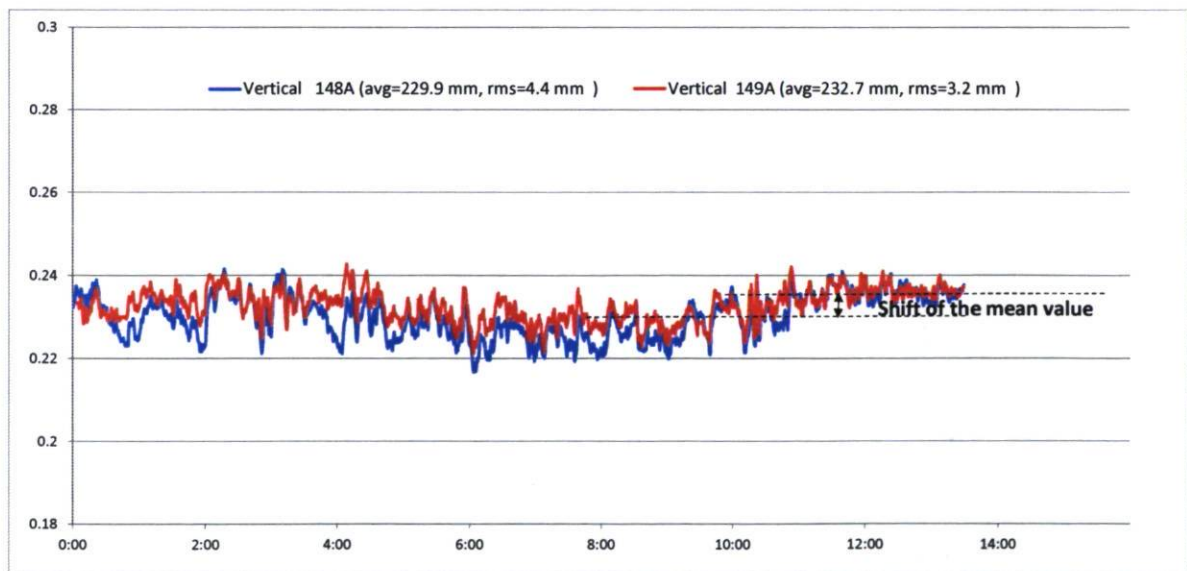


Figure 5.28 Comparison of vertical positioning between day 148 and day 149 for the proposed approach

We can see that the coordinates difference patterns are very similar from one day to the next. This indicates the presence of a multipath effect since satellites' constellation repeats itself with a periodicity of about 23 hr 56 min. A multipath effect of this size was not expected because both antennas were clear of obstructions and no important reflective surface was located near the antennas. Note, however, that the multipath effect was less important for the proposed approach than for the standard approach. Multipath is a problem that is independent of the design of the proposed system and depends on the location and type of antennas. Multipath rejecting antennas such as choke ring antennas could be used to reduce the multipath effects. In this case, however, it is possible to partially mitigate the multipath effect by taking advantage of the sidereal day repeatability of the satellite's constellation as long as the geometry relating the GPS satellites, the reflective surface and antenna, and the properties of the antenna and reflective surface remain unchanged. Several techniques exist but all are based on extracting a multipath pattern by comparing the observations from one sidereal day to the next. In our case, we used the simplest technique, which is based on forming the difference between the coordinates for a given period from those obtained after a sidereal day. As it is important that the same satellites are present in both periods, we kept only those observation epochs where exactly the same satellites were used and discarded the other. More efficient multipath sidereal filtering techniques exist such as the one based on the single difference residuals as explained in (Zhong et al., 2009). However, as multipath analysis was beyond the scope of this work, we used the simple technique previously mentioned. We took observations from sessions 148A and 149A since they are the ones where no antenna was moved and the technique could be applied. The results are shown in Figure 5.29. If we compare with the results without sidereal multipath filtering (Figure 5.23), we can see an improvement in the rms value for all the components. The most important improvement is observed in the vertical component for the standard approach, where the rms improves from 9.2 to 5.6 mm. For the other cases, the improvement is less significant. This is only an example of sidereal multipath filtering. It would be also advisable for future implementations to use better multipath rejecting antennas.

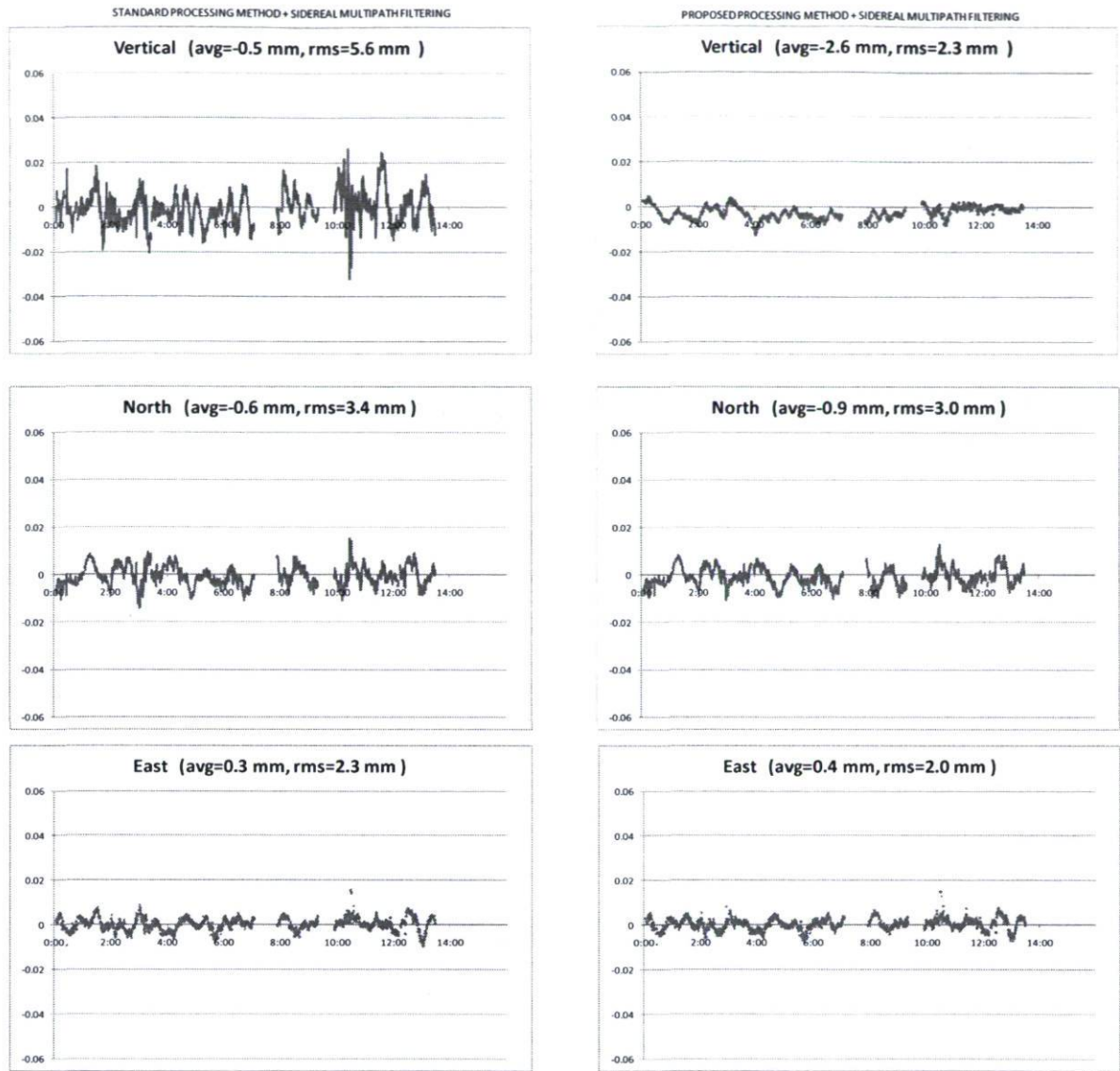


Figure 5.29 Positioning results for session 149A with the use of sidereal multipath filtering using data from session 148A

6 Conclusions and further works

6.1 Summary of results and analysis

Even though the theoretical analysis and the simulations conducted by (Santerre & Beutler, 1993) predicted the improvement of the vertical precision with a multi-antenna configuration and relative hardware monitoring, no implementation was available until now. Even though commercial multi-antenna receivers and GPS-over-fiber systems exist, several difficulties would arise when trying to combine these with a high precision real-time relative hardware delay monitoring system. The main innovation of the designed and implemented system is the successful combination of this monitoring system with a GPS-over-fiber multi-antenna architecture, which is currently patent pending (Macias-Valadez, Santerre, & LaRochelle, 2010). Our implementation and the experimental validation show that the vertical precision improves and becomes comparable to that of the horizontal precision, and we can thus consider that the main objective of this research has been met.

We first established the basic performance criteria for our GPS-over-fiber to meet for almost transparent operation. “Transparent operation” means that the GPS-over-fiber should operate with almost the same signal performance as a standard GPS-over-cable receiver. In other words, the GPS signal should not be deteriorated significantly by the use of the over-fiber transport system, when compared to the standard over-cable system. Also, since the optical fiber transports two signals, the GPS signal and the reference 1.55142 GHz oscillator, it is important to make sure that cross-interference is minimized. Using simulated and real GPS signals, we were able to identify the optimal operation points to minimize added noise and cross-interference. Experiments show that it is possible to operate the system with almost no degradation in the carrier-to-noise ratio (C/N_0) in the correlators. In all cases, the degradation was below 2 dB.

As the relative hardware delay monitoring is a critical part of the project, it was important to measure its performance. We were able to confirm that the phase detector used for the monitoring keeps sub-millimetric level for a 105° range, which is equivalent to about 40 mm of optical fiber relative length variation. It is also important to note is that the Relative Delay Monitoring (RDM) device does not monitor all of the relative hardware delay for which the GPS signal is subjected to: the path from the antenna to the remote station, the path through the RF front-end and a portion of the path in the local station are not monitored. We paid special attention to this propagation path because large temperature variations can be expected in this part of the system. Experiments with large temperature variations (40°C) between the RF front-ends of the remote stations were performed to quantify the possible repercussions on the positioning results. The effects were small, with only 1 mm additional bias due to this extreme temperature variation. However, it is also important to minimize as much as possible the length of the coaxial cable between the antenna and the remote station. Ideally it should be shorter than 1 meter.

The first tests of the system for positioning were done with a zero baseline. With this configuration, it was possible to estimate the relative hardware delay using GPS phase observations and compare the result with the Relative Hardware Delay (RHD) measured by the RDM device. At first glance, we found good agreement between these two independent estimations of the relative hardware delay as both had similar temporal evolution. This agreement was then validated with the positioning solutions. We found that, by using the measured delay by the RDM device and integrating it into the data processing, the precision of the vertical component improved by a factor of 2, reaching the level of precision as that of the horizontal components. Table 6.1 summarizes the main results. The zero baseline also allowed us to conclude that inter-channel biases in the software receiver used are negligible.

Table 6.1 Vertical positioning results for zero baseline

	STANDARD SOLUTION (with estimation of RHD as additional unknown)	PROPOSED SOLUTION (with RHD measured by the RDM as additional data)
Session	Average/rms value (Vertical component)	Average/rms value (Vertical component)
1	0.0 / 0.6 mm	0.2 / 0.3 mm
2	0.0 / 0.7 mm	0.0 / 0.3 mm

The final proof-of-concept was performed on a calibration beam used as a very short and precisely known baseline. The 3D reference coordinates of the beam were determined at millimetric level by carefully leveling and orientating the beam with respect to a known geodetic point. As in the case of the zero baseline, we compared the positioning solution for the standard approach (without using RDM measurements and estimating the relative hardware delay) and the proposed approach (using the RDM measurements for the relative hardware delay). The results are summarized in Table 6.2. It can be seen that by using the proposed method, there is a significant improvement in the rms value of the vertical coordinate when compared to the standard method. In all sessions, the rms value for the vertical coordinate improves almost by a factor of 3.

Two anomalies detected during the tests were identified: multipath and an offset in the average value of the vertical component for the proposed approach. For multipath, we used a simple sidereal multipath filtering technique which consisted of making temporal differences of the coordinates using a sidereal day temporal shift. This technique allowed it to slightly reduce the rms values of the 3D coordinates but further mitigation requires the use of multipath-rejecting antennas. The offset in the average value in the vertical component reached up to 3.7 mm, in one case. We suspect that this effect is due to the long cable length (15 m) between the antennas and the remote stations. In the final configuration, this length shall be reduced to below 1 meter but with the current prototype, this has not be realized. The estimation of an additional relative tropospheric zenith delay (RTZD) absorbs this offset to a great extend. For session 149A, the 3.7 mm bias in the

average vertical coordinate (232.7 mm to be compared to 229 mm external reference) was reduced to 1.5 mm by the inclusion of a RTZD in the estimation process.

Table 6.2 Summary of positioning results for small baseline

		STANDARD SOLUTION	PROPOSED SOLUTION (without tropospheric parameter estimation)	PROPOSED SOLUTION (with tropospheric parameter estimation)
Session	Baseline 3D component	Average/rms value (Average with respect to "true" value)	Average/rms value (Average with respect to "true" value)	Average/rms value (Average with respect to "true" value)
148A	Vertical	229.8 / 11.1 mm (0.8 mm)	229.9 / 4.4 mm (0.9 mm)	229.4 / 3.6 mm (0.4 mm)
149A	Vertical	230.5 / 9.2 mm (1.5 mm)	232.7 / 3.2 mm (3.7 mm)	230.5 / 2.7 mm (1.5 mm)
148R	Vertical	229.4 / 8.8 mm (0.4 mm)	227.1 / 4.1 mm (-1.9 mm)	228.5 / 3.7 mm (-0.5 mm)
150A	Vertical	288.7 / 17.4 mm (-0.3 mm)	286.6 / 4.9 mm (-2.4 m)	287.6 / 5.0 mm (-1.4 mm)
Reference 3D components of the baseline : -152 mm North, 988 mm East, 229 mm Vertical (289 mm Vertical for session 150A)				

6.2 Suggestions for further works

Even if a substantial improvement in the vertical precision could be realized with the current prototype, it still has some limitations but some ways of improving can be proposed. Two main issues were addressed in the previous sections: the multipath effect and the offset in the vertical position due to variations in the unmonitored coaxial cables of the system. The first issue has been addressed in the previous section. The second issue directly involves the design of our prototype. As was stated previously, the optimal and final design should take into consideration the shortening of the cables linking the GPS antennas to the remote stations. For this purpose, the remote stations should also be modified to make them weather-proof and tested for extreme weather conditions. In

general, all the system should be rebuilt with better electronic integration, miniaturization, portability and rugged-construction. This would allow it to conduct much needed tests of the remote stations outdoors.

Another important improvement is related to the relative delay monitoring (RDM) device. Currently, the linearity range of the phase comparator restricts the allowed variations of the relative hardware delay (RHD) to about 100° (40 mm of relative optical fiber length variation). This could be restrictive in extreme relative temperature variations between fibers. However, all standard phase comparators will suffer from this non-linearity limitation. Therefore, an in-phase (I) and quadrature-phase (Q) comparator is needed. In this kind of phase comparator, the phase of one signal is simultaneously compared to the in-phase and quadrature-phase versions of the other signal. When the phase comparison with the I signal loses linearity as it changes from 0 to 90° , the comparison with the Q signal is taken as its linearity increases. I and Q phase comparison is analogous to using the sin- and cos- functions. At 0° , the sin-function is close to linear and the cos-function is not, whereas at 90° , the inverse is true. Some additional engineering is needed to successfully implement and use the signals delivered by the I-Q phase comparators.

For the architecture design, more work has to be done to make the remote stations weather proof and compact, by means of better electronic integration and miniaturization. Currently, cumbersome laboratory equipment is used to control the temperature and current of the laser and the SOA and to generate the different oscillators. Such equipment must be replaced by small, portable circuits. The deployment of the system on a real structure such as a bridge or a dam with many remote stations is associated with challenges which will have to be dealt with and could lead to changes in the design and implementation. If existing optical fibers in the structure are to be used and only a few are available, the system could be modified so as to use a single fiber for both upstream and downstream communication and thus decrease the number of fibers needed. On the other hand, if new fibers have to be installed, a single cable containing several (12, 24 or more) optical fibers could be deployed along the remote stations. In this case, two optical fibers (one for upstream and one for downstream communication) would be taken apart from the cable and

directed to a given remote station from the cable. In this way, no changes in the design of the local and remote stations would be needed.

Further tests for longer periods of time would help to determine the possible long term effects of the aging of the components and the temperature variations effects. We have to keep in mind that a few uncalibrated components remain in the system, such as the cable between the antenna at the remote station and the RF front-end. It is important to assess the long term effects of these uncalibrated components.

The processing of the observations and the interpretation of the resulting positioning results need further work. An optimum way of filtering and/or smoothing the results to remove noise without removing information on the dynamics of the structure should be found. One interesting approach is proposed in (Li & Kuhlmann, 2010), where a multiple Kalman filtering model is used, which gives the advantages of Kalman of the movement filtering applied to a deformation monitoring application but without losing information for the detection of deformation.

Another area where further work is to be done is in the data processing software. Currently, the software successfully processes single difference observations with additional RDM data integration but this is done in the post-processing mode without a user-friendly interface. Important software engineering work can be done to enable real-time processing with an interface designed for the end-users. The data processing can even be integrated with the software used by the FPGA-based GPS receiver for a truly integrated software solution.

Even though the monitoring of engineering structures and of natural crustal deformations (landslides, ground subsidences, volcanoes,...) are the intended applications, we think that this architecture may be used for alternative applications such as attitude determination and GPS time-transfer. For the attitude measurement application, the proposed architecture would allow the precision of the roll and pitch angles to be as good as the yaw angle. For the time-transfer application, it would allow to remove the unwanted effects of cable (fiber)

relative delay variations due to temperature changes as the real-time precise monitoring of the relative hardware delays is an important issue in this kind of applications.

The final objective of the improvements and further work is the development of a system which could be used in real applications and commercialized. The market for high precision GPS applications is expected to grow in the next years (Research and Markets, 2008). Particularly, as current engineering structures become older and new ones are more audacious in terms of dimensions and capacity, the need for 3D high precision, autonomous, real-time monitoring of these structures increases. We think that with the promising results documented in this work, many end-users should show an interest in this technology.

Bibliography

- Ackerman, E., & Cox, C. (2001). RF fiber-optic link performance. *IEEE Microwave Magazine*, 2(4), pp. 50-58.
- AFW Technologies. (2010). *Singlemode Standard Tree Coupler Module*.
http://www.afwtechnology.com.au/coupler/single_mode_standard_tree_couple_modu_SMTC-MxN.htm
- Agrawal, G. (2001). *Nonlinear Fiber Optics, 3rd Edition*. Academic Press.
- Agrawal, G. (2002). *Fiber-Optic Communication Systems, 3rd edition*. Wiley-Interscience.
- Akrou, B. (1998). *Utilisation optimale du système de positionnement GPS pour les travaux d'auscultations de barrages, Mémoire M.Sc.*, Faculté de Foresterie et de Géomatique, Université Laval.
- Allan, D. W., Ashby, N., & Hodge, C. C. (1997). *The Science of Timekeeping*. Application Note 1289, Hewlett Packard.
- Arbour, B. (1994). *Étude des effets des multitrajets sur le positionnement GPS avec les mesures de phase des ondes porteuses, Mémoire M.Sc.*, Faculté de Foresterie et de Géomatique, Université Laval.
- Astronomical Institute - University of Bern. (2004). *Bernese GPS software version 5.0*. (R. Dach, U. Hugentobler, P. Fridez, & M. Meindl, Eds.) Bern.
- Barnes, J., Rizos, C., Lee, H.-K., Roberts, G., Meng, X., Cosser, E. (2005). The integration of GPS and pseudolites for bridge monitoring. *International Association of Geodesy Symposia*, 128, pp. 83-88.
- Bétaille, D., Cross, P., & Euler, H. (2006). Assessment and improvement of the capabilities of a window correlator to model GPS multipath phase errors. *IEEE Transactions on Aerospace and Electronic Systems*, 42(2), pp. 705-717.
- Beutler, G., Bauersima, I., Gurtner, W., Rothacher, M., & Geiger, A. (1988). *Atmospheric refraction and other important biases in GPS carrier phase observations*. Atmospheric Effects on Geodetic Space Measurements, Monograph 12, School of Surveying, University of New South Wales, Kensington, Australia.

- Bibey, M., Deborgies, F., Krakowski, M., & Mongardien, D. (1999). Very low phase-noise optical links - Experiments and theory. *IEEE Transactions on Microwave Theory and Techniques*, 47(12), pp. 2257-2262.
- Bock, O., & Doerflinger, E. (2001). Atmospheric modeling in GPS data analysis for high accuracy positioning. *Physics and Chemistry of The Earth Part A- Solid Earth and Geodesy*, 26(6-8), pp. 373-383.
- Bourassa, M. (1994). *Étude des effets de la variation des centres de phase des antennes GPS*, Mémoire M.Sc., Faculté de Foresterie et de Géomatique, Université Laval.
- Bruyninx, C., Defraigne, P., Dehant, V., & Paquet, P. (2000). Frequency transfer using GPS carrier phases : Influence of temperature variations near receiver. *IEEE Transactions on Ultrasonics, Ferroelectrics and Frequency Control*, 47, pp. 522-525.
- Cliche, J., & Shillue, B. (2006). Precision timing control for radioastronomy - Maintaining femtosecond synchronization in the Atacama Large Millimeter Array. *IEEE Controls Systems Magazine*, 26(1), pp. 19-26.
- Corning Inc. (2002). Corning SMF-28 Optical Fiber Product Information.
- Costa, B., Mazzoni, D., Puleo, M., & Vezzoni, E. (1982). Phase shift technique for the measurement of chromatic dispersion in optical fibers using LED's. *IEEE Journal of Quantum Electronics*, 18(10), pp. 1509-1515.
- Dennis, T., & Williams, P. (2005). Achieving high absolute accuracy for group-delay measurements using the modulation phase-shift technique. *Journal of Lightwave Technology*, 23(11), pp. 3748-3754.
- Essen, L., & Froome, K. (1951). The refractive indices and dielectric constants of air and its principal constituents at 24 000 Mc/s. *Proceedings of Physical Society*, 64(B), pp. 862-875.
- Georgiadou, Y., & Kleusberg, A. (1988). On carrier signal multipath effects in relative GPS positioning. *Manuscripta Geodaetica*, 13, pp. 172-179.
- Gliese, U., Christensen, E., & Stubkjaer, K. (1991). Laser linewidth requirements and improvements for coherent optical beam forming networks in satellites. *Journal of Lightwave Technology*, 9(6), pp. 779-790.
- Görres, B., Campbell, J., Becker, M., & Siemes, M. (2006). Absolute calibration of GPS antennas: laboratory results and comparison with field and robot techniques. *GPS Solutions*, 10, pp. 136-145.

- GPS Networking. (2010). *Focal Optic Network Systems*. <http://gpsnetworking.com/fiber-optic-network.asp>
- Hatch, R. (1990). Instantaneous ambiguity resolution. *Proceeding of the International Symposium on Kinematic Systems in Geodesy, Geomatics and Navigation (KIS)*, pp. 299-308. Banff, Canada.
- He, X., Sang, W., Chen, Y., & Ding, X. (2005). Steep slope monitoring - GPS multiple-antenna system at Xiaowan dam. *GPS World*, 16(11), pp. 20-24.
- Hemisphere GPS. (2010). *VS101 and VS111 GPS compass*. <http://www.hemispheregps.com/Products/PrecisionProducts/Main/tabid/543/LiveAccId/21971/Default.aspx>
- Henry, C. (1982). Theory of the linewidth of semiconductor lasers. *IEEE Journal of Quantum Electronics*, QE-18(2), pp. 259-264.
- Hilt, A. (2000). Microwave harmonic generation in fiber optical links. *Proceedings of the MIKON'2000 Conference*, 2, pp. 693-698. Wroclaw, Poland.
- International GNSS Service. (2010). *IGS - International GNSS Service*. <http://igsceb.jpl.nasa.gov/>
- Javad Navigation Systems. (2010). *JNSGyro-2T*. <http://www.javad.com/jns/index.html>
- Jekeli, C. (2000). *Inertial navigation systems with geodetic applications*. Berlin - New York: Walter de Gruyter.
- Kakimoto, S., & Watanabe, H. (1998). Threshold current, differential gain and relaxation resonance frequency of 1.55 micrometer bulk and MQW DFB laser diodes. *IEEE Journal of Quantum Electronics*, 34(7), pp. 1231-1239.
- Kalman, R., Fan, J., & Kazovsky, L. (1994). Dynamic range of coherent fiber-optic links. *Journal of Lightwave Technology*, 12(7), pp. 1263-1277.
- Kaplan, E., & Hegarty, C. (2006). *Understanding GPS principles and applications* (2nd Edition). Artech House.
- Keiser, G. (2000). *Optical fiber communications – 3rd edition*. Mc Graw Hill.
- Klobuchar, J. A. (1987). Ionospheric time-delay algorithm for single-frequency GPS users. *IEEE Transactions on Aerospace and Electronic Systems*, AES-23(3), pp. 325-331.
- Klobuchar, J.A. (2001). Eye on the ionosphere: correction methods for GPS ionospheric range delay. *GPS solutions*, 5(2), pp. 91-92.

- Kouba, J., & Héroux, P. (2001). Precise point positioning using IGS orbit and clock products. *GPS Solutions*, 5(2), pp. 12-28.
- Lamoureux, L. (1998). *Étude sur l'utilisation du système GPS pour l'auscultation topographique du Pont Pierre-Laporte*, Mémoire M.Sc. Faculté de Foresterie et de Géomatique, Université Laval.
- Larson, D., & Paulter Jr., N. (2007). A measurement of propagation delay. *Metrologia*, 44, pp. 64-69.
- Lau, K., & Blauvelt, H. (1988). Effect of low-frequency intensity noise on high-frequency direct modulation of semiconductor injection lasers. *Applied Physics Letters*, 52(9), pp. 694-696.
- Li, L., & Kuhlmann, H. (2010). Deformation detection in the GPS real-time series by the multiple Kalman filters model. *Journal of Surveying Engineering*, 136(4), pp. 157-164.
- Li, Y., Zhang, K., Roberts, C., & Murata, M. (2004). On-the-fly GPS based attitude determination using single- and double-differenced carrier phase measurements. *GPS Solutions*, 8(2), pp. 93-102.
- Lindlohr, W., & Wells, D. (1985). GPS design using undifferenced carrier beat phase observations. *Manuscripta Geodaetica*, 10, pp. 255-295.
- Lutes, G., & Diener, W. (1989). *Thermal coefficient of delay for various coaxial and fibre-optic cables*. Telecommunications and Data Acquisition (TDA) progress report 42-99, NASA Jet Propulsion Laboratory.
- MacDoran, P., Feuerstein, R., & Schreiner, W. (1992). GPS spread spectrum signal transmission over fiber optic links. *IEEE Transactions on Geoscience and Remote Sensing*, 30(5), pp. 1073-1076.
- Macias-Valadez, D., LaRochelle, S., Santerre, R., & Fillion, B. (2009a). Fiber optic synchronisation architecture for high precision GPS applications. *Conference on Optical Fiber Communication OFC 2009*, pp. 1-3. San Diego, U.S.A.
- Macias-Valadez, D., Santerre, R., LaRochelle, S., & Landry Jr., R. (2009b). GPS-over-fiber architecture with relative cable delay monitoring for high precision GPS applications. *Proceedings of the 22nd International Technical Meeting of the Satellite Division of the Institute of Navigation (ION GNSS 2009)*, pp. 622-634. Savannah, U.S.A.

- Macias-Valadez, D., Santerre, R., & LaRochelle, S. (2010). Method and system for high precision GPS applications, *Patent No. PCT/CA2010/000433 (Patent Pending)*. International Application.
- Mechels, S., Schlager, J., & Franzen, D. (1997). High-resolution differential-mode delay measurements in optical fibers using a frequency-domain phase-shift technique. *IEEE Photonics Technology Letters*, 9(6), pp. 794-796.
- Mendes, V., & Langley, R. (1994). A comprehensive analysis of mapping functions used in modeling tropospheric propagation delay in space geodetic data. *Proceeding of the International Symposium on Kinematic Systems in Geodesy, Geomatics and Navigation (KIS)*, pp. 87-98. Banff, Canada.
- Misra, P., & Enge, P. (2001). *Global Positioning System*. Ganga-Jamuna Press.
- Raven Precision (2010). *Raven Precision - Product Listing*.
<http://www.ravenprecision.com/atc/GPS/Products/productList.jsp?Category=5>
- Research and Markets (2008). *GPS Precise Positioning Markets 2008-2012*.
http://www.researchandmarkets.com/reportinfo.asp?report_id=668343&t=d&cat_id
- Rieck, C., Jarlemark, P., Jaldehag, K., & Johansson, J. (2003). Thermal influence on the receiver chain of GPS carrier phase equipment for time and frequency transfer. *Proceedings of the 2003 IEEE International Frequency Control Symposium and PDA Exhibition Jointly with the 17th European Frequency and Time Forum*, pp. 326-331. Tampa, U.S.A.
- Rothacher, M., Beutler, G., Gurtner, W., Geiger, A., Kahle, H., & Schneider, D. (1986). The 1985 Swiss GPS campaign. *Proceedings of the Fourth International Geodetic Symposium on Satellite Positioning*, pp. 979-991. Austin, U.S.A.
- RP Photonic Consulting. (2010a). *Acousto-optic Modulators*. (R. Paschotta, Editor) Encyclopedia for Photonics and Laser Technology: http://www.rp-photonics.com/acousto_optic_modulators.html
- RP Photonics Consulting. (2010b). *Electro-optic Modulators*. (R. Paschotta, Editor) Encyclopedia for Photonics and Laser Technology: <http://www.rp-photonics.com/encyclopedia.html>
- Saastamoinen, J. (1972). Contributions to the theory of atmosphere refraction. *Bulletin Géodésique*, 105, 106, 107, pp. 279-298, 383-397, 13-34.
- Santerre, R. (1989). *GPS satellite sky distribution: impact on the propagation of some important errors in precise relative positioning*, Ph.D. Dissertation. Department of Surveying Engineering Technical Report 145, University of New Brunswick.

- Santerre, R. (1991). Impact of GPS satellite sky distribution. *Manuscripta Geodaetica*, 16(1), pp. 28-53.
- Santerre, R., & Beutler, G. (1993). A proposed GPS method with multi-antennae and single receiver. *Bulletin Géodésique*, 67, pp. 210-223.
- Santerre, R., & Geiger, A. (1998). Geometrical interpretation of GPS positioning with single, double and triple difference carrier phase observations. *Proceedings of the Symposium on Geodesy for Geotechnical and Structural Engineering, IAG Special Commission IV*, pp. 465-470. Eisenstadt, Austria.
- Sauriol, B., & Landry Jr., R. (2007). FPGA-based architecture for high throughput, flexible and compact real-time GNSS software defined receiver. *Proceedings of the 2007 National Technical Meeting of the Institute of Navigation*, pp. 708-717. San Diego, U.S.A.
- Schreiner, W. (1990). A covariance study for orbit accuracy improvement of the GPS satellites using fiber optics tracking. *Proceedings of the Institute of Navigation ION GPS-90*, pp. 563-568. Colorado Springs, U.S.A.
- Skone, S., El-Gizawy, M., & Shrestha, S. (2001). Limitations in GPS positioning accuracies and receiver tracking performance during solar maximum. *Proceedings of the International Symposium on Kinematic Systems in Geodesy, Geomatics, and Navigation (KIS)*, pp. 129-143. Banff, Canada.
- Souza, E., & Monico, J. (2004). Wavelet shrinkage: high frequency multipath reduction from GPS relative positioning. *GPS Solutions* 8(3), pp. 152-159.
- Suhner Holding AG. (1999). Suhner coaxial cable type RG-58 C/U datasheet.
- Teunissen, P. (1996). GPS carrier phase ambiguity fixing concepts. In A. Kleusberg, & P. Teunissen, *GPS for Geodesy - Lecture Notes in Earth Sciences* pp. 263-335. Springer Berlin / Heidelberg.
- Thayer, G. (1974). An improved equation for the radio refractive index of air. *Radio Science*, 9(10), pp. 803-807.
- Topcon Positioning Systems. (2010). *Topcon Mobile Control Products*.
<http://www.topconsolutions.com/products.html>
- Tranquilla, J., & Colpitts, B. (1989). GPS antenna design characteristics for high-precision applications. *Journal of Surveying Engineering*, 115(1), pp. 2-14.

- U.S. Naval Observatory. (2010). *USNO GPS Time Transfer*.
<http://www.usno.navy.mil/USNO/time/gps/usno-gps-time-transfer>
- Vacondio, F., Sisto, M., Mathlouthi, W., Rusch, L., & LaRochelle, S. (2006). Electrical-to-optical conversion of OFDM 802.11g/a signals by direct current modulation of semiconductor optical amplifiers. *2006 International Topical Meeting on Microwave Photonics*, pp. 1-4.
- van Dierendonck, A., Fenton, P., & Ford, T. (1992). Theory and performance of narrow correlator spacing in a GPS receiver. *Navigation: Journal of the Institute of Navigation*, 39(3), pp. 265-283.
- Vialite-PPM (2010). *Vialite RF-over-fiber - Metro GPS*.
<http://www.vialite.co.uk/products/metro-gps/metro-gps.html>
- Wild, U., Beutler, G., Gurtner, W., & Rothacher, M. (1989). Estimating the ionosphere using one or more dual frequency GPS receivers. *Proceedings of the Fifth International Geodetic Symposium on Satellite Positioning*, pp. 724-736. Las Cruces, U.S.A.
- Wübenna, G., & Schmitz, M. (2000). Automated absolute field calibration of GPS antennas in real-time. *Proceedings of the 2000 Technical Meeting of the Institute of Navigation (ION GPS 2000)*, pp. 2512-2522. Salt Lake City, U.S.A.
- Zhong, P., Ding, X., Yuan, L., Xu, Y., Kwok, K., & Chen, Y. (2009). Sidereal filtering based on single differences for mitigating GPS multipath effects on short baselines. *Journal of Geodesy*, 84, pp. 145-158.

Appendix A Detailed schematics and components' list for the proposed architecture

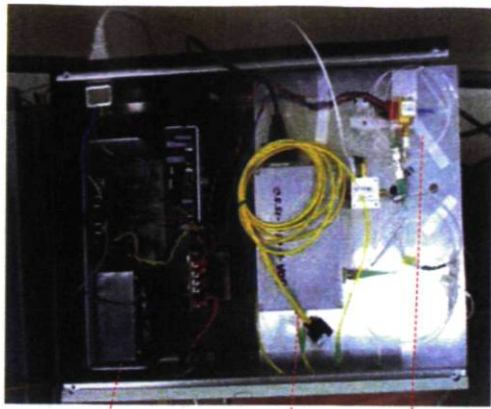
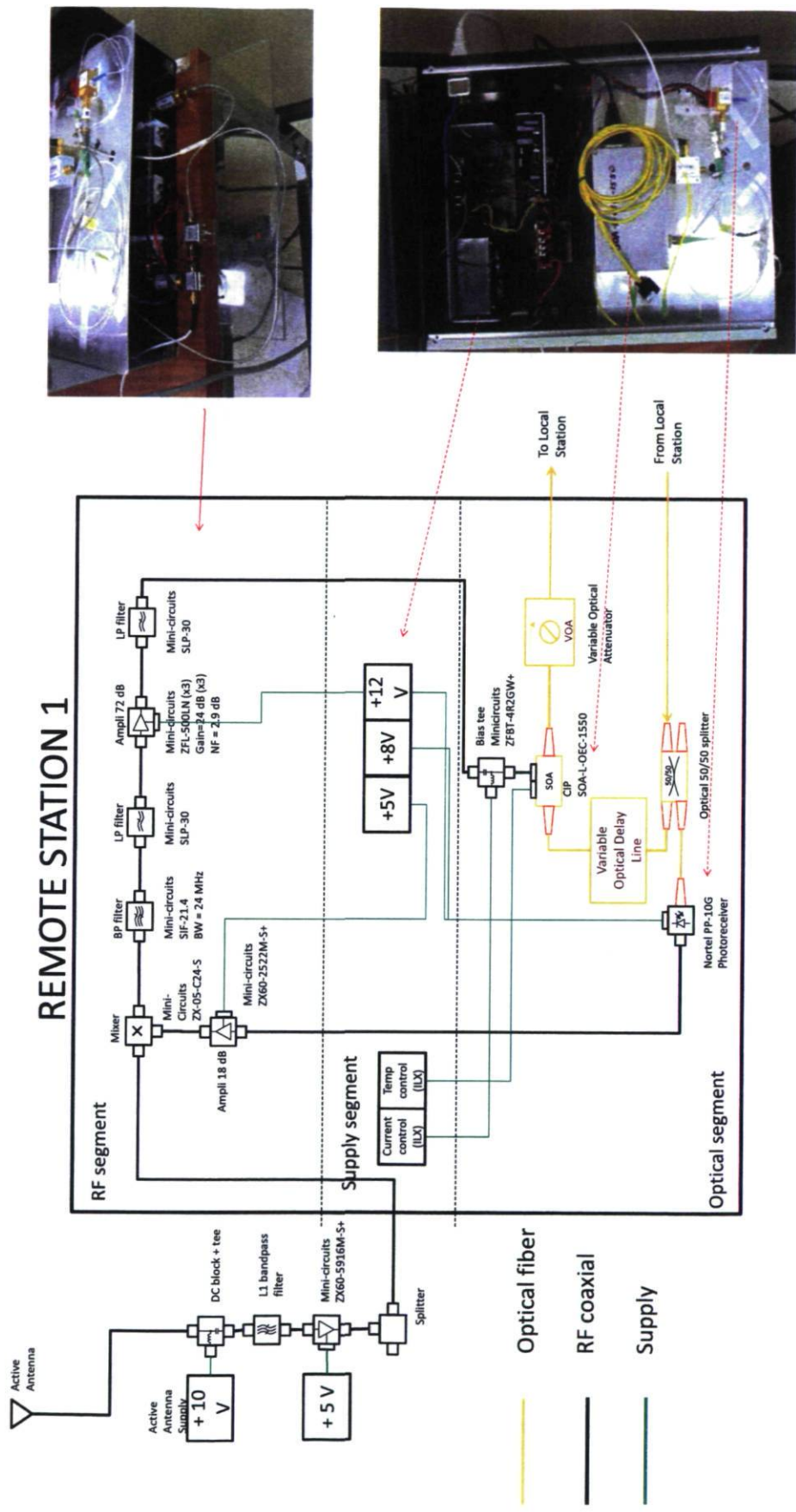


Figure A.1 Detailed schematics for the remote station

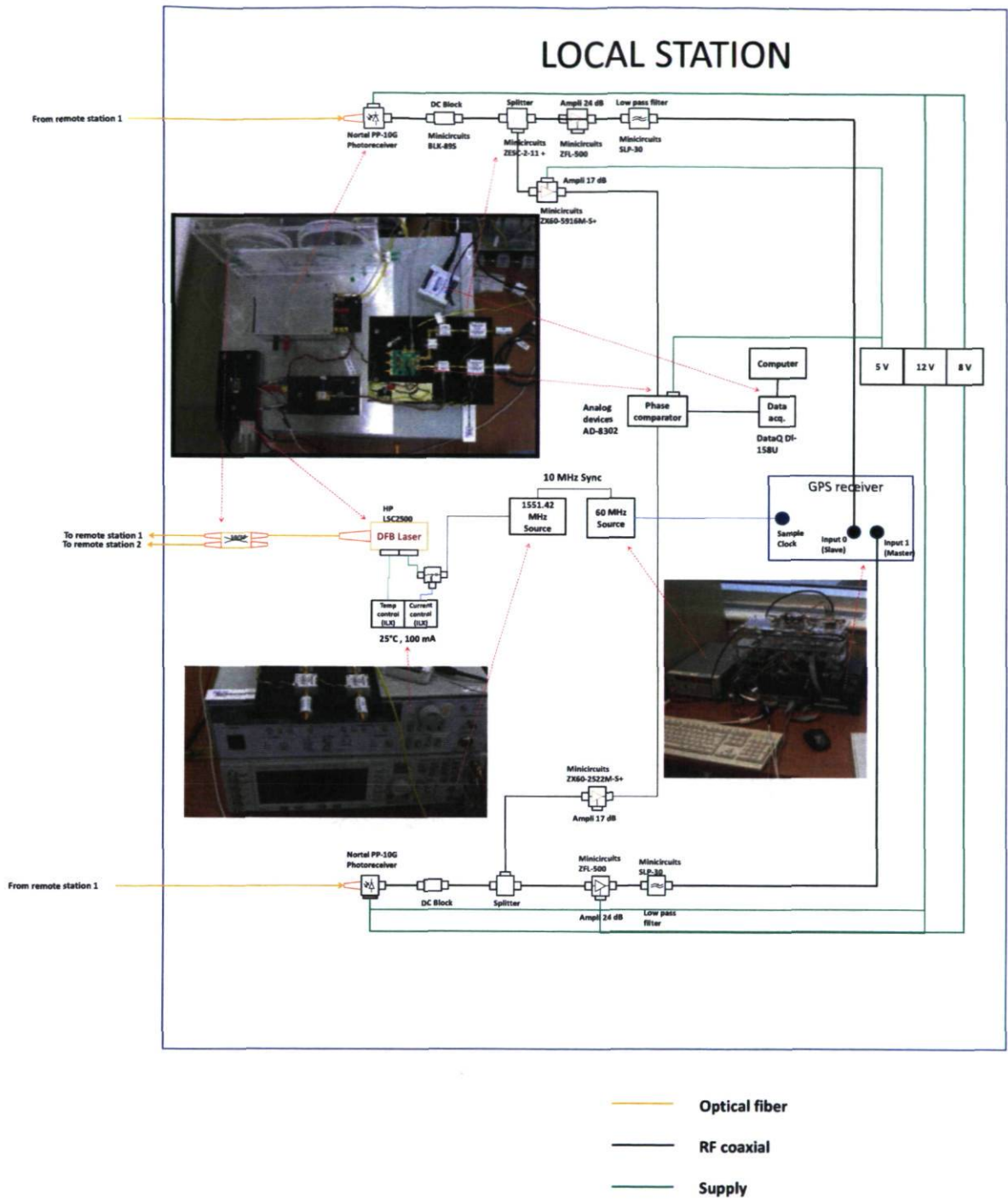
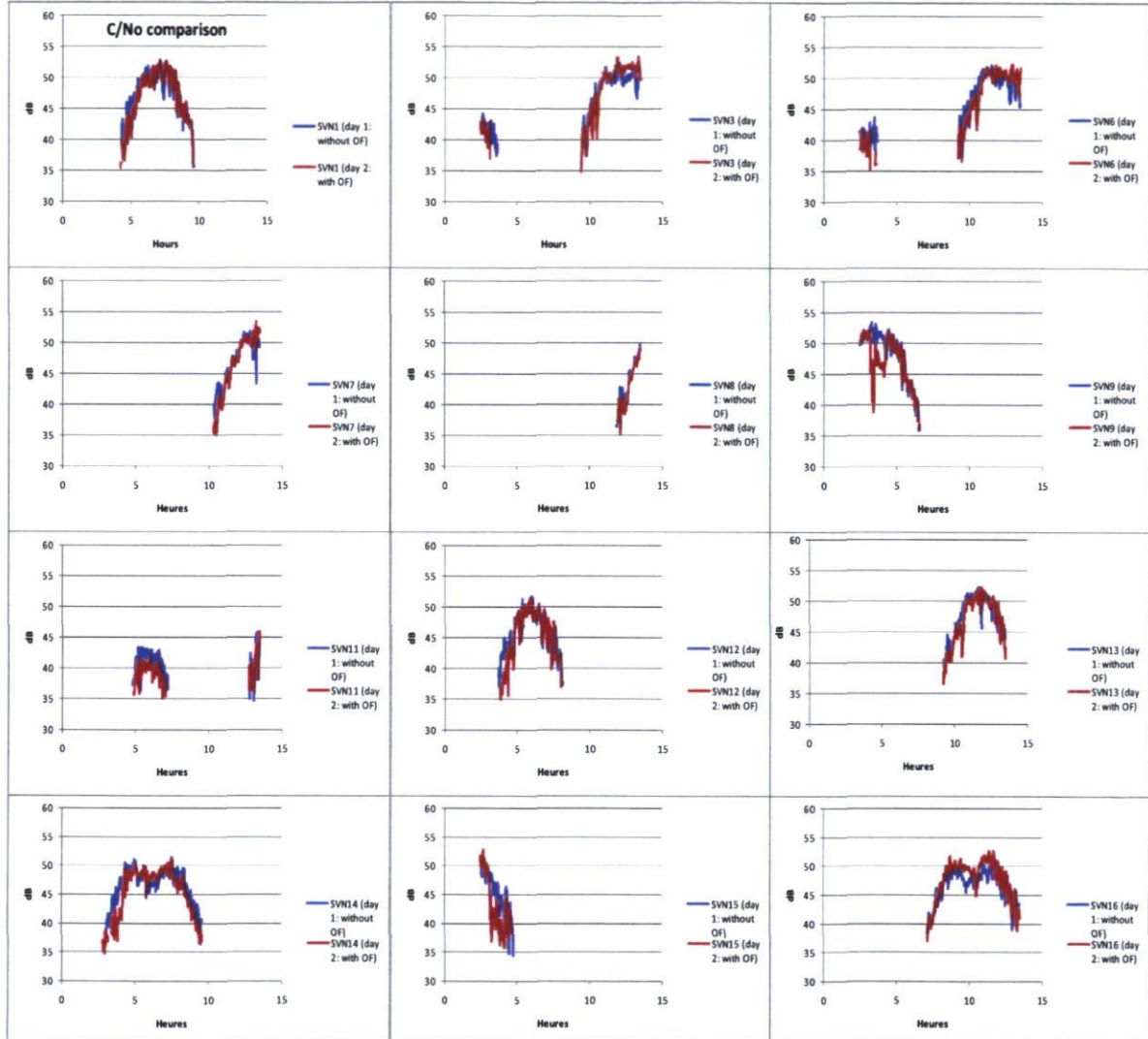


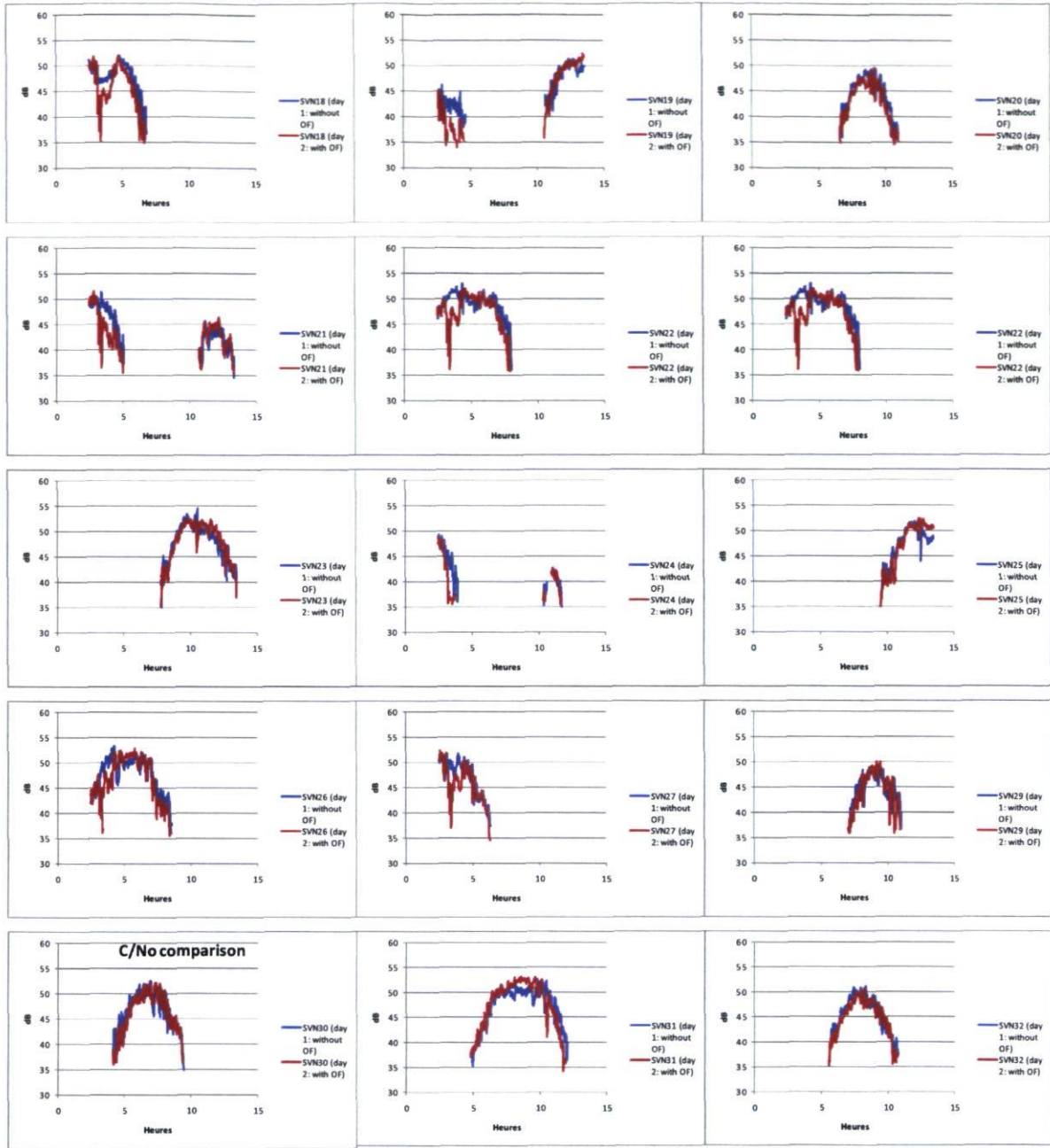
Figure A.2 Detailed schematics for the local station

Table A.1 Components' list

Set	Sub-set	Component	Company	Part number	Quantity	Unit price	Price	
ANTENNA TO REMOTE STATION ASSEMBLY		Antenna			1			
		TNC to BNC adaptor	Digikey	ARF1104-ND	2	32.66 \$	65.32 \$	
		BNC T connector	Digikey	ACX1064-ND	2	2.94 \$	5.88 \$	
		SMA female to BNC male adaptor	Digikey	501-1140-ND	2	9.00 \$	18.00 \$	
		L1 amplifier	Mini-circuits	ZX60-2522M-S+	1	59.95 \$	59.95 \$	
		DC-block	Mini-circuits	BLK-89-S+	1	14.95 \$	14.95 \$	
		L1 SAW band-pass filter	EPCOS	B4050	1	10.00 \$	10.00 \$	
REMOTE STATION	RF Front end	Mixer 1	Mini-circuits	ZX-05-C24-S	1	37.95 \$	37.95 \$	
		BP filter	Mini-circuits	SIF-21.4	1	38.95 \$	38.95 \$	
		LP filter	Mini-circuits	SLP-30	2	34.95 \$	69.90 \$	
		Amplifier IF (3 X 24 dB)	Mini-circuits	ZFL-500LN	3	79.95 \$	239.85 \$	
		Amplifier RF 18 dB	Mini-circuits	ZX60-2522M-S+	2	59.95 \$	119.90 \$	
		SMA male-male connector	Digikey	J633-ND	4	18.50 \$	74.00 \$	
		Bias tee 2	Mini-circuits	ZFBT-4R2GW+	1	79.95 \$	79.95 \$	
	Optical circuit	SOA	CIP	SOA-L-OEC-1550	1	1 925.00 \$	1 925.00 \$	
		50/50 splitter			1	50.00 \$	50.00 \$	
		Photodetector	Bookham	PP-10G	1	325.00 \$	325.00 \$	
		DC-block	Mini-circuits	BLK-89-S+	1	14.95 \$	14.95 \$	
		Câble SMA 24"	Digikey	J3724-ND	4	15.72 \$	62.88 \$	
		Câble SMA 48"	Digikey	J4148-ND	4	21.27 \$	85.08 \$	
		Supply and controller	DC supply +5 V			1	56.00 \$	56.00 \$
	DC supply +8 V				1	56.00 \$	56.00 \$	
	DC supply +12 V				1	56.00 \$	56.00 \$	
	Temperature controller		ILX Lightwave		1	550.00 \$	550.00 \$	
	Current controller		ILX Lightwave		1	550.00 \$	550.00 \$	
	Box assembly				1	87.00 \$	87.00 \$	
	Miscellaneous (connectors, cables, etc)				1	300.00 \$	300.00 \$	
	TOTAL REMOTE STATION							4 952.51 \$
	REMOTE STATION TO LOCAL STATION ASSEMBLY		12 fiber Singlemode Armored Cable	Hitachi Cable Manchester		1000 m	1.18 \$/m	1 180.00 \$
			Variable Optical Delay Line	General Photonics		1	2 150.00 \$	2 150.00 \$
			Fiber optic connectors					
	LOCAL STATION	Reference signals generation	Laser	HP	LSC-2500	1		400.00 \$
			1551.42 MHz oscillator			1		
			Temperature controller	ILX Lightwave		1	550.00 \$	550.00 \$
Current controller			ILX Lightwave		1	550.00 \$	550.00 \$	
Optical to electrical conversion		Photodetector	Bookham	PP-10G	2	325.00 \$	650.00 \$	
		DC-block	Mini-circuits	BLK-89-S+	2	14.95 \$	29.90 \$	
		Splitter	Mini-circuits	ZESC-2-11 +	2	64.95 \$	129.90 \$	
		Amplifier IF (24 dB)	Mini-circuits	ZFL-500LN	2	79.95 \$	159.90 \$	
		LP filter	Mini-circuits	SLP-30	2	34.95 \$	69.90 \$	
Phase detector		Phase comparator	Analog devices	AD-8302 (eval board)	1	200.00 \$	200.00 \$	
		Data acquisition	DataQ	DI-158-U	1	99.00 \$	99.00 \$	
Supply and controller		DC supply +5 V			1			
		DC supply +8 V			1			
		DC supply +12 V			1			
TOTAL LOCAL STATION							6 168.60 \$	

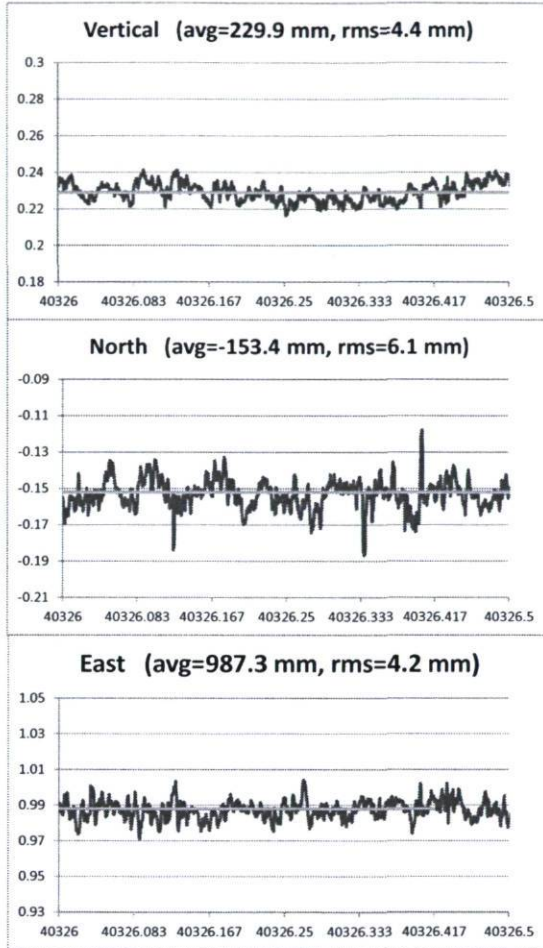
Appendix B C/N_0 comparison between the standard GPS-over-cable case and the proposed GPS-over-fiber case





Appendix C Comparison of positioning results without and with tropospheric parameter estimation

Proposed solution WITHOUT tropospheric parameter estimation



Proposed solution WITH tropospheric parameter estimation

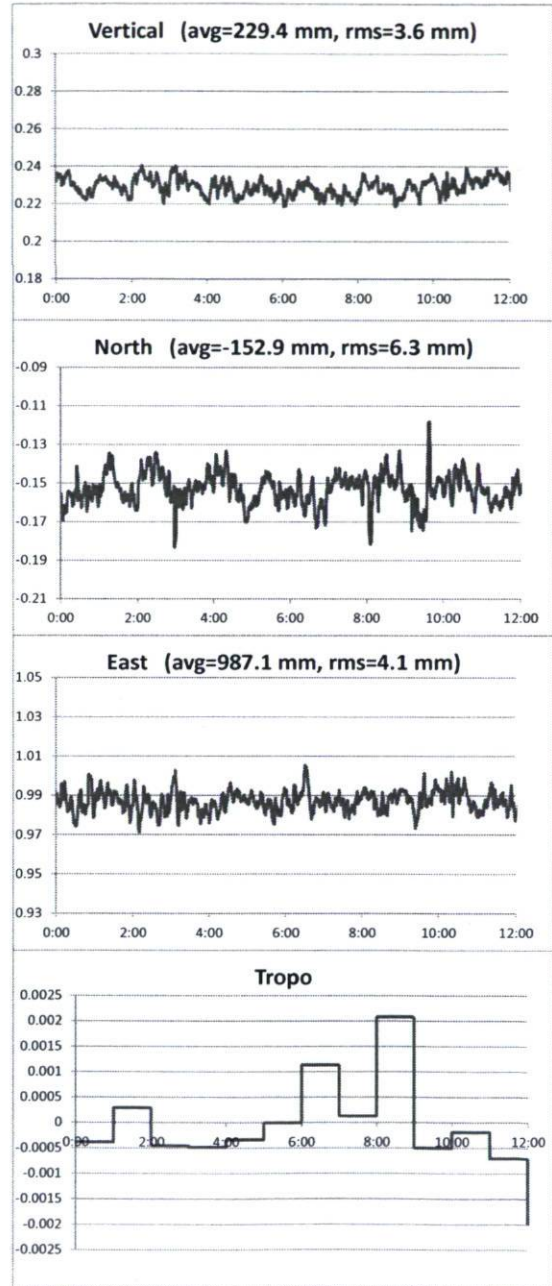
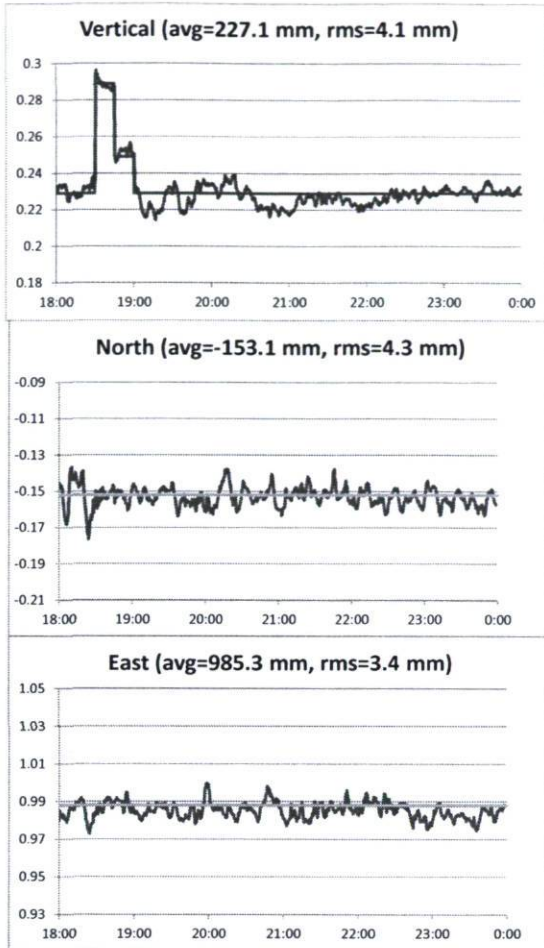


Figure C.1 Comparison without and with tropospheric parameter estimation for session 148A

Proposed solution WITHOUT tropospheric parameter estimation



Proposed solution WITH tropospheric parameter estimation

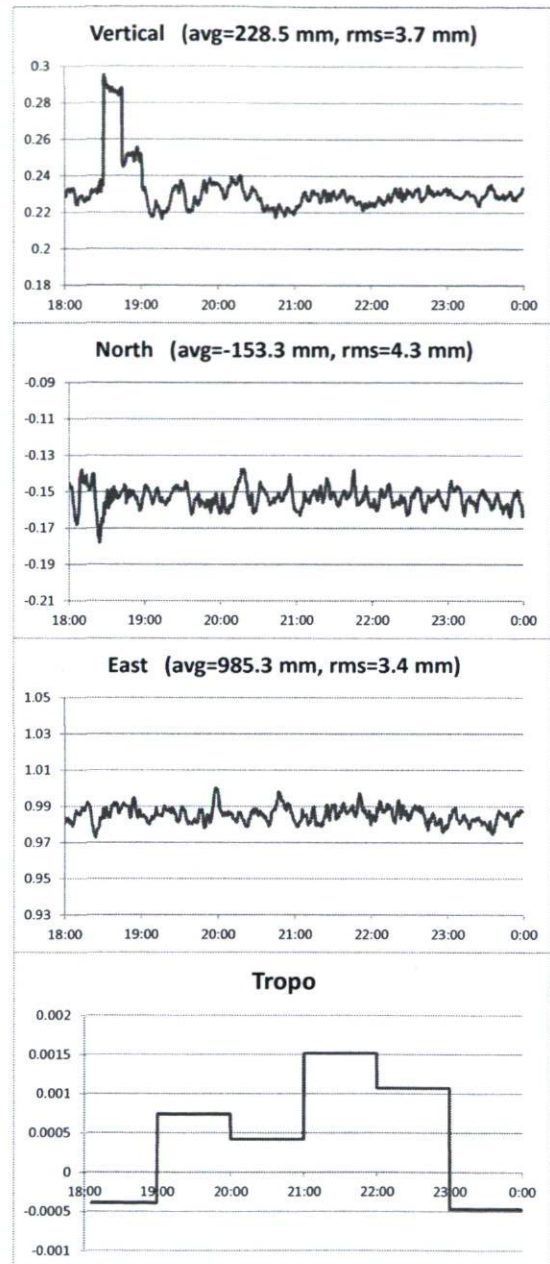
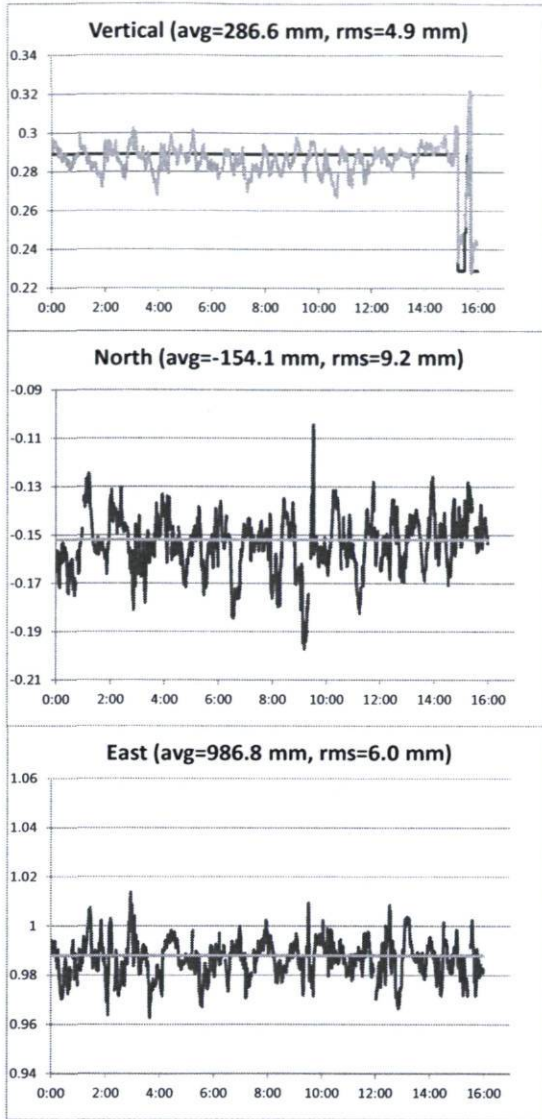


Figure C.2 Comparison without and with tropospheric parameter estimation for session 148R

Proposed solution WITHOUT tropospheric parameter estimation



Proposed solution WITH tropospheric parameter estimation

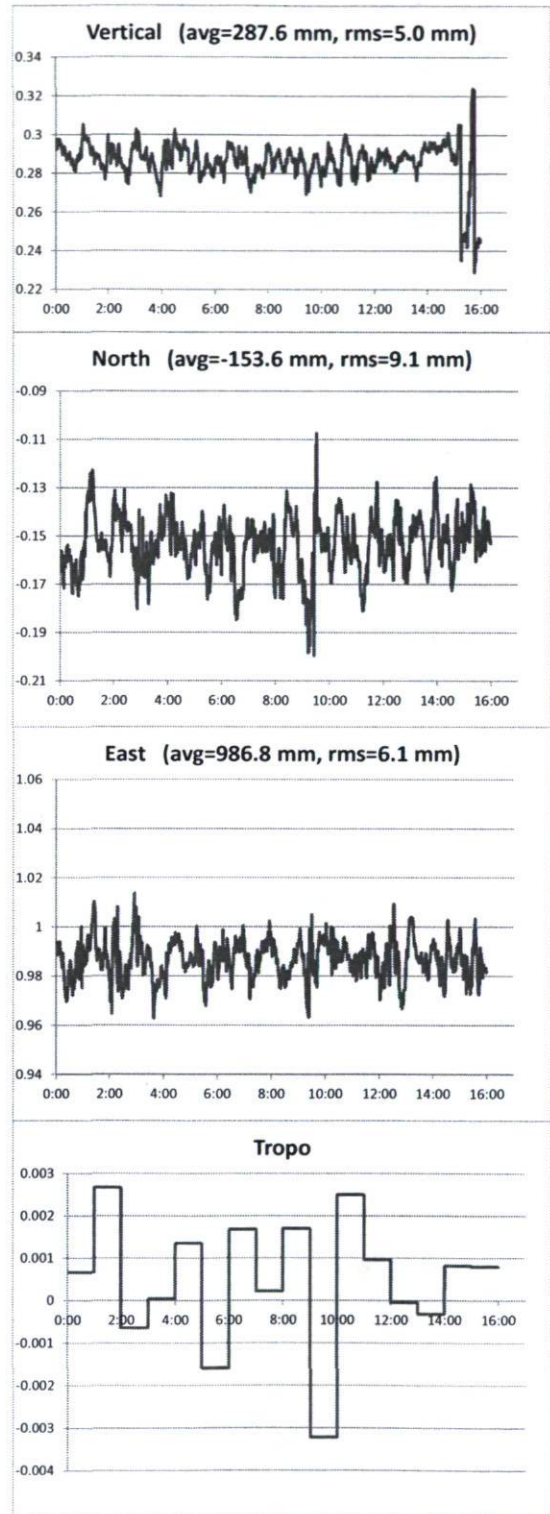


Figure C.3 Comparison without and with tropospheric parameter estimation for session 150A